Characterization of the ATLAS-type Micromegas Detectors

Dissertation zur Erlangung des naturwissenschaftlichen
Doktorgrades der Julius-Maximilians-Universität Würzburg

vorgelegt von

Ourania Sidiropoulou

aus

Thessaloniki, Griechenland

Würzburg 2018

CC BY

Eingereicht am 14.05.2018

bei der Fakultät für Physik und Astronomie

1. Gutachter: Prof. Dr. Thomas Trefzger

2. Gutachter: Prof. Dr. Otmar Biebel

der Dissertation

Vorsitzende(r): Prof. Dr. Matthias Kadler

1. Prüfer: Prof. Dr. Thomas Trefzger

2. Prüfer: Prof. Dr. Otmar Biebel

3. Prüfer: Prof. Dr. Werner Porod

im Promotionskolloquium

Tag des Promotionskolloquiums: 03.08.2018

Doktorurkunde ausgehändigt am: ....

Abstract

Micromegas are parallel-plate gaseous detectors with micro-pattern readout structures that are able to measure precisely and efficiently at high particle rates. Their difference with respect to other gaseous detectors is that the space in which particles ionise the gas and create electrons is separated from the region in which these electrons are multiplied (or amplified) by a thin metallic mesh. In the ionisation region, typically a few mm thick, a moderate field of a few hundred V/cm is applied. The amplification region with a homogeneous electrical field of 40–50 kV/cm is only 100–150 μm thick. The latter guarantees that the positive ions produced in the amplification process are rapidly evacuated and the possibility to build up space charge at high rate is reduced. Critical in micromegas detectors are sparks in the thin amplification region in the presence of the high electrical field. This problem was solved in 2011 by introducing a spark protection scheme. It consists of a layer of resistive strips on top of the readout strips, separated from the latter by a thin insulation layer.

Micromegas with the spark protection scheme were selected as instrumentation of the first ATLAS forward muon station (NSW) in the upgrade of the ATLAS detector for the operation of the Large Hadron Collider (LHC) at high luminosity (HL-LHC), expected for 2026.

The main subjects of this thesis are: the characterisation of the first micromegas quadruplet prototypes for the NSW detectors; the characterisation of the materials used in the spark-protection system; and the study of the influence of the mesh distance holders (pillars) on the detector performance.

The thesis starts with a brief introduction into the LHC and ATLAS projects, followed by a chapter that explains the reason for the upgrade of the ATLAS muon system and shows the layout of the NSW.

The first of the three main chapters covers the construction and the characterisation of the first two prototypes for the NSW detectors. These detectors comprise four detection layers and have the same mechanical structure as the NSW detectors. The mechanical precision as well as the homogeneity of the detector response are discussed. The latter has been measured using X-rays and cosmic rays. The spatial resolution that can be achieved with these detectors precision has been measured at the MAMI accelerator at Mainz with low-energy electrons. The chapter is completed by a section that describes the successful integration of a data acquisition system (DAQ) into the official ATLAS DAQ system that was required for an initially planned installation of one of the prototypes on the existing Small Wheel.

The next chapter presents a study of the influence of temperature and humidity changes on the resistive strips used in the spark protection system. In addition the long-term stability of the resistive material has been measured accumulating charge equivalent to 100 years of operation in the HL-LHC and exposing the samples to intense gamma irradiation equivalent to 10 years of HL-LHC operation.

The third part covers the impact of the mesh distance holders (pillars) on the performance of the detector. This study has been performed with a 10 x 10 cm^2 bulk-micromegas with two different pillar shapes. Both 5.9 keV gammas from a ^{55}Fe

and 8 keV X-rays from a Cu target were used. In this context also the electrostatic charge-up of the detector is discussed.

In the Appendices one finds a summary of the fundamental physics relevant for gaseous detectors as well as some supporting material for the topics covered in the main part of the thesis.

Kurzdarstellung

Micromegas-Detektoren sind Gas-Detektoren aus der Familie der Parallel-Platten-Detektoren mit sehr feinen Auslese-Elementen, die präzise und effizient bei hohen Teilchenraten messen können. Sie unterscheiden sich von anderen Gas-Detektoren dadurch, dass der Bereich, in dem die zu messenden Teilchen das Gas ionisieren und damit Elektronen produzieren, von dem Bereich, in dem diese Elektronen vervielfältigt werden, durch ein feines metallisches Gitter getrennt ist. Im Ionisationsbereich der gewöhnlich mehrere mm dick ist, wird ein moderates elektrisches Feld von einigen hundert Volt angelegt. Der Vervielfachungs- oder Verstärkungsbereich mit einem homogenen elektrischen Feld von $\sim$40–50 kV/cm ist nur 100–150 μm dick. Dadurch können die positiven Ionen, die im Vervielfältigungsprozess entstehen, schnell abgeleitet werden und der Aufbau von Raumladung bei hohen Teilchenraten wird begrenzt. Ein kritisches Element der Micromegas Detektoren sind spontane Entladungen in dem starken elektrischen Feld und dem sehr dünnen Verstärkungsbereich. Diese Problem wurde 2011 durch die Einführung einer Schutzschicht gelöst. Diese besteht aus einer dünnen Isolationsschicht über den Auslesestreifen, auf die Widerstandsstreifen aufgebracht werden.

Micromegas-Detektoren mit Widerstandsschutz wurden für die Instrumentierung der ersten Station des ATLAS Myon-Systems in Vorwärtsrichtung (NSW) als Mess- und Auslöse-Instrumente für den Betrieb des Large Hadron Colliders (LHC) bei höherer Luminosität (HL-LHC, ab 2020) gewählt.

Das Ziel dieser Arbeit ist: 1. die Messung der Eigenschaften der ersten Micromegas NSW Prototypen; 2. die Untersuchung der Eigenschaften des Materials, das für die Widerstandsstreifen benutzt wird; und 3. die Bestimmung des Einflusses der Gitter-Abstandshalter (pillars) auf die Eigenschaften des Detektors.

Die Arbeit beginnt mit einer kurzen Einführung, die den LHC und das ATLAS Projekt vorstellt, gefolgt von einem Kapitel, das erklärt, warum die jetzt installierten Myon-Detektoren ersetzt werden müssen, um bei einer konsequenten Erhöhung der LHC-Luminosität nicht an Messgenauigkeit zu verlieren. Es zeigt dann wie die neue Myon Station, das New Small Wheel (NSW), aussehen wird.

Im ersten der Hauptkapitel werden der Bau und die Untersuchung der ersten beiden Prototypen für die NSW Detektoren beschrieben. Diese Detektoren (MMSW) bestehen aus vier Messlagen und haben die gleiche mechanische Struktur wie die NSW Detektoren. Sowohl die mechanische Präzision als auch die Homogenität der Signale über den gesamten Detektor und die Teilchen-Nachweiswahrscheinlichkeit werden diskutiert. Letztere wurden mit Röntgenstrahlen und Teilchen aus der kosmischen Strahlung gemessen. Die Ortsauflösung wurde am MAMI Beschleuniger in Mainz mit nieder energetischen Elektronen gemessen. Das Kapitel wird komplettiert durch einen Abschnitt, der die erfolgreiche Integration eines Datenerfassungssystems für die MMSW Detektoren in das offizielle ATLAS Datenerfassungssystem beschreibt. Solch ein System wurde für die ursprünglich geplante Installation eines der MMSW Detektoren in ATLAS gebraucht.

Danach wird die Untersuchung der Eigenschaften der Widerstandsstreifen präsentiert, insbesondere deren Abhängigkeit von Temperatur und relativer Luftfeuch-

tigkeit, sowie ihr Langzeitverhalten. Dafür wurden die Streifen einem Stromfluss ausgesetzt der 100 Jahren Betrieb im LHC entspricht, zum anderen einer Gamma Strahlendosis ausgesetzt, wie sie bei einem 10-jährigen LHC Betrieb erwartet wird.

Im dritten Teil folgt eine ausführliche Studie des Einflusses der Gitter-Abstandshalter (pillars) auf die Ortsauflösung und die Nachweiswahrscheinlichkeit. Diese Studie wurde mit einem 10×10 cm^2 großen Micromegas Detektor mit zwei verschiedenen Abstandshalterformen sowohl mit 5.9 keV Gamma-Strahlen von einer ^{55}Fe Quelle, als auch mit 8 keV Photonen aus einer Röntgen-Quelle durchgeführt. In diesem Zusammenhang wird auch die elektrostatische Aufladung des Detektors diskutiert.

Im Anhang findet sich eine Zusammenfassung der physikalischen Grundlagen, die für Gasdetektoren relevant sind, sowie zusätzliches Material zu den oben beschriebenen Kapiteln.

Contents

Introduction

The main purpose of the Large Hadron Collider (LHC) is to provide a tool for particle physics searches at the TeV scale and to answer fundamental questions such as the origin of the mass, the nature of dark matter, the nature of quark-gluon plasma, any new forces and new particles beyond the Standard Model. In 2012, the successful operation of LHC resulted in the discovery of the Standard Model Higgs boson [1–3] by the ATLAS [4] and CMS [5] collaborations. This scalar boson was predicted in 1964 by the Brout-Englert-Higgs mechanisms [6,7] to explain the origin of the elementary particles masses.

The LHC has been designed to deliver proton-proton collisions at a centre-of-mass energy of $\sqrt{s} = 14$ TeV and an instantaneous luminosity of $\mathcal{L} = 10^{34}\,\mathrm{cm}^{-2}\mathrm{s}^{-1}$. In order to extend its discovery potential two upgrades are planned in 2019/20 (Phase-I upgrade) and in 2024/26 (Phase-II upgrade). In the first one the luminosity will be increased by a factor of two and in the second one by a factor of five to seven beyond its design value. While high luminosity will generate more data, it is essential that the LHC detectors (ATLAS, CMS, ALICE, LHCb) are still able to operate in the higher background environment while maintaining their performance as good as that at lower luminosities.

For the ATLAS detector one of the major upgrades during Phase-I is the replacement of the innermost end-cap muon stations with the so-called New Small Wheels (NSW). After an introduction to the LHC and the ATLAS detector in Chapter 1, the ATLAS muon spectrometer will be discussed in more detail in Chapter 2. There, the emphasis will be laid on the performance of the currently installed chambers in the end-cap region. In this way the need to replace the innermost muon chambers (Small Wheels) will arise and will be discussed. The NSW is designed such that it can operate efficiently in Run 3 (2021-2023) and beyond. The NSW will consist of two detector technologies: the small-strip Thin Gap Chambers (sTGC) and the MICRO-MEsh GAseous Structure (Micromegas).

This thesis focusses on the Micromegas technology. The Micromegas operation principle as well as the modifications of the original scheme for the construction of the NSW Micromegas modules are discussed in Chapter 3. The relevant detector physics is described in Appendix A. The first medium-size Micromegas quadruplets that have been built at CERN to evaluate detector design, construction and performance issues relevant for the construction of the NSW Micromegas detectors are discussed in Chapter 4 as well as the characterization and mechanical precision achieved with these prototypes. Chapter 5 focusses on the characterization of the resistive protection layer used in the ATLAS NSW Micromegas detectors. The influence of the pillars on the detector response and performance is discussed in Chapter 6.

Chapter 1

The LHC and the ATLAS experiment

Back in the 1980's, discussions started about the possibility to build a Large Hadron Collider (LHC) in the Large Electron-Positron (LEP) tunnel at CERN[1]. After considering the very low efficiency of producing antiprotons in order to make a proton-antiproton collider, it was decided to use proton-proton collisions at LHC with high luminosity that could exceed 10^{33} cm^{-2}s^{-1} and achieve collisions with centre-of-mass energies, at the constituent level (quarks and gluons), of at least 1 TeV. At this energy level, LHC would be able to offer a large range of physics opportunities such as sensitivity to the largest possible Higgs mass range which would give an answer to the origin of mass at the electroweak scale, searches for the production of heavy particles that would indicate physics beyond the standard model, such as SUSY particles, searches for compositiness of the fundamental fermions, investigation of CP violation in B-decays. The LHC would be also capable of being used as a collider for heavy ions to produce very hot and dense matter, the quark-gluon plasma. This exploration would shed further light on the properties of the strong interaction which binds quarks into protons and neutrons. In 1994, the CERN council approves the construction of the LHC in two stages with different center-of-mass energies and two years later in a single stage [8–12].

The ATLAS collaboration proposes to build a general-purpose pp detector able to exploit the full discovery potential of the LHC. To be sensitive to a variety of physics processes (see Table 1.1), the basic design considerations of the ATLAS detector were the following [13]:

- Very good electromagnetic calorimetry for electron and photon measurements, complemented by full-coverage hadronic calorimetry for accurate jet and missing transverse energy measurements;
- High-precision muon momentum measurements with the capability of using the muon spectrometer alone for accurate measurements at the high luminosity;

---

[1] The name CERN derives from the acronym Conseil Européen pour la Recherche Nucléaire. CERN was founded in 1954 and it is one of the largest scientific research centres worldwide focused mainly on fundamental particles.

- Efficient tracking at high luminosity for high-p_{T} lepton-momentum measurements, electron and photon identification, τ-lepton and heavy-flavour identification, and full event reconstruction capability at lower luminosity;

- Large acceptance in pseudorapidity with almost full azimuthal angle coverage everywhere;

- Triggering and measurements of particles at low-p_{T} thresholds, providing high efficiencies for most physics processes of interest at LHC.

Table 1.1: Detector requirements for various physics processes.

Physics processes	**Detector requirements**
SM Higgs	High resolution e, μ and γ detection; Excellent secondary vertex detection for τ-leptons and b-quarks. For the Vector Boson Fusion production Higgs searches aim for a stand-alone muon-system at high energies and forward jet production.
SUSY	Hermeticity
Heavy bosons	High p_{T}-leptons and large bending power
Compositeness	High p_{T}-jets
W and top mass	Good knowledge of the absolute energy scale of the calorimeters
CP-violation and B-decays	Excellent secondary vertex detection and reconstruction of final states with low-p_{T} particles

This chapter describes briefly the LHC complex, the ATLAS detector and the Trigger and Data Acquisition System (TDAQ). Since the muon spectrometer is more relevant to the subject of this thesis it will be discussed in detail in the next chapter.

1.1 The LHC complex

The Large Hadron Collider (LHC) [14] is a particle accelerator and collider at CERN installed in the same tunnel that was initially constructed for the LEP collider. The tunnel has a circumference of 27 km in a maximum depth of 175 m. It is located beneath the Franco-Swiss border near Geneva, Switzerland.

The LHC machine accelerates and collides protons as well as heavy ions. The acceleration process involves a number of smaller accelerators prior to the LHC in order to increase gradually the energy of the particles (Fig. 1.1). After acceleration to their peak energy the particles are brought into collision at the four intersection points where the LHC detectors (ALICE [15], ATLAS [4], CMS [5], LHCb [16]) are hosted. The LHC design parameters are $\mathcal{L} = 1 \times 10^{34}\,\mathrm{cm}^{-2}\mathrm{s}^{-1}$ with $\sqrt{s} = 14$ TeV (Fig. 1.2).

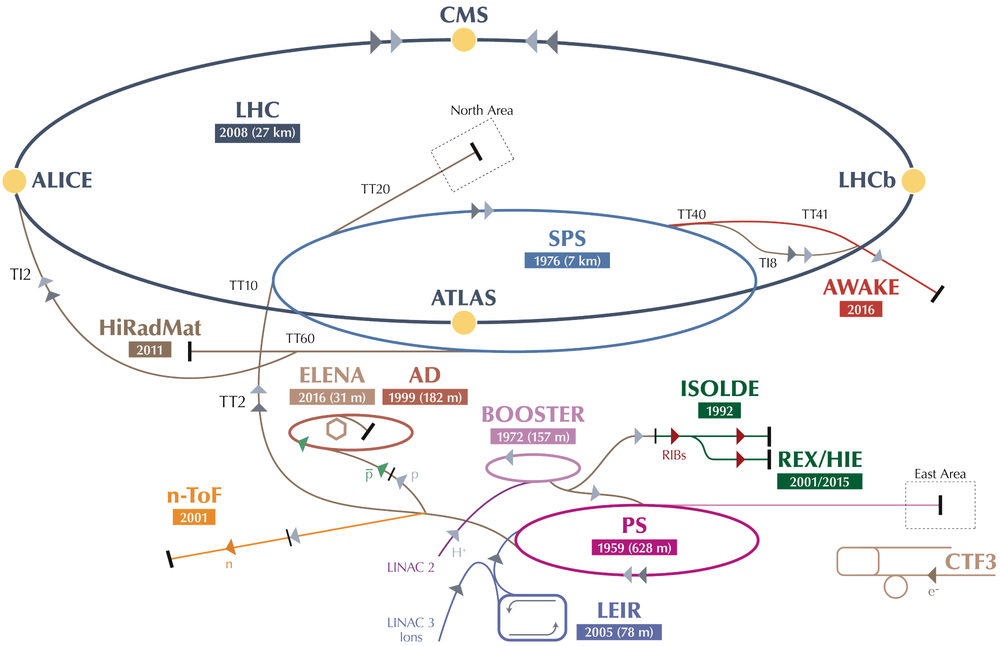

Figure 1.1: The CERN accelerator complex with the four main experiments: ALICE, ATLAS, CMS and LHCb [CERN©2001-2017].

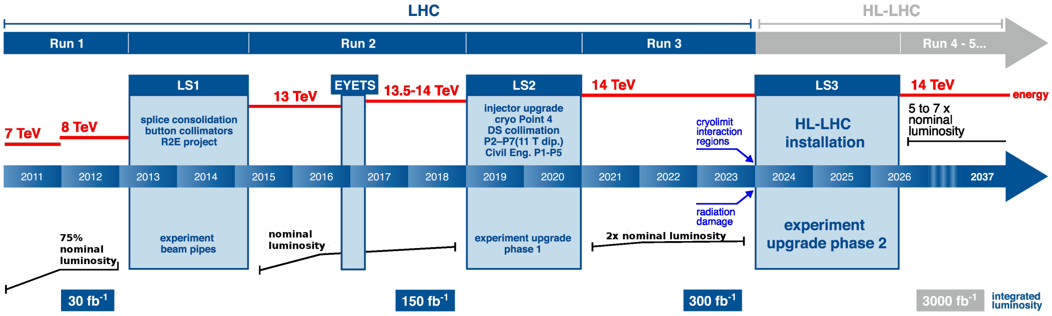

Figure 1.2: LHC baseline plan for the next decade and beyond showing the energy of the collisions (upper red line) and the integrated luminosity (lower black lines) as a function of time [CERN©2015-2017, modified for legibility].

The main purpose of the LHC is to provide a tool for particle physics searches at the TeV scale. After commissioning in 2010, the peak luminosity has been gradually increased to about two times the design value with a center-of-mass energy $\sqrt{s} = 13$ TeV. In order to extend its discovery potential a major upgrade, the High-Luminosity LHC (HL-LHC) [17], is foreseen in the 2020s with an increase of its luminosity by a factor of five to seven beyond its design value.

1.2 The ATLAS detector

The ATLAS (A Toroidal LHC ApparatuS) detector is one of the two general-purpose detectors at the LHC (Fig. 1.3). It is designed for a broad programme of particle physics from precision measurements of the standard model particles to extra dimensions and particles that could make up dark matter. Beams of particles from the LHC collide at the center of the ATLAS detector producing new particles which fly out from the interaction point (IP) in all directions. ATLAS is a forward-backward symmetric detector with respect to the IP. It is made up of a barrel region and two end-caps and consists of three sub-detector systems: the inner tracker, the calorimeters, and the muon spectrometer. The inner tracker is sensitive to all charged particles. Electrons and photons are absorbed mainly by the electromagnetic calorimeter while heavier particles like hadrons and jets are absorbed by the hadronic calorimeter. Muons above a few GeV can penetrate all these sub-detectors and reach the muon spectrometer. To measure the momentum of the particles the inner tracker and the muon spectrometer are embedded in magnetic fields.

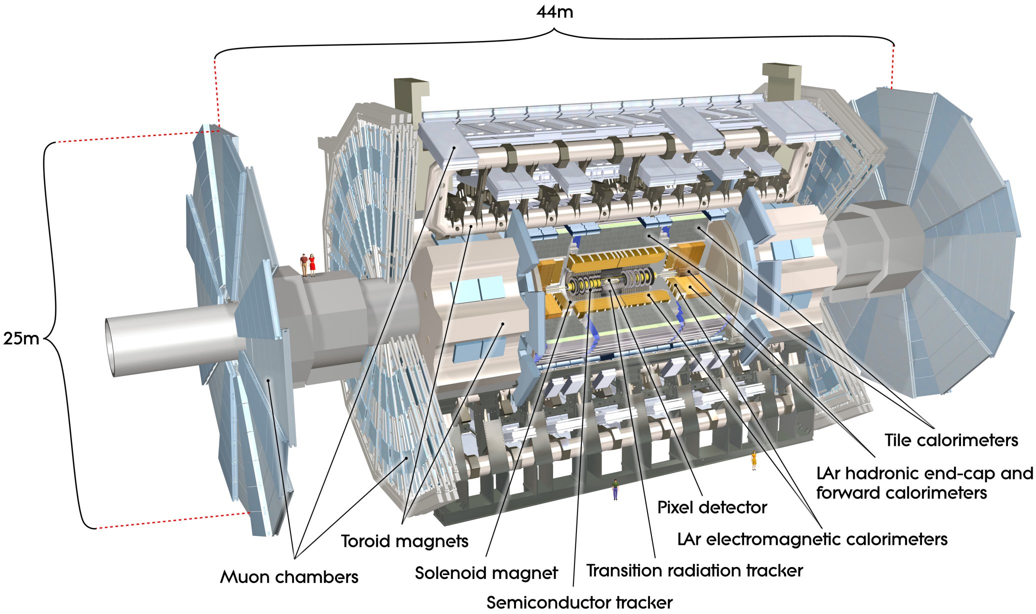

Figure 1.3: Cut-away view of the ATLAS detector. The dimensions of the detector are 25 m in height and 46 m in length. The overall weight of the detector is approximately 7000 tons [CERN ©2008-2017].

1.2.1 Magnet System

The ATLAS detector contains two types of superconducting magnets, the solenoid magnet surrounding the inner tracker and the toroid magnets outside of the calorimeters. Both systems are operated at the temperature of liquid helium < 4.5 K.

The solenoid magnet (Fig. 1.4(a)) provides a 2 T axial magnetic field parallel to the beam direction[2]. It is housed in a cryostat which is shared with the electromagnetic calorimeter to minimize the usage of material.

The magnet system of the muon spectrometer consists of three air-core toroidal magnets, one in the barrel region ($|\eta| < 1.4$) and two in the end-caps ($1.6 < |\eta| < 2.7$) (Fig. 1.4(b)). Each of them consists of eight coils that are symmetrically positioned around the beam axis. The barrel coils are rotated by 22.5° with respect to the coils of the end-cap system in order to provide for radial overlap and optimize the bending power in the transition region. In the barrel region the bending power of the magnetic field ranges from 1.5 Tm to 5.5 Tm while in the end-cap toroid it ranges from 1 Tm to 7.5 Tm (Fig. 1.5(a)). In the transition region, $1.4 < |\eta| < 1.6$, where the two systems overlap the bending power is smaller. Owing to the finite number of coils the magnetic field is not perfectly toroidal, in particular in the transition regions and between the coils (Fig. 1.5(b)).

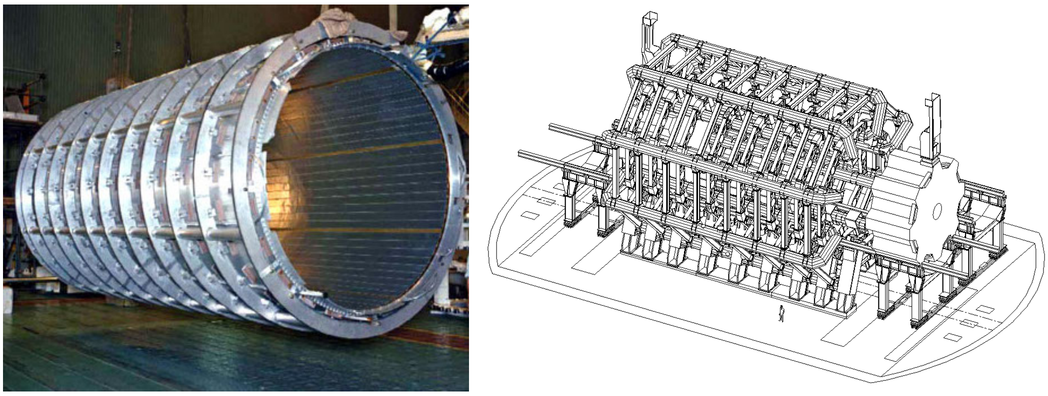

(a)

(b)

Figure 1.4: (a) Superconducting solenoid magnet for the inner tracker [CERN©2008-2017]; (b) three-dimensional view of the superconducting air-core toroid magnets for the muon spectrometer. The right hand end-cap magnet is shown retracted from its operating position [18]. Note: the two figures are not to scale.

---

[2] ATLAS uses a right-handed coordinate system with its origin at the IP. The z-axis coincides with the beam pipe, the x-axis points from the IP to the centre of the LHC ring, and the y-axis points upwards. Cylindrical coordinates (r,ϕ) are used in the transverse plane, ϕ being the azimuthal angle around the beam pipe. The pseudorapidity and the transerve momentum are defined in terms of the polar angle θ as η = -ln(tan(θ/2)) and $p_{\mathrm{T}} = p \cdot \sin\theta$ respectively.

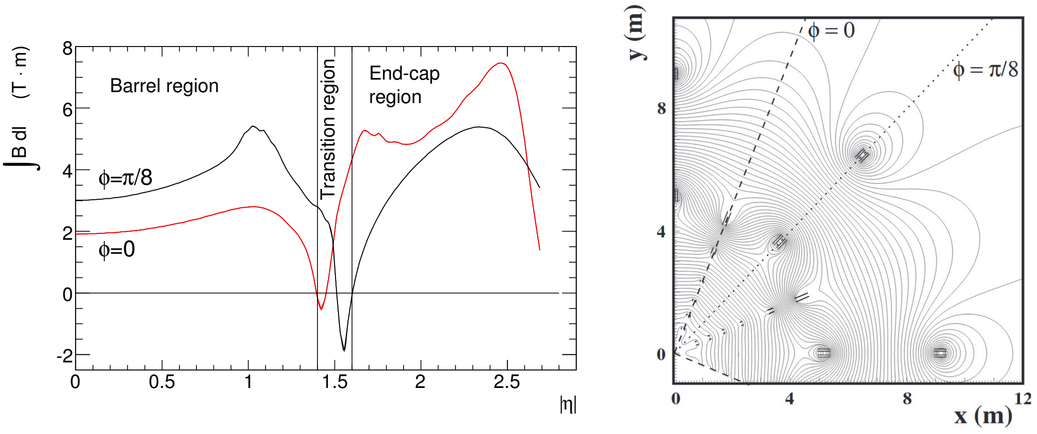

(a) (b)

Figure 1.5: (a) Field integral as a function of $|\eta|$ in one toroid octant, for infinite-momentum muons [CERN©2008-2017]; (b) Magnetic field map in the transition region between barrel and end-cap. The field lines are shown in the transverse plane and are located in the middle of an end-cap toroid. Note, that in this plot the coordinate system of the magnetic field is rotated by $\frac{\pi}{8}$ with respect to the ATLAS coordinate system [18].

1.2.2 Inner Tracker

Closest to the IP is the inner tracking detector [19] (Fig. 1.6), located within the 2 T axial magnetic field. It measures the direction, momentum, and charge of electrically-charged particles that are produced in each collision in the pseudorapidity range $|\eta| \leq 2.7$. It consists of three systems of sensors: silicon pixels (Pixel Detector), silicon micro-strips (SemiConductor Tracker, SCT) and straw tubes (Transition Radiation Tracker, TRT).

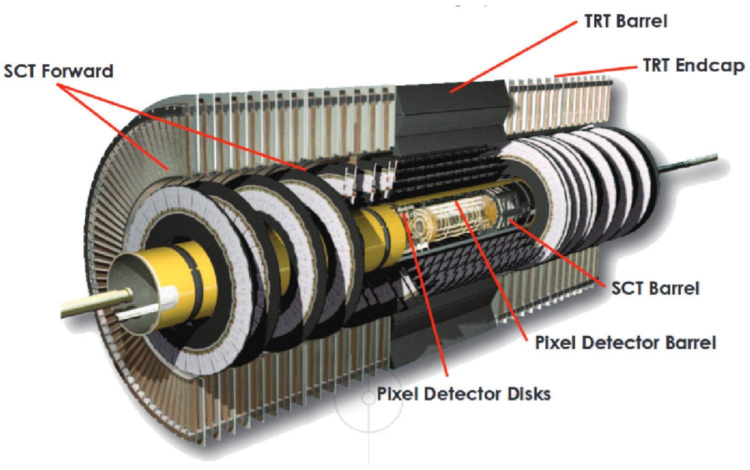

Figure 1.6: Cut-away view of the ATLAS inner detector [CERN©2008-2017].

Situated in the highest fluence environment the finest granularity is achieved using the silicon technology. The Pixel detector is the innermost part of the ATLAS detector and consists of three barrel layers and three end-cap disk layers on each side to provide for three space points with a resolution of 10 µm in the r–ϕ direction and 115 µm in the direction along the beam (z). The pixel layer closest to the beam pipe, the B-layer, was designed to operate efficiently up to 300 fb^{-1}. In order to keep the performance of the tracking with increasing luminosity and to obtain an additional space point, a forth pixel layer, the Insertable B-Layer (IBL) [20], was installed between the B-Layer and a new (smaller radius) beam-pipe during the first long shutdown (2013-2014).

The pixel detector is surrounded by the SCT which consists of four layers in the barrel and nine layers in each of the two end-caps. The silicon modules, built from two single-sided sensors, are glued back-to-back at a stereo angle of 40 mrad in order to measure hit positions in two dimensions with a resolution of 17 µm in the r–ϕ direction and 580 µm in the z direction.

The TRT is the outermost layer of the inner tracker consisting of a barrel and two end-cap layers. It is a multi-wire proportional chamber made up of drift tubes, the straw tubes, with a diameter of 4 mm. The tube walls consists of Kapton® coated on the inside with a conductive layer and reinforced with thin carbon fibers. In the centre of each tube there is a gold-plated tungsten wire with a diameter of 31 µm. With the wall kept at a voltage of -1.5 kV and the wire at ground potential, each tube acts as a small proportional counter. The space between the straws is filled with radiator material. Photons emitted in the radiator are absorbed in the gas inside the straw tubes, which serve as detecting elements both for tracking and for particle identification[3]. The detector is operated with a gas mixture of 70% Xe, 27% CO_2 and 3% O_2[4]. Xenon is used for its high efficiency to absorb transition radiation photons (soft X-rays) of typical energy 6 – 15 keV. The TRT provides for an average of 30 space points with a single wire resolution of 130 µm for tracks within $|\eta| < 2$ and $p_T > 0.5\,\text{GeV/c}$ and contributes to particle identification.

The current inner tracker is expected to degrade in performance owing to radiation damage with the increased collision rate that is expected during the HL-LHC. It is, therefore, foreseen to replace the complete inner tracker during the upgrade phase II by the new Inner Tracker (ITk) [22], consisting only of pixel detectors.

1.2.3 Calorimeters

The inner tracker is surrounded by sampling calorimeters (Fig. 1.7), consisting of alternating layers of absorber (dense material that degrades the energy of the

---

[3] Transition radiation photons in the X-ray range are created when particles cross stacked layers of different dielectric materials. As the transition radiation yield and spectrum depend on the Lorentz factor γ of the incident charged particle a discrimination between electrons and pions is possible. As the electrons are much lighter than the pions they have a higher γ and therefore radiate more.

[4] During Run 1 some pipes that supply the gas to the detector had large leaks (∼150 l/d) owing to corrosion [21]. Since Xenon is very expensive it was decided to replace it by Argon in the detectors that were affected.

incident particle) and active medium that produces a signal proportional to the input energy.

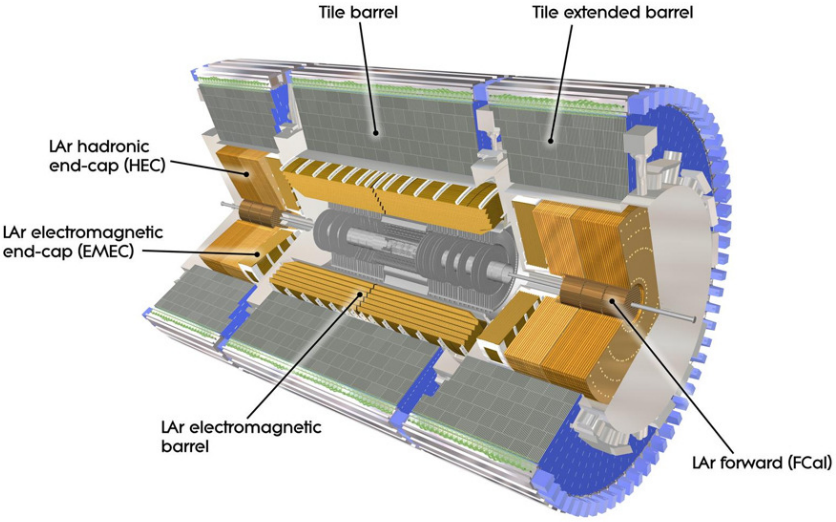

Figure 1.7: Cut-away view of the ATLAS calorimeters. The LAr calorimeters are surrounded by the scintillator-based Tile hadronic calorimeters [CERN©2008-2017].

In the calorimeters, incident particles produce showers of secondary particles with progressively degraded energy. The calorimeters are divided into two types. The first calorimeter, outside of the solenoid magnet, is the electromagnetic calorimeter. It measures mainly electrons and photons. It consists of lead absorbers with liquid-argon (LAr) as active material [23]. Further outside is the hadronic calorimeter [24]. In the barrel region it consists of steel absorbers and scintillating tiles whereas in the end-cap and forward region (FCal) it is based on copper and tungsten absorbers with LAr as active material. The design energy resolution is $\frac{10\%}{\sqrt{E}} \oplus 0.7\%$ and $\frac{50\%}{\sqrt{E}} \oplus 3\%$ in the electromagnetic and the hadronic calorimeter respectively. The hadronic calorimeter, having a very good muon signal to noise ratio, assists the muon spectrometer in the identification and reconstruction of muons.

Under HL-LHC conditions the electromagnetic and hadronic calorimeters will be able to tolerate the increased particle flux, but the performance of the FCal will be affected. The replacement of the FCal or the installation of an additional calorimeter in front of the existing is currently under study. Besides this, the exchange of all the on-detector readout electronics with one that can withstand larger radiation levels is foreseen in the next upgrade periods.

1.2.4 Muon Spectrometer

The muon spectrometer surrounds the calorimeters. Muons traverse all the subdetectors and produce hits in the muon detectors after having deposited a few GeV of ionisation energy in the calorimeters. Muons are used to make precision measurements of known physics processes and to explore new physics. For example, low–p_T muons are investigated through J/ψ decays, b-jet and flavor tagging; high–p_T muons are produced in W, Z, Higgs decays and many processes beyond the Standard Model. Since the subject of this thesis is related to the muon system it will be described in some more detail in the next chapter.

1.3 The ATLAS TDAQ System

The ATLAS trigger and data acquisition (TDAQ) system is responsible for the selection and the transportation of interesting physic data for later offline analysis. It reduces the initial LHC frequency of 40 MHz to a rate of stored events of few hundred Hz.

Figure 1.8 shows a schematic overview of the Run2 configuration of the ATLAS TDAQ system. The trigger system consists of a hardware based Level-1 (L1) and a software based high-level trigger (HLT). The L1 system is composed of the L1 calorimeter trigger system (L1Calo), the L1 muon system (L1Muon), the new topological trigger module (L1Topo) and the Central Trigger Processor (CTP) [25].

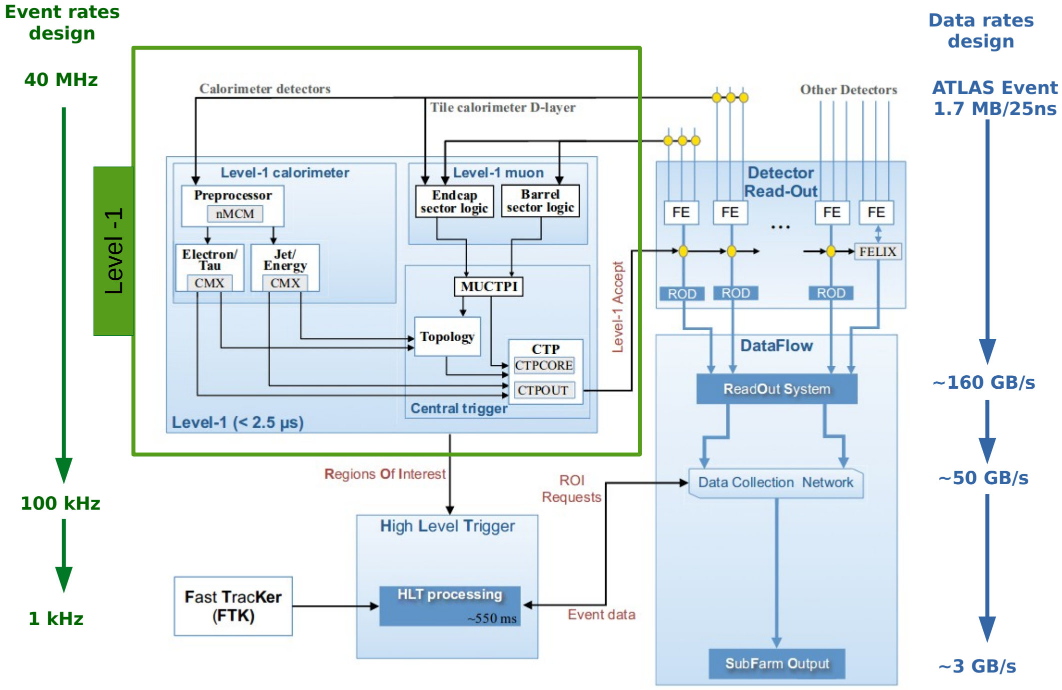

Figure 1.8: The ATLAS TDAQ architecture for Run 2.

The L1Calo and L1Muon process signals from the calorimeters and the muon trigger detectors respectively and send trigger signals to the CTP. The new L1Topo calculates topological quantities (Fig. 1.9(a)) between L1 objects within the L1 latency of ∼ 2 μs and allows the CTP to perform L1 selections based on these quantities. The CTP itself, after receiving information from the detectors and the L1Topo, makes the final Level-1 Accept (L1A) decision. The L1A together with other timing and trigger signals is fanned out to the sub-detector front-end electronics. The events that are accepted by the Level-1 trigger, at a rate of ∼100 kHz, are transferred from the sub-systems Read-Out Drivers (RODs) to the Read-Out System (ROS) where they are buffered until requested by the High-Level trigger (HLT). At the HLT, fast algorithms access data from a Region of Interest (RoI) (Fig. 1.9(b)), or offline-like algorithms. Finally the events of interest are collected by the Data Collection Network (DCN) and transferred to the permanent storage via the SubFarm Output (SFO) server.

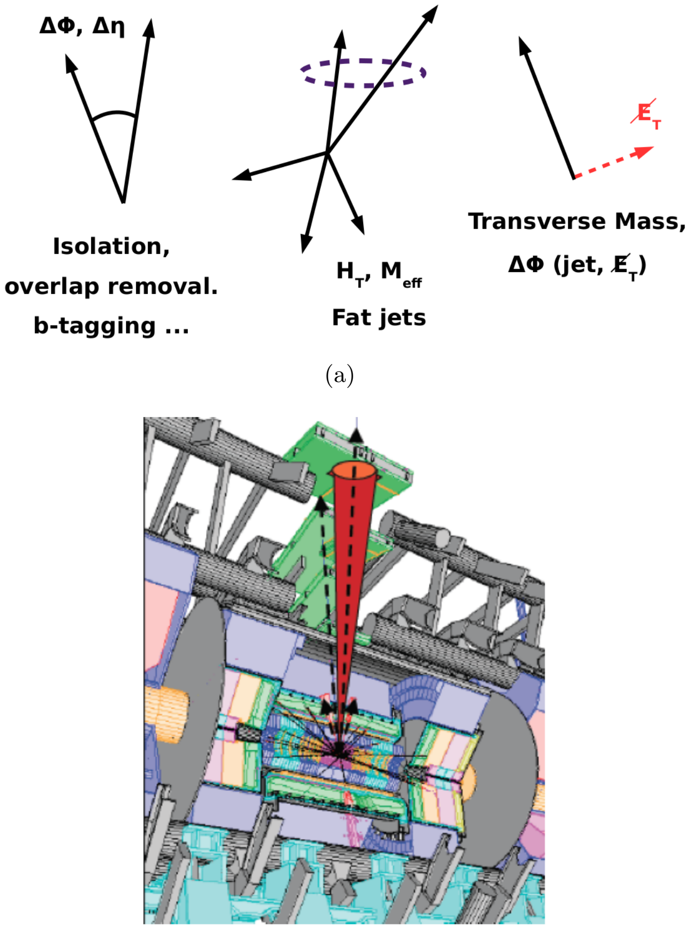

(a)

(b)

Figure 1.9: (a) Typical quantities that can be calculated by the new L1Topo modules. (b) Schematic view of a Region of Interest (RoI).

Chapter 2

ATLAS Muon Spectrometer

In this chapter the ATLAS muon spectrometer will be presented. Emphasis will be laid on the performance of the currently installed chambers in the end-cap region. In this way the need to replace some of these chambers will arise and will be discussed. Most of the information given below is based on Ref. [18]. Further sources are explicitly cited.

2.1 Introduction

The prime focus of the ATLAS muon spectrometer is stand-alone muon momentum measurements up to the highest expected energies. The design goal was to measure the transverse momentum (p_T) with a resolution of $\Delta p_T/p_T = 10\%$ at $p_T = 1$ TeV. For this reason, ATLAS has opted for a muon system based on an air-core toroid system. It minimizes the material between the chambers and, therefore, multiple scattering. In order to be able to measure 1 TeV muons to 10% precision, tracking chambers with very good spatial resolution are used and their position is monitored constantly. In the present muon system, precision tracking and triggering are performed by different detectors.

2.2 Detector layout

Precision and trigger chambers are installed both in the barrel and the end-caps. Figure 2.1 shows the layout of the muon spectrometer indicating the areas covered by the four different detector technologies that will be discussed in Section 2.3. The chambers are arranged such that particles from the interaction point traverse three stations[1] of chambers. In the barrel, the muon chambers have a rectangular shape. They are arranged in three concentric stations around the beam axis (Fig. 2.2(a)) covering the space between 4.5 m and 11 m in radius. In the end-caps, the chambers

---

[1] Muon chambers are labelled with three letters. The first one denotes whether they are located in the barrel "B" or in the end-caps "E"; the second letter stands for the muon stations. Closest to the IP are the inner stations denoted with "I", further outside the middle stations denoted with "M" and the outer stations denoted with "O"; the third letter specifies whether the chamber is located between two toroid coils (large, "L") or it is found in a line with one of them (small, "S").

have a trapezoidal shape and are mounted on wheels (Fig. 2.2(b)). Three different wheels, each, are installed perpendicular to the beam pipe between 7 m and 23 m longitudinally on both sides of the IP (Fig. 2.3).

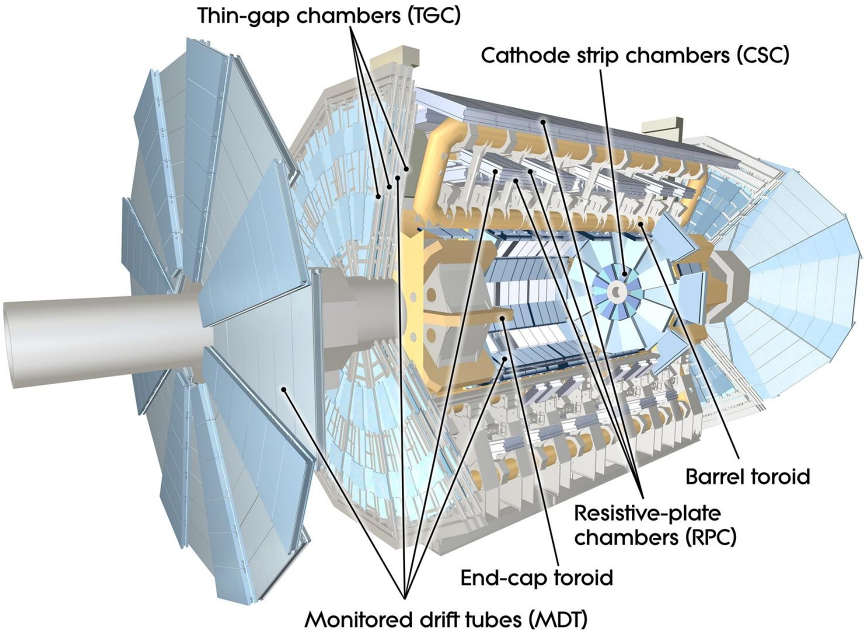

Figure 2.1: Layout of the muon spectrometer indicating the areas covered by the four different detector technologies.

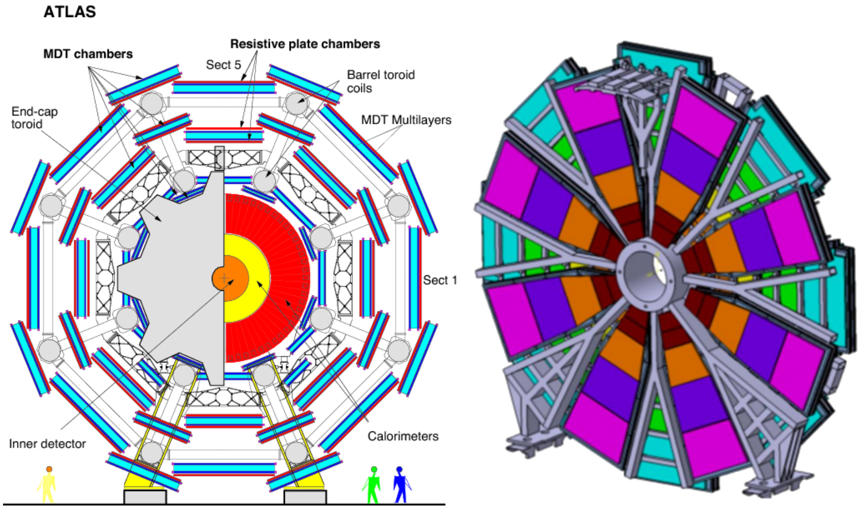

(a) (b)

Figure 2.2: (a) Barrel cross-section of the muon spectrometer; (b) Drawing of one of the wheels (Small Wheel) in the end-cap region.

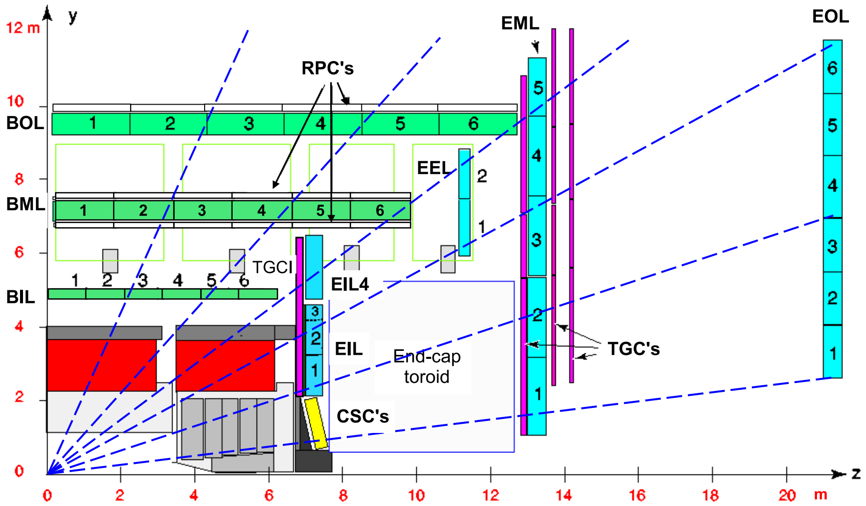

Figure 2.3: Cross-section of the muon system in the bending plane containing the beam axis.

2.3 Detector technologies

Four different types of gas-filled detectors are currently used in the muon spectrometer. The Resistive Plate Chambers (RPC) in the barrel and the Thin Gap Chambers (TGC) in the end-caps are used primarily for triggering but they also provide for the coordinate measurement in the non-bending plane. As precision tracking chambers Monitored Drift Tubes (MDT) are used both in the barrel and in the end-caps except in the innermost end-cap stations (Small Wheels) and close to the beam pipe where particle fluxes are higher. In this region, $2 < |\eta| < 2.7$, Cathode Strip Chambers (CSC) are employed. The CSCs measure both track coordinates simultaneously and have higher rate capability ($1\,\mathrm{kHz/cm^2}$) with respect to that of the MDTs ($150\,\mathrm{Hz/cm^2}$). Table 2.1 shows the detector technologies of the present muon system with their main parameters.

Table 2.1: Detector technologies of the current muon spectrometer and their main parameters. The quoted spatial resolution does not include the uncertainties of the chamber-alignment.

			Resolution (r.m.s.)		
Technology	**Function**	**Coverage**	**z/R**	**phi**	**time**
MDT	tracking	$\|\eta\| < 2.7$	80 µm (z or R)	-	-
CSC	tracking	$2.0 < \|\eta\| < 2.7$	90 µm (R)	5 mm	7 ns
RPC	trigger	$\|\eta\| < 1.05$	10 mm (z)	10 mm	1.5 ns
TGC	trigger	$1.05 < \|\eta\| < 2.7$[2]	2-6 mm (R)	3-7 mm	4 ns

---

[2] For triggering they cover the pseudorapidity region $1.05 < |\eta| < 2.4$

2.4 Muon momentum measurement and alignment system

The muon spectrometer is designed such that every muon crosses at least three muon stations. In the barrel, all three stations are located inside the magnetic field thus the momentum of the particle is determined from the sagitta of the trajectory. In the end-caps, the momentum is measured differently as there is no magnetic field between the middle and outer stations. Here the direction between the IP and the track position in the inner layer is compared with the track direction between the middle and outer layer (point-angle measurement).

The momentum measurement accuracy relies crucially on the knowledge of the relative positions of the chambers. For this, the deformation of the chambers and their positions are constantly monitored by means of an optical alignment system and are corrected for in the off-line analysis.

In the barrel, the widths, the lengths, and the positions of the muon chambers were chosen such that one set of chambers in the inner, middle and outer stations forms a projective tower that covers part of the solid angle as viewed from the IP (Fig. 2.4(a)). Most muons traverse only one tower thus the momentum measurement is performed per tower. The alignment of the chambers within one tower is therefore more relevant for the precision of the momentum measurement than the alignment between towers [26]. In the end-caps, a reference grid is set up with alignment bars using a quasi-projective alignment system as shown in Fig. 2.4(b). The bars are considered self-aligning precision rulers [27]. The chambers are also equipped with an in-plane alignment system, used to monitor chamber deformations with an accuracy of 10 μm.

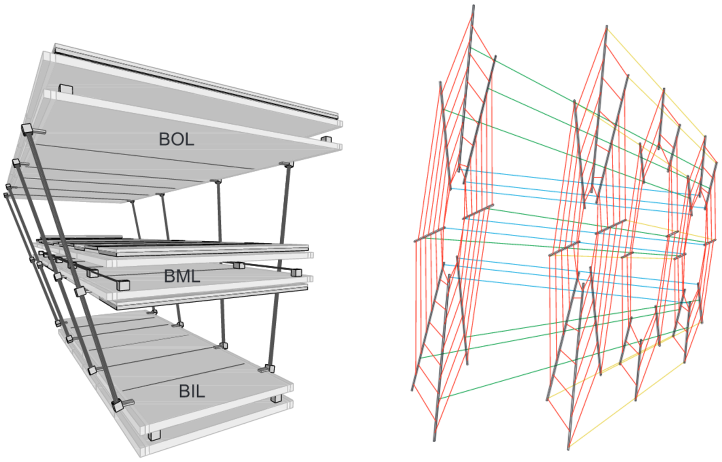

(a) (b)

Figure 2.4: (a) Three dimensional view of the projective alignment system of one half octant interconnecting three barrel stations [26]; (b) Alignment bars and rays used in one end-cap of the muon spectrometer [27].

The contributions to the momentum resolution of muons taking into account the detector geometry, the material distribution and the magnetic field are shown in Fig. 2.5.

- for low momentum muons, $p_T < 20$ GeV, the resolution in the barrel is dominated by the fluctuations of the energy loss in the calorimeters; in the end-caps by multiple scattering;
- for intermediate momentum muons, $20 < p_T < 200$ GeV, the resolution is dominated everywhere by multiple scattering;
- for high momentum muons, $p_T > 200$ GeV, the resolution is determined by the intrinsic MDT tube resolution and the alignment of the chambers;

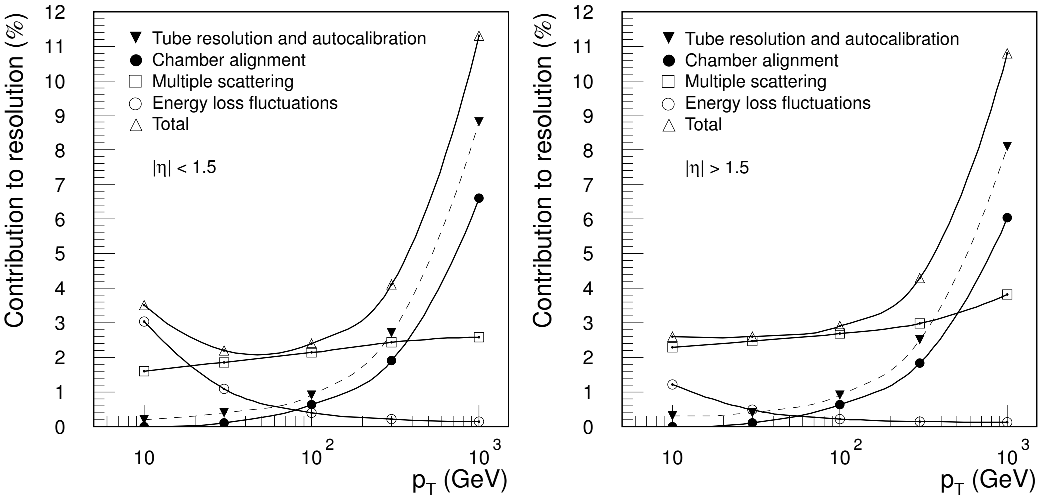

(a)

(b)

Figure 2.5: Contributions to the momentum resolution (a) in the barrel and (b) in the end-caps.

2.5 Background conditions

Sources of background to the muon signal in a typical collider detector are: uncorrelated neutrons and photons coming from hadronic interactions in the forward direction, muons from π and K decays in the tracking volume in front of the calorimeter, and hadronic punch-through. Hadronic punch-through consists of two components: penetrating muons from π and K decays in the hadronic shower cascade and unabsorbed remnants of the hadronic shower, mainly soft hadrons and electrons.

Fig. 2.6(a) shows the pseudorapidity dependence of the total counting rate in the three precision-chamber stations at the design luminosity. In the middle and outer muon stations the total counting rate is almost constant at about 10 Hz/cm^2 with a slight increase at $|\eta| > 1.7$. In the inner muon end-cap stations, the total counting rate is increasing from ~ 10 Hz/cm^2 to about 1 kHz/cm^2 in the very forward region ($|\eta| = 2.7$). The peak at $|\eta| \simeq 0.5$ in the inner stations corresponds to particles escaping between the barrel and the end-cap calorimeters. The contribution to the total counting rate in the inner stations is dominated in the barrel by neutrals while in the end-caps neutral and charged particles contribute more or less equally as shown in Fig. 2.6(b).

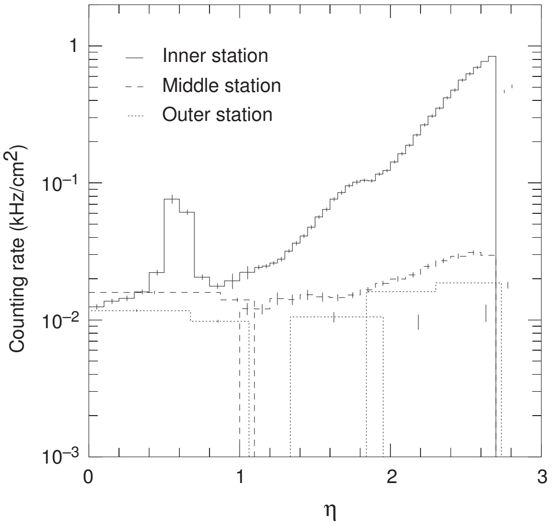

(a)

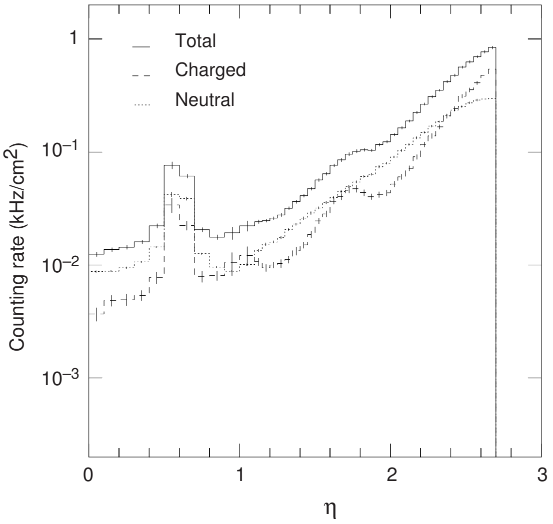

(b)

Figure 2.6: (a) Simulation of the total counting rates in the three stations of the MDTs as a function of η at the design luminosity; (b) Simulation of the pseudorapidity dependence of the total counting rate in the innermost MDT station at the design luminosity.

The contributions to the muon rate in the ATLAS muon spectrometer are shown in Fig. 2.7(a). At small $p_{\mathrm{T}} < 10$ GeV, the largest component are muons from π/K decays in flight while the contribution of hadronic punch-through is negligible. Muons with momentum $3-6$ GeV are absorbed in the calorimeters. At moderate $p_{\mathrm{T}} > 10$ GeV, the production cross-section is dominated by charm and beauty decays. At larger $p_{\mathrm{T}} > 30$ GeV, top and Z decays give a sizeable contribution. The muon rate produced by the different decays is almost constant as a function of pseudorapidity (Fig. 2.7(b)).

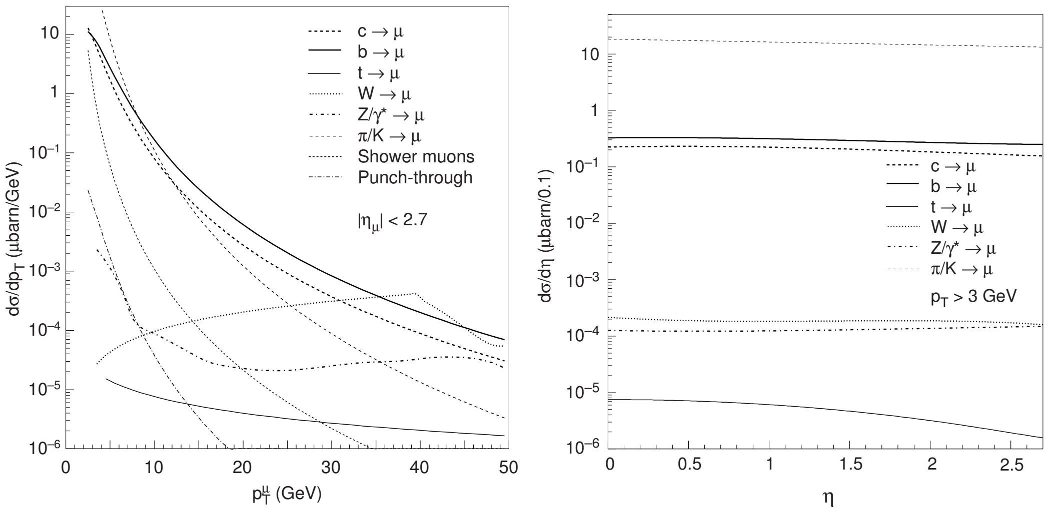

(a) (b)

Figure 2.7: (a) Simulation of the transverse momentum dependence of inclusive muon production cross-sections from various sources. The horizontal scale is the transverse momentum at production; (b) Simulation of the rapidity dependence of the muon production cross-sections.

2.6 Performance of the current muon end-cap trigger

The L1 muon trigger is based on signals from the RPCs in the barrel region and the TGCs in the end-caps as shown in Fig. 2.8(a). In the barrel, a hit coincidence between RPC1 and RPC2 chambers is required for low-p_{T} muons (6–10 GeV/c). For high-p_{T} muons (>10 GeV/c) an additional coincidence is performed taking into account the RPC3 chambers. In the end-caps, during the first period of LHC data taking (Run 1, 2011-2012), the muon trigger was relying only on the TGC chambers that are located in the middle station. In this period, a coincidence between TGC2 and TGC3 chambers was required for low-p_{T} muons, while for high-p_{T} muons an additional coincidence was performed with the TGC1 chambers. This trigger schema in the end-cap region had as a result that the L1 trigger rate was dominated by triggers from tracks not pointing to the IP (called fake triggers). Figure 2.8(b) shows the η distribution of the L1 muon signals having a transverse momentum of at least 11 GeV. The distribution of those L1 candidates that indeed have an offline reconstructed muon track is also shown, together with the muons reconstructed with p_{T}> 10 GeV. More than 80% of the muon trigger rate comes from the end-caps ($|\eta| > 1.05$), and most of the triggered objects are not reconstructible offline.

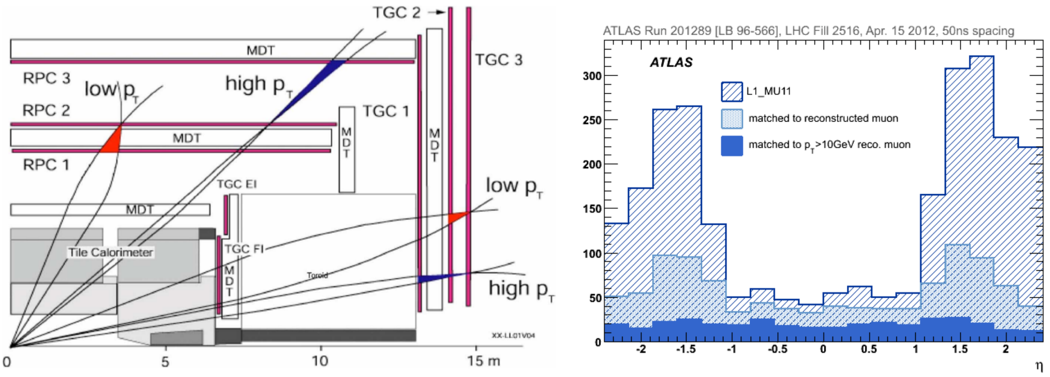

(a) (b)

Figure 2.8: (a) Layout of the trigger chambers in the muon spectrometer. In the barrel region, the RPC detectors are placed in the middle (RPC1 and RPC2) and outer station (RPC3) of the Muon Spectrometer. In the end-cap region, the TGC detectors are placed in three stations. The outer station placed at $|z| \sim 22$ m is not shown here. (b) Trigger rate of the L1 muons with $p_{\mathrm{T}} > 10$ GeV as a function of η, requiring a coincidence of hits across three–stations both in the barrel and in the end-caps. The distribution of the muon reconstruction, combined inner detector and muon spectrometer track with $p_{\mathrm{T}} > 3$ GeV and reconstructed muons with $p_{\mathrm{T}} > 10$ GeV are also shown.

In the second period of LHC data taking (Run 2, 2015-2018) a new coincidence requirement had been introduced in the end-cap region in order to reduce the number of fake triggers [28]. Figure 2.9(a) shows a schematic view of the muon spectrometer with the new coincidence schema. In the rapidity range 1.3< $|\eta|$ <1.9 a signal in the TGC chambers in the Small Wheel region (Forward Inner, FI) is required to confirm the L1 object from the middle station. The curved arrow shows an example of a trajectory from a slow particle generated in the beam pipe around z $\sim$ 10 m. Triggers owing to events of this type are mitigated in this pseudorapidity region by the new coincidence schema. In the rapidity range 1.0< $|\eta|$ <1.3 a coincidence between the inner TGC chambers (EIL4) or the Tile hadronic calorimeter and the outer EM TGCs is required. This schema led to a reduction of the trigger rate up to 60% (Fig. 2.9(b)) for low-p_{T} muons ($p_{\mathrm{T}} > 15$ GeV) [29]. The event rate reduction in the regions with no TGC-FI chambers is consistent with zero within the uncertainty[3].

---

[3] The asymmetry in the end-cap region ($|\eta| > 1.0$) is a result of the magnetic field and the background particles being mostly positive charged.

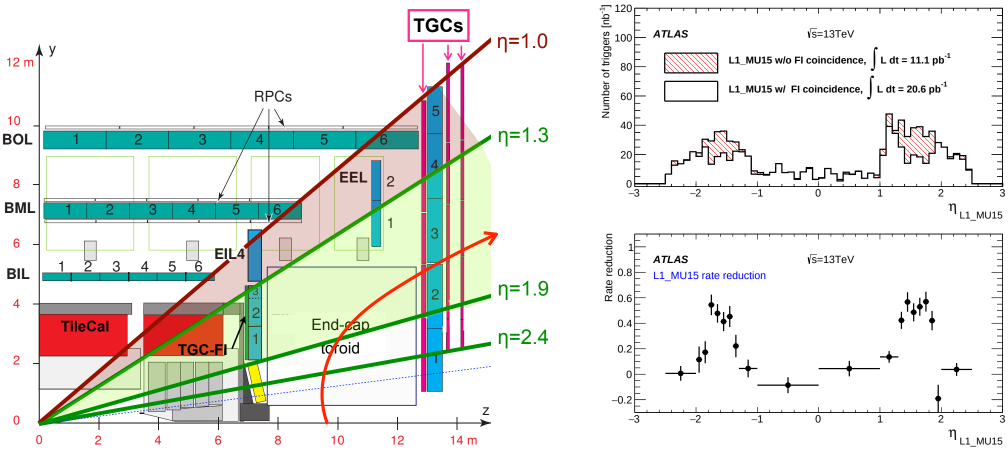

(a) (b)

Figure 2.9: (a) A schematic view of the muon spectrometer with lines indicating various pseudorapidity regions. The curved arrow shows an example of a trajectory from slow particles generated in the beam pipe at z $\sim$ 10 m; (b) Number of events with L1 muon trigger with $p_{\mathrm{T}} > 15$ GeV (L1_MU15) as a function of the muon trigger η coordinate, requiring a coincidence with the TGC-FI chambers (open histogram) and not requiring it (cross-hatched histogram), together with the fractional event rate reduction in the bottom plot [29].

However with increasing instantaneous luminosity, the rate of single muon L1 trigger will increase proportionally as the rate of muons will increase in the muon spectrometer. Figure 2.10 shows as an example the trigger rate for muons with $p_{\mathrm{T}} > 20$ GeV from 2016 and 2017 data.

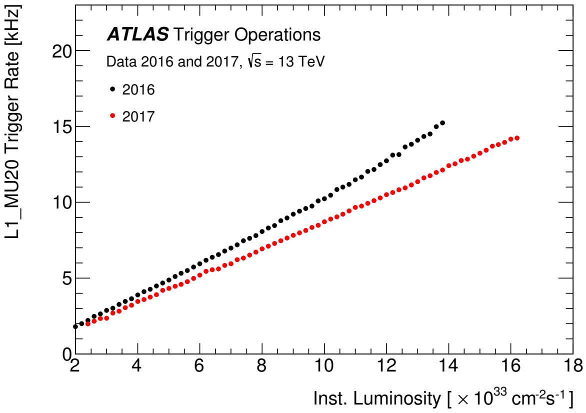

Figure 2.10: Trigger rate of the L1_MU20 trigger for 2016 (black) and 2017 (red) as a function of the instantaneous luminosity. The L1_MU20 trigger requires that a candidate muon passed $p_{\mathrm{T}} > 20$ GeV threshold.

Low p_{T} muons are of great importance for the ATLAS physics program as will be discussed in Section 2.8. From Run 3 and beyond these low p_{T} thresholds must be kept and at the same time the L1 muon trigger rate must not exceed 20 kHz.

2.7 Performance of the current precision chambers

An example of how well the present precision detectors work is shown in Fig. 2.11. It shows the invariant mass of the dimuon system ($\mathrm{m}_{\mu^+\mu^-}$) from the decays of $J/\Psi \rightarrow \mu^+\mu^-$ (Fig. 2.11(a)) and $Z \rightarrow \mu^+\mu^-$ (Fig. 2.11(b)), and the dimuon mass resolution ($\sigma_{\mu^+\mu^-}$) of these resonances (Fig. 2.11(c) and Fig. 2.11(d)) respectively as a function of pseudorapidity from proton-proton collision data collected in 2016 by the ATLAS detector at a centre-of-mass energy of $\sqrt{s}$ = 13 TeV at 33.3 fb^{-1}. For the $J/\Psi \rightarrow \mu^+\mu^-$ decay, each event contains two opposite-charge muons with 2.6 GeV $< p_T <$ 3.6 GeV while for the $Z \rightarrow \mu^+\mu^-$ decay 22 GeV $< p_T <$ 300 GeV.

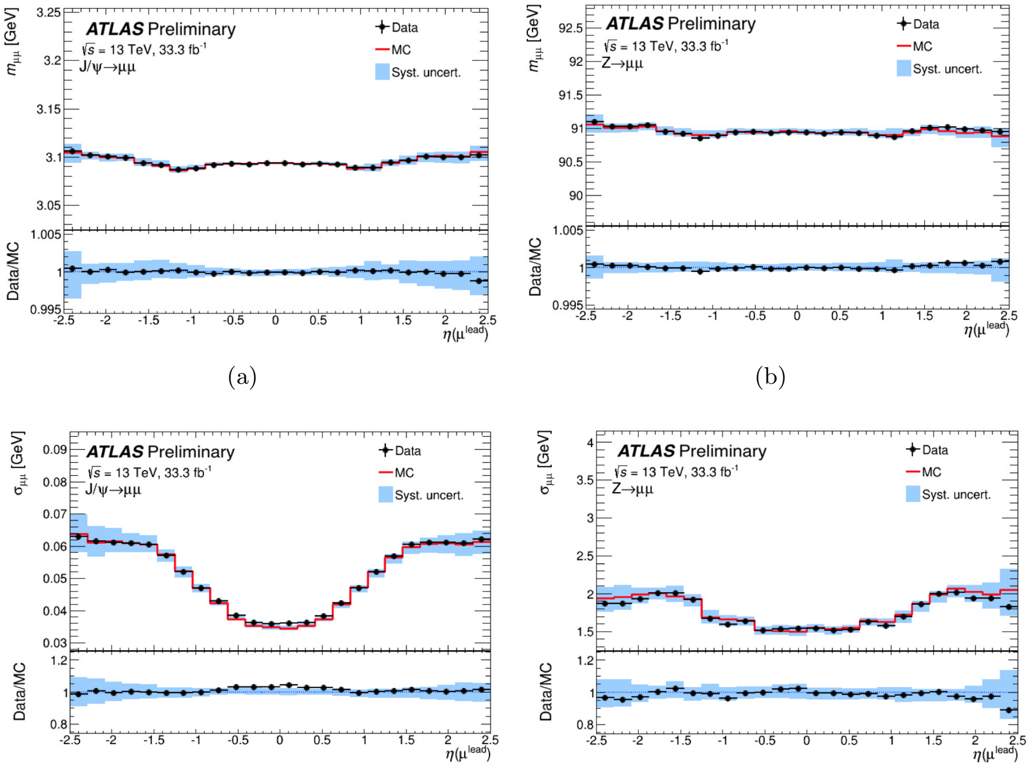

(a) (b) (c) (d)

Figure 2.11: Invariant mass distribution ($\mathrm{m}_{\mu^+\mu^-}$) of (a) J/Ψ from $J/\Psi \rightarrow \mu^+\mu^-$ candidates and of (b) Z from $Z \rightarrow \mu^+\mu^-$ candidates, as a function of pseudorapidity compared to simulation; Dimuon invariant mass resolution ($\sigma_{\mu^+\mu^-}$) for the resonance (c) $J/\Psi \rightarrow \mu^+\mu^-$ and for (d) $Z \rightarrow \mu^+\mu^-$, as a function of pseudorapidity [30].

The dimuon mass resolution is about 1.2 and 1.6 % at small η values for J/Ψ and Z bosons, respectively, and increases to 2.0 and 2.2 % in the endcaps. This corresponds to a relative muon p_T resolution of 1.7 and 2.3 % in the centre of the detector and 2.8 and 3.1 % in the endcaps for J/Ψ and Z boson decays, respectively. [30, 31].

From the next run period (Run 3) and beyond, the luminosity will gradually increase and the counting rate in the Small Wheel region is expected to reach approximately 15 kHz/cm^2 at $\sqrt{s}$ = 14 TeV for $|\eta|$>2.5. Even at the outer rim of the Small Wheels the counting rate will exceed ∼1 kHz/cm^2, much in excess of what the currently installed muon chambers are designed for.

The currently installed MDT chambers[4] were designed to cope with a hit rate up to 100–150 Hz/cm^2. The detection efficiency of the MDT chambers as a function of the background hit rate is shown in Fig. 2.12(a). It can be seen that as the hit rate is increasing there is a significant loss of the detection efficiency and the spatial resolution is strongly affected by space charge fluctuations (Fig. 2.12(b)).

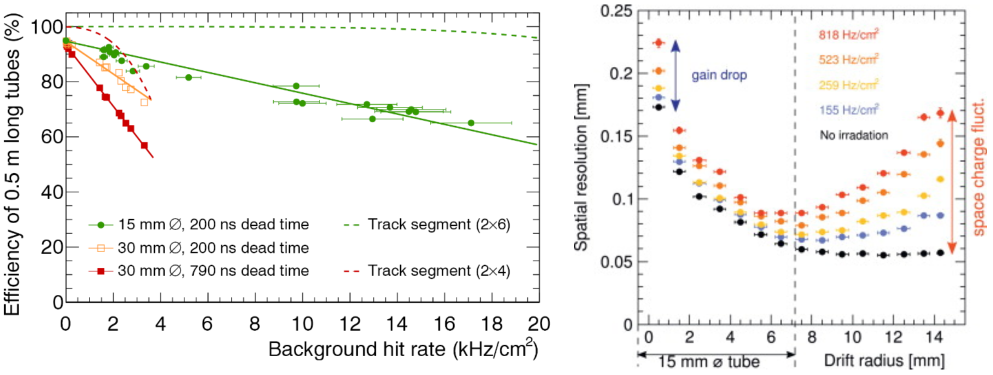

(a) (b)

Figure 2.12: (a) Efficiency of individual drift tubes as a function of the background hit rate as measured at the Gamma Ray Facility at CERN. Results for 15 mm and 30 mm diameter tubes are compared. The corresponding track segment reconstruction efficiencies in 2×4 layer MDT chambers and 2×6 layer sMDT chambers are indicated as dashed lines [32]; (b) Spatial resolution of 30 mm diameter drift tubes as a function of the drift radius r measured for increasing γ hit rate at the CERN Gamma Irradiation facility [33].

2.8 Impact on physics performance with increasing luminosity

From Run 3 and beyond the single lepton L1 trigger must be kept at low p_T thresholds and the tracking efficiency and resolution must be maintained for high momentum muons.

Low-p_T muons are important for several measurements with pp collision data. An example is shown in Fig. 2.13. It shows an event display of a Higgs decay to

---

[4] The ATLAS MDT chambers have an outer tube diameter of 30 mm

the four lepton channel ($H \to ZZ^* \to 4l$) where two muons traverse the barrel muon chambers and the other two the end-cap muon chambers [34]. The p_T of these muons is relatively low as listed in Table 2.2

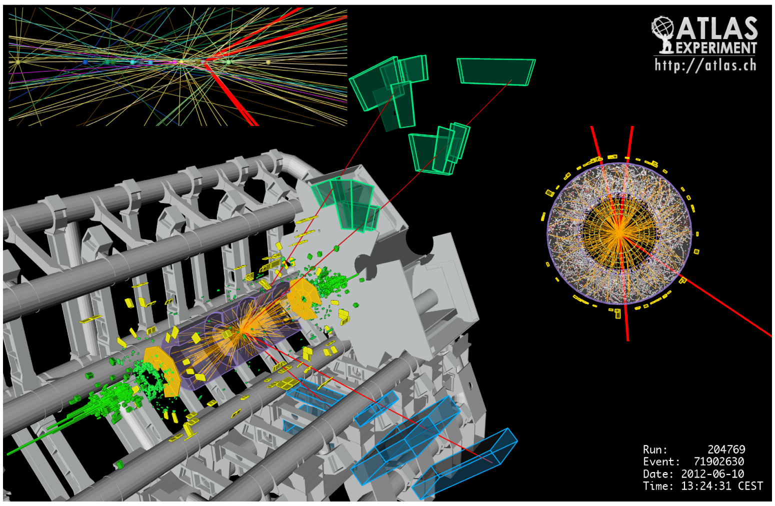

Figure 2.13: Event display of four muon candidates from the Higgs decay channel $H \to ZZ^* \to 4l$ [34].

Table 2.2: Transverse momentum and η-ϕ region of the four muons from the $H \to ZZ^* \to 4l$ channel [34].

	μ_1	μ_2	μ_3	μ_4
p_T (GeV)	47.6	36.2	26.4	7.2
η	0.8	1.3	0.47	1.85
ϕ	-1.66	1.33	-2.52	1.65

Another example for the significance of low-p_T muons is shown in Fig. 2.14(a). It shows the simulated p_T distribution of leptons from the H $\to \tau^+\tau^-$ decay channel by the vector boson fusion (VBF)[5] process where a significant fraction of muons have a $p_\mathrm{T} \simeq$ 10–15 GeV [35]. With an increased integrated luminosity, the Higgs production by the VBF will become useful taking advantage of its distinct signature.

High–p_T muons are used for searches beyond the standard model. For these muons the momentum resolution is primarily determined by the muon spectrometer where a precise measurement requires the presence of track segments in all three muon stations. With increasing luminosity high quality muon tracking in the end-caps will be lost because the MDTs lose hits at high occupancy because of their long dead time (∼800 ns) and the CSCs, having only four detection layers, lose accuracy at high occupancy from overlaps of multiple hits on the readout strips.

---

[5] The VBF is the second most dominant production mode at the LHC.

This has been studied by overlaying multiple zero-bias events[6] collected during the 8 TeV LHC runs [35]. Figure 2.14(b) shows the reconstructed invariant mass of the dimuon system ($m_{\mu^+\mu^-}$) in the simulated $Z' \rightarrow \mu^+\mu^-$ decay for a Z' mass of ∼2 TeV. Both muon track segments were required to pass all three muon stations in the region $1.3 < |\eta| < 2.0$ where the MDTs provide for the precision measurement. The reconstructed Z' signal is reduced by 30% and by 70% for a luminosity of 3×10^{34} $\text{cm}^{-2}\text{s}^{-1}$ and 5×10^{34} $\text{cm}^{-2}\text{s}^{-1}$ respectively.

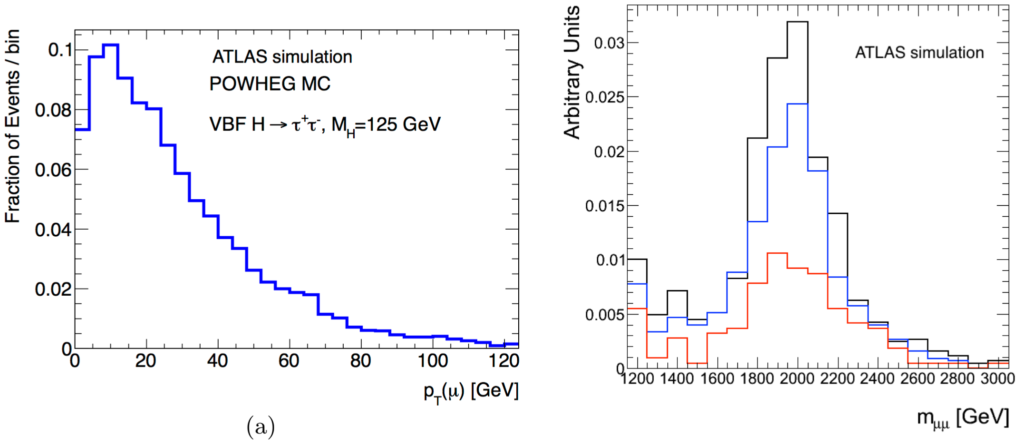

(a)

(b)

Figure 2.14: (a) Transverse momentum distribution of lepton in τ pair final states from simulated Higgs decays produced by the VBF process at $\sqrt{s} = 14$ TeV with $m_H = 125$ GeV; (b) Reconstructed invariant mass of the dimuon system ($m_{\mu^+\mu^-}$) in the simulated $Z' \rightarrow \mu^+\mu^-$ decay. The black, blue and red histograms correspond to luminosity of 0.3, 3 and 5 $\times$ 10^{34} $\text{cm}^{-2}\text{s}^{-1}$ respectively [35].

2.9 Upgrade of the Muon Spectrometer in view of the HL-LHC

In the barrel, the muon chambers can cope with the increased collision rate that is expected during the HL-LHC conditions. However, in the Small Wheel region there is a need to replace the currently installed chambers. Figure 2.15 shows the extrapolated hit rate[7] that is expected in the Small Wheel region for the MDT and the CSC detectors as a function of the radial distance from the beam line for a luminosity of 3×10^{34} cm^{-2} s^{-1} at $\sqrt{s} = 7$ TeV. During the HL-LHC conditions where the luminosity is expected to be increased by a factor of ∼2.3 and taking into account $\sqrt{s} = 14$ TeV, the expected hit rate in the very forward region where the CSC detectors are located will be $\simeq 15$ kHz/cm^2.

---

[6] Events that are triggered on random (filled) bunches are called zero-biased.

[7] The extrapolation was done by measurements in the same region with a luminosity of 9.6×10^{32} cm^{-2} s^{-1} at $\sqrt{s} = 7$ TeV.

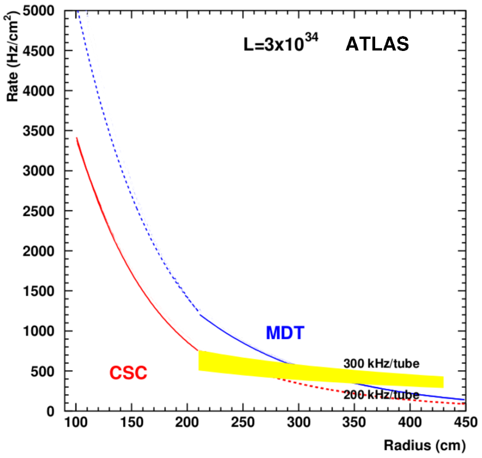

Figure 2.15: Extrapolated hit rate in the Small Wheel region for the MDT and CSC detectors as a function of the radial distance from the beam line for a luminosity of 3×10^{34} cm^{-2} s^{-1} at $\sqrt{s} = 7$ TeV. The yellow band indicates the area corresponding to a hit rate of 200–300 kHz per tube of the MDTs [35].

2.9.1 Requirements of the New Small Wheel detectors

The New Small Wheel (NSW) detectors must be able to operate safely during HL-LHC and their performance should be at least as good at high luminosity as that of the current detectors at low luminosity. The requirements on the NSW detectors for the precision tracking performance are the following:

- They should operate safely up to 15 kHz/cm^2 which is the maximum expected rate in the Small Wheel region in the high pseudorapidity region;

- The detectors including the readout electronics should not age significantly with a collected charge[8] up to 1 C/cm^2;

- In order to be able to measure the transverse momentum with a precision of 10% for 1 TeV muons in the full pseudorapidity coverage, track segments[9] should be reconstructed with a position resolution better than 50 µm in the bending plane (r-z);

- The efficiency of finding a track segment off-line should be better than 97% for muons with a $p_T > 10$ GeV;

- They should measure the second coordinate with a resolution of a few mm;

---

[8] The collected charge has been calculated with a safety factor of 5 within 10 years of detector operation during HL-LHC.

[9] Track segments are built from hits in all layers of a given station of the detector. Segments from different stations are linked together to form tracks.

In order to reduce the L1 trigger rate to 20 kHz for muons with a $p_{\mathrm{T}} > 20$ GeV the detectors should deliver track segments for the trigger with the following requirements:

- The decision from the muon trigger electronics that combines information from the various detectors to provide for one or more Regions of Interest (ROI) per bunch crossing should not come later than ~ 2 µs;
- The angular resolution of the track segment reconstruction should be 1 mrad RMS or better;
- The granularity of track segments should be better than 0.04×0.04 in the η–ϕ plane in order to match the granularity of the current muon trigger system;
- Online reconstruction of track segments should be possible with high efficiency, better than 95%, in the full η coverage ($1.3 < |\eta| < 2.5$);

2.9.2 NSW detectors

The NSW detectors that have been chosen to meet the above requirements are the small-strip Thin Gap Chambers (sTGC) and the Micromegas.

Both detectors have high rate capability. The sTGC detectors will provide for the main trigger signal. The Micromegas detectors having exceptional precision tracking capabilities will give the precision points for the determination of the muon trajectories before entering the end-cap toroid magnets. In addition, both detector technologies will complement each other. The sTGC will contribute to the off-line track reconstruction and the Micromegas will contribute to the trigger.

The sTGC detectors are described in detail in Ref. [35] and will not be discussed here. The operational principle of the Micromegas detectors, and the design and construction of the NSW Micromegas detectors will be presented in Chapter 3.

The anticipated performance of the NSW detectors has been compared with Run 2 data. Figure 2.16 shows the p_{T} distributions of the reconstructed muons that match a L1 muon candidate with $p_{\mathrm{T}} > 20$ GeV from the coincidence between the Big Wheel and the TGC detectors in the Small Wheel region. The simulated p_{T} distributions from a coincidence between the Big Wheel and the NSW detectors are also shown. Fake triggers with $p_{\mathrm{T}} < 10$ GeV are expected to be reduced significantly.

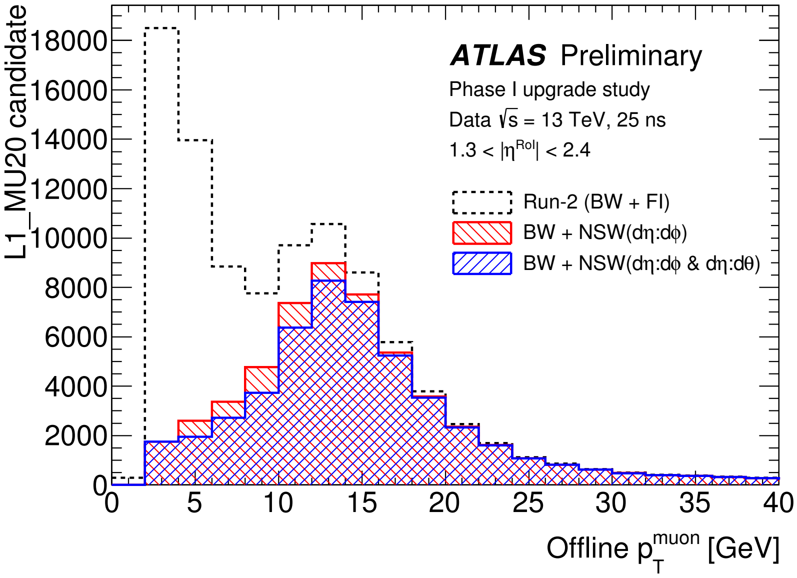

Figure 2.16: p_{T} distributions of offline reconstructed muons matched to a L1 trigger for a single muon with transverse momentum above 20 GeV for Run2. The hatched distributions show the L1_MU20 candidates if the NSW is installed (simulation) [CERN©2008-2017].

The NSW layout (Fig. 2.17) follows the design of the current Small Wheels in order to ensure compatibility with the existing tracking detectors and the end-cap alignment system. Each wheel consists of sixteen sectors, eight small and eight large that overlap in azimuthal angle with each other. The small sectors will be facing the IP while the large sectors will be closer to the end-cap toroid magnet (HO side).

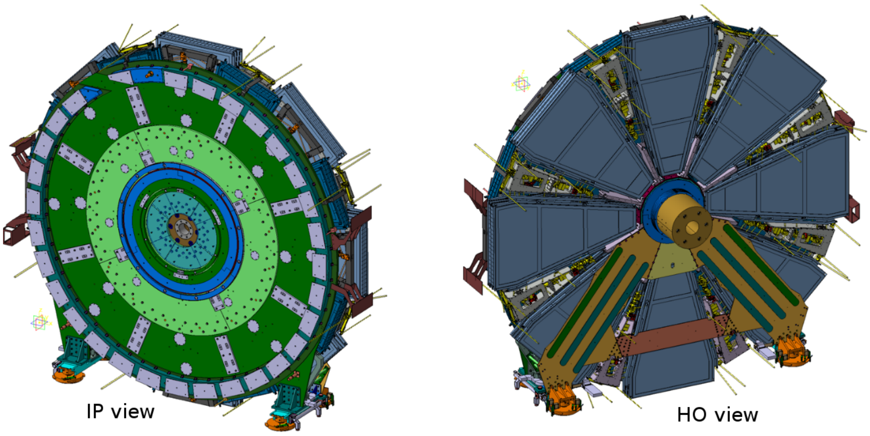

Figure 2.17: Layout of the New Small Wheels (NSW) as seen from the interaction point (left) and the HO side (right) [35].

Figure 2.18 shows a drawing of one large sector. Each sector consists of two Micromegas and two sTGC wedges. Each Micromegas wedge is composed of two modules. The four Micromegas modules are rigidly connected to a central spacer frame (one wedge per side). The sTGC wedges consist of three modules each, held together by an external frame. The sTGC wedges are linked to the spacer frame (one wedge per side) with kinematical mounts. Each wedge has four detection layers, sixteen detection layers in total such that they ensure an appropriate performance even if some layers will fail to work properly. In this configuration, the sTGC as primary trigger detectors have the maximum possible lever arm, thus maximizing their angular resolution.

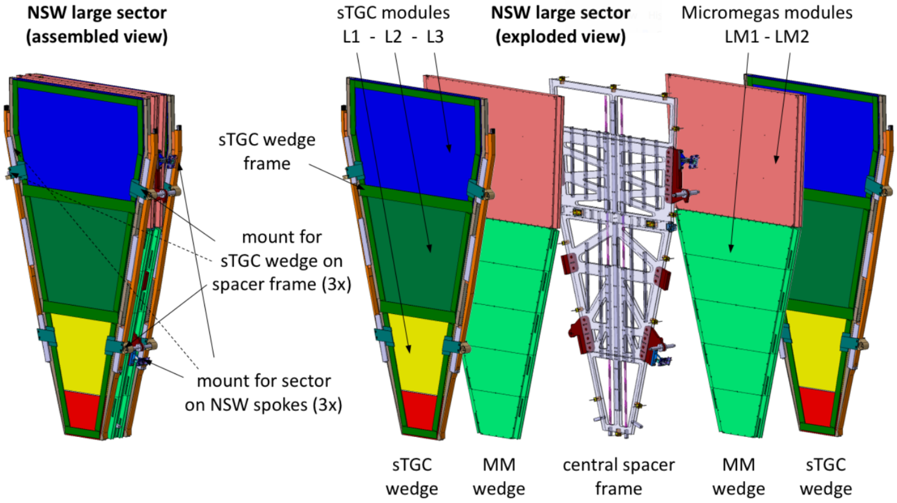

Figure 2.18: Drawing of one large NSW sector in assembled (left) and exploded view (right) [35].

The positions of the sixteen sectors and their detectors are monitored by sixteen alignment bars. Active elements on these bars sense the planar position and shape of each detector by means of optical rays projected from one bar to the adjacent one. Fig. 2.19 shows the elements of one NSW in an exploded view. Small and large sectors are mounted on the mechanical support and between the alignment bars. The support structure itself is rigidly fixed to the shielding disc called New JD (NJD). The NJD provides for an adequate thickness of low[10] and high[11] atomic number materials in order to shield the detectors against low-energy electrons, neutrons and photons.

---

[10] Borated polyethylene is used to capture thermal neutrons.

[11] Brass and carbon steel are used to stop charged particles due to energy loss by electromagnetic or strong interactions. Lead is used to absorb secondary photons emitted by the neutron capture and low-energy electrons.

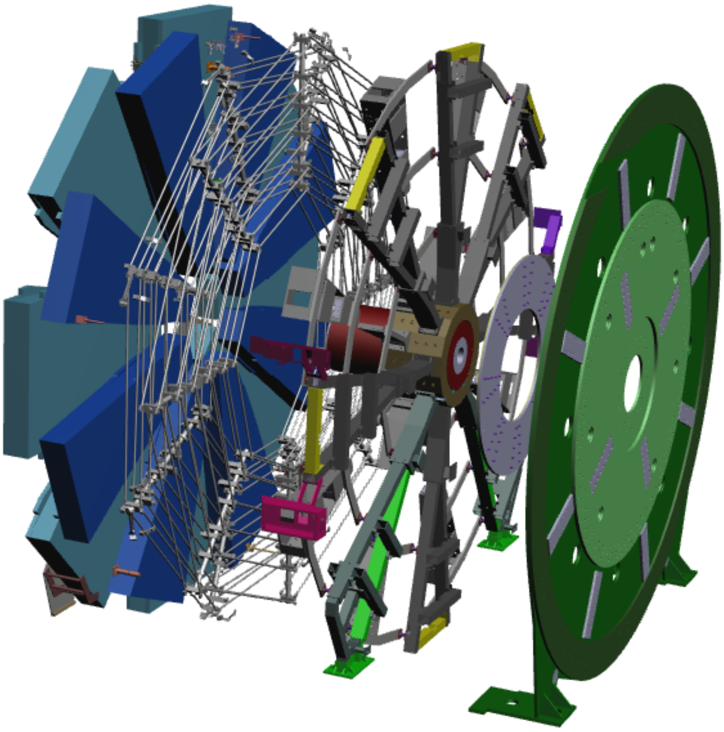

Figure 2.19: Components of one New Small Wheel. From left to right: large and small sectors; alignment bars and rays; the mechanical support; the NJD shielding [36].

Chapter 3

Micromegas for the New Small Wheels

The Micromegas[1] technique was invented in the middle of the nineties by Giomataris et al. [37]. Micromegas belong to the family of Micro Pattern Gas Detectors (MPGDs) based on the printed circuit board (PCB) technology combined with photolithography and thin-layer polyimide deposition. Because of the fast ion collection Micromegas detectors can achieve stable operation at high gains and at high particle fluxes. The Micromegas technology, since its birth, has been under constant development. Breakthrough examples are the bulk-Micromegas (2003) and the resistive anode[2] Micromegas (2011). The latter has been employed for the ATLAS NSW Micromegas detectors.

In this chapter the Micromegas principle as well as the modifications that have been employed from the original scheme towards the construction of the NSW Micromegas modules are discussed.

3.1 Micromegas principle

Micromegas consist of a planar drift electrode, a gas gap of a few mm thickness acting as a conversion and drift region and a conductive mesh that is kept at a fixed distance, typically 0.1 mm, from the readout electrode by regularly spaced insulating pillars (Fig. 3.1(a)). The amplification takes place between the mesh and the readout electrode. The high voltage potentials are chosen such that the electric field in the drift region is a few 100 V/cm while in the amplification region it is 40–50 kV/cm. For the ATLAS Micromegas detectors, the drift electrode is at negative high voltage (HV) potential, the readout electrode is at positive HV potential and the mesh is at ground potential.

Charged particles traversing the drift space ionize the gas creating electron-ion pairs. The electrons liberated in the ionization process drift towards the mesh

---

[1] The term is the abbreviation of MICRO-MEsh GAseous Structure

[2] The resistive anode Micromegas was developed by the MAMMA (Muon ATLAS Micromegas Activity) Collaboration [38] at CERN in the context of the RD-51 Collaboration [39]

following the electric field lines (Fig. 3.1(b)) while the ions drift towards the cathode. The time it takes the electrons to reach the mesh depends on the drift distance, the type of the gas, and the electric field. When the electrons approach the mesh, owing to the much stronger electric field in the amplification region, they are guided through the mesh openings to the readout electrode. In the amplification region, the electrons have sufficient energy to further ionise the gas and multiply. This process is very fast and happens within a nanosecond. The movement of the charges induces signals on the metallic readout electrode. The ions that are created in the amplification region drift towards the mesh, however, on a much larger timescale. Most of them are neutralized in the mesh within a few 100 ns, but few of them can move back into the drift region. Further details of these processes are discussed in Section 6.2.3 and in Appendix A.

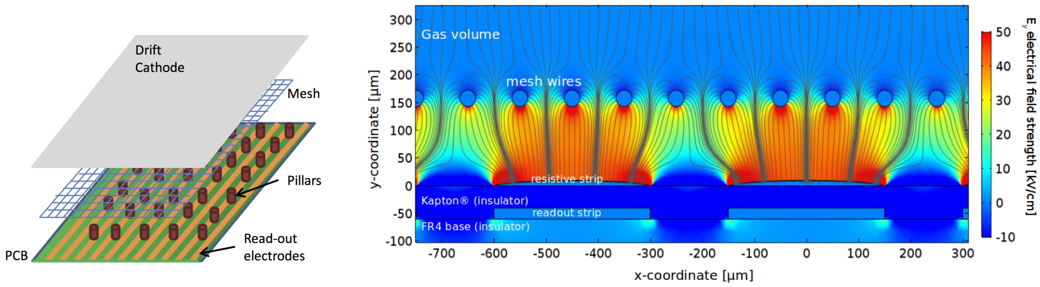

(a)

(b)

Figure 3.1: (a) Structure of a non-resistive Micromegas showing the mesh that is kept at a fixed distance from the readout electrode by small pillars made of photo resistive material, (b) Electrical field strength in the vicinity of the mesh wires as simulated with COMSOL Multiphysics®. In this illustration the mesh wires have a diameter of 30 µm and an opening of 70 µm; the strip pitch is 450 µm and the strip width 300 µm [40].

3.2 Resistive-strip Micromegas

The Micromegas detectors, because of their thin amplification gap, are prone to sparks[3]. Sparks occur when the total number of electrons in the multiplication process reaches a value of 10^7–10^8, close to the Raether limit [41]. In this case, a transition from the avalanche mode to the streamer mode takes place which leads to an electrical breakdown[4]. Micromegas detectors are usually operated at a gas gain of the order of 10^4 to have a high detection efficiency for minimum ionizing particles. Ionization processes that produce more than 1000 electrons in the amplification region over a distance of 0.1 mm carry the risk of sparks. Sparks can damage the detector and/or lead to large dead times as a result of HV breakdown. To protect the readout electrode, a resistive protection scheme was introduced in 2011 [42].

---

[3] The term sparks refers to electric arcs that are created between the mesh and the anode.

[4] Electrical breakdown occurs within a gas when the dielectric strength of the gas is exceeded.

Figure 3.2 shows a sketch of the protection scheme. It consists of a thin (50 µm) insulating layer[5] on top of which resistive strips are deposited. The resistive strips have the same strip pitch and width as the copper readout strips. Neighbouring resistive strips are interconnected between each other every 20 mm along the strips. The interconnection bridges are shifted by 10 mm from one strip to the next one (Fig. 3.3). They allow for a more homogeneous impedance between the high voltage supply line and the resistive strips. Thanks to these interconnections the charge is evacuated through a network of strips and not a single strip[6] equalising the effective resistance over the full area of the detector. Another advantage of these interconnections is that defects in the resistive pattern like for e.g. broken strips, become uncritical unless they are too massive.

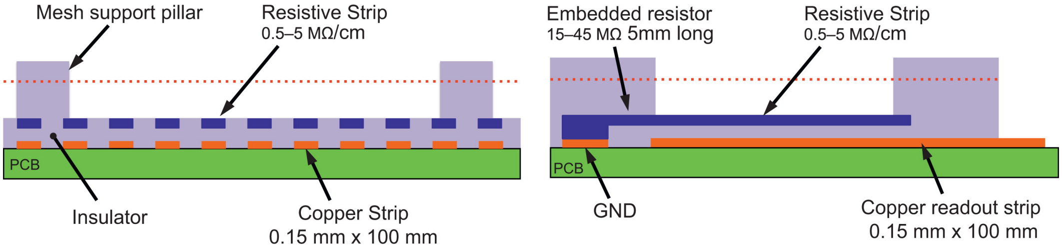

Figure 3.2: Resistive protection scheme in a bulk-Micromegas detector; (left) view along the strip direction, (right) side view, orthogonal to the strip direction [42]

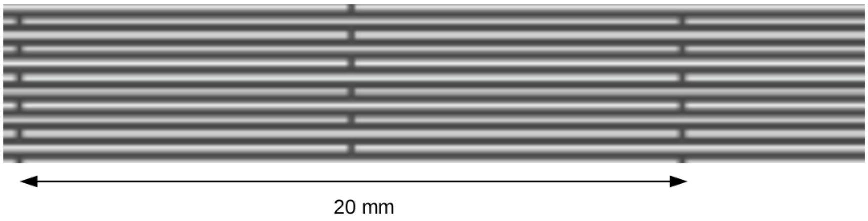

Figure 3.3: Connection lines of the resistive strips.

In the Micromegas detectors discussed in this thesis the resistive strips are produced by screen-printing. In the early stages of R&D to produce the resistive strips for the Micromegas detectors other than the well-established screen-printing technology, the more novel sputtering technique was also investigated.

Figure 3.4(a) shows the steps needed in the production of the resistive strips with the sputtering process. At first the negative pattern of the electrode image is formed by photo-resist on the Kapton® substrate. Then, the carbon is sputtered on the surface, and finally the remaining photo-resist is removed chemically. The molecular structure of the resistive material is an amorphous diamond like carbon (a-DLC) doped with nitrogen with a thickness in the nanometre range. The resistivity

---

[5] The insulating material is Kapton® which is a polyimide film.

[6] The charge along the resistive strip spreads over a few mm.

of the strips depends on the exposure time of the sputtering process. For example for a carbon thickness of 30 nm the surface resistivity is $\sim$4 G$\Omega/\square$ while for a thickness of 360 nm it is $\sim$500 k$\Omega/\square$. Like that the resistivity of the strips can be controlled very well. The spatial precision of the sputtering pattern is determined by the photo-resist imaging reaching an accuracy of $<$10 µm.

The steps of the screen-printing process are shown in Fig. 3.4(b). In this case, the negative pattern of the electrode image is first prepared on the screen. Like that the same screen can be used for printing on a large number of Kapton® substrates. Printing is done with a commercial ink[7] through the screen with an accuracy of 20–30 µm. The viscosity of the ink and the speed during the printing process influence the thickness of the resistive strips and the resistivity.

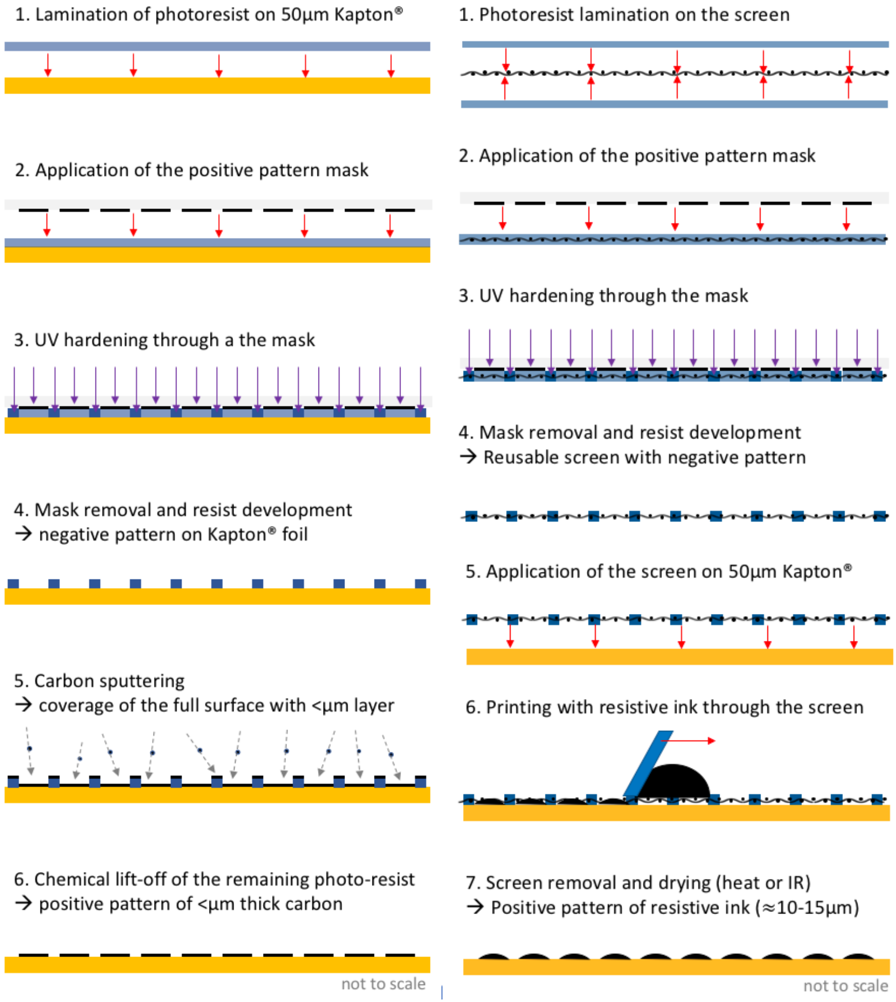

(a) (b)

Figure 3.4: Process for producing the resistive strips with (a) sputtering and with (b) screen-printing technology [40].

---

[7] ESL Electroscience® RS 12115

The difference between the sputtering and the screen-printed resistive strips is shown in Fig. 3.5. The resistive strips formed with sputtering are flat, very thin, and have sharp edges (Fig. 3.5(a)). The screen-printed resistive strips have a bump-like cross section with a height of 10–15 µm and their boundaries are not sharp (Fig. 3.5(b)).

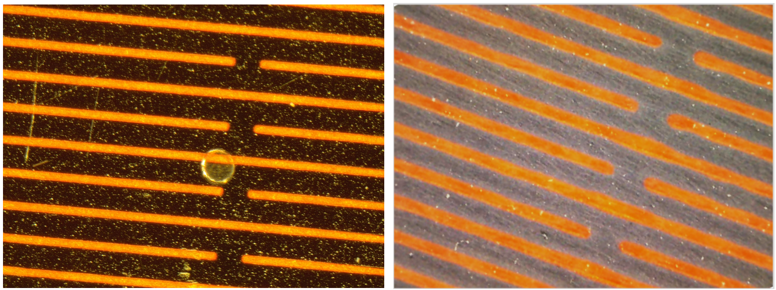
(a) (b)

Figure 3.5: Pictures taken with a Dino-Lite® digital microscope for (a) sputtered and for (b) screen-printed resistive strips. The resistive strips with their interconnects are coloured black. Between the resistive strips, the readout strip layer (orange colour) is visible. The fact that one can see the readout strips means that they are not perfectly aligned to the resistive strips.

Even if the sputtering technique yields a more accurate resistive pattern, due to the more complex process and higher cost, the screen printing technology was decided to be used for the NSW Micromegas detectors.

The schematics of a resistive-strip Micromegas detector is shown in Fig. 3.6. The insulating layer carrying the resistive strips is glued on top of the copper strips. In this case, the resistive electrode and the copper electrode form a capacitor. The positive HV is applied on the resistive strips. Charge induced on the resistive strips is capacitively coupled to the copper strips.

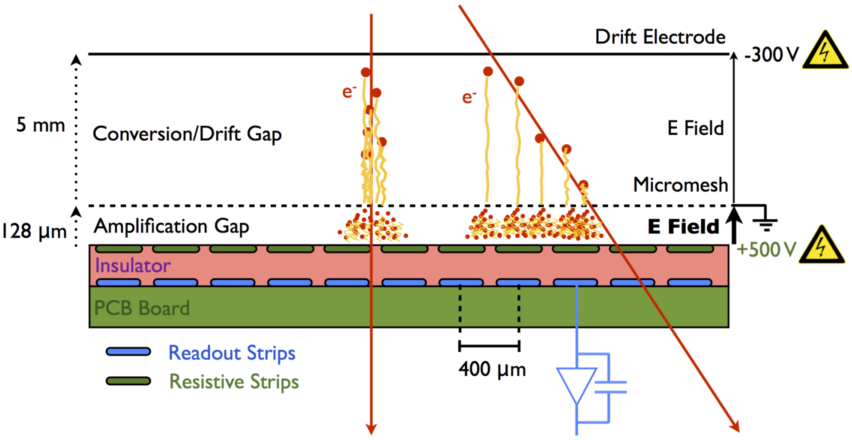

Figure 3.6: Schematics of a resistive-strip Micromegas detector.

3.3 Layout of NSW Micromegas

The NSW detectors are currently under construction. For each wheel sixteen sectors will be built in total (eight small and eight large) as described in Section 2.9.2. One Micromegas sector (see Fig. 2.18) consists of eight detection layers, grouped into two wedges of four layers each (quadruplets), separated by a 40 mm thick spacer. Figure 3.7 shows this arrangement.

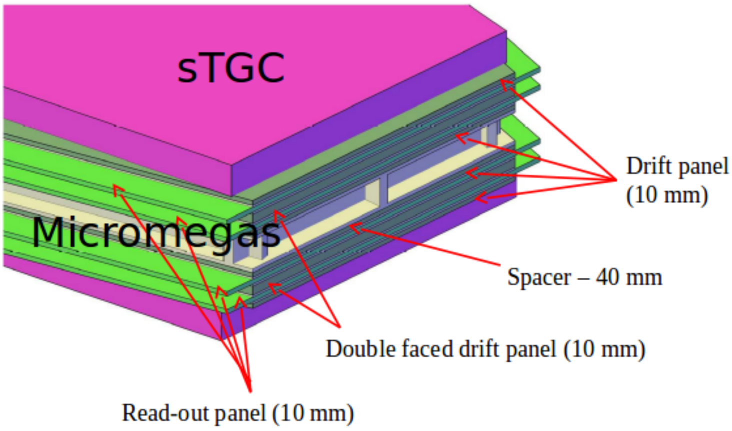

Figure 3.7: Arrangement of the NSW detectors in a sector.

Each wedge is divided radially into two modules. Figure 3.8 shows the segmentation of the Micromegas wedges (small and large). The naming convention is as shown in the figure. For the small wedges, the lower radius module is called Small Module 1 (SM1) while the upper radius is called Small Module 2 (SM2). The same naming convention stands for the large wedges; Large Module 1 (LM1) for the lower radius and Large Module 2 (LM2) for the upper one.

Each module type is constructed by a different consortium[8]. The small modules cover an area of ~ 2 m^2, while the area of the large modules is ~ 3 m^2. The exact dimensions of each module are quoted in the figure in millimeters. The segmentation of each module will be discussed in Section 3.4.1.

Each module contains four Micromegas detectors, grouped into two pairs as shown in Fig. 3.9. In each pair (readout panel) the detectors are mounted back-to-back[9]. On one readout panel the strips on both detectors are arranged perpendicular to the η-coordinate (eta-panel). Each detector measures the η-coordinate (precision coordinate). On the second panel the strips are inclined by $\pm 1.5°$ (stereo-panel)

---

[8] SM1 modules are constructed in Italy by INFN, SM2 in Germany by BMBF, LM1 in France by IRFU CEA/Saclay. For the LM2 modules, the drift panels are constructed in Greece by the Aristotle University of Thessaloniki while the readout panels are constructed in Russia by the Joint Institute for Nuclear Research (JINR) in Dubna. Each construction site will build 32 modules.

[9] This configuration has been chosen in order to reject hits that will not be synchronous to the bunch crossing.

with respect to the η-strips. By combining the information of the two stereo layers the precision and the second coordinate (ϕ) coordinate[10] can be measured.

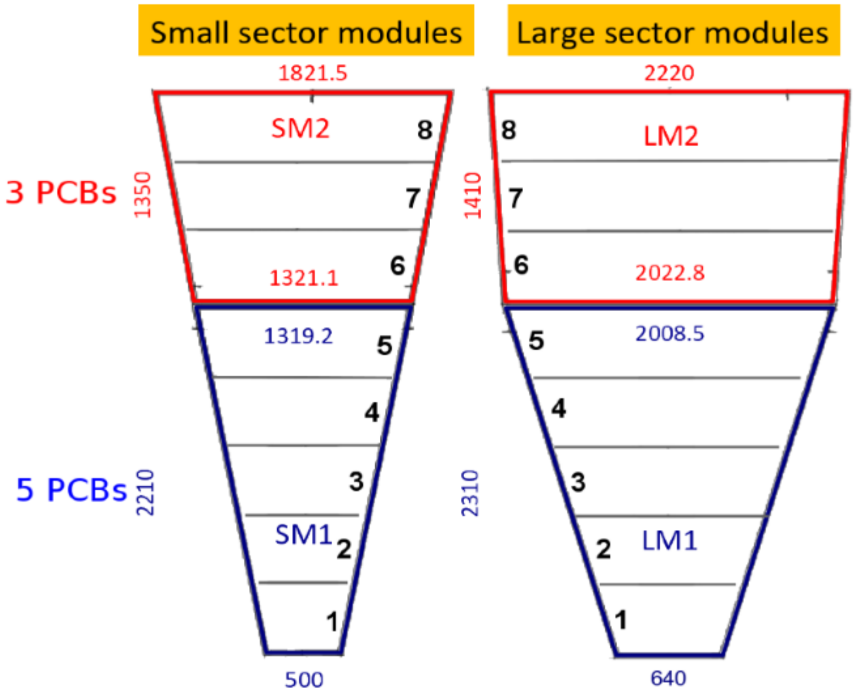

Figure 3.8: Segmentation of small and large sectors.

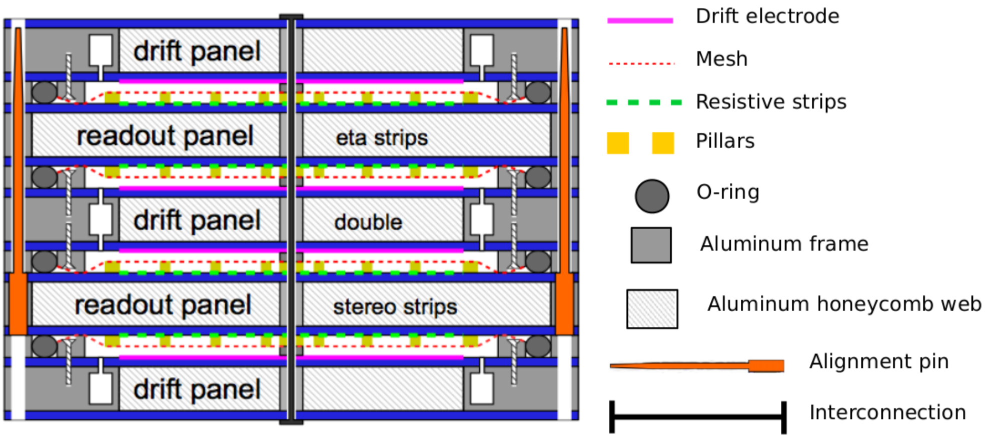

Figure 3.9: A Micromegas quadruplet showing the arrangement of the detectors in assembled view. Not to scale.

---

[10] The second coordinate can also be reconstructed from the combination of one or two eta layers with one stereo layer.

To build a Micromegas quadruplet two readout panels and three drift panels (two external and one internal) are needed (Fig. 3.9). Figure 3.10 shows these two types of panels (drift and readout). The readout panel carries the readout boards. The drift panel comprises the drift electrode, the micro-mesh and the gas distribution system. These components and the construction procedure of the panels will be discussed in some more detail in the next two sections.

Contrary to the bulk-Micromegas technology where the mesh is embedded in the pillars, for the NSW Micromegas detectors the mesh is mechanically supported by the drift panel. In this way, both readout and drift panels are directly accessible for cleaning before closing the detector. When the detector is closed the mesh is resting on the pillars and is kept in position by electrostatic force when high voltage is applied.

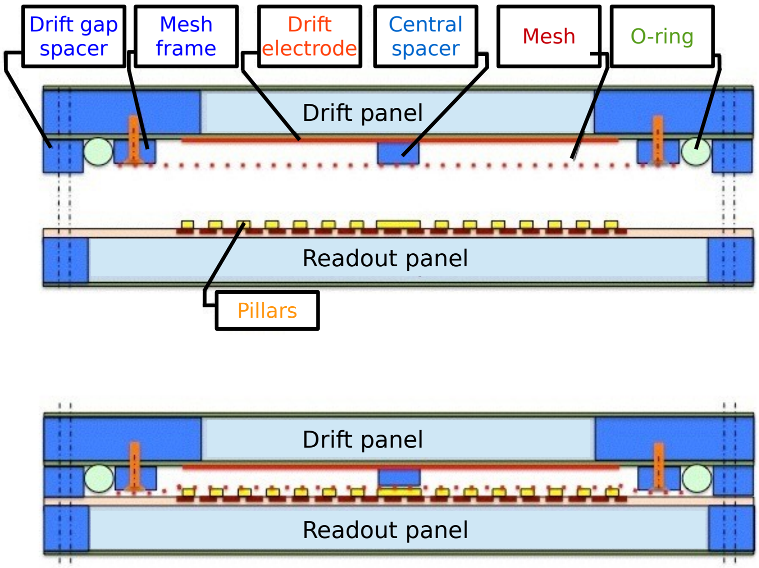

Figure 3.10: Assembly of a single Micromegas detector showing the drift and readout panels in open (top) and closed (bottom) view. Not to scale.

3.4 Components of the NSW Micromegas

In the following, the main components used in the panels will be addressed prior to the discussion of the panel construction.

3.4.1 Readout boards

As described before, the NSW Micromegas detectors employ the resistive-strip protection scheme. Figure 3.11(a) shows the structure of a Micromegas readout board. It is composed of a PCB with the copper readout strips. On top of the readout strips a 50 µm thick Kapton® foil carrying the resistive strips is glued. Geometrically, the resistive strips match the pattern of the readout strips but they are split in the middle. Each side can be connected to its own HV potential. Both readout and resistive strips have a width of 300 µm and a pitch of 425/450 µm for small/large sector boards. On top of the resistive strips the mesh support pillars are deposited. The pillars have a rectangular shape of 1000 µm in length and 200 µm in width with 7 mm spacing and are positioned perpendicular to the strips (Fig. 4.4). The choice of the pillars size and their influence on the detector performance are discussed in Chapter 6.

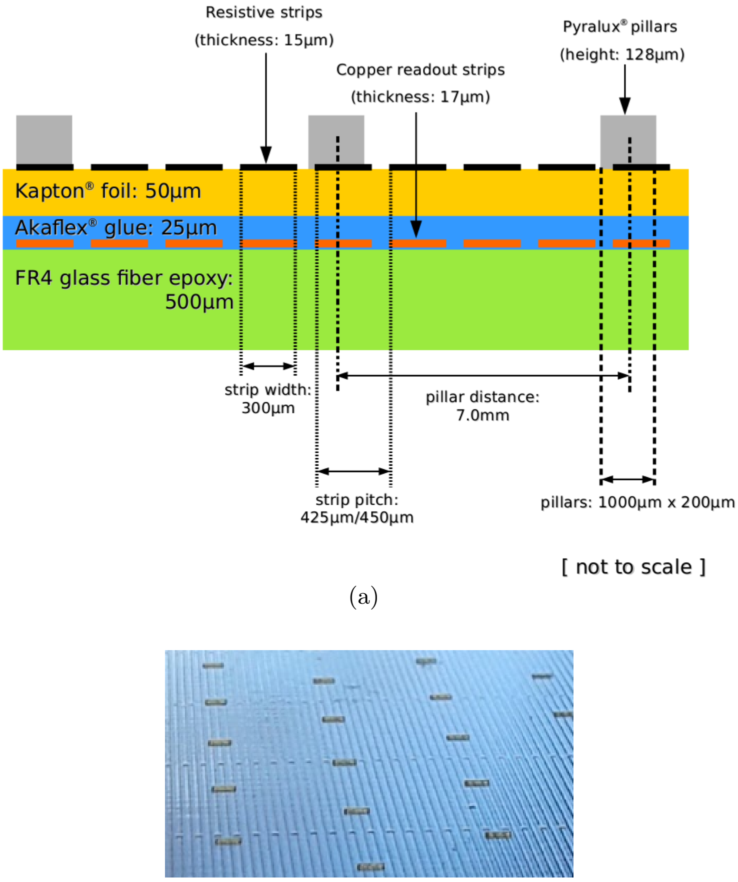

(a)

(b)

Figure 3.11: (a) Structure of a Micromegas readout board; (b) Photo of the surface of a readout board for the NSW showing the resistive strips and the pillars.

The NSW Micromegas boards are manufactured in industry[11]. Since most PCB industry is limited to 600 mm wide PCBs, the size of the PCBs was kept in one dimension below 600 mm while the other dimension can be up to 2500 mm. Figure 3.12 shows a drawing of the smallest readout board for the SM1 modules.

Each PCB accommodates up to 1022 strips. The strips are split into two groups of 511 strips each. The upper 511 strips are routed out of the active area to the

---

[11] ELVIA (Coutances, France) and ELTOS (Arezzo, Italy).

right side, while the lower strips are routed to the left side (see Fig 3.12(b)). The areas on the side of the boards accommodate the readout electronics.

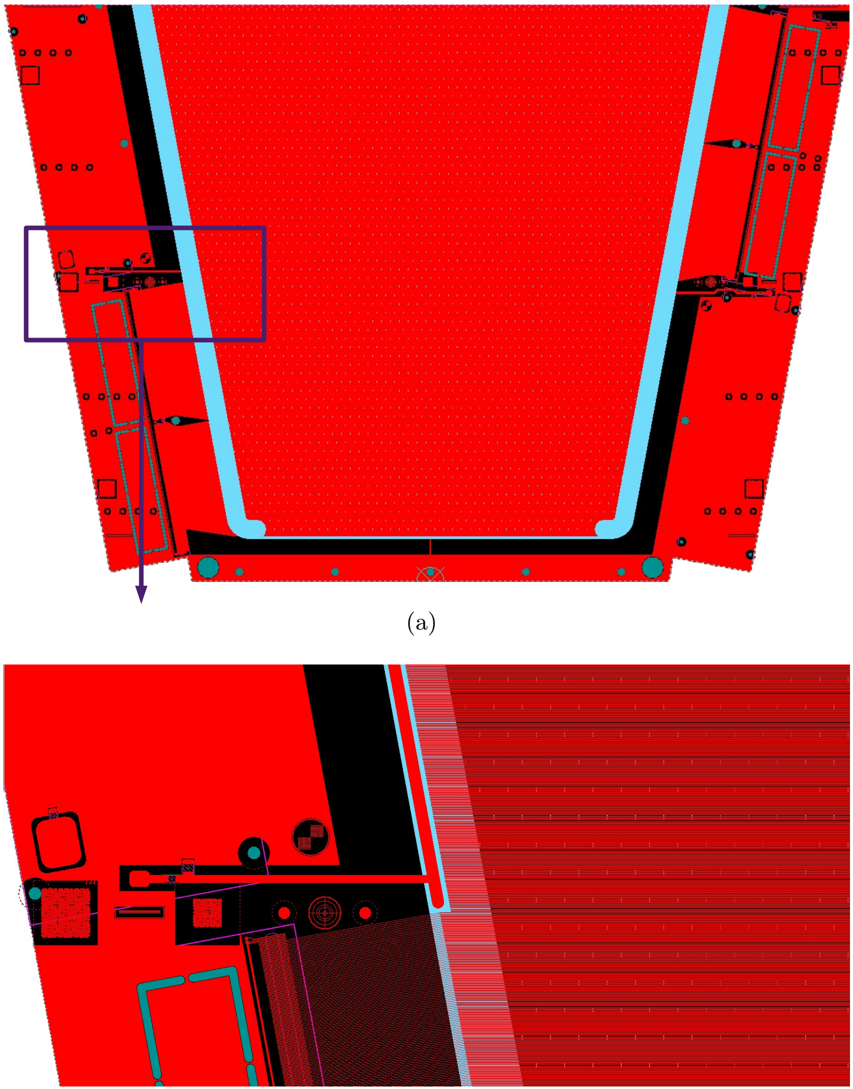
(a)

(b)

Figure 3.12: (a) Drawing of a Micromegas readout board; (b) Zoom showing the area of the HV connection and the precision alignment targets (see text). The copper readout strips that are routed out of the active area are visible, as well as the pillars.

The steps of the readout board production are illustrated in Fig. 3.13. Starting from the base material (fiber glass epoxy (FR4) with a 17 µm copper layer), the copper is etched[12] via photolithography in order to create the readout strips. The

---

[12] During this process also precision targets and coded masks that are used for the construction of the panels are etched outside the active area.

resistive protection layer[13] is glued under high pressure[14] and temperature[15] on top of the readout strips with a 25 µm thick layer of glue[16]. On top of the resistive strips, the pillar pattern is created after lamination of a double layer of 64 µm thick photoimageable coverlay[17] via a photo-lithographic process.

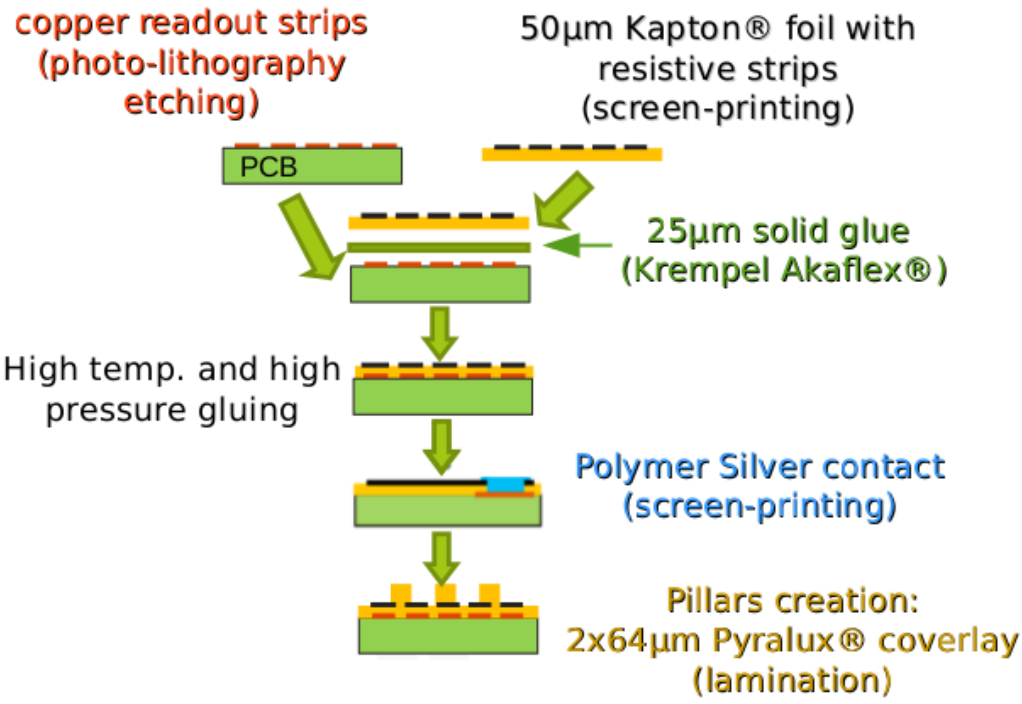

Figure 3.13: Construction process of the Micromegas readout boards.

3.4.2 Drift boards

Contrary to the complexity of the readout boards, the drift boards are much simpler. The base material of the drift boards is the same as the one of the readout board. It is a 0.5 mm FR4 printed circuit board (PCB) clad with a 17 µm thick Cu layer used as the drift electrode. Figure 3.18 shows a picture of the smallest drift board for SM2 modules.

---

[13] It is produced in industry by Matsuda-Screen Inc. (Japan)

[14] 5–7 kg/cm^2.

[15] 170°C.

[16] Krempel Akaflex® CDF 25.

[17] Pyralux® PC1025.

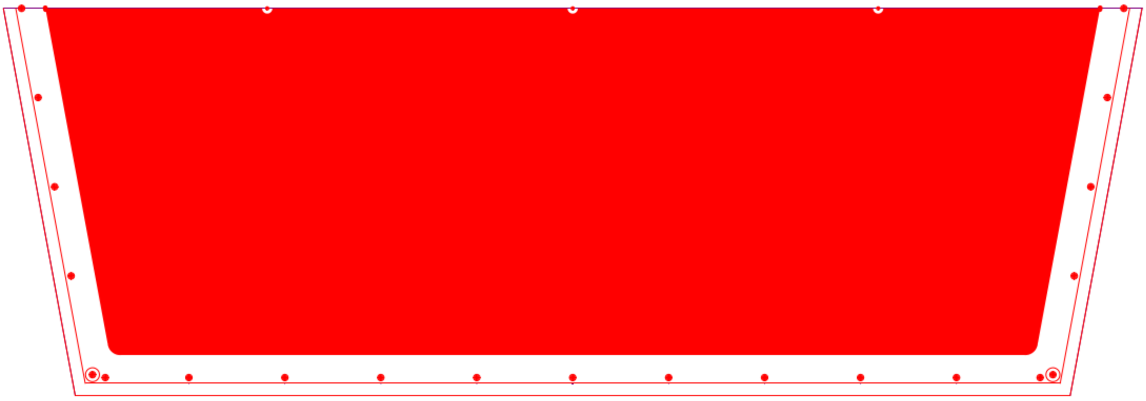

Figure 3.14: Drawing of a drift board.

3.5 Construction of Micromegas modules

To build Micromegas modules several PCBs must be glued on a support panel with the precision as required to reach the expected performance. For the SM1 and LM1 modules each panel side is composed of five single PCBs while for SM2 and LM2 modules three single PCBs are glued onto each panel side (see Fig. 3.8).

3.5.1 Module requirements

For the Micromegas detectors to be able to measure 1 TeV muons to 10% precision, the strip position should be measured with a precision of 50 µm R.M.S. in the η-direction and 80 µm R.M.S. in the z-direction. These requirements determine the mechanical constraints that should be taken into account during module construction.
To achieve the precision in the η-direction:

- The readout PCB must be positioned on one side of a readout panel with a tolerance of ±40 µm;
- The two sides of a readout panel must be aligned within ±60 µm;
- The two readout panels (eta and stereo) must be aligned within ±60 µm;
- Each pair of modules must be precisely aligned on the spacer frame within ±200 µm;

To achieve the precision in the z-direction:

- The thickness and planarity of the panels must be controlled within ±110 µm with respect to the nominal plane;

- Mesh frames and gas gap frames should be precisely machined within ±25 µm[18];
- The drift gap size must be precise in the area of a module within ±110 µm;

3.5.2 Panel construction procedure

A panel is a sandwich of two FR4 skins and an aluminum honeycomb web with a thickness of 10 mm surrounded by an aluminum frame 10 mm thick and 30 mm wide (Fig. 3.15). The FR4 skins are created by the Micromegas readout or drift boards. The readout panels are wider than the drift panels. The additional space hosts the readout electronics and their cooling system.

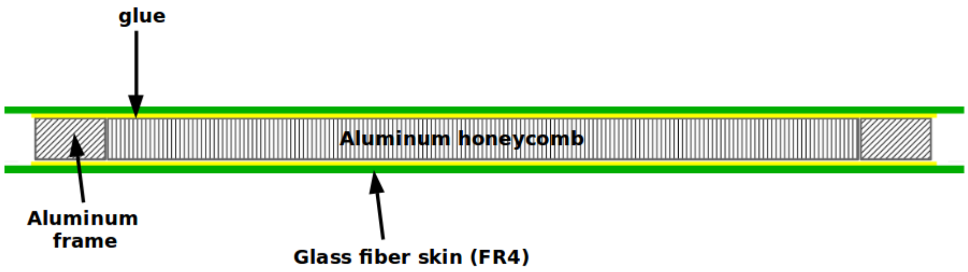

Figure 3.15: Schematic view of a Micromegas panel.

To fulfil the requirements for the planarity and the alignment of the panels, different approaches have been developed in each consortium for the construction of the panels. In all cases the basic idea is to transfer the planarity of a precision surface (e.g. a granite table or a stiff-back[19]) to the panel. Two construction procedures were chosen, either to glue a panel in only one step or in two steps. Here the latter procedure will be described as used in Germany.

The two-step gluing process is illustrated in Fig. 3.16. In a first step, all the PCBs needed for a module are aligned on top of the precision surface. The PCBs are sucked to the precision surface using vacuum. Afterwards glue[20] is distributed homogeneously on top of the PCBs in order to glue them to the aluminum honeycomb web and the aluminum frames. A sealed bag is placed over the materials and vacuum is applied to press the frames and the honeycomb into the glue. The glue is cured for 24 hours. After the curing process, the half panel is removed from the granite table and it is sucked by vacuum to a stiff-back. The second set of PCBs is placed and aligned on the precision surface and again glue is distributed on top. The stiff-back with the half panel is then lowered onto the precision surface and placed

---

[18] This is important in order to keep the mesh at the correct position and at the same time to avoid that the mesh frame touches the readout board when the quadruplet is closed.

[19] A stiff-back is made of 60 mm perforated aluminum honeycomb web sandwiched between two thick skins of aluminum alloy. In order to be used as a vacuum table several holes are drilled into one of the aluminum skins. The perforated honeycomb allows for a uniform distribution of the vacuum across the full surface.

[20] Araldite® 2011

on precision distance pieces, which define the thickness of the panel. The glue has to cure again for 24 hours.

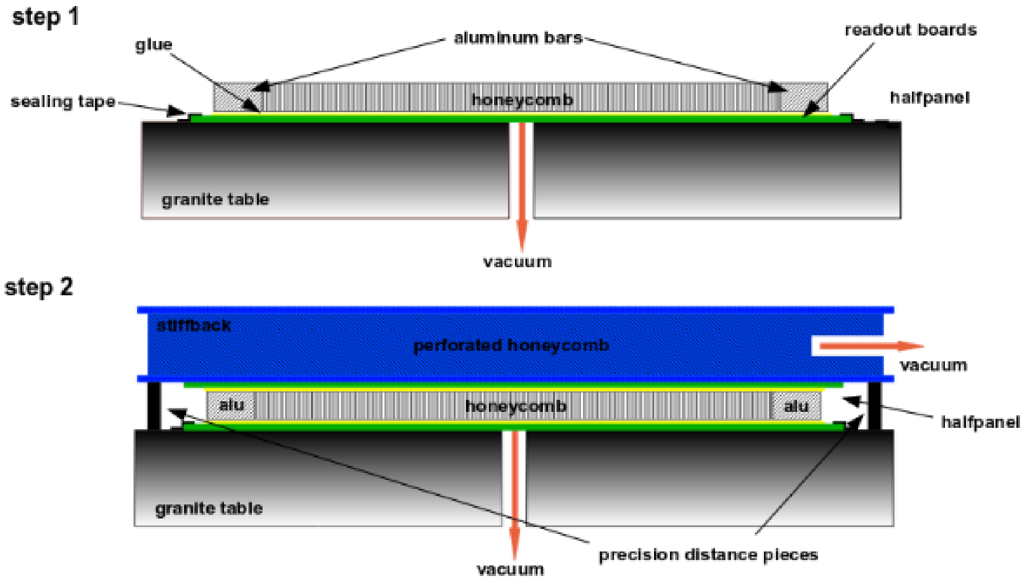

Figure 3.16: Schematics of the panel construction method [44].

The only difference for the panel construction in one gluing step is to suck the second set of PCBs during the first gluing step to the stiff-back with glue distributed on top. Then the stiff-back is lowered onto the half panel. In this method no vacuum bag is used.

Readout panels

In the readout panels the readout boards form the two skins of the panel. For the construction of the readout panels the alignment of the readout boards is very important in order to meet the precision requirements. On each readout PCB precision targets and coded masks are produced outside of the active area in the same lithographic process in which the readout strips are produced (Fig. 3.17(a)). Precision holes are drilled in the position of the targets or metallic precision washers are glued concentrically at the position of the coded masks or the precision targets.

On the assembly table aluminum plates are used as reference to place and align the PCBs needed to construct a panel. The plates themselves are aligned and blocked on the precision surface of the assembly table with pins that are protruding from precision holes in the surface. Precision pins are then mounted on the plates to ensure the position of the PCBs (Fig. 3.17(b)).

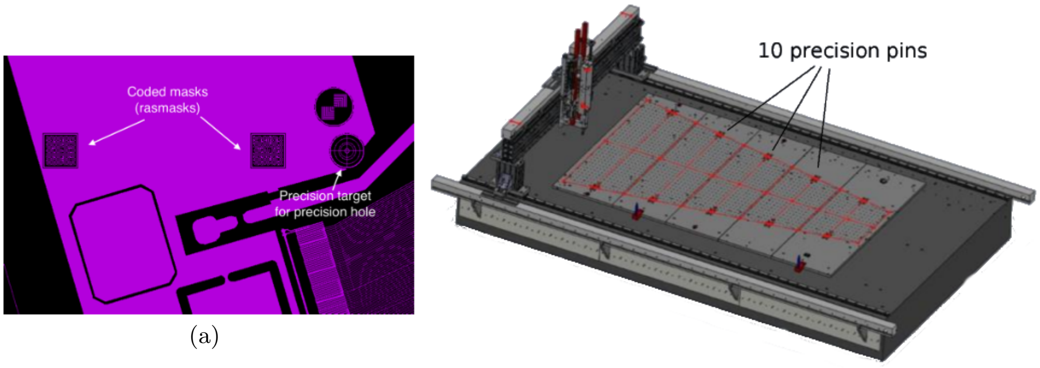

(a)

(b)

Figure 3.17: (a) Precision target and coded masks; (b) Granite table and five reference aluminum plates with pins mounted for the alignment of the readout PCBs.

Drift panels

A drift panel consists of the drift boards, the gas gap spacer frame, the mesh frame, the gas distribution pipes and feed-through, and the interconnection holes as shown in Fig. 3.18.

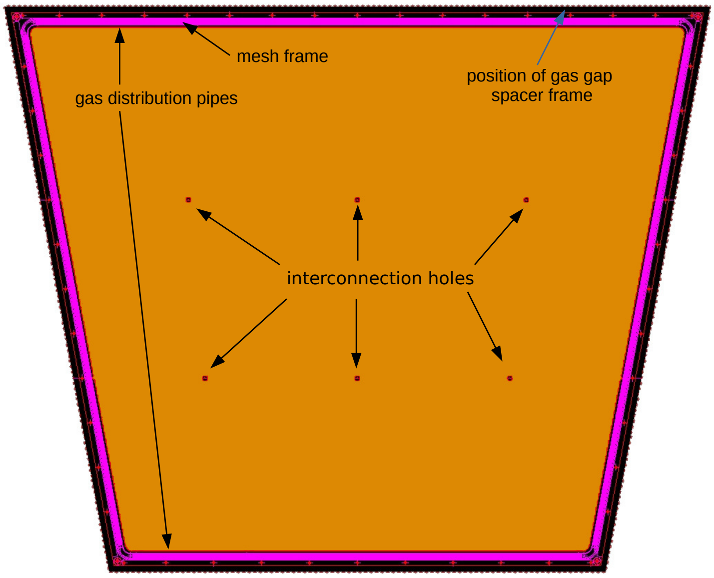

Figure 3.18: Drift panel showing the drift electrode (in brown) and some of the necessary components needed to build the drift panels.

Figure 3.19 shows in some more detail the components used in the drift panels. The gas gap spacer frame defines the drift gap thickness. The mesh frame that holds the mesh is ∼100 µm thinner than the gas gap frame. It consists of extruded aluminum bars with an enlarged surface optimized for glueing. On the inside of the mesh frame there are two 3 mm diameter stainless steel tubes along the two long sides of the panel. They serve for the gas distribution inside the chamber. The tubes have a number of small holes of different diameter along their length in order to equalize the gas flow. At both ends of each gas tube gas feed-troughs connect the tubes to the external gas lines. In the groove between the gas gap frame and the mesh frame a 7 mm thick O-ring[21] is inserted to assure gas tightness.

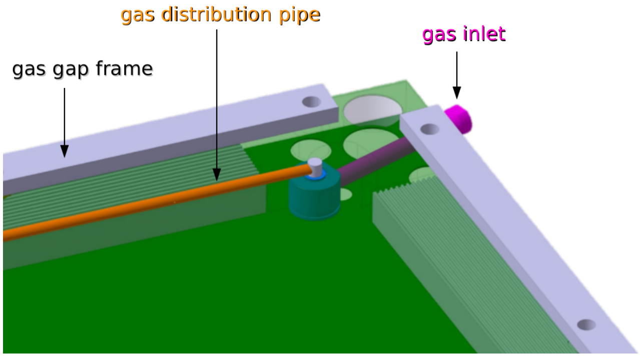

(a)

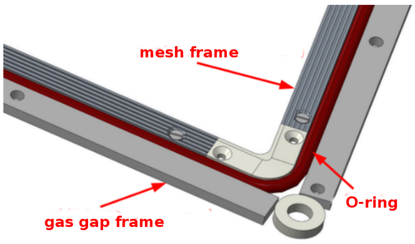

(b)

Figure 3.19: (a) Schematics of the gas gap frame, the mesh frame is missing, the gas distribution pipe and gas inlet; (b) The O-ring placed in between the gas gap frame and the mesh frame.

The mesh used in the NSW Micromegas detectors is a plain weave stainless steel mesh with 71 μm aperture and 30 μm wire diameter. It is pre-stretched and glued onto a transfer frame with a tension of 10 Ncm^{-1} using pneumatic clamps, as shown in Fig. 3.20. This process helps to decouple the construction process of the drift panels. In a later step, the mesh is transferred and glued onto the mesh frame. The two external drift panels carry the mesh on one side while the internal drift panel has meshes on both sides.

---

[21] The O-ring is a string of Ethylene Propylene Diene Monomer (EPDM) elastomer with a round cross-section.

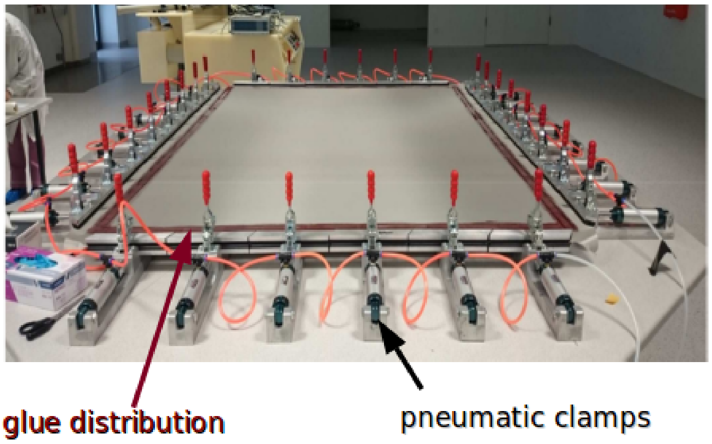

Figure 3.20: Mesh stretching with pneumatic clamps.

The interconnection holes allow for the interconnection of the two external drift panels of the quadruplet when the detector is assembled (Fig.3.21(a)). It limits the deformations of these panels when the detector is operated with a gas overpressure of 1–2 mbar with respect to the atmospheric pressure. Fig. 3.21(b) shows a simulation of a SM2 quadruplet with six interconnections. The maximum deformations are ~ 50 µm well below the maximum tolerance [45].

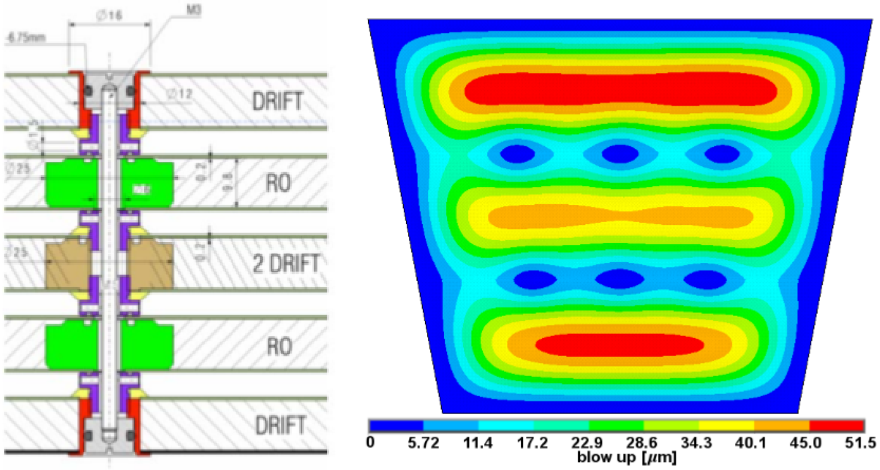

(a)

(b)

Figure 3.21: (a) The interconnection passing through all panels ; (b) Simulation of the expansion of a quadruplet for 2 mbar overpressure inside the chambers with six interconnections [45].

3.5.3 Module assembly

After the construction of the panels and the installation of the mesh the Micromegas quadruplets can be assembled. Fig. 3.22 shows a schematic view of the positions of the gas gap frame, the O-ring, the mesh frame and the mesh after the assembly of a readout panel and an external drift panel.

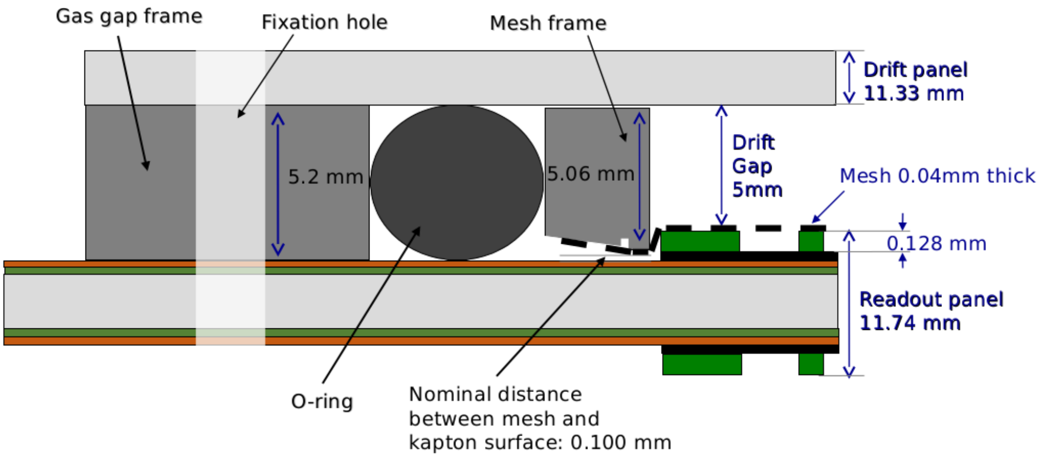

Figure 3.22: Assembly of a readout panel and an external drift panel. Not to scale.

The two readout boards have to be aligned precisely in order to meet the precision requirements. Precision alignment pins are glued on the first readout panel and precision alignment bushes are embedded in the second readout panel (Fig. 3.23). This guarantees that, during assembly the two readout panels are precisely aligned. For the position of the drift panels an accuracy of a millimeter is sufficient.

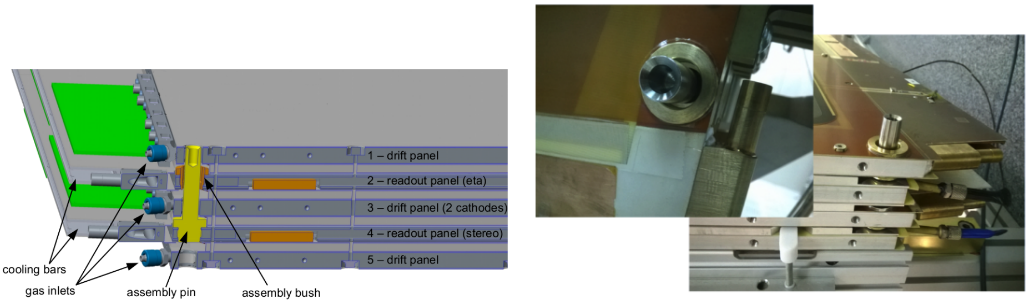

(a)

(b)

Figure 3.23: (a) Design of a NSW Micromegas quadruplet consisting of three drift panels and two readout panels. Dedicated pins and bushes are used to align the two readout panels perfectly during assembly; (b) Photo of an alignment pin.

Chapter 4

The first medium-size resistive-strip Micromegas quadruplet prototypes

In 2014, two resistive-strip Micromegas quadruplet prototypes (Fig. 4.1) have been built at CERN to evaluate detector design, construction and performance issues relevant for the construction of the NSW Micromegas detectors. The two quadruplets follow as much as possible the layout of the NSW Micromegas detectors, however, not full size. They were built in a similar approach as described in Section 3.5. More details on the construction process can be found in Ref. [46]. The dimensions of the quadruplets were chosen such that one of these detectors could be installed on the existing Small Wheel behind the currently installed Cathode Strip Chambers in the ATLAS cavern thus their name MicroMegas Small Wheel (MMSW). For this reason there was the need to develop a data acquisition system (DAQ) and integrate it into the ATLAS Trigger and DAQ (TDAQ) infrastructure. The project was cancelled one year later. By this time a DAQ system based on the official ATLAS TDAQ software had been developed and was tested within the ATLAS partition during cosmic runs before the start of Run 2 (Section 4.4).

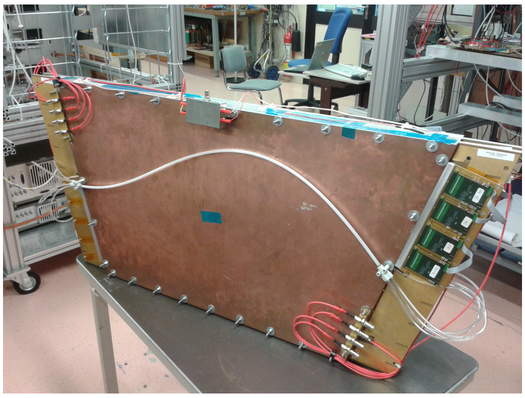

Figure 4.1: One of the two MMSW quadruplet prototypes.

4.1 Detector description

Figure 4.2 shows the layout of a MMSW quadruplet. Like the NSW quadruplets, it consists of three drift panels, two readout panels and four gas gaps. The readout panels carry identical Micromegas structures on both sides mounted back-to-back. On one of the readout panels the strips on both sides are parallel to the long side of the trapezoid. This will be referred to as η-coordinate and the corresponding panel as η-panel. On the second panel the strips are inclined by $\pm 1.5°$ with respect to the η-coordinate. This panel will be referred to as stereo-panel. The mesh is integrated on the drift panels.

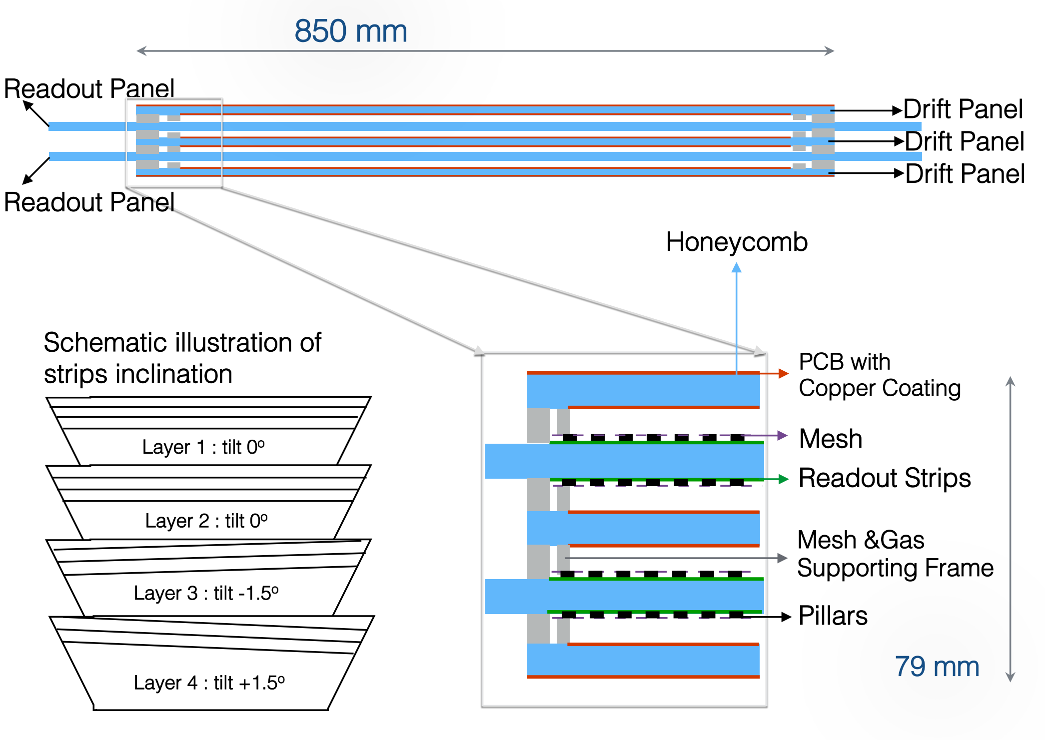

Figure 4.2: Layout of the MMSW detectors.

Figure 4.3 shows a photo of one readout panel. It has a trapezoidal shape, with an upper base of 1150 mm, a lower base of 870 mm, and a height of 492 mm with 0.3 m^2 active area per detection layer. Each PCB comprises 1024 readout strips with lengths increasing from $\simeq$600 mm to $\simeq$800 mm between the short and long sides of the boards. The strips have a width of 300 µm and a pitch of 415 µm. The readout strips are split into two groups. The upper 512 strips are routed out of the active area to the right side of the board, the lower 512 strips to the left side.

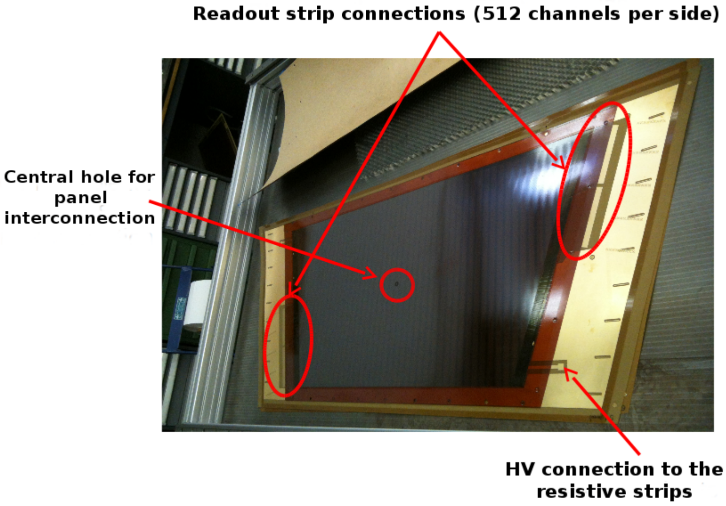

Figure 4.3: MMSW readout panel

On the stereo panel, the strips are rotated by ±1.5° around the geometrical center of the board. By this rotation the first and last 20–24 strips at the upper and lower edges of the readout PCB move out of the area defined by the η-strips. For this reason, the strips in these areas were shortened accordingly. The readout strips are covered by a 50 µm thick Kapton® foil on top of which carbon resistive strips with a surface resistivity of 0.5–1 MΩ/□ are sputtered[1] [47] (see Section 3.2).

On top of the resistive strips a pattern of insulating pillars that sustain the mesh has been deposited. The pillars are circular with $\sim$ 400 µm diameter and a height of $\sim$ 128 µm. Figure 4.4 shows the top left side of the one MMSW PCB showing the pillar pattern. The distance between two pillars is 5 mm along the direction of the readout strips. The next row of pillars is at a distance of 2.5 mm shifted by 2.5 mm along the strip direction.

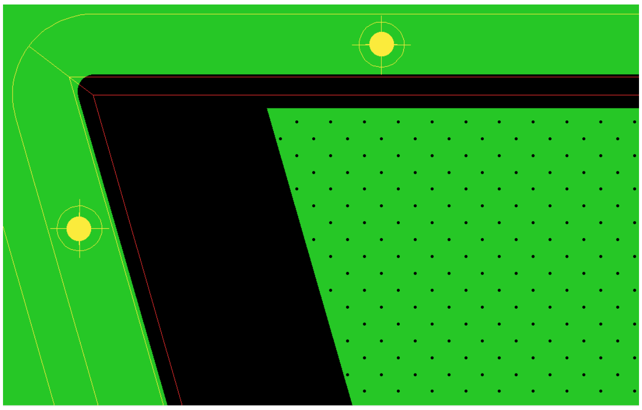

Figure 4.4: Top left side of the one MMSW PCB showing the pillar pattern.

---

[1] The foils with the sputtered resistive strips were produced in Japan by Be-Sputter Co., Ltd.

The mesh used for the MMSW detectors is woven from 30 µm steel wires with 50 µm aperture (325 lines per inch)[2]. The electron transparency for different meshes has been measured and can be found in Ref. [40]. For this mesh, the electron transparency is 64% at an electric field[3] of 0.6 kV/cm.

4.2 Alignment of the readout layers

The alignment of the strips on the two faces of the readout panels is of prime importance for the reconstruction of tracks. For the NSW Micromegas detectors the requirement is to know the strip positions to better than 30 µm.

Before the assembly of MMSW2, the relative alignment of the two η–readout layers was measured with a laser triangulation sensor[4]. Figure 4.5 shows how this measurement was performed. It takes advantage of the fact that two strips of each group of 128 readout strips were routed to the side of the readout panel close to the edge of the PCB. A precise pin with 10 mm diameter head was inserted close to one of the pair of strips. A scan with the laser tracker was performed along the edge of the PCB passing over the strips and the pin. The same procedure was repeated on the opposite side.

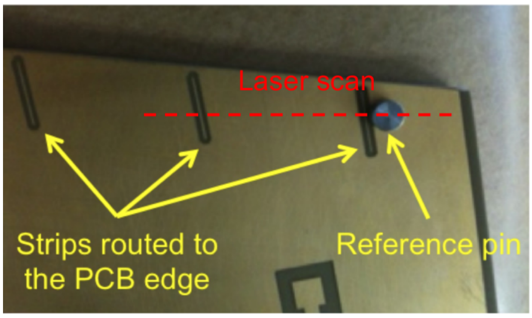

Figure 4.5: Strips routed to the edge of the PCB with the reference pin to measure the relative alignment of the two η–readout layers.

The results of the laser scans are shown in Fig. 4.6. Data acquired from the scans of both sides of the readout panel are superimposed at the position of the pin. The magnification in Fig. 4.6(b) shows the alignment of the strips on both sides of the readout panel to be better than 20 µm.

After the assembly of the quadruplet we wanted to measure also the relative alignment between the η- and the stereo-panel with X-rays. To do so, the Amptek® Mini-X Silver gun that produces X-rays with an energy of up to 50 keV was used.

---

[2] For the NSW Micromegas detectors a woven mesh with 30 µm wire diameter and 71 µm aperture (250 lines per inch) is used which has a higher transparency of 96% at an electric field of 0.6 kV/cm.

[3] This electric field corresponds to V_D = -300 V and is the usual drift voltage that we apply to Micromegas detectors.

[4] Micro-Epsilon® optoNCDT. This sensor operates with a laser diode, which produces a short visible laser pulse onto the measurement target. The light reflected from the target is detected by a CCD camera.

X-rays from the most common X-ray sources like the ^{55}Fe source with the main emission line at 5.9 keV or the Cu X-ray gun with an energy of 8 keV are not able to penetrate the first drift panel. Figure 4.7 shows a numerical estimation of the X-ray fluxes that reach the different readout layers of a quadruplet for different X-ray energies[5]. To be able to penetrate both readout panels their energy should be >25 keV.

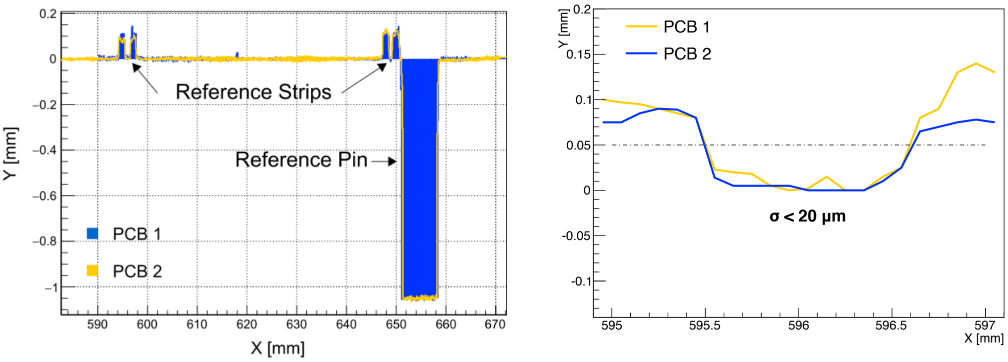

(a)

(b)

Figure 4.6: Measurements performed with the laser tracker. (a) Blue and yellow data points refer to the PCBs on the two sides of the panel, PCB1 and PCB2 respectively. The centers of the precision pin in the two measurements have been aligned; (b) zoom showing the region with the two strips; note that the two strips are not separated, however, the position of the pair of the two strips is very well defined.

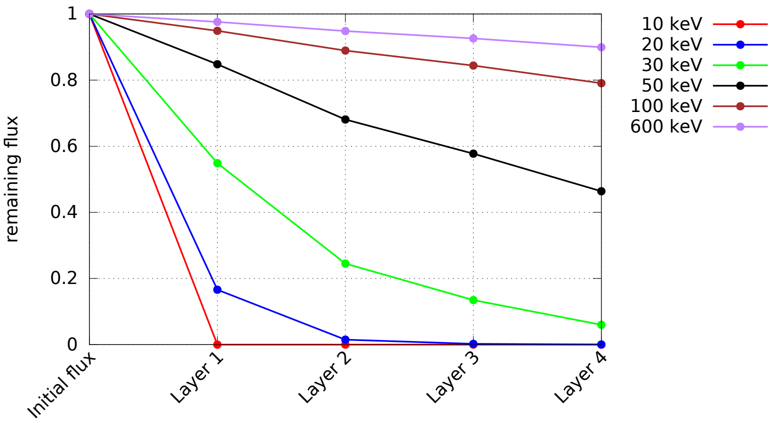

Figure 4.7: Estimated reduction of the photon flux in the MMSW for different photon energies.

---

[5] The exact materials used for the panels and the absorption of different energy X-rays for each readout layer can be found in Appendix B.

The output spectrum of the Ag X-ray gun at different tube voltages and the corresponding energy of the X-rays is shown in Fig. 4.8(a). The two spikes correspond to the characteristic X-rays from the silver Ka and Kb lines at $\sim$ 22 keV and $\sim$ 25 keV respectively. The continuous spectrum corresponds to Bremsstrahlung radiation[6].

The current induced by the X-rays on the MMSW detector as a function of the tube voltage for a tube current of 80 µA is shown in Fig. 4.8(b). For this measurement the X-ray gun was facing the first η-layer (Layer 1) and was operated without collimator[7]. The amplification voltage was set to V_A = 500 V in all readout layers and the drift voltage to V_D = -300 V. To get reasonable currents in all readout layers the X-ray gun was operated at a tube voltage of 50 kV so that a sufficient fraction of the X-rays reach the last layer. At a tube voltage of 50 kV we have measured a reduction of the X-ray flux of 27%, 65%, and 75% in layers two, three and four with respect to the first layer.

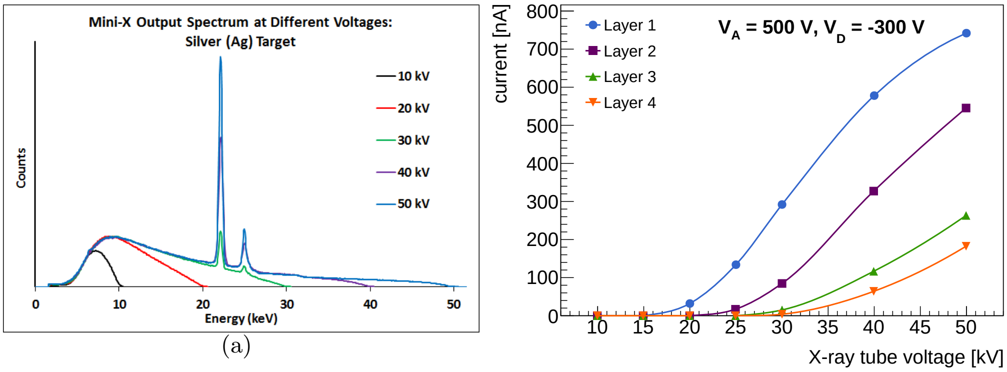

(a)

(b)

Figure 4.8: (a) Output spectrum of the Amptek® Ag X-ray gun at different tube voltages [48]; (b) Current induced by the X-ray Ag gun in the different readout layers of the MMSW detector as a function of the tube voltage for a tube current of 80 µA.

For the alignment measurement, the X-ray gun was operated at a tube voltage of 50 kV and a tube current of 50 µA using a 2 mm collimator[8]. The detector was irradiated in different positions along the strips as shown in Fig. 4.9. The amplification voltage in all detection layers was set to V_A = 560 V and the drift voltage to V_D = -300 V. The charge and time information were recorded with the APV-25 Front End ASICs and the RD51 Scalable Readout System (see Appendix E) using random triggers.

---

[6] Electrons that penetrate the anode material which is the silver and pass close to a nucleus are deflected and slowed down by the attractive force of the nucleus. The energy lost by the electron during this process appears in the form of an X-ray photon.

[7] The irradiation cone without using a collimator is 120°.

[8] The irradiation cone of the 2 mm collimator is 5°.

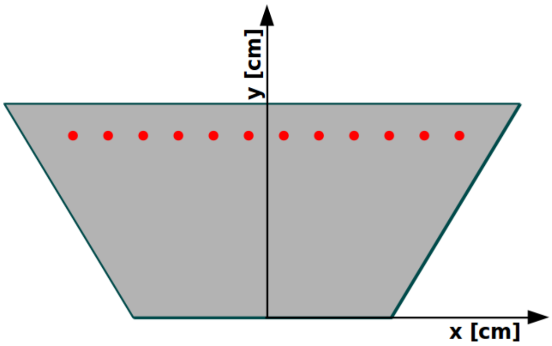

Figure 4.9: Measurement positions on the detector surface along the same strips.

Figure 4.10 shows a schematic of the measurement set-up indicating the distances between the X-ray gun and each detection layer. The X-ray gun was facing Layer 1. The areas on each detection layer that are expected to be hit under the cone of irradiation are also listed in mm and in number of strips.

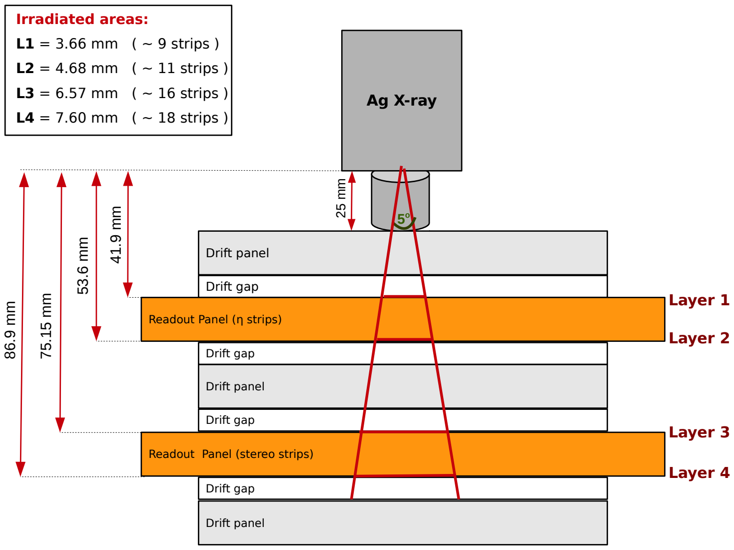

Figure 4.10: Illustration of the irradiated areas in all detection layers using the 2 mm collimator. Not to scale.

Figure 4.11 shows the charge-weighted[9] number of hits per strip as a function of the strip number for all detection layers. For the third and fourth layer this profile is slightly shifted with respect to the first two layers owing to the stereo angles of the strips. As the intensity of the beam is attenuated when passing through the detector, the number of hits per strip is reduced by a factor of 2.6, 4.3 and 6.3 for Layers 2, 3 and 4 with respect to Layer 1.

---

[9] Each hit is entered in the distribution with its charge. In this way the tails of the distribution are suppressed.

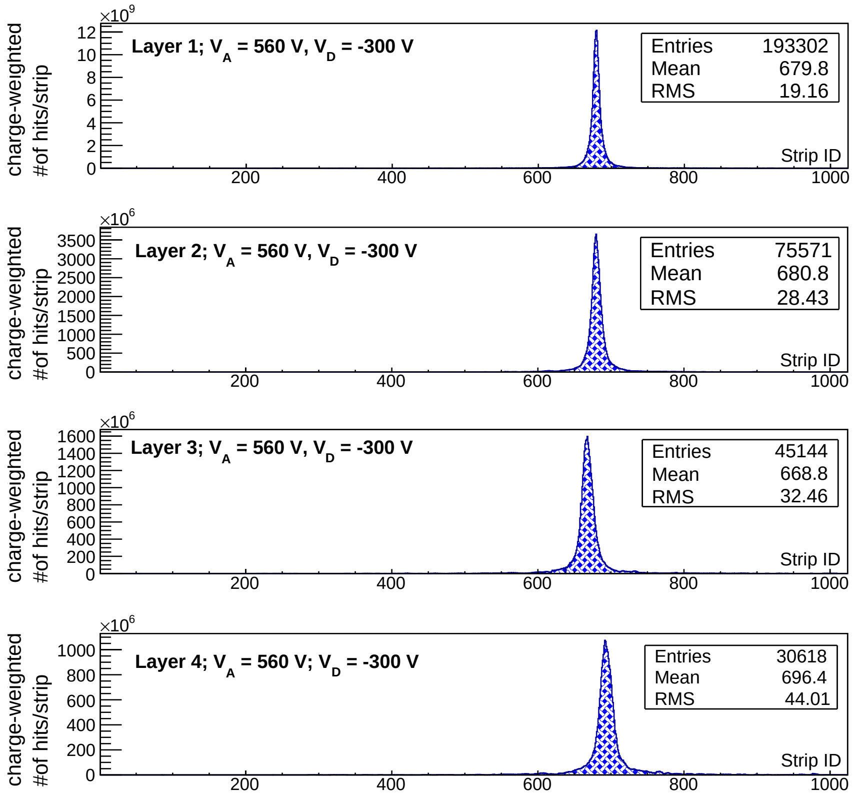

Figure 4.11: Charge weighted number of hits per strip as a function of the strip number.

The hit profiles in all detection layers are fit with a double Gaussian (Fig. 4.12) to extract the mean value and the sigma[10] of the core distribution.

From the combination of the two stereo layers with local coordinates η' and η'' tilted by $\theta = \pm 1.5^\circ$ with respect to the global η-coordinate, the η-coordinate is calculated according to the formula [49]:

$$\eta = \frac{\eta' + \eta''}{2 \cdot \cos\theta} \tag{4.1}$$

To compensate for a possible inclination of the gun inside the box, each time two runs were taken by rotating the box by 180°. At each position the average of the two runs is calculated. The relative alignment between two layers (or between a layer and the combination of the stereo layers) is calculated by subtracting the average values.

Figure 4.13 shows the relative alignment between the two η-layers (L1-L2) and the relative alignment between one η-layer (L1 or L2) and the combination of the stereo layers (L34) at 12 positions along the strips. The numbers in purple show the uncertainty of each measurement in µm for L1-L2.

---

[10] The sigma of the core distribution is consistent with the half of the irradiated area that is listed in Fig. 4.10.

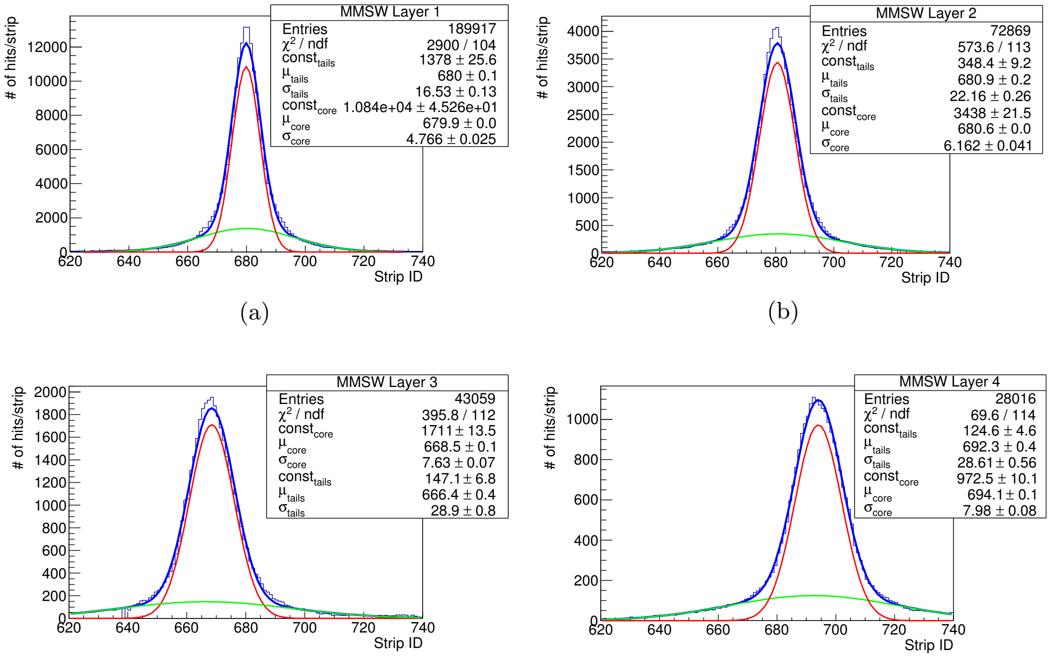

(a) (b)

(c) (d)

Figure 4.12: Double Gaussian fits for all detection layers.

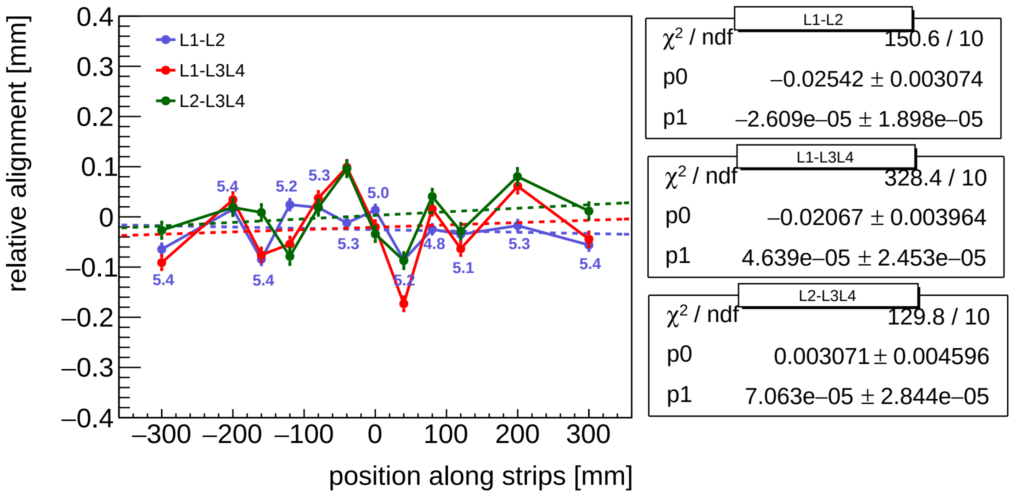

Figure 4.13: Relative alignment between the two η-layers and between the η-layers and the combination of the stereo layers along the strips. The straight lines show the linear fits of the three series. The numbers in purple give the uncertainties in µm of the L1-L2 points.

The straight lines in Fig. 4.13 correspond to the linear fits of the three series of points. They show that the strips in the two η-layers (L1-L2) are parallel to better than 30 µrad. The difference between L1 and L3L4 (or L2 and L3L4) shows the relative alignment of the strips on the two panels. Table 4.1 summarizes the rotation and the average values over all data points, for each difference between the η-layers and the two readout panels. The alignment of the strips on the two sides of the panels in the MMSW is better than 26 µm. This result is comparable with the laser scan measurement. The panel-to-panel alignment is better than 25 µm, even without special alignment pins.

Table 4.1: Rotation between layers and average relative alignment extracted from the measurements that are shown in Fig. 4.13.

Difference between layers	**Rotation between layers [µrad]**	**Average relative alignment [µm]**
L1-L2	26	-25.4 ± 3.1
L1-L3L4	46	-20.7 ± 4.0
L2-L3L4	71	3.07 ± 4.6

4.3 Basic performance studies

The performance of the MMSW detectors has been studied with X-rays and cosmic rays in the CERN RD51 [39]/Gaseous Detector Development (GDD) laboratory and in test-beams. In the following the main performance parameters, such as efficiency, gain homogeneity and spatial resolution will be discussed.

4.3.1 Event reconstruction and efficiency measurements

The performance studies with cosmic muons were performed in the ATLAS cosmic ray stand in the RD51/GDD laboratory at CERN. Two layers of twelve plastic scintillator slabs with an active area of $2.5 \times 1.1\,\mathrm{m}^2$ in each plane at a distance of 2 m have been used as coincidence trigger. The MMSW has been operated with a gas mixture of Ar:CO_2 (93:7) at atmospheric pressure, amplification voltages ranging from $V_\mathrm{A} = 500\,\mathrm{V}$ to $V_\mathrm{A} = 600\,\mathrm{V}$, and a fixed drift voltage of $V_\mathrm{D} = -300\,\mathrm{V}$.

Figure 4.14 shows a typical cosmic muon event where the charge and time for a single particle passing through the four layers of the MMSW is displayed. Clean hits are observed in each layer, characterized by a cluster of neighbouring strips. Owing to the stereo angles of the strips in the third and forth layer the hit positions in these layers are shifted with respect to the ones in the η-layers. The line filled distributions in Layers 3 and 4 with a mean strip value of 449 correspond to the average cluster position in these two layers. This distribution is well aligned with the first two η-layers.

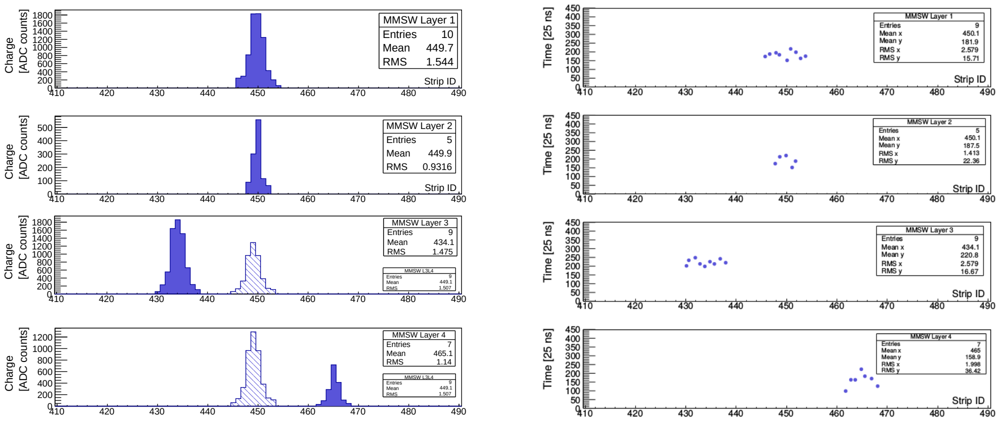

(a) (b)

Figure 4.14: (a) Charge per strip and (b) signal arrival time, as a function of the strip position.

A cluster of strips is defined by the following criteria:

- it must contain at least three readout strips with a signal
- the strips are contiguous and not separated by more than one missing strip. This requirement is important to allow for faulty readout strips or problems in the readout electronics
- the sum of all strip charges (cluster charge) must be above a minimal threshold

The cluster position is defined as the charge-weighted average position of all strips of the cluster. This definition, strictly speaking, holds only true for perpendicular incoming particles. However, the corresponding systematic uncertainties for incoming particles under different angles can be neglected for the following studies.

The cluster distribution as a function of the readout strip position for the four detector layers is shown in Fig. 4.15 for amplification voltages of $V_\mathrm{A} = 560\,\mathrm{V}$ and $V_\mathrm{A} = 580\,\mathrm{V}$ and a drift voltage of $V_\mathrm{D} = -300\,\mathrm{V}$. A similar count rate is observed for all layers at $V_\mathrm{A} = 580\,\mathrm{V}$, while the full efficiency for the layers 2-4 is not yet reached at $V_\mathrm{A} = 560\,\mathrm{V}$ as discussed later. The increase of the number of clusters with increasing strip number in all four layers is a geometrical effect. About half of the effect comes from the length increase of the readout strips, the other half can be attributed to the efficiency of the scintillators used for triggering. The decrease at very high and very low strip numbers in the third and fourth layer is the result of the shorter strips at the detector edges. The saw-tooth pattern in the distributions of Layers 2, 3 and 4 indicates that for these layers the detector gain at $V_\mathrm{A} = 560\,\mathrm{V}$ was not sufficient to reach full efficiency[11]. At an amplification voltage of $V_\mathrm{A} = 580\,\mathrm{V}$ (Fig. 4.15(b)) where all layers have a higher efficiency this effect is no longer visible.

---

[11] The pattern is the result of the pedestal subtraction method. It is based on the pedestal fluctuations that are larger for the first and last channels in each APV chip (see Fig. 4.16). As a result the pedestal cut removes more small signals in these channels.

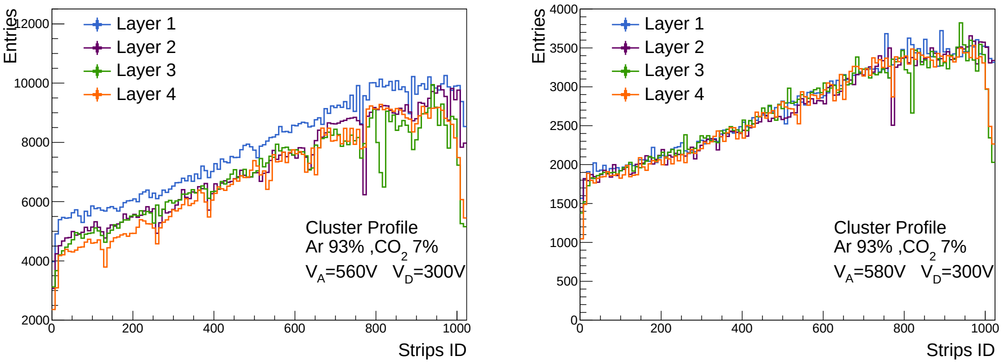

(a) (b)

Figure 4.15: Cluster distribution as a function of the strip number for all layers for an amplification voltage of (a) V_A=560 V and (b) V_A=580 V.

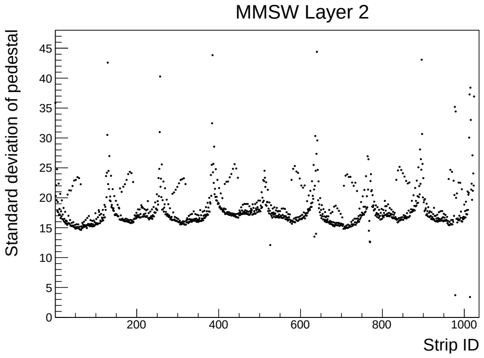

Figure 4.16: Standard deviation of pedestal as a function of the strip number for Layer 2.

The efficiency of the MMSW detector was studied without the use of an external tracker. Three out of four detection layers were used as reference layers while the remaining layer was defined as the test layer. We require exactly one cluster per reference layer and we apply a tracking algorithm for the prediction of the cluster position in the test layer. A cluster is defined as correctly reconstructed if its position is within 1.6 mm for the two η-layers and 2.0 cm for the stereo layers from the predicted position.

Figure 4.17(a) shows as an example the charge distribution for the reconstructed clusters that are within the acceptance region of the predicted position for the fourth layer. This distribution is fitted with a Landau function in order to extract the most probable value (MPV). The MPV is proportional to the gas gain. Figure 4.18(b) shows the MPV of the cluster charge for all layers as a function of the amplification voltage. For the first layer the cluster charge at 600 V was saturated (see Appendix E.4) thus it is not included in this figure. The non-exponential behaviour of the curves (in particular at low HV) shows that the cluster selection algorithm introduces a bias to the data. Only above 560 V the gain shows an approximately exponential behaviour in all readout layers. For low voltages the threshold cut in the charge distribution makes the MPV unreliable.

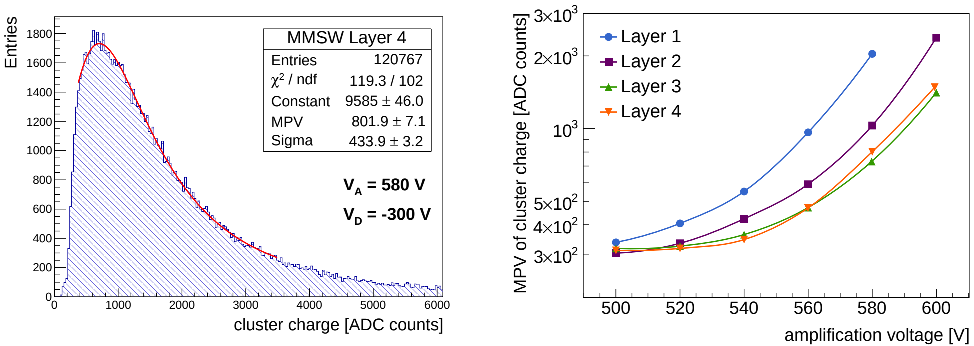

(a) (b)

Figure 4.17: (a) Cluster charge distribution of Layer 4; (b) MPV of cluster charge distribution as a function of the amplification voltage for all layers.

The dependence of the detector efficiency on the amplification voltage and the efficiency as a function of the strip number (strip ID) for $V_\mathrm{A} = 580\,\mathrm{V}$ is shown in Fig. 4.18. Full efficiency is reached at 560 V for the first layer, at about 570 V for the second layer, and at 580 V for the third and fourth layers. The fact that Layers 2,3 and 4 have lower efficiency than Layer 1 is most likely the result of gas leaks[12].

For amplification voltages higher than $V_\mathrm{A} = 580\,\mathrm{V}$, the reconstruction efficiency in Layers 1 and 2 is above 95% across all readout strips while for Layers 3 and 4 it is above 90% (Fig. 4.18(b)).

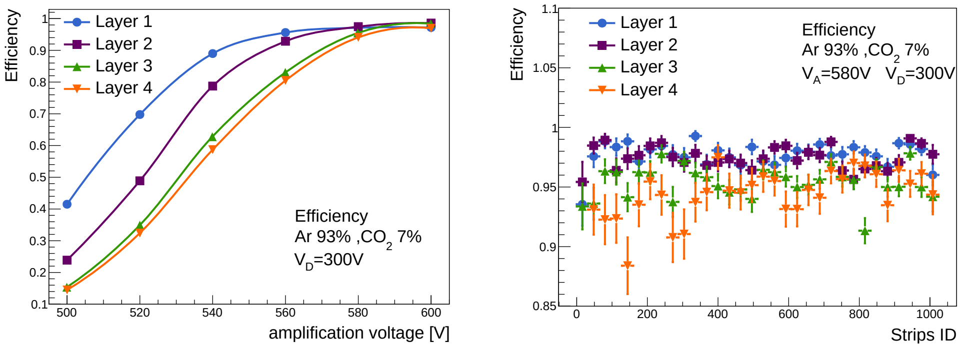

(a) (b)

Figure 4.18: (a) Efficiency of all layers as a function of the amplification voltage; (b) cluster reconstruction efficiency as a function of the strip position for $V_\mathrm{A} = 580\,\mathrm{V}$ for all layers.

---

[12] When the detector was opened few months later several defects on the O-rings were found.

The detector efficiency in the fourth layer for $V_\mathrm{A} = 560\,\mathrm{V}$ and $V_\mathrm{A} = 580\,\mathrm{V}$ is shown in a two-dimensional representation of the detector surface in Fig. 4.19. The inefficiencies at the boundaries are the results of inclined strips (28 on the top, and 17 on the bottom), which are shorter at the edge and result to the corners which are not covered by the parallel strips. While we observe a higher efficiency in the top part compared to the lower part of the detector for $V_\mathrm{A} = 560\,\mathrm{V}$, a much more homogeneous detector efficiency is found for $V_\mathrm{A} = 580\,\mathrm{V}$.

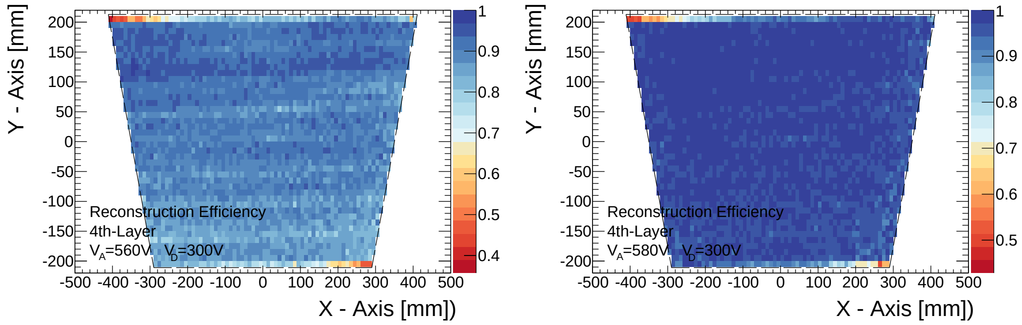

(a)

(b)

Figure 4.19: Two-dimensional cluster reconstruction efficiency over the full detector surface of the 4th layer for (a) $V_\mathrm{A} = 560\,\mathrm{V}$ and (b) $V_\mathrm{A} = 580\,\mathrm{V}$.

In summary, an average signal reconstruction efficiency of $\geq$95% per layer was found for an amplification voltage $\mathrm{V_A}$ $\geq$580 V, almost homogeneous across the full detector.

4.3.2 Gain uniformity

To measure the gain uniformity over the surface of the MMSW2, the cluster charge of cosmic events was reconstructed in 208 different points. Figure 4.20 shows the cluster charge (MPV) normalized to the average cluster charge obtained with cosmic events and the MPV of the cluster charge for the four detection layers. For this measurement the amplification voltage was set to $V_\mathrm{A} = 560\,\mathrm{V}$, and the drift voltage to $V_\mathrm{D} = -300\,\mathrm{V}$.

At the amplification voltage of $V_\mathrm{A} = 560\,\mathrm{V}$ the first layer shows a much higher gain than the other layers. The average cluster charge has on average a MPV of 1010 ADC with a spread of 8% (rms) and an overall gain uniformity (maximum deviation) of ±20%. The second layer has a higher gain in the upper part with an average MPV of 570 ADC and an overall gain uniformity of ±23%. The third layer is quite homogeneous over the full surface. It has an average MPV of 510 ADC counts and an overall gain uniformity of ±16%. Layer 4 has a lower gain in the bottom part with respect to the upper part with an overall uniformity of ±24%. These variations in the overall uniformity correspond to <2 µm variations on the amplification gap.

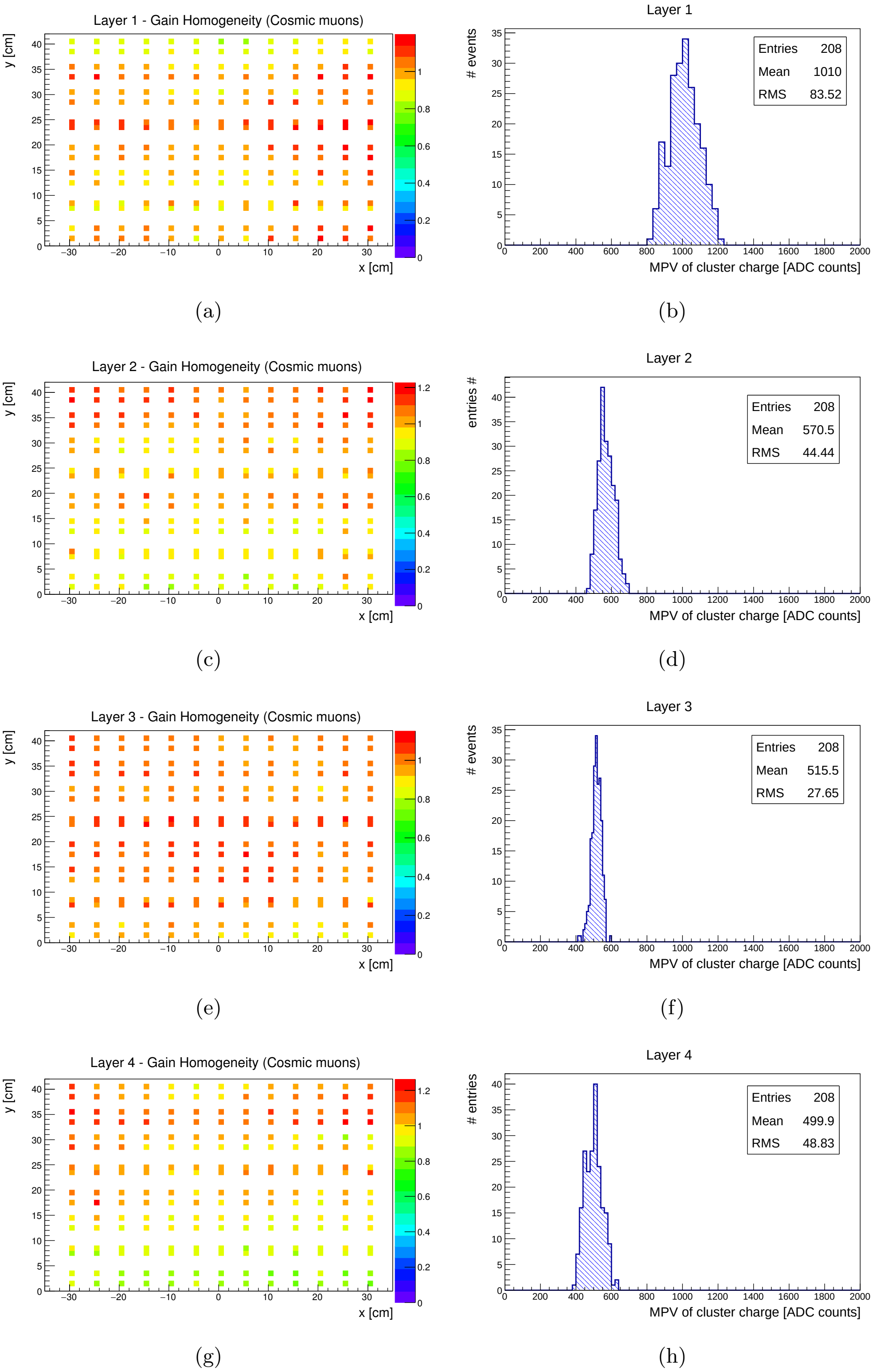

(a) (b)

(c) (d)

(e) (f)

(g) (h)

Figure 4.20: (left) Two-dimensional normalized cluster charge (MPV) and (right) MPV of cluster charge for all detection layers obtained with cosmic events.

These results have been cross-checked with X-rays. The detector was irradiated with the Ag X-ray gun using the 2 mm collimator in 228 different points, close to the points of the reconstructed clusters obtained with cosmics. The tube voltage was set to 50 kV and the tube current to 50 µA. This measurement was performed in two steps. At each step two layers at a time were irradiated while the layers closer to the X-ray gun were switched off. This was done in order to avoid very high currents in the layers that were closer to the X-ray gun as the rate with the 2 mm collimator is about a few MHz/mm^2. The HV settings for this measurement are the same as with the cosmic ray measurements. To measure the gain uniformity of the two η-layers (Layer 1 and 2) the X-ray gun was facing Layer 4. The order of penetration by the X-rays is L4-L3-L2-L1 with the HV of layers 3 and 4 switched off. Figure 4.21 shows the currents normalized to the average current in a two-dimensional representation of the detector surface on the left and the currents for all measurement points on the right. The very low currents correspond to the edges of the active area.

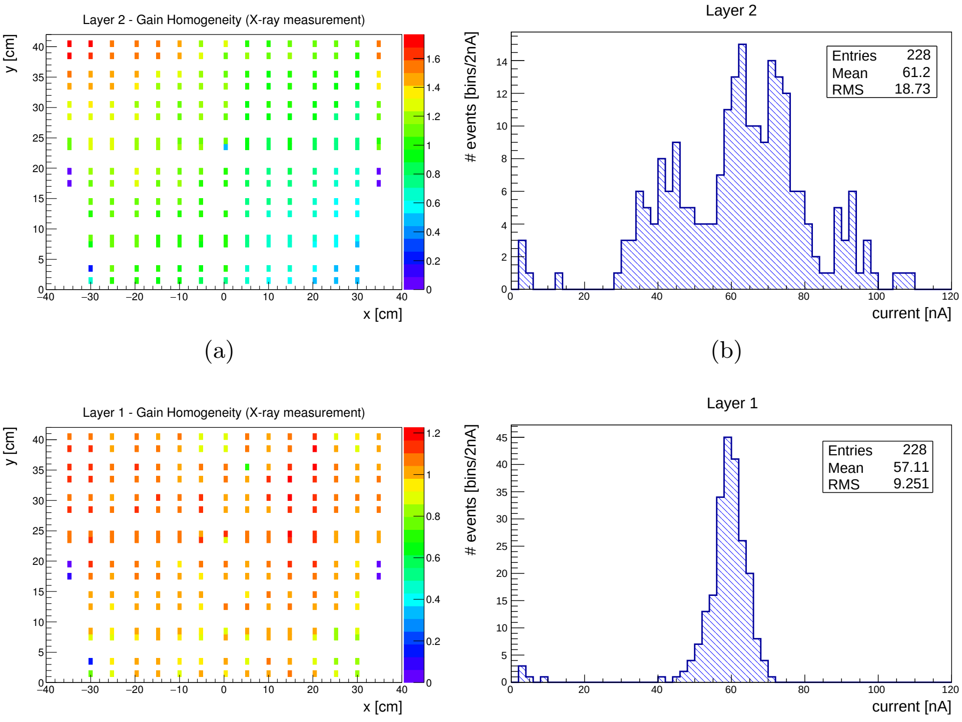

(a) (b)

(c) (d)

Figure 4.21: (left) Two-dimensional normalized amplification current map and (right) current distributions for Layers 2 and 1 as a result of the X-ray irradiation. For this measurement the X-ray gun was facing Layer 4 thus the order of the X-rays penetration is L4-L3-L2-L1. The HV on layers 3 and 4 was switched off.

As discussed before, because of the strongly falling absorption cross section (see Fig. 4.7), the X-rays that reach Layer 2 need to have an energy in the range 30–50 keV while for Layer 1 they need to have an energy in the range 35–50 keV.

The fact that the mean current value of the two layers is approximately the same comes from the higher gain and efficiency of Layer 1 compensating the larger X-ray absorption. From the two-dimensional plots we see that in Layer 1 a slightly higher amplification is observed in the upper part. The overall uniformity for this layer is ±20%, corresponding to <2 μm uniformity of the amplification gap. The second layer shows a gain variation from the bottom-right to the top-left of ±60%. This corresponds to <4 μm difference of the amplification gap between the two corners and the rest of the detector area.

To measure the gain uniformity of Layer 3 and Layer 4 the X-ray gun was facing Layer 1. In this case, the order of penetration by the X-rays is L1-L2-L3-L4 with the HV of Layers 1 and 2 switched off. Figure 4.22 shows the corresponding currents normalized to the average current in a two-dimensional representation of the detector surface on the left and the currents for all measurement points on the right, for Layer 3 and Layer 4.

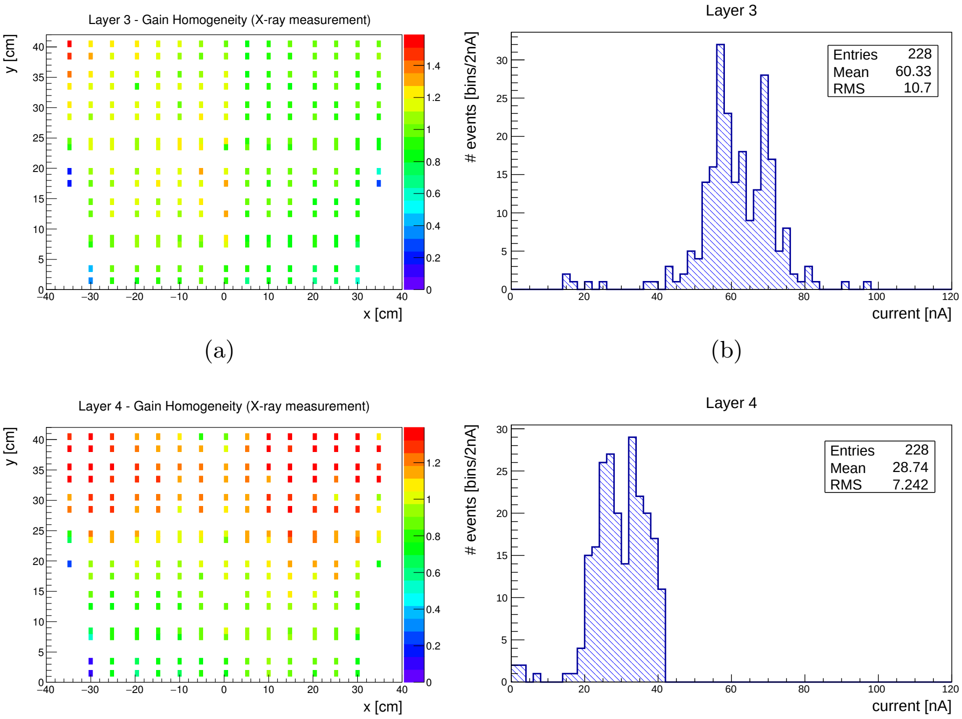

(a) (b)

(c) (d)

Figure 4.22: (left) Two-dimensional normalized amplification current map and (right) current distributions for Layers 3 and 4 as a result of the X-ray irradiation. For this measurement the X-ray gun was facing Layer 1 thus the order of the X-rays penetration is L1-L2-L3-L4. The HV on layers 1 and 2 was switched off.

These two layers have approximately the same gain at $V_\mathrm{A} = 560\,\mathrm{V}$. Given the stronger absorption, the current of Layer 4 is lower by a factor of 2 with respect to Layer 3. Looking at the two-dimensional plots, for the third layer a difference of about 20% between the left and the right side of the detector is observed. The fourth layer shows a higher amplification in the upper part with an overall gain uniformity of ±40%. These variations of the gain correspond to <3 μm variations on the amplification gap.

In Figures 4.21 and 4.22 a larger spread of the current values is evident for Layer 2 and Layer 3 compared to Layer 1 and Layer 4. The origin of this is not well understood but could be related to an inhomogeneous absorption of the X-rays in the material above these layers together with X-rays from the lower part of the energy spectrum reaching these layers.

Table 4.2 summarizes the overall currents and MPVs for all layers and the spread of these quantities. To be able to compare the X-ray with the cosmic ray measurements we should scale the current of Layer 4 with respect to Layer 3 by the corresponding absorption, and do the same for Layer 1 with respect to Layer 2. With an absorption/correction factor of ≈2 between these two layers and by normalizing the currents and the MPVs to their maximum values both measurements show the same relative behaviour (Fig 4.23).

Table 4.2: Overall current and MPV of the MMSW layers

	Quantity	**L1**	**L2**	**L3**	**L4**
X-rays	Mean current [nA]	57.10	61.20	60.33	28.74
	RMS [nA]	9.25	18.73	10.7	7.24
	RMS in %	16.20	30.60	17.74	25.19
	Correction factor	2	1	1	2
	Mean current corrected [nA]	114.20	61.2	60.33	57.48
	Normalized mean current	1.00	0.54	0.53	0.50
Cosmics	Mean MPV [ADC counts]	1010	570.5	515.5	499.9
	RMS [ADC counts]	83.52	44.44	27.65	48.8
	RMS in %	8.27	7.79	5.36	9.76
	Normalized mean MPV	1	0.56	0.51	0.49

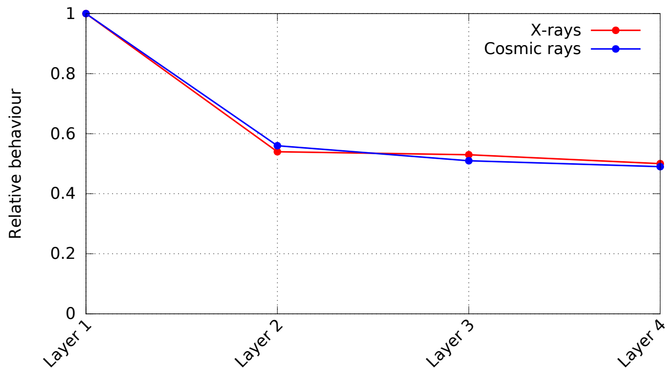

Figure 4.23: Relative behaviour between X-ray and cosmic ray measurements.

Figure 4.24 shows a more detailed comparison of X-ray and cosmic muon measurements. Each point corresponds to the average value taken along the x-axis, i.e.

along the η strips, of the two-dimensional maps. Both measurements show the same trends across the strip direction. However, for the second and fourth layer the X-ray measurement show a variation of ±30% while the cosmic measurement show only a variation of ±10%.

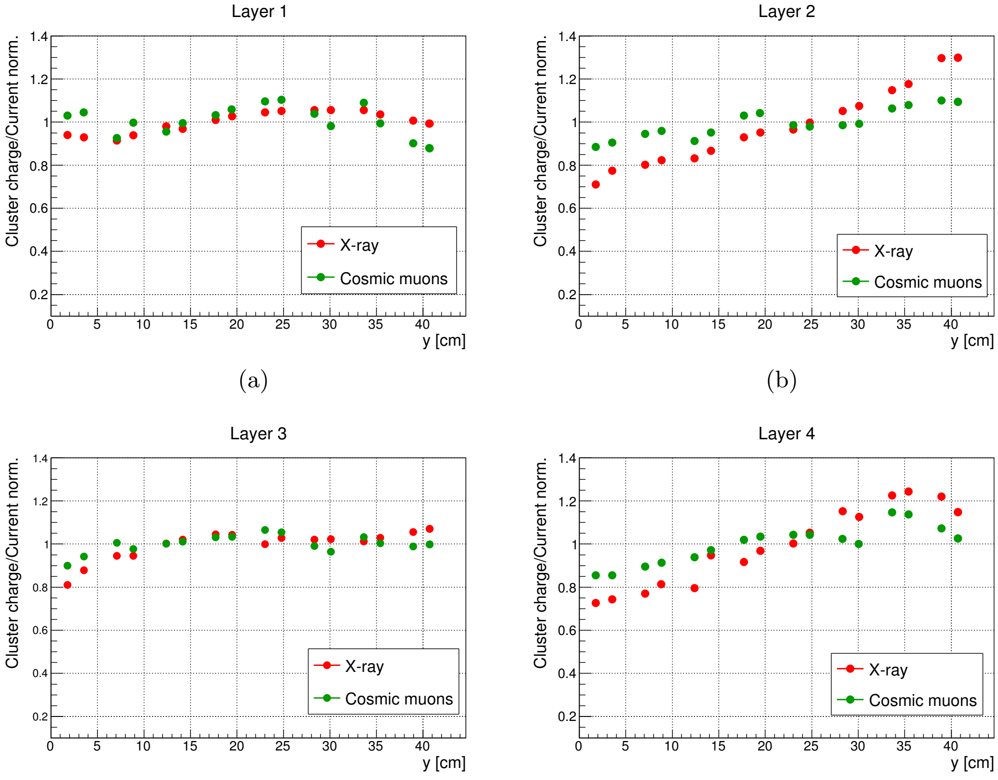

(a)

(b)

(c)

(d)

Figure 4.24: Normalized ratio of the average cluster charge and the detector current for all detection layers.

In summary, cosmic rays and X-rays show an average gain variation of less than ±30% in all detection layers, well within the requirements of the NSW Micromegas detectors. Both measurements show the same relative behaviour. However, with the X-rays a larger spread was observed for Layers 2 and 3 with respect to Layers 1 and 4, while with the cosmics the spread in all layers is approximately the same. The differences observed with the X-rays could be related to an inhomogeneous absorption of the X-rays in the material above these layers together with the lower energy spectrum of the X-rays that reach these layers.

4.3.3 Spatial resolution in test beam measurements

Test-beam measurements have been conducted in August 2014 at the MAMI accelerator facility at the Johannes Gutenberg-University Mainz for a study of the spatial resolution of the MMSW1 detector. The MAMI accelerator delivers a quasicontinuous electron beam with energies up to 1.5 GeV. For the measurements presented here the beam energy was set to 855 MeV. A small $10 \times 10\,\text{cm}^2$ micromegas chamber with two-dimensional readout and a spatial resolution of 70 µm has been operated at a distance of 30 cm behind the MMSW detector. This chamber, called Tmm, served for reference measurements. Details of this reference chamber are summarized in [50]. The MMSW1 and the reference detector have been operated with an Ar:CO_2 93:7 gas mixture.

We define the strip direction of the first and second layer of the MMSW1 as x axis. The spatial resolution in y direction can therefore be measured by comparing the reconstructed position of perpendicular incident particles in both layers on an event-by-event basis. Figure 4.25 shows the difference of the reconstructed track positions in Layers 1 and 2. The offset of the observed distribution is an effect of the chamber inclination with respect to the beam. The width of the distribution σ_{Diff} is given by:

$$\sigma_{Diff} = \sqrt{\sigma_1^2 + \sigma_2^2 + \sigma_{BD}^2 + \sigma_{MS}^2} \tag{4.2}$$

where σ_i is the spatial resolution of the i-th layer, σ_{MS} is the contribution from multiple-scattering and σ_{BD} the contribution of the beam divergence. The vertical emittance of the beam is ~0.076 mrad and with a distance of 11.7 mm between the two η-layers this corresponds to 0.88 µm. The multiple scattering between these two layers is ~10 µm. Thus the contributions to the measured resolution from multiple scattering and the average opening angle of the electron beam are negligible compared to σ_i. The distribution can be described by a Gaussian function[13]. Assuming that the intrinsic resolution is the same for both layers, we find a spatial resolution of σ_y =88 µm for Layer 1 and Layer 2.

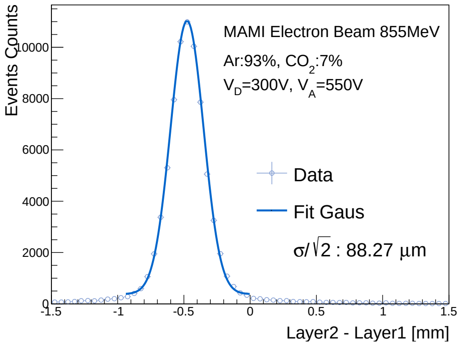

Figure 4.25: Difference of the reconstructed cluster position of the first and second layer [51].

The strips of the third and fourth layer of the MMSW detector are inclined by $\theta = \pm 1.5^\circ$ and hence allow for the reconstruction of both x and y coordinates using the relations:

---

[13] The Gaussian accounts for more than 95% of the events.

$$\mathrm{x}_{\mathrm{L3L4}} = \frac{\mathrm{L3} - \mathrm{L4}}{2 \cdot \sin\theta} \tag{4.3}$$

$$\mathrm{y}_{\mathrm{L3L4}} = \frac{\mathrm{L3} + \mathrm{L4}}{2 \cdot \cos\theta} \tag{4.4}$$

To determine the spatial resolution of the x coordinate (also called second coordinate) the small 2D Micromegas detector at a distance of 30 cm is used as reference. Given the low beam energy and the relative large distance between the two detectors a substantial contribution from multiple scattering and the beam divergence to the result is expected. This contribution is experimentally determined by comparing the y positions in MMSW and the reference chamber. The result is shown in Fig. 4.26(a). The width of the distribution $\sigma_{\mathrm{y}} = 1.76\,\mathrm{mm}$ is described by Eq. 4.2. With an intrinsic spatial resolution of $\mathrm{y}_{\mathrm{L3L4}} = \frac{\sigma_{\mathrm{L1}}}{\sqrt{2}} = 62\ \mu\mathrm{m}$ and a spatial resolution of 70 µm of the small chamber it is clear that the result is completely dominated by the contributions of multiple scattering and the beam divergence. Figure 4.26(b) shows the difference of the x coordinate measurements between MMSW and the reference chamber. After subtraction of the combined contribution from multiple scattering and the beam divergence, the resolution of the x coordinate is $\sigma_{\mathrm{x}} = 2.3\,\mathrm{mm}$.

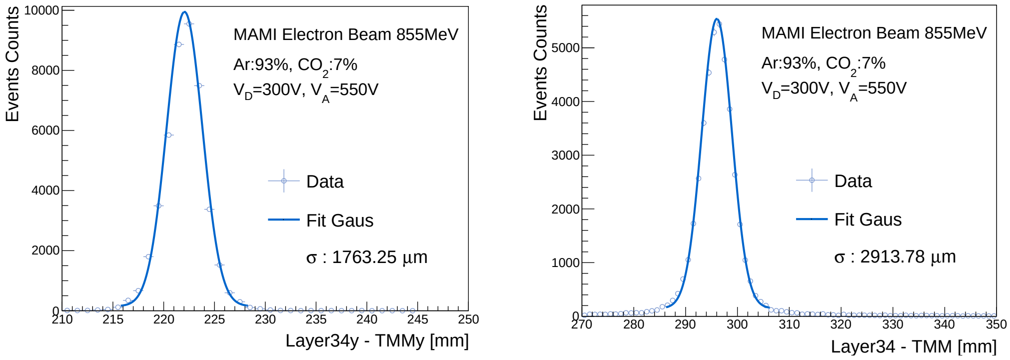

(a) (b)

Figure 4.26: Difference of the (a) y-coordinate position and of the (b) x-coordinate position reconstructed with the third and fourth layer of the MMSW chamber and the reference chamber [51].

These results are within the requirements of the NSW upgrade and are consistent with the results obtained for MMSW1 in a 10 GeV/c proton beam [52]. Very similar results were also found for MMSW2 in a 150 GeV/c pion beam [53].

4.4 Development of a DAQ system based on the ATLAS TDAQ software

Originally it was planned to install one of the MMSW detectors on one of the existing Small Wheels behind the Cathode Strip Chambers in order to test it under real ATLAS conditions in the LHC Run 2. Therefore there was the need to develop a data acquisition system (DAQ) and to integrate it into the ATLAS Trigger and DAQ (TDAQ) infrastructure [54], [55]. The project was cancelled one year later. By this time a DAQ system based on the official ATLAS TDAQ software had been developed and was tested within the ATLAS partition during cosmic runs before the start of Run 2. This section describes the Micromegas DAQ system and the tests that were performed at that time.

4.4.1 The proposed readout schema

Two different readout schemas were proposed to readout the MMSW in the ATLAS cavern. The first one was to use the RD51 Scalable Readout System (SRS) [56] based on the Advanced Telecommunications Computing Architecture® (ATCA) platform [57] that is described in [54]. This idea was abandoned after several months due to the lack of manpower working with the non-standard NSW electronics.

The second proposed schema was using a preliminary version of the NSW electronics as it is shown in Fig. 4.27. The MMFE8 board [58] is the front-end electronics card of the ATLAS NSW detectors that hosts eight VMM ASIC's [59]. The VMM ASIC performs amplification and shaping, peak finding and digitization of the detector signal. Low-Voltage Differential Signals (LVDS) are tranfered to the ATLAS NSW aggregator board, the Level-1 Data Driver Card (L1DDC) [60]. The Level-1 data (time, charge and strip address corresponding to a single hit) are transferred with bi-directional optical links to the ROD, the Scalable Readout Unit (SRU).

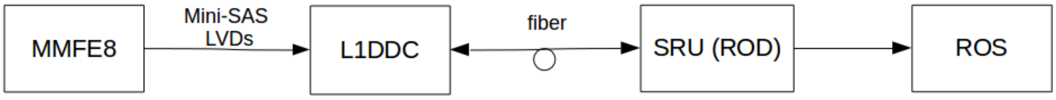

Figure 4.27: The proposed schema to readout the MMSW with the NSW electronics.

The SRU is a custom FPGA board from the RD51 SRS electronics series developed within the RD51 Collaboration. It hosts a Xilinx Virtex6 FPGA and all the necessary circuitry to interface it to the ATLAS TDAQ infrastructure. Figures 4.28 and 4.29 show the SRU board with all the connections and a coarse schematic view of the SRU firmware functionalities respectively. The FPGA firmware was designed by Andre Zibell [61]. The board hosts the following connections:

- 40 RJ45 plugs with LVDS signal pairs called Data Trigger Clock and Control (DTCC) links for detector synchronization and data collection.

- A Trigger Timing and Control (TTCrx) ASIC receiver which receives triggers and asynchronous data from the ATLAS trigger network, as well as the LHC bunch crossing clock for synchronous operation.
- LEMO00 plugs for miscellaneous purposes like connection to the ATLAS BUSY tree structure
- SFP+ plugs for network connectivity and data connection to the ROS via emulated S-LINK

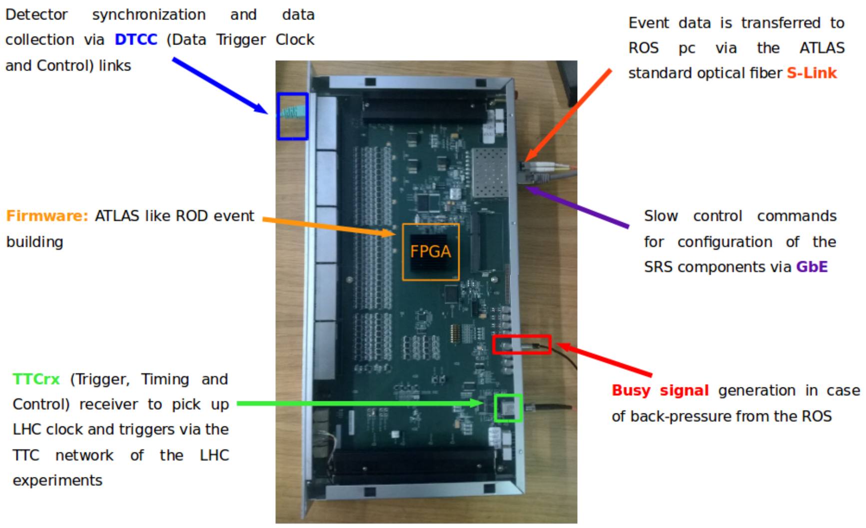

Figure 4.28: The RD51 SRU board with all the connections.

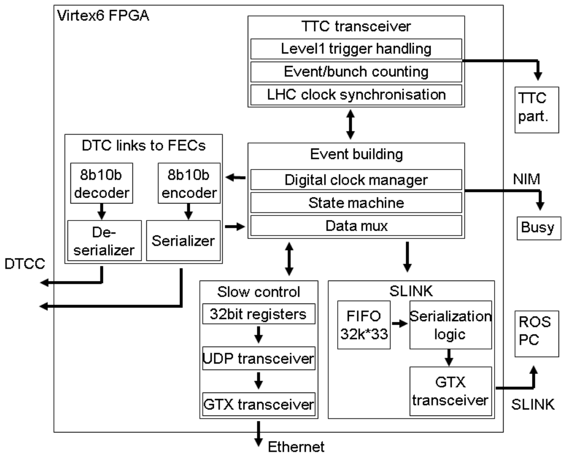

Figure 4.29: Coarse schematic view of the SRU firmware functionalities and connections [61].

4.4.2 Integration of the Micromegas ROD to the ATLAS network

Figure 4.30 shows the schematic of the SRU connectivity to the ATLAS network in order to be able to run with the other sub-systems (top) and the connectivity for standalone debugging (bottom).

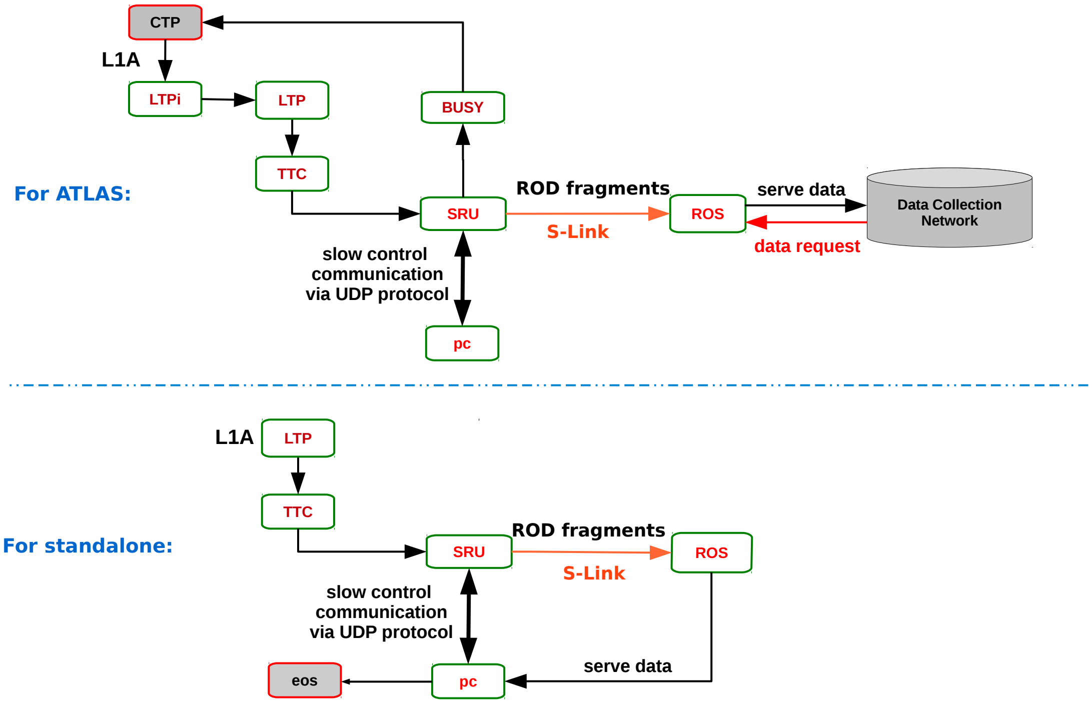

Figure 4.30: (top) SRU connectivity to the ATLAS network for running in the ATLAS partition; (bottom) SRU connectivity for standalone tests.

The CTP, after receiving the L1A signal, fans it out to the Timing, Trigger and Control (TTC) partitions. Each TTC partition contains one Local Trigger Processor (LTP) [62], a TTC system [63] and a tree of ROD_BUSY modules [64]. The LTP provides the facility to run with the trigger and timing signals from the CTP, but it can also generate the signals locally for standalone tests. In order to allow for several combinations of TTC partitions to run independently from the CTP, an LTP interface module (LTPi) [65] is used. It allows for concurrent calibration runs with the muon or calorimeter trigger without requiring any re-cabling. The ROD_BUSY module is used to throttle the generation of the upcoming L1A signals when a ROD module is busy processing previous trigger data.

A dedicated PC was used for slow control communication via the User Datagram Protocol (UDP) with the SRU. Events are sent to the ROS via the S-Link connection.

When running in the ATLAS private network[14] data are sent to the DCN while when running standalone they are buffered in the dedicated PC and then sent to the EOS storage system.

All these modules were described in a configuration database and they were included to the ATLAS Online system [66] in order to be configured, controlled and monitored.

4.4.3 Tests of the Micromegas configuration database in the ATLAS Online system

Even if the complete readout schema to readout the MMSW chamber was not available at that time, the SRU module had been integrated into the ATLAS readout chain, inserting valid ATLAS event fragments with empty detector data fragments. A configuration database that describes all the necessary modules needed to interact with the SRU had been implemented using the ATLAS Online TDAQ software. The Micromegas segment had been successfully tested within the ATLAS partition during cosmic runs, before the start of Run 2 data taking (Fig. 4.31).

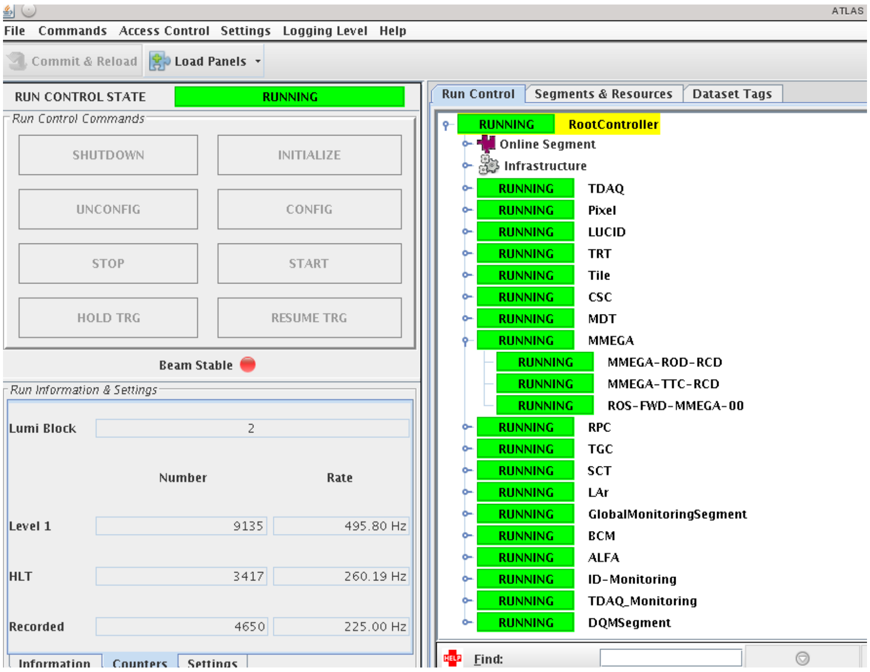

RUN CONTROL STATE: RUNNING

Beam Stable ●

	Number	Rate
Lumi Block	2	
Level 1	9135	495.80 Hz
HLT	3417	260.19 Hz
Recorded	4650	225.00 Hz

- RUNNING RootController
  - Online Segment
  - Infrastructure
  - RUNNING TDAQ
  - RUNNING Pixel
  - RUNNING LUCID
  - RUNNING TRT
  - RUNNING Tile
  - RUNNING CSC
  - RUNNING MDT
  - RUNNING MMEGA
    - RUNNING MMEGA-ROD-RCD
    - RUNNING MMEGA-TTC-RCD
    - RUNNING ROS-FWD-MMEGA-00
  - RUNNING RPC
  - RUNNING TGC
  - RUNNING SCT
  - RUNNING LAr
  - RUNNING GlobalMonitoringSegment
  - RUNNING BCM
  - RUNNING ALFA
  - RUNNING ID-Monitoring
  - RUNNING TDAQ_Monitoring
  - RUNNING DQMSegment

Figure 4.31: The Micromegas segment (MMEGA) in the ATLAS partition running with the other sub-systems.

The individual detector signals must be synchronized to a common module clock at the rate of the LHC bunch crossings. Thus the alignment with the LHC bunch

---

[14] ATLAS has its own technical and control network for the management and operation of equipment installed in the ATLAS experiment. This is a restricted private network and the access is permitted only to the ATLAS users.

structure (in steps of clocks) must be performed to assign correct bunch crossing identification (BCID) to the acquired data through the TTC system. Figure 4.32 shows the BCID as extracted from the Micromegas event fragments during cosmic tests in the beginning of Run2. The visible bunch train structure shows that the Micromegas system was correctly synchronized with the ATLAS trigger.

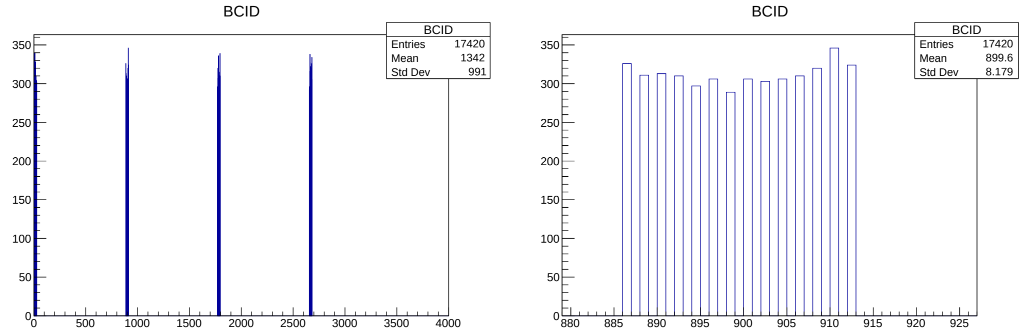

(a)

(b)

Figure 4.32: The Bunch Crossing Identifier (BCID) in the Micromegas event fragments (a) every 25 ns; (b) zoom to one bunch structure.

As part of the integration tests, it had been verified that the readout system did not introduce additional busy time to the ATLAS detector. Figure 4.33, shows the results of a measurement of the fraction of busy time and the event building efficiency as a function of the trigger rate. The maximum expected trigger rate during Run 2 is ∼100 kHz. The SRU busy fraction at 90 kHz was measured to be zero. The rise of the curve above 100 kHz was the result of the bandwidth limitations of the common ATLAS upstream systems; the SRU hardware and firmware alone could stand a much higher trigger rate of up to 1 MHz.

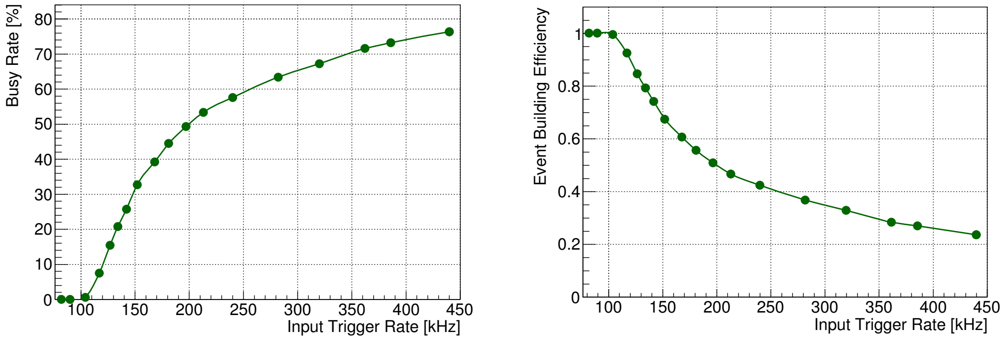

(a)

(b)

Figure 4.33: (a) Busy rate and (b) event building efficiency as a function of the input trigger rate.

Figure 4.34(a) shows the time in milliseconds for all the subsystems during configuration, data taking, stop and unconfigure in a cosmic run on 5th of March 2015. The SRU itself during configuration and the prepare for run stage was measured to be 18 ms and 15 ms respectively (Fig. 4.34(b)). Adding the front-end electronics of course would have taken longer.

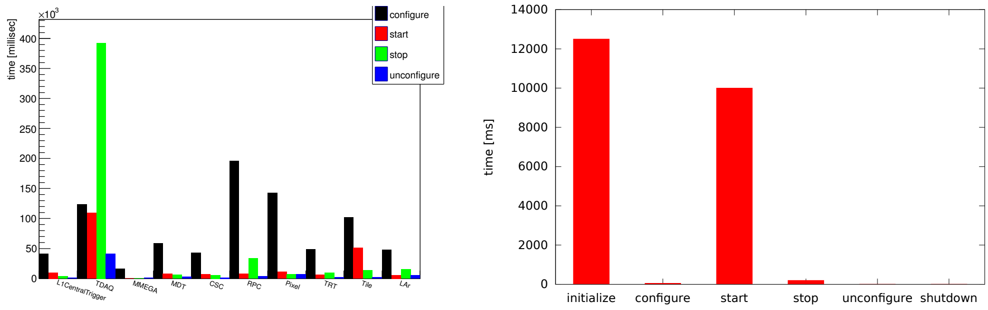

(a) (b)

Figure 4.34: The time measured in milliseconds in a cosmic run on 5th of March 2015 (a) for all the subsystems and (b) for the SRU, to pass through all the stages.

Like all the other sub-systems the Micromegas segment was programmed to support the execution of recovery commands that could be issued by a human operator or by the software itself. The recovery commands were the following:

- **Stop-less removal**: A part of the readout schema that is blocking the trigger due to any fault can be excluded from data taking during the running stage without stopping the data acquisition.

- **Resynchronization**: Re-alignment of the Event Counter Reset (ECR) and L1ID counters when they go out of synchronization.

- **TTC restart**: Complete restart and reconfiguration of the system during the running stage in case the system for any reason is blocking the data acquisition.

Figure 4.35 shows a TTC restart test of the Micromegas segment at ∼ 60 kHz trigger rate as function of time. After the TTC restart was issued the system was fully recovered in few milliseconds.

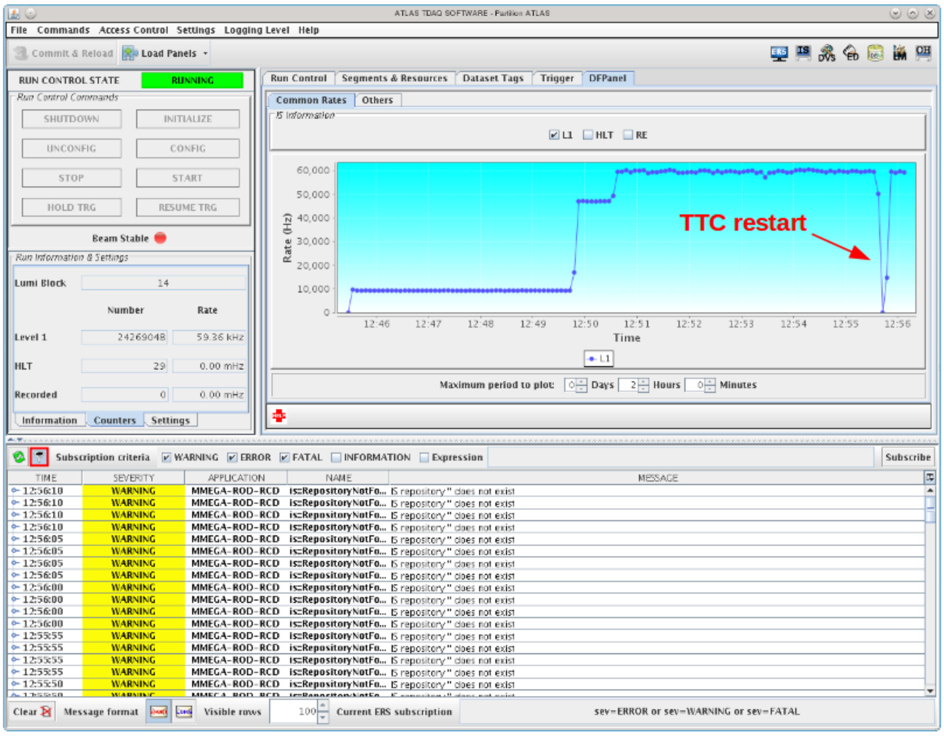

RUN CONTROL STATE: RUNNING

Beam Stable ●

Lumi Block: 14

	Number	Rate
Level 1	24269048	59.36 kHz
HLT	29	0.00 mHz
Recorded	0	0.00 mHz

Maximum period to plot: 0 Days 2 Hours 0 Minutes

Subscription criteria ☑ WARNING ☑ ERROR ☑ FATAL ☐ INFORMATION ☐ Expression

TIME	SEVERITY	APPLICATION	NAME	MESSAGE
12:56:10	WARNING	MMEGA-ROD-RCD	is::RepositoryNotFo...	IS repository " does not exist
12:56:10	WARNING	MMEGA-ROD-RCD	is::RepositoryNotFo...	IS repository " does not exist
12:56:10	WARNING	MMEGA-ROD-RCD	is::RepositoryNotFo...	IS repository " does not exist
12:56:10	WARNING	MMEGA-ROD-RCD	is::RepositoryNotFo...	IS repository " does not exist
12:56:05	WARNING	MMEGA-ROD-RCD	is::RepositoryNotFo...	IS repository " does not exist
12:56:05	WARNING	MMEGA-ROD-RCD	is::RepositoryNotFo...	IS repository " does not exist
12:56:05	WARNING	MMEGA-ROD-RCD	is::RepositoryNotFo...	IS repository " does not exist
12:56:05	WARNING	MMEGA-ROD-RCD	is::RepositoryNotFo...	IS repository " does not exist
12:56:00	WARNING	MMEGA-ROD-RCD	is::RepositoryNotFo...	IS repository " does not exist
12:56:00	WARNING	MMEGA-ROD-RCD	is::RepositoryNotFo...	IS repository " does not exist
12:56:00	WARNING	MMEGA-ROD-RCD	is::RepositoryNotFo...	IS repository " does not exist
12:56:00	WARNING	MMEGA-ROD-RCD	is::RepositoryNotFo...	IS repository " does not exist
12:55:55	WARNING	MMEGA-ROD-RCD	is::RepositoryNotFo...	IS repository " does not exist
12:55:55	WARNING	MMEGA-ROD-RCD	is::RepositoryNotFo...	IS repository " does not exist
12:55:55	WARNING	MMEGA-ROD-RCD	is::RepositoryNotFo...	IS repository " does not exist
12:55:55	WARNING	MMEGA-ROD-RCD	is::RepositoryNotFo...	IS repository " does not exist
12:55:50	WARNING	MMEGA-ROD-RCD	is::RepositoryNotFo...	IS repository " does not exist

Visible rows: 100

Current ERS subscription: sev=ERROR or sev=WARNING or sev=FATAL

Figure 4.35: TTC restart test of the Micromegas segment.

4.5 Conclusions

The construction of the two MMSW detectors served as a starting point for the construction of the NSW Micromegas detectors. The alignment between the strips on the two faces of the η-panel has been measured with a laser tracker and with an Ag X-ray gun. The two measurements gave comparable results with an average alignment better than 20 µm and a rotation of less than 25 µm over the length of the strips. The relative alignment between the η-panel and the stereo-panel was measured only with the X-ray gun. Without the use of special precision pins to align the two panels, an alignment of better than 25 µm was measured.

The gain uniformity of all MMSW layers was measured with X-rays and cosmics. Both measurements show the same relative behaviour with a maximum non-uniformity of ±24% corresponding to a <2 µm variation of the amplification gap thickness.

An average signal reconstruction efficiency of ≥95% per layer was found for an amplification voltage $V_A \geq 580$ V, almost homogeneous across the full detector.

The intrinsic spatial resolution was determined in an electron beam of 855 MeV to be better than 90 µm in the precision coordinate and 2.3 mm in the second coordinate. Comparable results were also found in a 10 GeV/c proton beam for MMSW-1 and in a 150 GeV/c pion beam for MMSW-2.

All the results obtained from the measurements that were presented in this section are well within the specifications of the NSW Micromegas detectors.

The Micromegas DAQ system based on the ATLAS TDAQ software was developed and successfully tested during cosmic tests before the start of Run 2 proton collisions. The necessary recovery and synchronization methods were implemented and tested.

Chapter 5

Characterization of the resistive protection layer used in the ATLAS Micromegas detectors

For the ATLAS type Micromegas detectors a resistive protection layer is used on top of the readout electrode to protect the detector from electrical discharges and/or voltage breakdown. The protection layer consists of a 50 µm thick Kapton® substrate on top of which strips of resistive paste are deposited with the same pattern as the copper readout strips.

Two different types of Kapton® substrates (the HN-type[1] produced in Europe and the EN-type[2] produced in Japan) with different thermal and hygroscopic expansion coefficients were studied as a function of temperature and humidity. These results are compared with tests performed with the same resistive paste deposited on a ceramic[3] substrate. The ceramic substrate is insensitive to humidity [67] and has a two to three times lower thermal expansion coefficient than the Kapton® substrates; for these reasons the ceramic substrate is used as a reference.

In addition, ageing tests have been performed to investigate any degradation of the strip resistance with time and under irradiation.

In the following, prior to the discussion of these studies, the test samples and the properties of the materials will be described.

5.1 Description of the test samples

Three samples were tested: resistive strips on HN-type Kapton®, on EN-type Kapton®, and on a 0.5 mm thick ceramic substrate. The latter is composed of aluminium oxide (Al_2O_3).

The resistive pattern in all substrates has dimensions 10×10 cm^2 with 256 strips in total (Fig. 5.1). The strips have a width of 300 µm and a pitch of 400 µm. In

---

[1] The HN-type Kapton® is produced by DuPont.

[2] The EN-type Kapton® is produced by Toray-Dupont Co. Ltd.

[3] Kyocera® ceramics.

order to measure the surface resistivity, a silver paste line was screen-printed across the two edges of the strips. The resistance of the resistive paste was measured with a Fluke® 289 industrial logging multimeter [68] and the data were recorded with the software provided by the company. Small pieces of copper foils were glued with Kapton® tape on top of the silver lines in order to make the contacts with the probes of the multimeter.

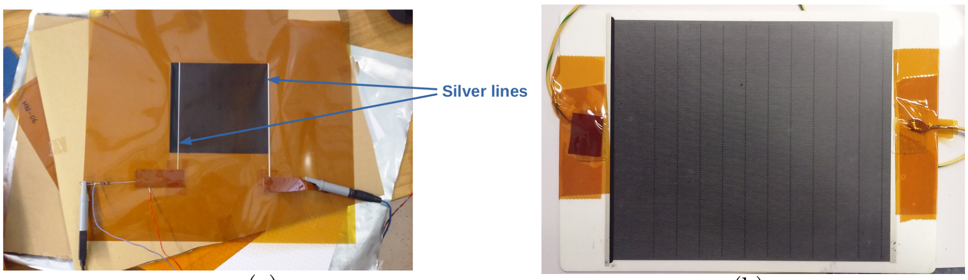

(a) (b)

Figure 5.1: Resistive paste screen-printed (a) on Kapton® and (b) on Al_2O_3 substrate.

5.2 Properties of materials

The resistive paste:

The resistive paste[4] is a composite formed by an epoxy matrix in which carbon-based particles are dispersed, adding conductivity to the material. The resistivity of the paste has a linear dependence with the temperature, described by the equation:

$$\mathrm{R} = \mathrm{R_{ref}}[1 + \alpha(\mathrm{T} - \mathrm{T_{ref}})] \tag{5.1}$$

where α is the temperature coefficient of the resistance (TCR), and $\mathrm{R_{ref}}$ and $\mathrm{T_{ref}}$ are the reference resistance and temperature respectively. The TCR of the resistive paste is -700 ppm/°C[5]. A negative TCR means that with increasing temperature the electrical resistance of the paste will decrease and vice versa.

The substrates:

The coefficients of the thermal (CTE) and hygroscopic (CHE) expansion for all substrates are listed in Table 5.1. The HN-type Kapton® has a higher CTE and CHE with respect to the EN-type thus it is expended to expand more in both humidity and temperature scans. The Al_2O_3 substrate is insensitive to humidity and has a two to three times lower CTE than the Kapton® substrates. For these reasons, the Al_2O_3 substrate will help to measure the behaviour of the bulk strip resistance at different environmental conditions.

---

[4] ESL D-RS-12115 [69].

[5] This value was taken from the old data-sheet of ESL D-RS-12100 series resistors for a reference temperature of 125°C. The TCR is no longer listed in the new data-sheet [69].

Table 5.1: Thermal and Hygroscopic Expansion Coefficients

Expansion Coefficients		**Al_2O_3**	**HN-type Kapton®**	**EN-type Kapton®**
CTE (ppm/°C)	MD[6]	7[7]	20[8]	17[8]
	TD[9]		20[8]	13[8]
CHE (ppm/%R.H.)		N/A	22[10]	9[10]

The thermal or hygroscopic expansion of the substrates leads to a mechanical stretching of the paste. This results in an increase of the strip resistance. To measure by how much the strip resistance increases as a function of the mechanical stretching of the paste, we performed a test[11] with both Kapton® substrates. Figure 5.2 shows the set up for this measurement.

Figure 5.2: Set-up of the mechanical stretching test of the Kapton® substrates.

One edge of the Kapton® was constrained while the other edge was free to move by applying weight. During the expansion of the Kapton® substrates we used a digital microscope[12] to measure by how much the free edge of Kapton® was moving and at the same time we were measuring the strip resistance. For both substrates, we measured that 50 μm expansion of the Kapton® corresponds to 1.5–1.6 kΩ increase of the strip resistance of 400 kΩ or $\Delta R/R \simeq 8\times10^{-5}/\mu m$. A 100 mm long resistive

---

[6] MD stands for Machine Direction.

[7] Test condition: 40–400°C

[8] Test condition: -14–38°C

[9] TD stands for Transverse Direction.

[10] Test condition: 23°C, 20–80% R.H.

[11] This measurement was performed in the RD51/GDD laboratory at CERN.

[12] Dino-Lite®.

strip on HN-type Kapton® will expand by 20 ppm/°C or 2 µm/°C. Thus a 1°C temperature change results in an increase of $\simeq$ 0.06 kΩ for a resistance of 400 kΩ.

5.3 Strip resistance as a function of temperature and humidity

In the ATLAS cavern the Micromegas detectors will be operated in a stable temperature environment and the humidity of the operating gas will be on the ppm level. However, during the Quality Assurance & Quality Control (QA/QC) of the protection layers in Japan and the Micromegas readout boards at CERN, the strip resistivity is measured in laboratories where the temperature and humidity is not controlled. Furthermore, even if the temperature of the gas can be controlled, the temperature of the detectors during different seasons is not always the same. The studies performed aim to understand the changes of the strip resistance as a function of humidity and temperature.

All samples were tested in an environmental chamber[13] in the Quality Assurance & Reliability Testing Lab [71] at CERN. The specific environmental chamber is able to control temperatures in the range -70°C to +180°C and relative humidities (R.H.) in the range 10–95% for temperatures from +10°C to +85°C. The temperature and humidity inside the test chamber were recorded with a Rotronic® HygroClip HC2-IC105-HH probe.

The humidity and temperature cycles performed are listed in Tables 5.2 and 5.3. During the humidity scans, the humidity changes in steps of 5% every 10 min. During the temperature scans, the temperature changes in steps of 1°C every 10 min.

Table 5.2: Humidity cycles

Measurement	**Stable Condition**	**Cycle**	**Step**	**Time of step**
Humidity cycles	20 °C	45–80–45 % R.H	5% R.H.	10 min.
	25 °C	30–85–30 % R.H		
	60 °C	10–95–10 % R.H		

Table 5.3: Temperature cycles

Measurement	**Stable Condition**	**Cycle**	**Step**	**Time of step**
Temperature cycles	80 % R.H.	10–60–10 °C	1°C	10 min.
	45 % R.H.	20–60–20 °C		

In the following, the results obtained with the Al_2O_3 substrate from the humidity and temperature cycles will be discussed first in order to have a reference for the behaviour of the resistive paste.

---

[13] CLIMATS EXCAL1423-HE [70]

5.3.1 Resistive strips on Al_2O_3 substrate

Figure 5.3 shows the relative humidity (R.H) and the strip-resistance as a function of time on the left and the temperature as a function of time on the right for the three humidity cycles performed with the Al_2O_3 substrate. The first cycle is at 20°C, the second one is at 25°C and the third one is at 60°C with maximum temperature fluctuations of ±0.3°C, ±0.6°C and ±0.2°C respectively.

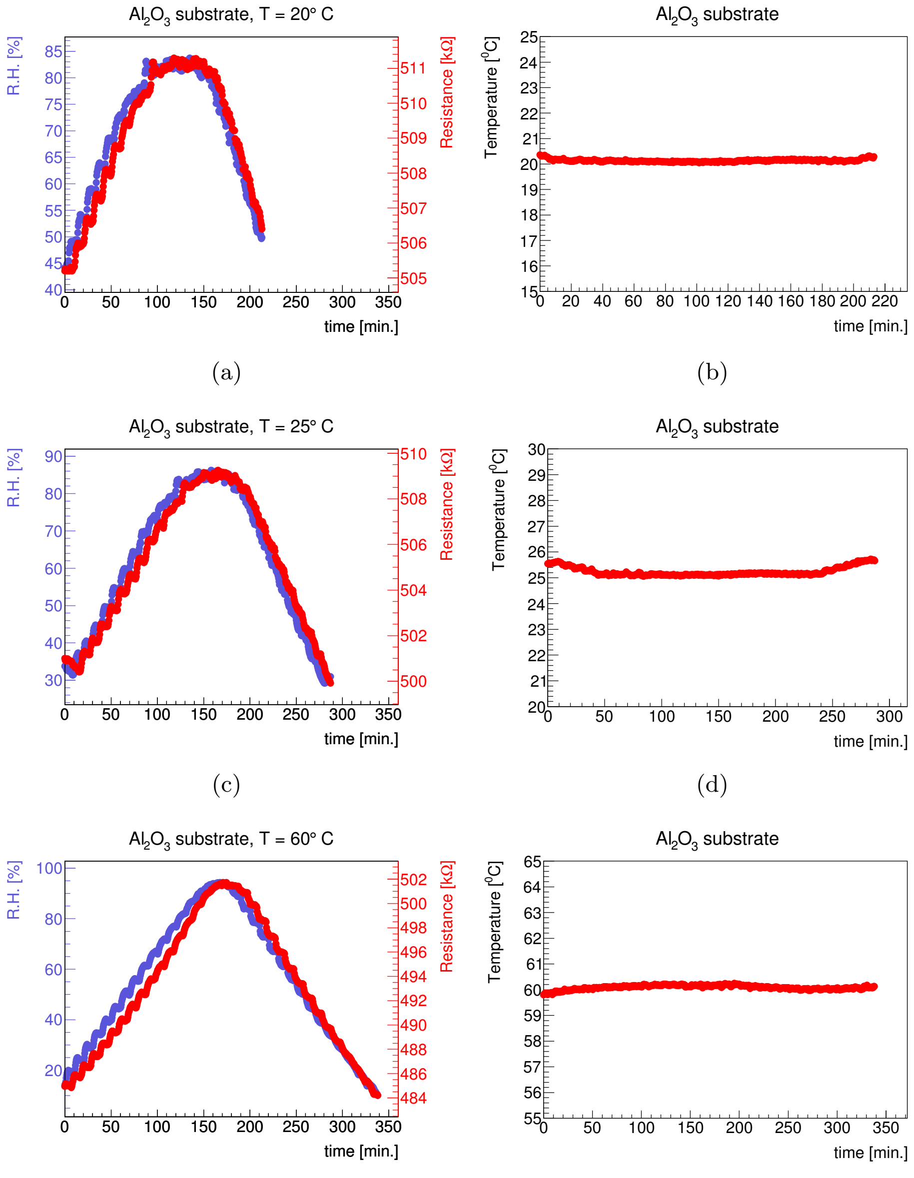

(a) (b)

(c) (d)

(e) (f)

Figure 5.3: (left) Relative humidity and strip resistance as a function of time; (right) Temperature as a function of time, for the humidity scans performed with the Al_2O_3 substrate.

In all humidity cycles, the strip resistance follows the changes of the humidity. However, when the humidity increases it takes some time for the resistive paste to react to the changes of humidity and this appears as an hysteresis. This time is about 3 min. for the humidity cycles at 20°C and 25°C and it is about 10 min. for the humidity cycle at 60°C.

The strip resistance as a function of humidity for the three humidity cycles is shown in Fig. 5.4. At higher temperatures the strip resistance is lower. This is expected from the negative TCR of the paste. When changing the humidity in 5% steps it seems that the 10 min. time step is not long enough for the resistive paste to stabilize. This is confirmed by the fact that the measured resistance is slightly different at the same humidity value going up and down in the humidity scan. Nevertheless, we see that the dependence of the strip resistance on the humidity is linear.

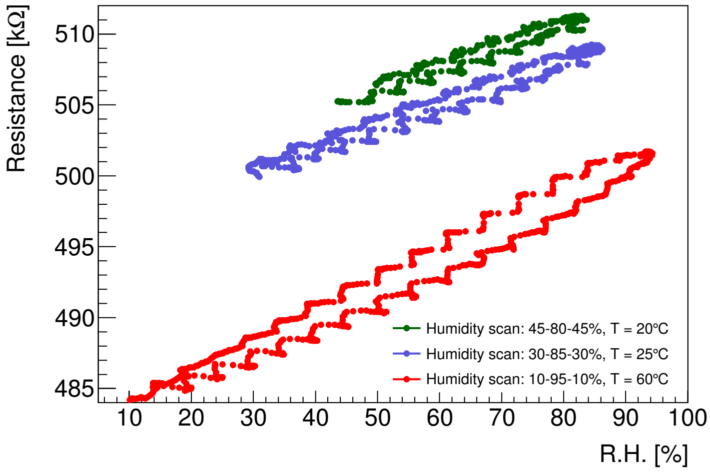

Figure 5.4: Strip resistance as a function of humidity for the three humidity scans performed with the Al_2O_3 substrate.

The relative change of the strip resistance per % of R.H for all humidity cycles is summarized in Table 5.4. It is $<5\times10^{-4}$/%R.H. which is negligible.

Table 5.4: Relative change of strip resistance per % of R.H on the Al_2O_3 substrate.

R.H. cycle (%)	**Temperature (°C)**	$\frac{\Delta R}{R}$**/% R.H.**
45-80-45	20	3.4×10^{-4}
30-85-30	25	3.2×10^{-4}
10-90-10	60	4.7×10^{-4}

The two temperature cycles performed with the Al_2O_3 substrate are shown in Fig. 5.5. In the first cycle, 10–60–10°C, the humidity fluctuated a lot. It was on average 84.4% in the time interval 0–400 min. and 79.8% afterwards while it was expected to fluctuate around 80% during the whole cycle. Similar fluctuations were also observed in the temperature cycle, 20–60–20°C, with an expected R.H. of 45%.

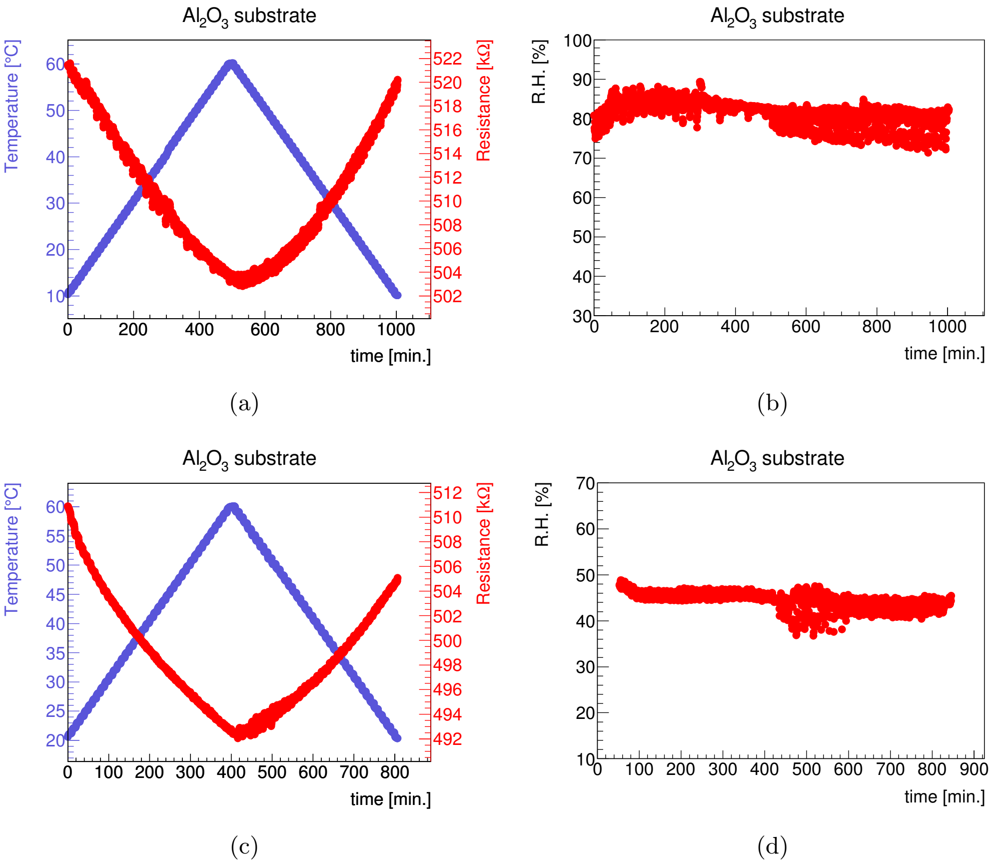

(a)

(b)

(c)

(d)

Figure 5.5: (left) Temperature and strip resistance as a function of time; (right) humidity as a function of time, for the two temperature scans performed with the Al_2O_3 substrate.

In both temperature cycles, the strip resistance decreases when the temperature goes up and vice versa as expected from the negative TCR of the resistive paste. Figure 5.6 shows the measured strip resistance as a function of time and the expected values as calculated with Eq. 5.1 with α = -700 ppm/°C. In the first temperature cycle at 80% R.H. we see that when the temperature increases the strip resistance shows a small deviation from the expected linear behaviour. This is due to the expansion of the Al_2O_3 substrate. Given the CTE value quoted in Table 5.1 one expects an expansion of the Al_2O_3 substrate by 0.7 µm·ΔT = 35 µm. This corresponds to +1.08 kΩ which should be added to the expected values. However, when the temperature goes down there is an hysteresis which leads to a larger deviation from the linear expected behaviour. Nevertheless, when the temperature reaches 10°C the strip resistance has reached almost the same value as before starting the scan within ±1kΩ. This is better shown in Fig. 5.7 where the strip resistance is plotted as a function of the temperature.

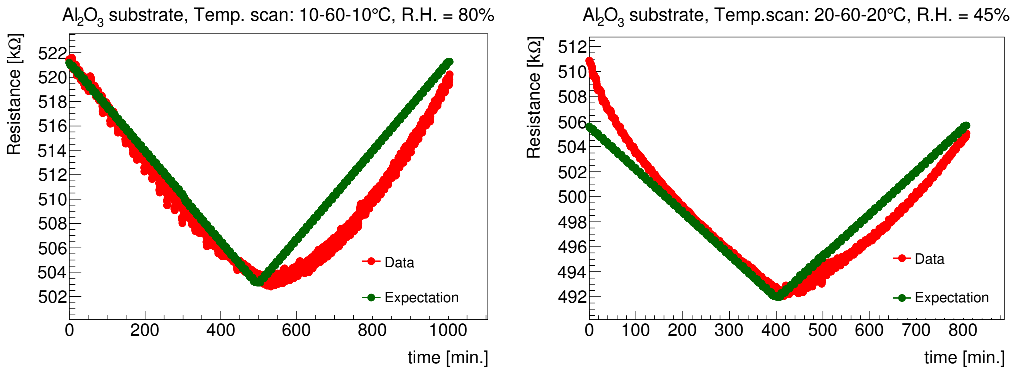

(a) (b)

Figure 5.6: Strip resistance as a function of time compared with the expectation for the temperature cycle (a) 10–60–10°C and (b) 20–60–20°C.

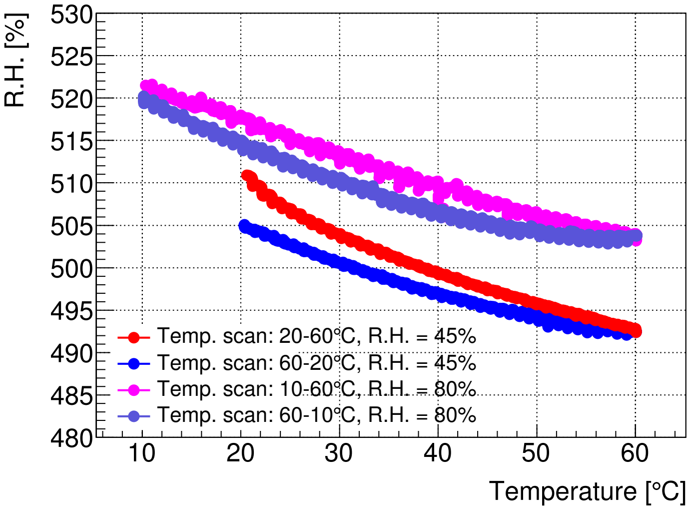

Figure 5.7: Strip resistance as a function of temperature for the two temperature scans performed with the Al_2O_3 substrate.

During the second temperature cycle at 45% R.H. in the beginning of the scan and up to ~35°C (red data points in Fig. 5.7) there is a fast drop of the strip resistance. Because the two temperature cycles were performed directly one after the other it seems that there was not enough time in between the two cycles for the resistive paste to stabilize. This drop seems to correspond to the decrease of the relative humidity from 80% to 45% between the two temperature cycles. However, for temperatures above ~35°C and during the decreasing temperature scan the data points (blue coloured) have the same trend as for the temperature scan at 80% R.H. (purple coloured). Furthermore, we see that at 60°C the difference between the two temperature scans at 80% R.H. and 45% R.H. is ~10kΩ. Also the difference between the blue and the purple data points at 20°C is ~10kΩ. This confirms that indeed the red data points up to ~35°C correspond to the transition from 80% R.H. to 45% R.H. In Fig. 5.6(b) the expected values were calculated with a reference temperature at 60°C in order to see the deviation from the linear behaviour in the beginning of the cycle without taking into account the expansion of the Al_2O_3 substrate. The expansion accounts for $0.7\ \mu m \cdot \Delta T = 20\ \mu m$ which correspond to +0.6 kΩ.

Table 5.5 summarizes the relative change of the strip resistance per °C for the two temperature scans. It is $<8\times10^{-4}/°C$.

Table 5.5: Relative change of strip resistance per °C on the Al_2O_3 substrate.

Temperature cycle (°C)	**Relative Humidity (%)**	$\frac{\Delta R}{R}$**/°C**
10-60-10	80	7.3×10^{-4}
20-60-20	45	6.9×10^{-4}

To summarize, the strip resistance follows the changes of the humidity. However, it takes more than 10 min. to reach a stable value every time the humidity changes. From the temperature scan, we saw that when the temperature increases the strip resistance decreases almost linearly. But when the temperature decreases there is an hysteresis effect. This means that also here 10 min./°C are not enough for the strip resistance to reach a stable value. However, the relative changes of the strip resistance due to the humidity or the temperature are very small. They are $<5\times10^{-4}$/%R.H. and $<8\ \times10^{-4}/°C$ for a resistance of 500 kΩ.

5.3.2 Resistive strips on Kapton® substrates

The same temperature and humidity scans were also performed with the EN-type and the HN-type Kapton® substrates. Figure 5.8 shows the strip resistance as a function of relative humidity for both Kapton® substrates at 20°C, 25°C and 60°C. The resistance as a function of time and the temperature fluctuations can be found in Appendix C.1.

For both Kapton® substrates the changes of the strip resistance are a factor of 1.5–2 larger than for the Al_2O_3 substrate. This can be explained by the large expansion of the Kapton® substrates due to the humidity. The Al_2O_3 substrate is insensitive to humidity. The EN-type Kapton® has a CHE of 9 ppm/% R.H. and the HN-type 22 ppm/% R.H. The results are consistent with these values except for the third humidity cycle at 60°C where a larger relative change of the resistance is observed. Since the humidity cycles were performed directly one after the other at different temperatures the thermal expansion coefficient (CTE)[14] of the substrates should also be taken into account. Furthermore, the hysteresis within a humidity cycle is much larger for the Kapton® substrates than what was observed with the

---

[14] The CTE values listed in Table 5.1 are for the temperature range -14–38°C.

Al_2O_3 substrate. This and the behaviour at 60°C will become clearer below in another test that we performed with much longer waiting time in between temperature and humidity changes.

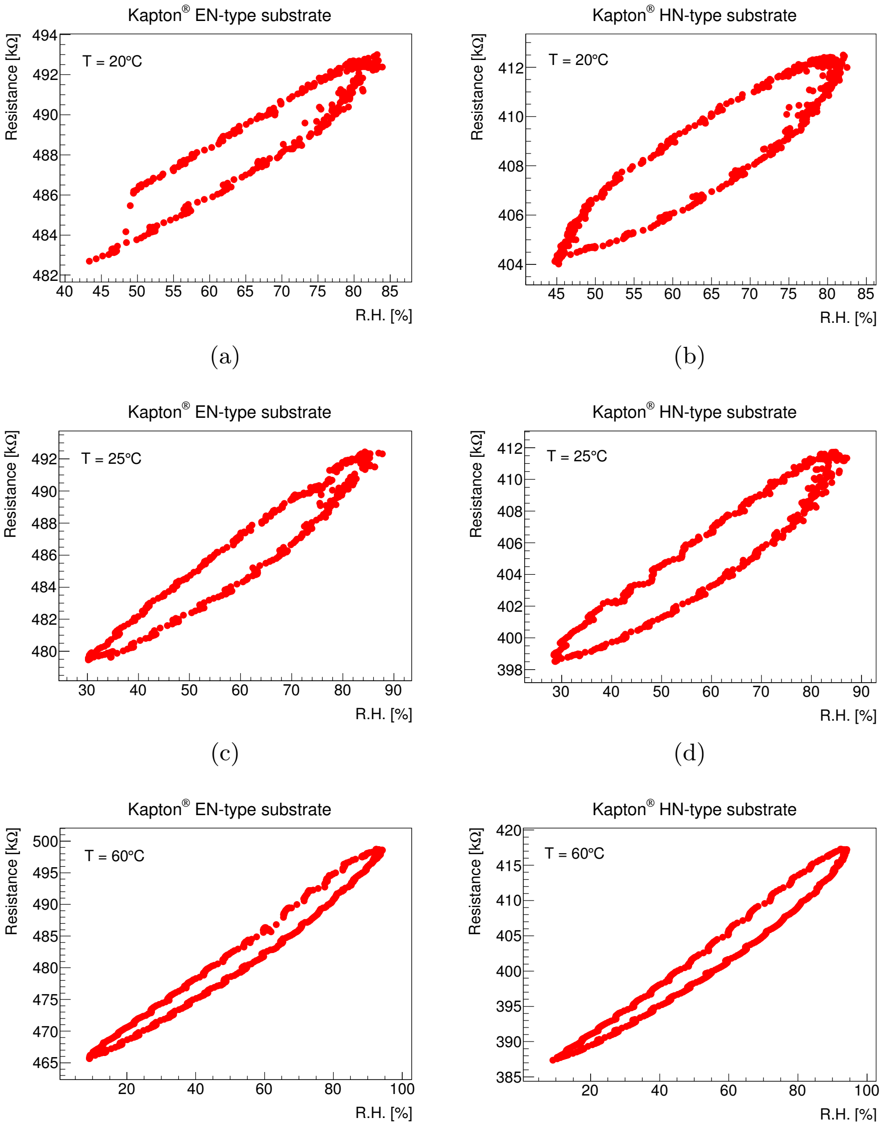

(a) (b)

(c) (d)

(e) (f)

Figure 5.8: (left) Strip resistance as a function of relative humidity for the EN-type Kapton® and (right) for the HN-type Kapton®.

The relative changes of strip resistance per % of R.H. for all substrates are listed in Table 5.6.

Table 5.6: Relative change of strip resistance per % of R.H. for all substrates.

R.H. Cycle (%)	**Temperature (°C)**	$\frac{\Delta R}{R}$/% **R.H.**		
		Al$_2$O$_3$	**EN-type Kapton®**	**HN-type Kapton®**
45–80–45	20	3.4×10^{-4}	4.6×10^{-4}	5.5×10^{-4}
30–85–30	25	3.2×10^{-4}	4.8×10^{-4}	5.7×10^{-4}
10–95–10	60	4.7×10^{-4}	8×10^{-4}	8.9×10^{-4}

Figure 5.9 shows the strip resistance of the Kapton® substrates and the temperature as a function of time for the two temperature scans. At ∼80% R.H. the behaviour of the strip resistance is very different from what was observed with the Al$_2$O$_3$ substrate, in particular when the temperature increases. Due to the very high humidity the Kapton® substrates are expanding and the strip resistance increases. On the other hand the temperature increases so the resistance should decrease. The convolution of these two effects results in this strange behaviour.

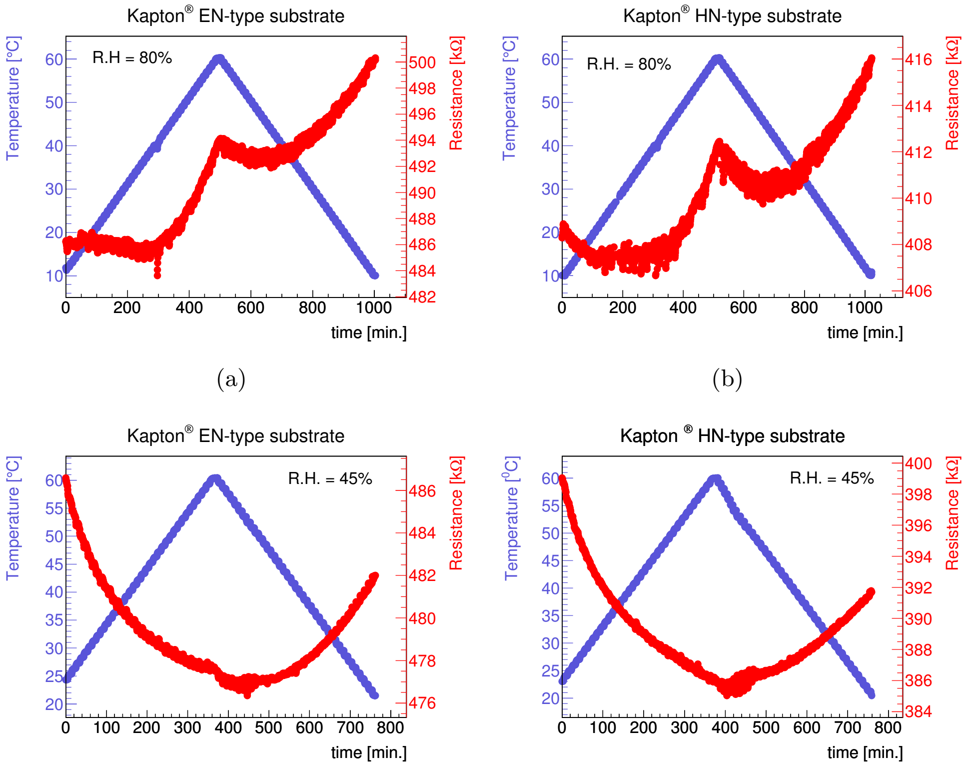

(a) (b)

(c) (d)

Figure 5.9: ((a) and (c)) Strip resistance and temperature as a function of time for the two temperatures scans performed at 80% and 45% R.H. with the EN-type Kapton® and ((b) and (d)) with the HN-type Kapton®.

At ∼45% R.H. the behaviour is similar to the behaviour of the strip resistance on the Al$_2$O$_3$ substrate. Also here in the beginning of the thermal cycle the strip resistance is higher than it should be at ∼45% R.H. due to the non proper waiting time in between the two thermal cycles. However, the change of the resistance when the temperature decreases is only half as large. This and the behaviour at ∼80% R.H. can be explained by the thermal and hygroscopic expansion of the Kapton® if temperature and humidity dependent expansion factors are considered. The time it takes for the substrates to expand is very important; this will become clearer below.

To better understand the behaviour of the Kapton® substrates with time, we performed another test with the HN-type Kapton® with much longer waiting time in between temperature and humidity changes. The test was conducted in the same environmental chamber in the Quality Assurance & Reliability Testing Lab at CERN. The test lasted 13 days and 18 hours. Figure 5.10 shows the strip resistance as a function of time during this period. Table 5.7 summarizes the environmental conditions and the duration of each step.

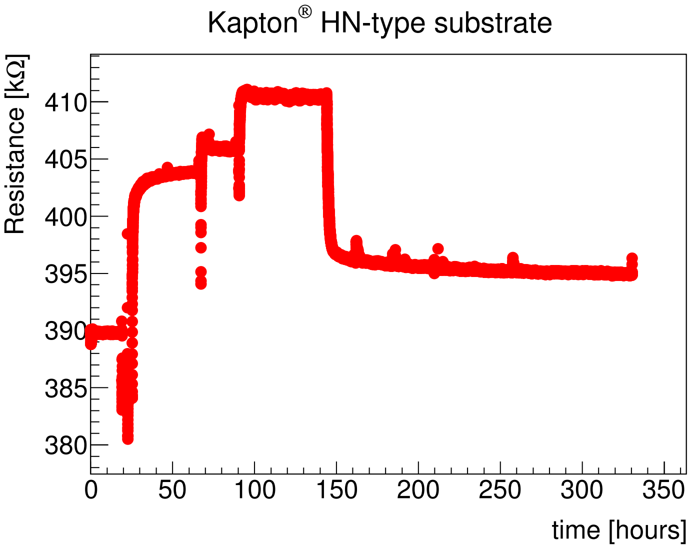

Figure 5.10: Strip resistance as a function of time for the HN-type Kapton®.

Table 5.7: Environmental conditions and duration of the test performed with the HN-type Kapton®.

Time interval [hours]	Duration [hours]	Temperature [°C]	Rel. Humidity [%]
0–19	19	20	50
19–22.5	3.5	40	
22.5-25.3	2.8	60	
25.3–67.2	41.9	60	85
67.2–90.5	23.3	40	
90.5–144	53.5	20	
144–330	186	20	50

Figure 5.11 shows the first ∼25 hours of the test. In the first 1.5 hours we observe a small fluctuation of the strip resistance which corresponds to a temperature drop from 23°C (temperature outside the environmental chamber) to 20°C. It took in total

1.5 hours for the strip resistance to stabilize at 20°C. After 19 hours the temperature was changed to 40°C for 3.5 hours and afterwards to 60°C for 2.8 hours. During the temperature transitions from 20°C to 40°C and from 40°C to 60°C we see that the strip resistance stabilizes after ~5–10 minutes. This means that at 50% R.H. the thermal expansion of Kapton® is achieved fast.

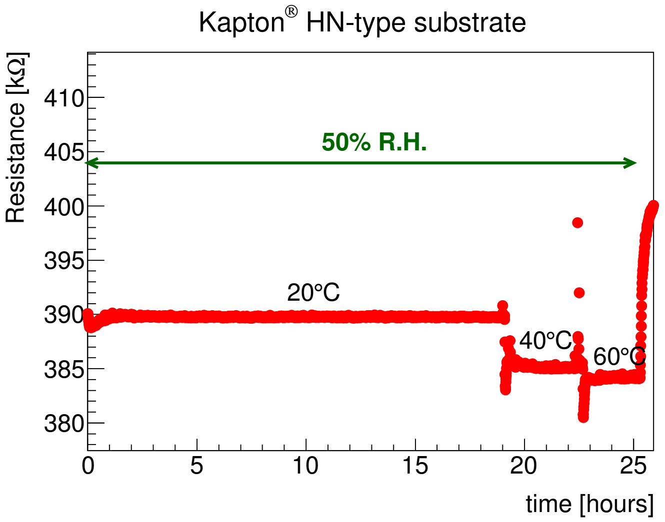

Figure 5.11: Zoom of Fig. 5.10: Strip resistance as a function of time at 50% R.H.

Table 5.8 summarizes the conditions inside the chamber, the measured strip resistance and the expected strip resistance as calculated with Eq. 5.1 by using α = - 700 ppm/°C and T_{ref} = 20°C. From 20°C to 40°C we measured a difference of -4.5 kΩ while we expected a difference of -5.5 kΩ. The additional ~1 kΩ that we see can be explained by the expansion of the Kapton® substrate. A temperature difference of 20°C leads to an expansion of ~35–40µm which corresponds to an increase of the strip resistance by +1 kΩ.

From 40°C to 60°C we measured only -1 kΩ difference while from the resistive paste we were expecting a difference of -5 kΩ. It seems that in this temperature range the expansion of the Kapton® is 4 times higher than in the temperature range 20–40°C[15].

Table 5.8: Summary of the test at ~50% R.H.

Time interval [hours]	**R.H. (%)**	**Temperature (°C)**	**Strip resistance measured (kΩ)**	**Strip resistance expected (kΩ)**
0–19	48.1	20.2	389.8	389.8
19–22.5	48.2	40.3	385.1	384.3
22.5–25.3	47.6	60.1	384.2	378.9

The test at 85% R.H. is shown in Fig. 5.12. When the humidity changed from

---

[15] The CTE value listed in Table 5.1 is for the temperature range -14–38°C taken from the Dupont data sheet [72].

50% to 85% there is a fast increase of the resistance as expected. But afterwards there is a very slow increase over a time of about 30 hours until the strip resistance becomes stable. Since the temperature didn't change at this step it seems that the Kapton® during these 30 hours was still absorbing humidity and expanding. After it has reached the maximum expansion at 85% R.H., going from 60°C to 40°C or from 40°C to 20°C it took about 2 hours for the strip-resistance to stabilize. This means that the shrinkage of the Kapton® due to the temperature change at high humidity takes long.

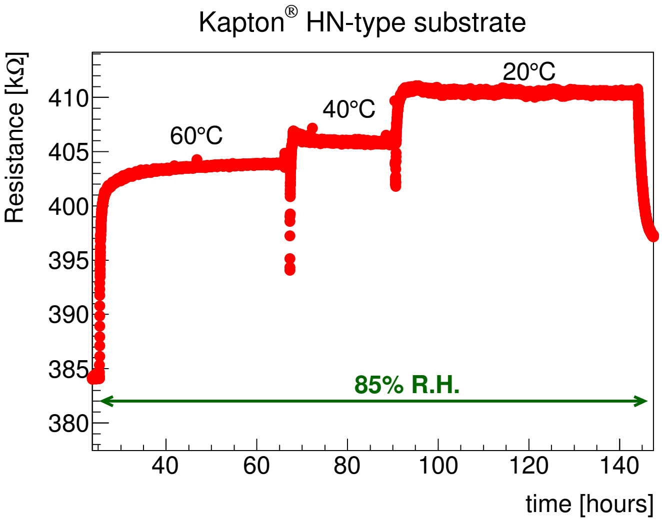

Figure 5.12: Zoom of Fig. 5.10: Strip resistance as a function of time at 85% R.H.

Table 5.9 summarizes the conditions inside the chamber, the measured strip resistance after stabilization and the expected strip resistance at 85% R.H. Here the expected strip resistance was calculated with $T_{ref} = 60°C$. The strip resistance difference from 60°C to 40°C and from 40°C to 20°C is almost the same as what we saw before with the test at 50% R.H.

Table 5.9: Summary of the test at ~85% R.H.

Time interval [hours]	**R.H. (%)**	**Temperature (°C)**	**Strip resistance measured (kΩ)**	**Strip resistance expected (kΩ)**
25.3–67.2	86.7	60.1	403.9	403.9
67.2–90.5	86.9	40.2	405.9	409.5
90.5–144	86	20.1	410.5	415.2

Figure 5.13 shows the last step of the test in the environmental chamber where the humidity was decreased from 85% back to 50% in order to see how fast the strip resistance will return to its initial value. After 186 hours we saw that the strip resistance was still decreasing very slowly. By fitting with an exponential function we calculated that it needs ~39 days more for the strip resistance to reach 390 kΩ.

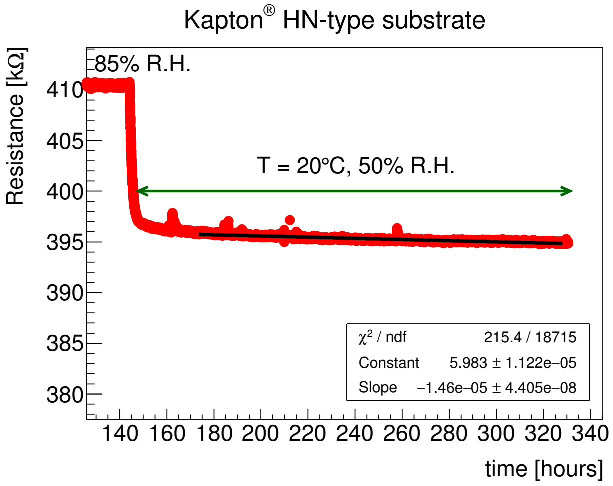

Figure 5.13: Zoom of Fig. 5.10: Strip resistance as a function of time at 20°C and 50% R.H.

We started measuring again after ∼1.5 week in the RD51/GDD laboratory. After one day we measured at 50% R.H. a resistance of 393 kΩ consistent with the expected slow decrease of the strip resistance.

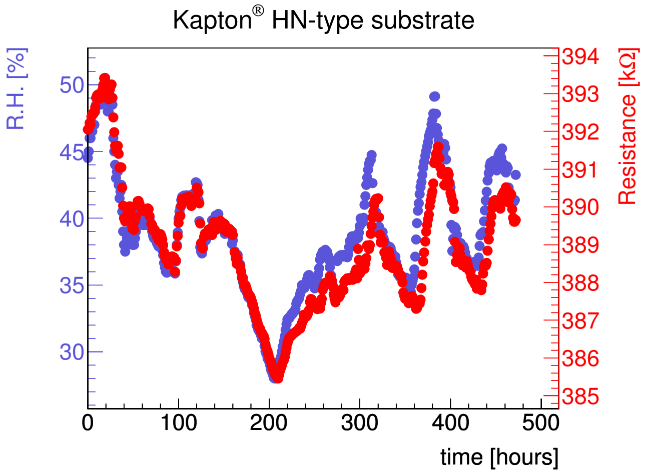

Figure 5.14: Strip resistance as a function of time. This measurement started ∼1.5 week after the test shown in Fig. 5.13.

In conclusion, since the Al_2O_3 substrate is insensitive to humidity we were able to measure the behaviour of the resistive paste as a function of humidity. The strip resistance shows a linear dependence on the humidity. From the temperature scan with the Al_2O_3 substrate we verified that the TCR of the strip resistance is as listed in the data-sheet of the company. The observed small hysteresis we attribute to the thermal expansion of the Al_2O_3 substrate.

The long term test performed with the HN-type substrate showed the following behaviour. The strip resistance is affected by the thermal and hygroscopic expansion of the Kapton® substrate. In particular at temperatures above 40°C the CTE of the Kapton® seems to be four times larger than at 20°C. Once Kapton® has reached its maximum expansion due to humidity absorption, if the temperature changes by 20°C the strip resistance stabilizes after 5–10 min. when the humidity is relative low (50% R.H.) and after 2 hours if the humidity is relative high (85% R.H.). At very high temperature (60°C) if the humidity increases from 50% R.H. to 85% R.H. the strip resistance stabilizes after 30 hours. At room temperature, if the humidity decreases from 85% R.H. to 50% R.H., it takes more than 3 weeks for the strip resistance to stabilize. Since the EN-type has an almost two times lower CTE and CHE we expect the same behaviour but on a two times shorter timescale.

For the NSW Micromegas detectors the EN-type Kapton® was chosen due to its lower thermal and hygroscopic expansion coefficients. These detectors will be operated in the ATLAS cavern at very low humidity (in theory 0% owing to the gas circulation). At the QA/QC laboratories extreme changes of environmental conditions occur mainly during the summer period. The humidity can change by ∼50% within a day and the temperature also but not more than 20°C. In these conditions, the changes of the strip resistance on the Kapton® substrates are only a few %. A 10% change in R.H. corresponds to ∼1% change of the strip resistance. For a 10°C temperature change the strip resistance changes by <1%. These changes are negligible for our application.

5.4 Ageing studies

So far, ageing studies of resistive-strip Micromegas detectors performed with different types of irradiation (X-rays, neutron, gamma and alpha exposure) showed no degradation of the detector performance as reported in Ref. [73–77]. In these detectors the HN-type Kapton® substrate was used.

Complementary to these studies, ageing effects were studied for both HN-type and EN-type Kapton® substrates without irradiation by accumulating a total amount of current equivalent to 100 years of operation at the HL-LHC[16]. In addition, ageing tests have been performed with gamma irradiation in the Gamma Irradiation Facility (GIF++) [78] (see Appendix D) at CERN.

5.4.1 Strip resistivity as a function of the accumulated charge

The aim of the test without irradiation is to check for any degradation of the resistive paste over time or accumulated charge. It is well known that the rate capability of RPCs[17] is mainly limited by the plate resistivity [79]. Systematic studies of RPC plates [80,81] have revealed that ionic conductive materials, e.g. conventional glasses and Bakelite, show a charge depletion behaviour resulting in an increased resistivity

---

[16] 10 years of HL-LHC operation in the ATLAS NSW region corresponds to 0.2 C/cm^2 [35]

[17] RPC stands for Resistive Plate chambers.

over time or accumulated charge. However, electron conductors seem not to suffer from resistivity ageing as shown in Fig. 5.15.

The carbon composition of the resistive paste used to form the resistive strips of the ATLAS Micromegas chambers is an electron conductor, thus no time dependent resistivity degradation is expected. Nevertheless, we performed a similar study with both Kapton® substrates.

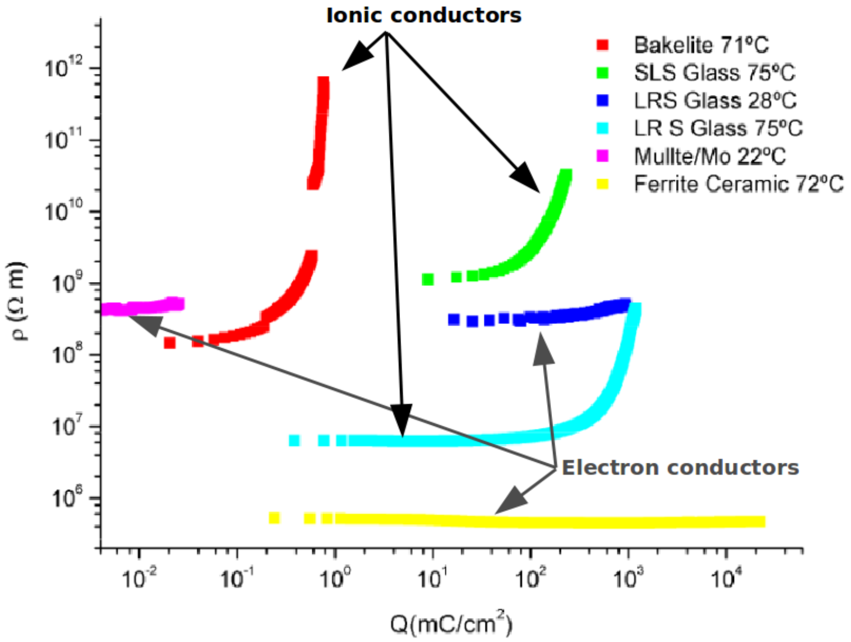

Figure 5.15: Resistivity as a function of the accumulated charge measured for several materials and different temperatures. Taken from [81] and modified for legibility.

Experimental set-up

Figure 5.16 shows the experimental set-up used for this study. The two Kapton® substrates were placed inside a plexi-glass box where N_2 was flowing to dry the environment. The relative humidity and temperature inside the plexi-glass box were recorded with a data-logger[18] with a temperature accuracy of ±0.5°C and R.H. accuracy of ±3.0% in the range 20% to 80% R.H. A micro-controller (Arduino® Mega 2560) was programmed for continuous data taking and monitoring. Fig. 5.16(b) shows the equivalent circuit. The resistive strips (R_{res}) of each Kapton® substrate are connected through silver contact lines in series with a power supply and a small resistor ($R_{control}$=∼5.5 kΩ) that is used to protect the Arduino®. The Arduino® was connected in parallel with the small resistor. Details of the conversion output of the Arduino and the calibration of the system can be found in Appendix C.2. This

---

[18] Lascar EL-USB-2-LCD.

study was performed in the RD51 [39]/Gas Detector Development (GDD) laboratory at CERN.

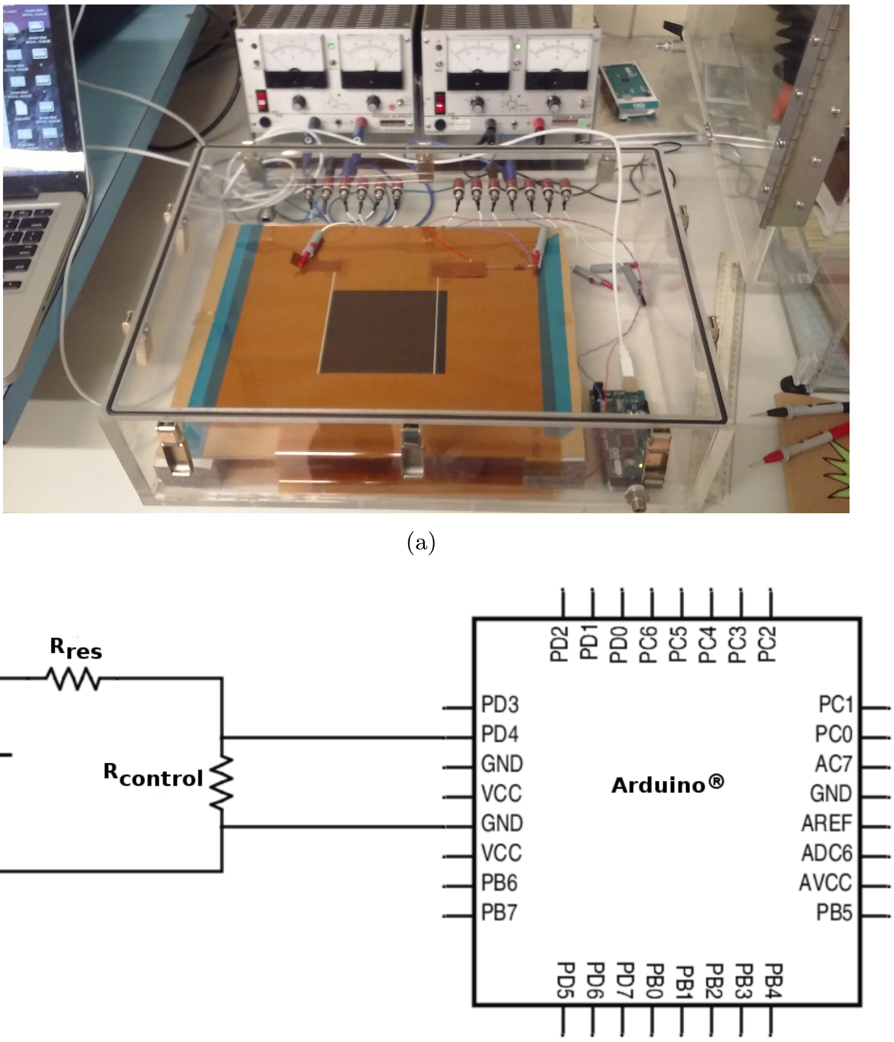

(a)

(b)

Figure 5.16: (a) The two Kapton ® substrates placed on top of each other inside the plexi-glass box; (b) The equivalent circuit for each Kapton ® substrate.

Results

Figure 5.17 shows the relative humidity and the strip resistance as a function of time for both Kapton ® substrates. A current of ∼70 μA for the EN-type and ∼85 μA for the HN-type was flowing in the circuit for ∼27 days. In this time period the temperature was stable at 20±0.5°C while the relative humidity was decreasing gradually from 44±3% to 23±3%. The strip resistance in both Kapton ® substrates decreases over time following the decrease of the relative humidity.

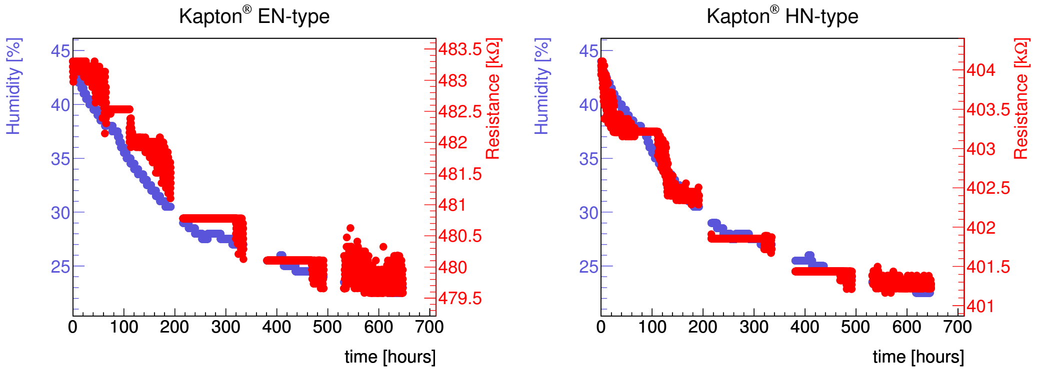

(a)

(b)

Figure 5.17: Relative humidity and strip resistance as a function of time for (a) the EN-type Kapton® and (b) the HN-type Kapton®.

The strip resistance as a function of relative humidity is shown in Fig. 5.18 for both Kapton® substrates. In this test, since the humidity was changing slowly over a long time period we see that there was enough time for the Kapton® substrates to shrink. The strip resistance shows a rather linear dependence on the humidity consistent with the behaviour observed with the Al_2O_3 substrate. Thus linear fits can be considered as a good approximation to correct the data for the humidity.

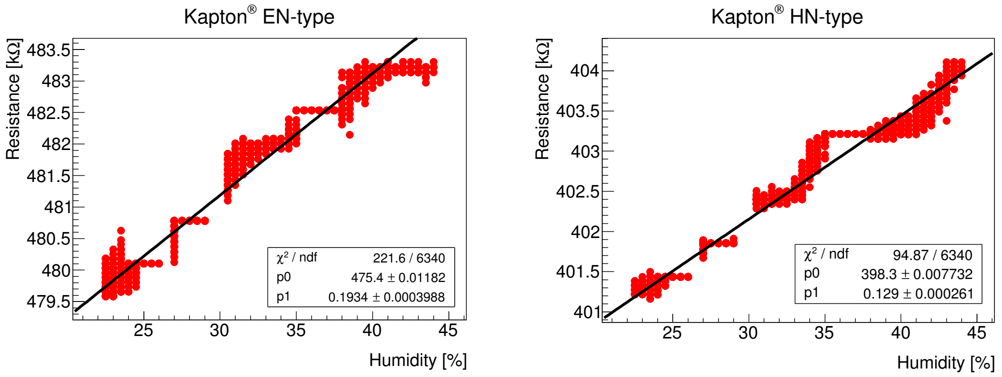

(a)

(b)

Figure 5.18: Strip resistance as a function of the relative humidity for (a) the EN-type Kapton® and (b) the HN-type Kapton®.

The formula used for the correction is the following:

$$\mathrm{R_{corrected}} = \mathrm{R_{measured}} + \alpha(\mathrm{R.H_{ref}} - \mathrm{R.H_{measured}}) \tag{5.2}$$

where α was extracted from the slopes of the fits (see Fig. 5.18) and the reference humidity ($\mathrm{R.H_{ref}}$) was considered to be 45%. The relative change of strip resistance in this case is about 3.6×10^{-4} for the EN-type Kapton® and 3.2×10^{-4} for the HN-type. These values are 1×10^{-4} (for the EN-type) and 2.3×10^{-4} (for the HN-type) smaller than the values listed in Table 5.6. The difference is consistent with the fact that in the measurements for Table 5.6 the expansion of the Kapton® was not yet completed.

Figure 5.19 shows the strip resistance as a function of the accumulated charge for both substrates. For the EN-type the strip resistance is constant within ±1 kΩ and the accumulated charge corresponds to 100 years of operation at HL-LHC conditions. The HN-type also shows a constant strip resistance within ±1 kΩ, here the accumulated charge corresponds to 150 years of operation at HL-LHC conditions. The strip resistance variations are not significant thus we conclude that the resistive paste does not show a charge depletion behaviour.

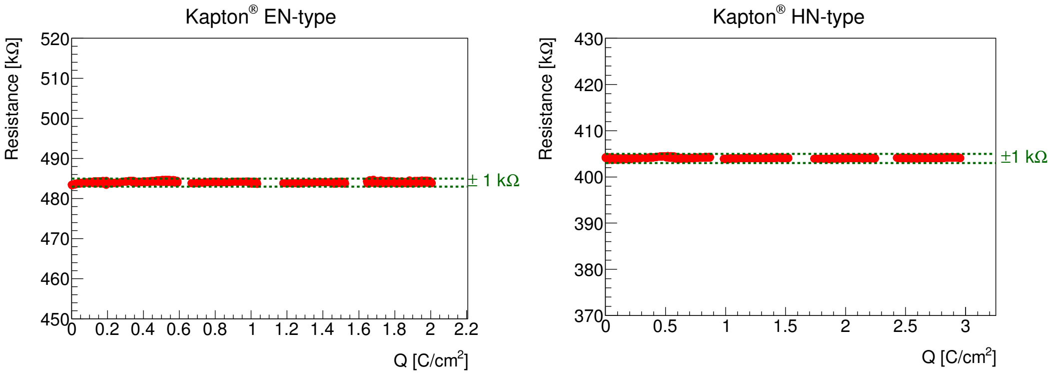

(a) (b)

Figure 5.19: Strip resistance as a function of the accumulated charge for (a) the EN-type Kapton® and (b) the HN-type Kapton®.

5.4.2 Ageing studies under intense gamma irradiation

The two Kapton® substrates were exposed to gamma irradiation at the Gamma Irradiation Facility (GIF++) at CERN for ∼240 days. Figure 5.20 shows the set-up inside the GIF++ bunker. The substrates were placed at about 1 m from the irradiator where the gamma flux is up to 4.4 × 10^7 Hz/cm^2. The strip resistance was recorded for few days every 2–4 months with the Fluke® 289 industrial logging multimeter and the software provided by the company. The environmental conditions inside the GIF++ bunker were extracted from the CERN ICE-DIP database.

Figure 5.21(a) shows the strip resistance as a function of time for the two Kapton® substrates. From the summer period and afterwards an increase of 5 kΩ is observed in both substrates. The recorded relative humidity as a function of time is shown in Fig. 5.21(b). The data recorded are only up to July 2016. During the summer period the relative humidity increased from ∼30% to ∼50% on average. During this period the temperature was ∼23°C.

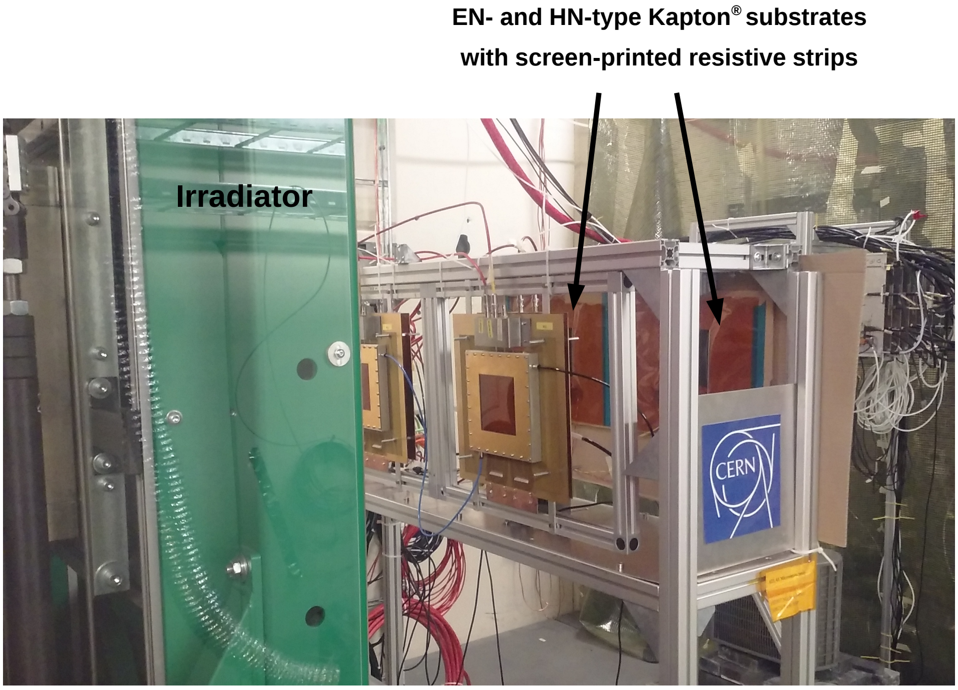

Figure 5.20: Set-up in GIF++

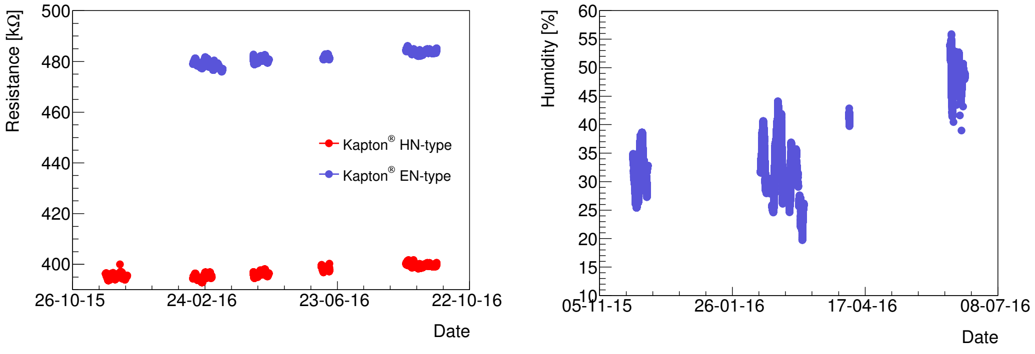

(a) (b)

Figure 5.21: (a) Strip resistance as a function of time for both Kapton® substrates; (b) Relative humidity as a function of time inside the GIF++ bunker up to July 2016.

Figure 5.22 shows the strip resistance and the relative humidity as a function of time for both substrates from two measurement periods. In the second period (period2) the humidity is on average ∼35% and in the fourth period (period4) it is ∼50%. For both periods we see that the strip resistance follows almost exactly the fluctuations of the relative humidity.

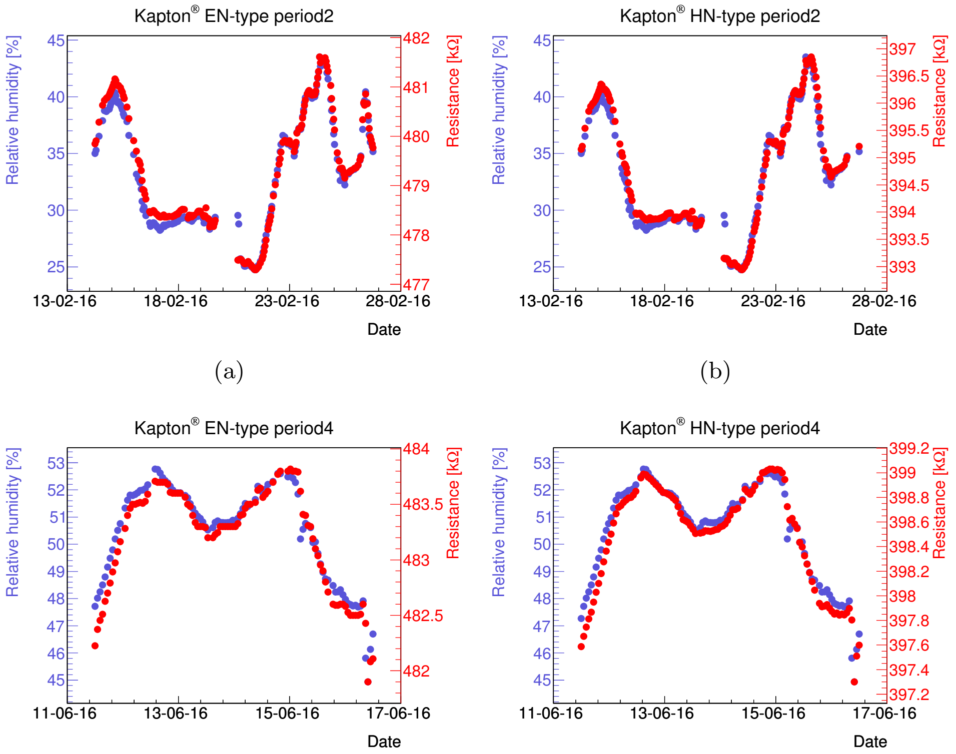

(a) (b)

(c) (d)

Figure 5.22: Strip resistance for both Kapton® substrates and relative humidity as a function of time from two different periods.

The correlation of the strip resistance as a function of relative humidity is shown in Fig. 5.23. Linear fits were considered as a good approximation to correct the data for the humidity.

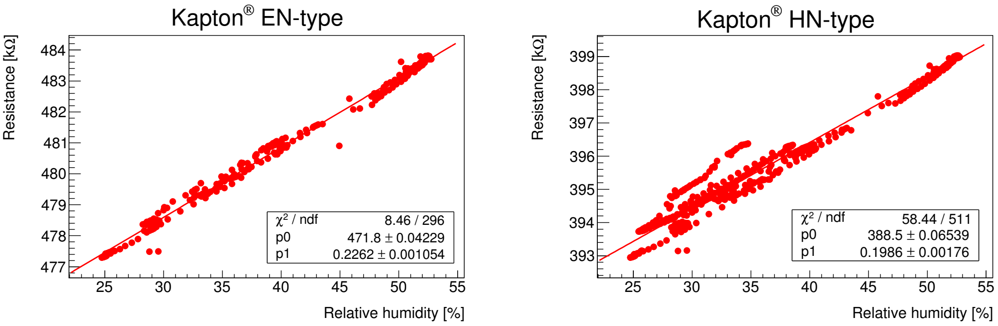

(a) (b)

Figure 5.23: Strip resistance as a function of the relative humidity for both Kapton® substrates.

Data were corrected for the humidity using Eq. 5.2 where α are the slopes of the fits shown in Fig. 5.23 at a reference humidity of 30%. These slopes obtained at 23°C are slightly higher (by 0.04 for the EN-type Kapton® and by 0.07 for the HN-type) than the slopes shown in Fig. 5.18. This can be explained by the different thermal expansion of Kapton® in these temperature conditions. After correction a residual variation of ±0.5% in the strip resistance is observed for both substrates as shown in Fig. 5.24.

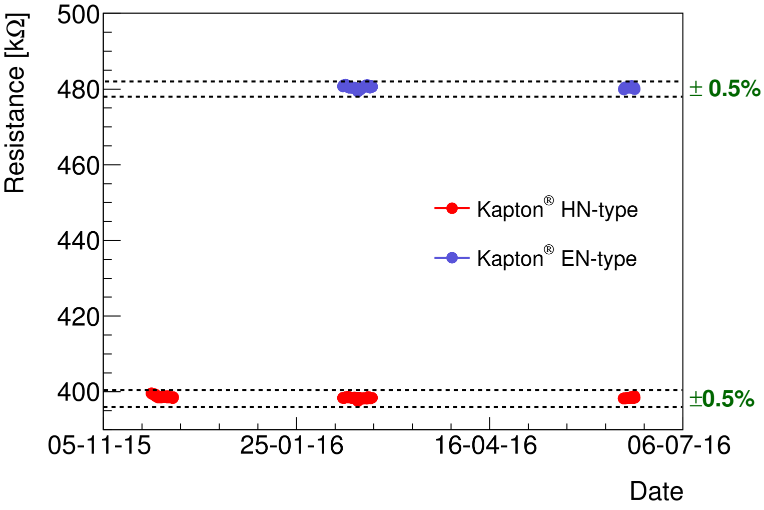

Figure 5.24: Strip resistance as a function of time for both Kapton® substrates after correction of the strip resistance for the relative humidity.

The substrates after irradiation were moved back to the RD51/GDD laboratory and were checked under a microscope. Other than the silver paste line which changed to brown colour probably due to oxidation, we did not observe any damage on the resistive paste. The strip resistance variations are not significant thus we conclude that no ageing effect was observed under gamma irradiation.

5.5 Conclusions

For the ATLAS NSW Micromegas detectors the EN-type Kapton® was chosen for its lower thermal and hygroscopic expansion coefficients. We performed several tests in an environmental chamber with the same resistive paste screen-printed on different substrates and we conclude the following.

The resistance of the paste itself follows temperature and humidity changes more or less immediately, proportional to the R.H. and inverse proportional to the temperature. In addition to these changes the thermal and hygroscopic expansion of the Kapton® substrates modifies the resistance, however, on a much longer timescale. The Kapton® substrates following temperature changes expand and shrink rather fast, $\sim$10 min and $\sim$2 hours respectively. However, the absorption or release of moisture are much slower processes. We measured that the hygroscopic expansion of the HN-type takes about 30 hours while the shrinkage takes more than 3 weeks.

The total relative change of the strip resistance of $<8\times10^{-4}/°\mathrm{C}$ and $<5\times10^{-4}/\%$ R.H. is negligible for our application.

Furthermore, from the ageing studies that we performed we concluded that the resistive paste does not show a charge depletion behaviour and does not suffer from ageing effects.

Chapter 6

Characterization of a resistive-strip bulk-Micromegas detector with the new pillar pattern used in the NSW Micromegas detectors

The pillars in a Micromegas chamber define the distance between the mesh and the anode. They are produced by photo-lithography from thin layers of insulating material[1] laminated to the anode and can take any shape.

Figure 6.1 shows the spatial distribution of clusters reconstructed in a two-dimensional Micromegas with circular pillars of ∼300 µm diameter and 2.5 mm spacing. The positions of the pillars are clearly visible as areas with no or few reconstructed hits. The fact that no or few clusters are reconstructed where the pillars are located can be explained as follows. Electrons that are generated above a pillar will end up on the pillar surface and, since the pillar material is insulating, stay there. This results in a charging up of the pillar surface and a deformation of the electric field close to the pillars. As a result, electrons generated above a pillar or close-by will be deviated and end up on the anode displaced from their original position (Fig. 6.2(a)). This is clearly visible in Fig. 6.2(b) where the number of reconstructed clusters as a function of their distance squared from the center of a pillar is shown. The excess at $r^2 \simeq 0.25$ mm^2 corresponds to tracks reconstructed close to the circumference of the pillars that in reality should have been reconstructed in the pillar area. This leads to a systematic position mismeasurement from tracks in the vicinity of a pillar and a degradation of the spatial resolution.

---

[1] Dupont ™Pyralux ® 1025, with a resistivity of a few 10^{16} Ohm·cm.

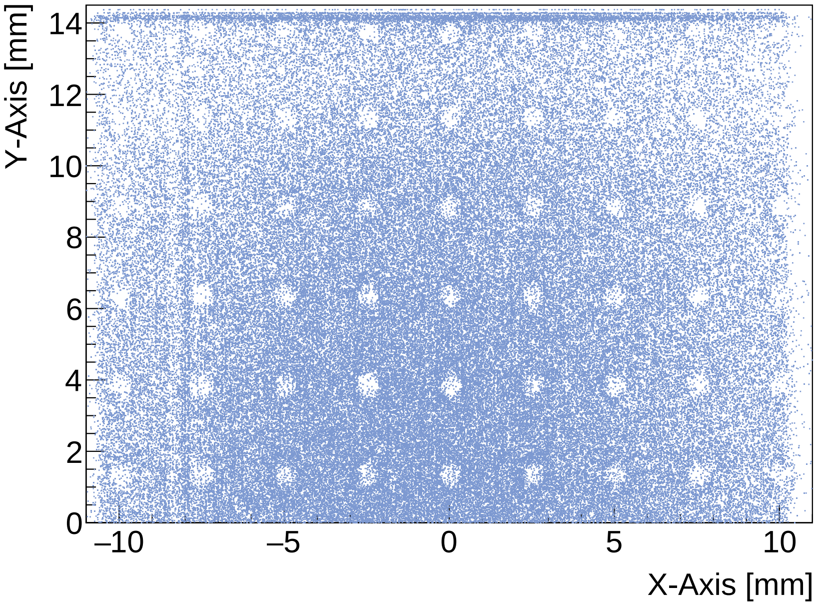

Figure 6.1: Cluster positions reconstructed in a two-dimensional Micromegas detector.

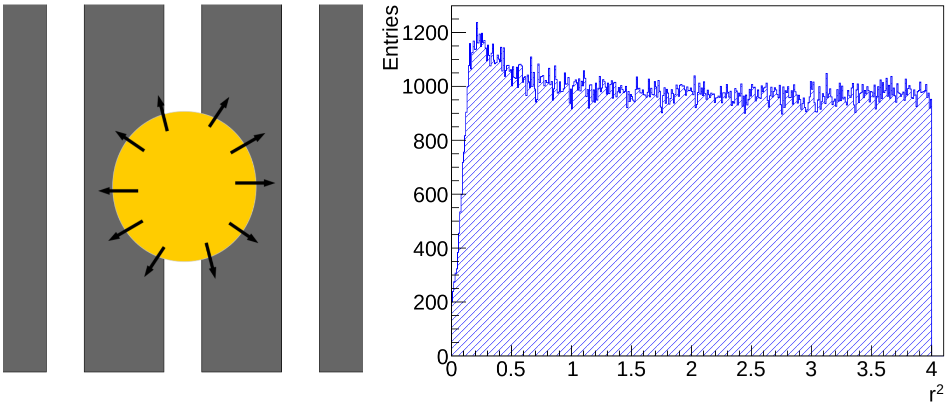

(a)

(b)

Figure 6.2: (a) Illustration of the displacement of electrons from their original path on top of a pillar to the anode strips in the vicinity of a pillar. The grey rectangles represent the resistive strips and the yellow circle represents a pillar. The black arrows represent the path of electrons. Not to scale; (b) Number of reconstructed clusters as a function of their distance from the centre of a pillar squared.

The choice of the pillars is, therefore, an important parameter in the design of the detectors.

In the first design of the readout boards for the NSW Micromegas detectors the size of the pillars was minimized to a diameter of 220 µm with a distance of 7 mm to avoid as much as possible this effect. However, during the quality control of the first readout boards produced in industry missing or weakly attached pillars have been observed [82]. To overcome this issue a new elongated pillar shape with a larger surface[2] and, therefore, better adhesion was proposed. To test the effect of the new pillar pattern in the track reconstruction, a resistive-strip bulk-Micromegas detector, called TLP[3] was built.

The detector was first characterized in the CERN RD51 [39]/Gas Detector Development (GDD) laboratory. Basic properties of the detector such as the gas gain, the ion backflow fraction and the charge-up (or charge accumulation) were measured. The performance of the detector was tested in a muon beam and its spatial resolution was compared with a Micromegas detector with circular pillars.

Part of the following studies have been published in Ref. [83].

6.1 Detector Description

The TLP detector is a resistive-strip bulk-Micromegas with the mesh embedded in the pillars. It has an active area of 10×10 cm^2 with 256 strips in total. The strips have a width of 300 µm and a pitch of 400 µm.

The resistance of the resistive strips measured from the HV supply line to the end of the strips is ∼15 MΩ.

The micro-mesh is a woven stainless steel fabric with 18 µm diameter wires and 45 µm opening. The drift gap height is 5 mm. The drift electrode is made of a copper foil.

The active area of the detector was split in two sections with two different pillar shapes as shown in Fig. 6.3. In one region the detector features pillars with dimensions 2 mm × 0.2 mm with 4.8 mm pitch. In the other region the pillars extend over the full width of the detector (100 mm × 0.2 mm). They cover approximately 2% and 4.8% of the active area, respectively. In both regions, the distance between two consecutive pillar rows is 4.2 mm. In the region, with the shorter pillars the next row of pillars is shifted by 2.4 mm along the strip direction. The height of the pillars is 192 µm[4]. The pillars run perpendicular to the readout and resistive strips.

---

[2] For the NSW Micromegas detectors the pillars have dimensions 1 mm × 0.2 mm with 7 mm pitch.

[3] TLP stands for Test Long Pillars

[4] In the bulk Micromegas detectors the pillars are made of three layers of insulating material with a thickness of 64 µm each. Two of these layers (128 µm) form the pillars in the amplification region, then the mesh is placed on top and the remaining 64 µm layer is placed on top of the mesh.

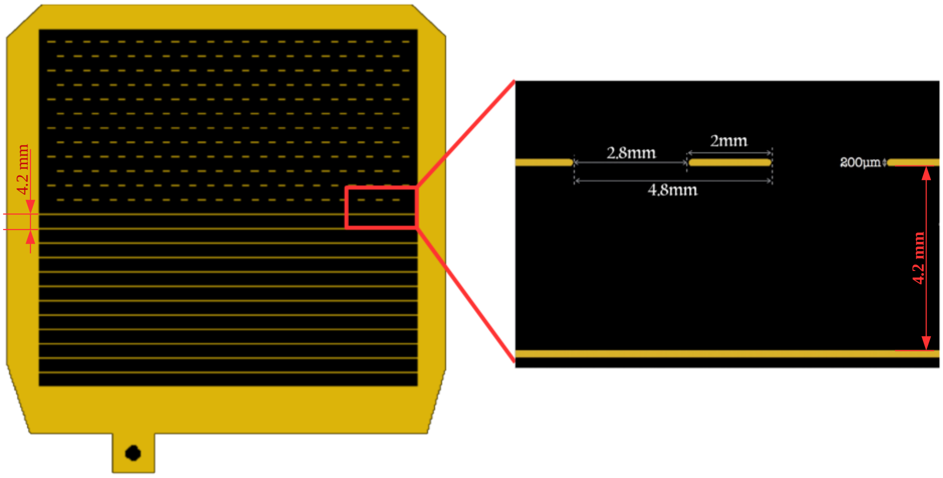

Figure 6.3: Schematic view of the active area of the TLP detector showing the pillar arrangement.

6.2 Detector Characterization

For the characterization of the detector 5.9 keV photons from a ^{55}Fe source and 8 keV photons from a Cu X-ray gun have been used.

6.2.1 Experimental set-up

To study the gain and the charge-up of the detector the signal from the mesh was read out with a picoammeter[5] and a multi-channel analyser (MCA)[6]. For the ion backflow studies the signal from the drift electrode was also read out with an additional picoammeter. The experimental set-up used for these studies is shown in Fig. 6.4. The signal from the mesh was first sent to a pre-amplifier[7]. One of its outputs was connected to a picoammeter to measure the current from the mesh. The other output was connected to an ORTEC 474 amplifier. The output of the amplifier was split in two. One output was connected to the MCA in order to measure the energy of the gammas. The other output was connected to a scaler[8] to measure the rate of the converted gammas. The current between the resistive strips and the ground was monitored through the analogue output of a CAEN N471A high voltage power supply by a multimeter. For the IBF studies, the drift electrode (cathode) was connected to a second picoammeter.

The detector was continuously flushed with Ar:CO$_2$ 93:7 at ~5 L/h.

---

[5] Keithley 6487

[6] Amptek® MCA-8000D

[7] ORTEC 142

[8] This connection was realized through the LRS Model 428A Linear Fan-In Fan-Out, and a ORTEC 935 quad constant fraction discriminator (CFD). The scaler is the CAEN module N145 quad scaler and preset counter-timer.

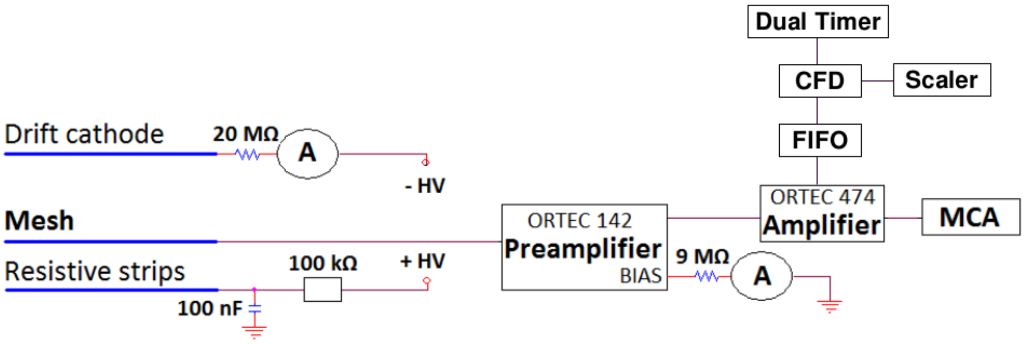

Figure 6.4: The experimental set-up used to characterize the TLP detector.

6.2.2 Gas Gain

The gain has been measured with the ^{55}Fe source. Figure 6.5 shows an example of the photon energy spectrum of the ^{55}Fe source. Here, the main emission line of the ^{55}Fe at 5.9 keV is around 4000 ADC counts while the Ar escape peak can be seen around 2000 ADC counts.

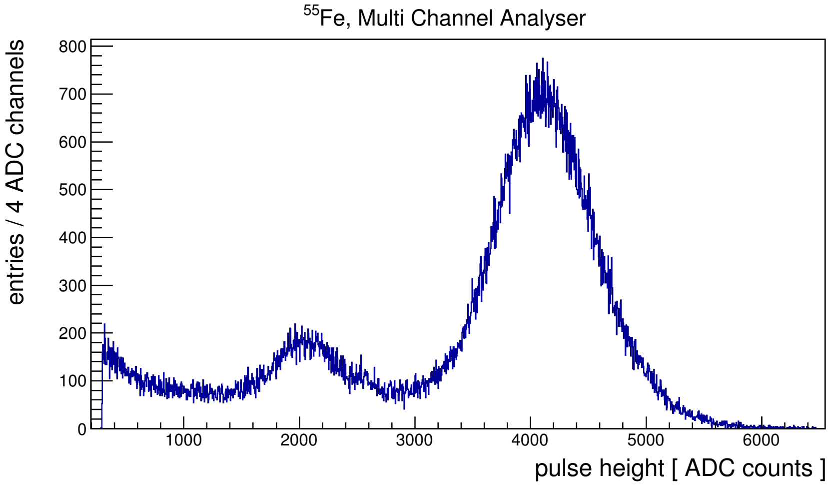

Figure 6.5: Photon energy spectrum of the ^{55}Fe source.

The effective detector gain is defined as the ratio between the number of electrons at the end of the amplification process and the number of produced electrons in the drift region. The gain (G) of the TLP detector was determined by measuring the mesh current (I) using the following equation:

$$G = \frac{I}{f \cdot n_\mathrm{e} \cdot q_\mathrm{e} \cdot t} \tag{6.1}$$

where f is the rate of gamma interactions[9], n_e is the average number of ioniza-

---

[9] From the ^{55}Fe source that was used for this measurement the rate was ∼2 kHz.

tion electrons per conversion, q_e is the electron charge, and t is the transmission coefficient[10].

The average number of ionization electrons (n_e) was estimated from the photon energy spectrum of the ^{55}Fe source using the following formula:

$$n_\mathrm{e} = \frac{\overline{ph} \cdot N_\mathrm{p}}{ph_{5.9}} \tag{6.2}$$

where $\overline{ph}$ is the mean pulse height determined from averaging over the pulse height distribution and $ph_{5.9}$ is the pulse height of the dominant 5.9 keV line, determined with a Gaussian fit. The number of primary electrons produced at this dominant line (N_p), for the Ar:CO_2 93:7, is calculated as:

$$N_\mathrm{p} = \frac{5900\ \mathrm{eV}}{W_\mathrm{Ar}} \cdot 93\% + \frac{5900\ \mathrm{eV}}{W_{\mathrm{CO}_2}} \cdot 7\% = 223 \tag{6.3}$$

where the averagy energy ($\mathrm{W_i}$) to produce an electron-ion pair in a gas mixture is $\mathrm{W_{Ar}} = 26$ eV and $\mathrm{W_{CO_2}} = 34$ eV (see Table A.1).

The transmission coefficient (t) has been determined in two steps. The relative transmission coefficient can be extracted from Fig. 6.6(a). It shows the detector response as a function of the field ratio ($\mathrm{E_{ampl}/E_{drift}}$) at a fixed amplification field of 40.6 kV/cm. The 5.9 keV peak position (corresponding to the collected charge) first rises with the field ratio as the collection efficiency improves[11]. The maximum is reached at 67.6 which corresponds to the drift field of 0.6 kV/cm. For higher field ratios the position decreases slightly. This can be explained by the electron attachment to oxygen contamination which leads to small electron losses. The absolute value of the transmission coefficient has been measured with a different Micromegas detector [40][12]. It is 0.96 for our mesh and 0.6 kV/cm drift field.

Figure 6.6(b) shows the gain as a function of the amplification voltage at a drift field of 0.6 kV/cm. We see the expected exponential behaviour. A gas gain of 10^4 is reached for an amplification field of 41 kV/cm, corresponding to 525 V HV at the resistive strips.

---

[10] The term transmission coefficient includes the fraction of ionization electrons that are transferred through the micro-mesh (transparency) and the probability of charge recombination (or attachment) in the drift region.

[11] As the field ratio decreases below the maximum more and more electric field lines from the drift region end on the mesh instead of reaching into the amplification region, thus more electrons are lost on the mesh.

[12] The experimental set-up used for these studies is similar to what was described in Section 6.2.1. More details can be found in Ref. [40]. In this case the detector was irradiated with a Cu X-ray gun.

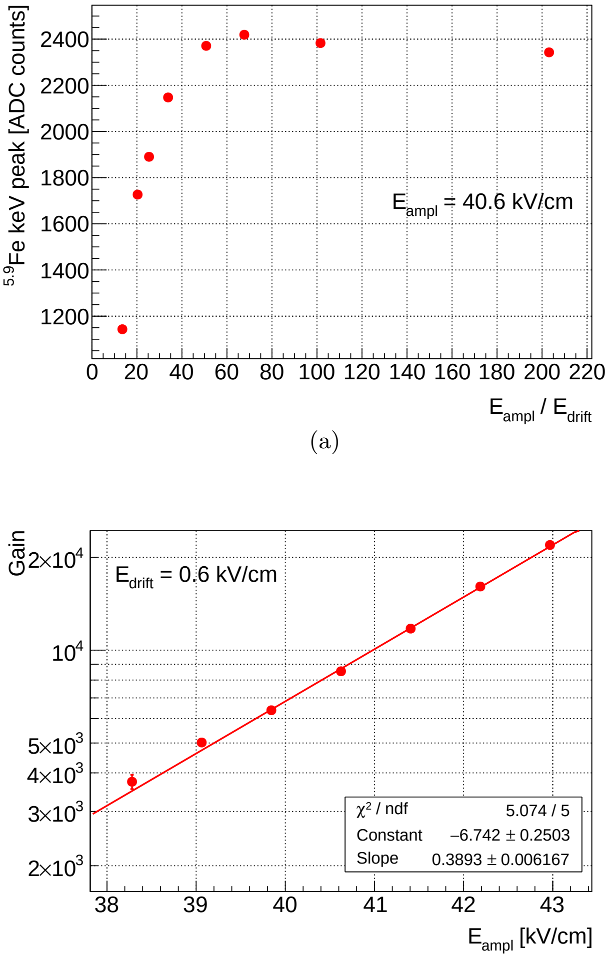

(a)

(b)

Figure 6.6: (a) Detector response as a function of the drift field at a fixed amplification field of 40.6 kV/cm; (b) Gas gain as a function of the amplification field at fixed 0.6 kV/cm drift field.

6.2.3 Ion Back-flow

Ion back-flow (IBF) is one of the effects limiting the operation of a gas detector at very high rates. The ion back-flow fraction is defined as the fraction of all positive ions produced in the avalanche that traverse the mesh and flow back to the cathode. The back-flowing ions create space charge which disturbs the electric field in the drift region locally. This can affect the drift behaviour of the electrons from a later track. The IBF is calculated as the ratio of the current on the drift electrode (I_D) and the sum of the currents at the drift electrode and the mesh (I_M):

$$IBF = \frac{I_D}{I_D + I_M} \tag{6.4}$$

For this measurement, an intense ^{55}Fe source was used creating an event rate of approximately 50–70 kHz over an area of approximately 1 cm^2. The amplification field has been kept constant at 39.8 kV/cm while the drift field has been varied from 0.2 to 0.6 kV/cm (Fig. 6.7). The IBF increases when the ratio between the amplification and drift field decreases. Generally speaking, a lower field ratio leads to a configuration of the electric field around the mesh that permits an easier passage of ions through the mesh. With the standard operating parameters the IBF is of the order of 2%.

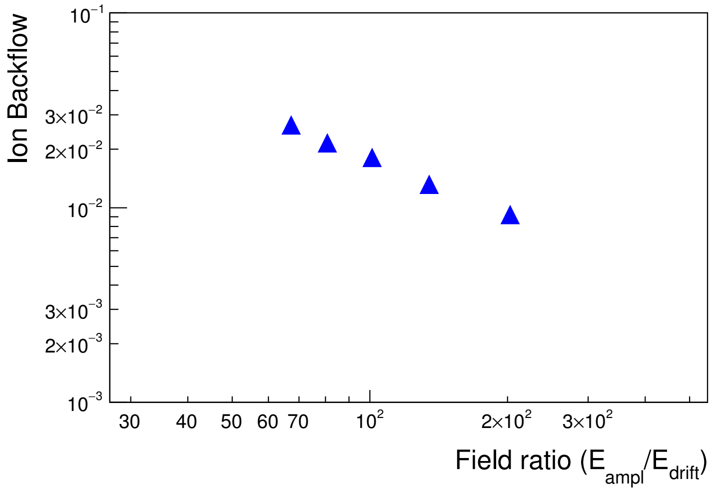

Figure 6.7: The ion backflow fraction as a function of the ratio between amplification and drift field.

6.2.4 Influence of the pillars on the detector response

The influence of the pillars on the detector response was measured with a Cu X-ray gun. Figure 6.8 shows the top view of the set-up. The detector is mounted on a frame that can move in three directions: along the direction of the X-rays (z-direction) and perpendicular to the direction of the X-rays on the transverse plane (x-y plane). Two Newport ® SM Vernier Micrometers are used to position the detector with a precision of 10 µm.

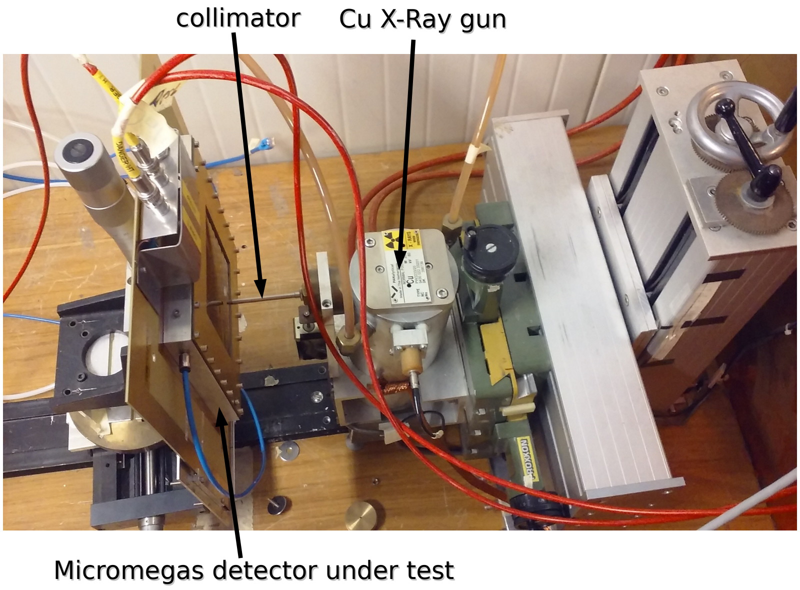

Figure 6.8: Photo of the TLP detector with the Cu X-ray gun.

For these studies, a 10 cm long collimator with an aperture of 1 mm diameter was used. The detector was positioned as close as possible to the head of the collimator. The tube current was set to 30 μA and the photon conversion rate was ∼ 6 kHz. The detector was operated at an amplification voltage of 520 V and at a drift field of 0.6 kV/cm. Figure 6.9 shows an example of the photon energy spectrum. Here, the main emission line is around 1010 ADC counts while the Ar escape peak can be seen around 700 ADC counts.

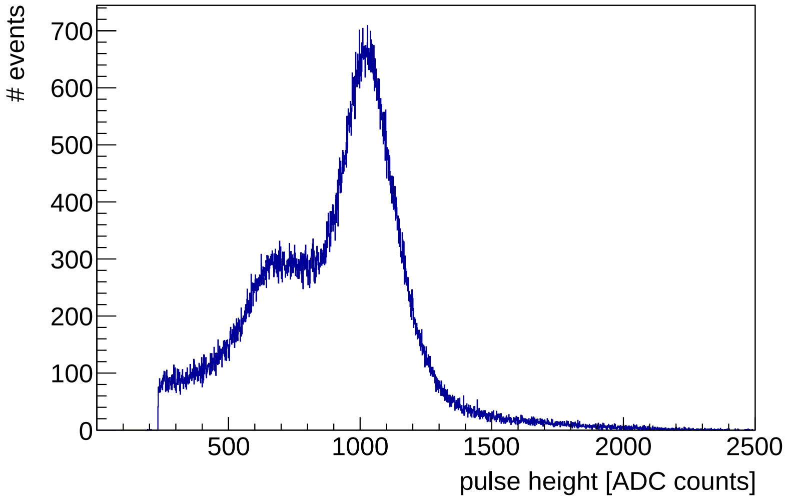

Figure 6.9: Cu X-ray photon energy spectrum.

To measure the irradiated area on the detector, data were recorded with the APV-25 chip and the SRS system (see Appendix E). Figure 6.10(a) shows the charge as a function of the strip number for a single gamma conversion in the gas giving signals in eight strips. Figure 6.10(b) shows the same distribution for all converted gammas from the X-ray gun with a 1 mm diameter collimator. The area of irradiation is ∼3.2 mm, much larger than the aperture of the collimator and comparable to the range of strips for a single photon conversion. This suggests that the size of the irradiated area is dominated by the track length induced by an 8 keV photon in the gas[13] and can not be reduced.

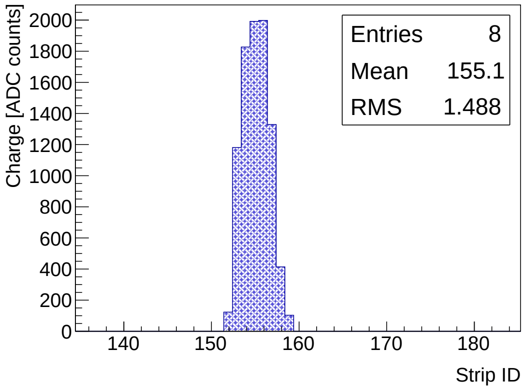

(a)

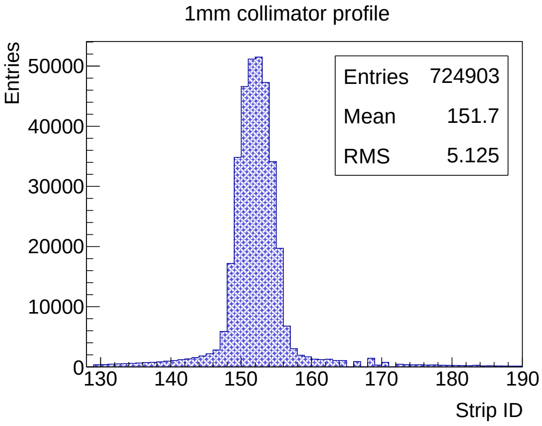

(b)

Figure 6.10: (a) Charge as a function of the strip number for a single event; (b) Intensity profile as a function of the strip number for a collimated (1 mm) X-ray beam.

Figure 6.11(a) shows the layout of the pillars on the TLP detector. Starting at an arbitrary position we irradiated the detector in a scan across 8 mm passing

---

[13] The track length of an 8 keV electron in argon is ≃2 mm.

over two pillars (red line in Fig. 6.11(a)). Figure 6.11(b) shows the recorded mesh current as a function of the position. Each 30–100 seconds the detector was moved by 100 μm. The position of the pillars are clearly visible in the regions where the current is ∼1 nA. The current on top of and close to the pillars is 15–20% lower with respect to the current measured in between the pillars.

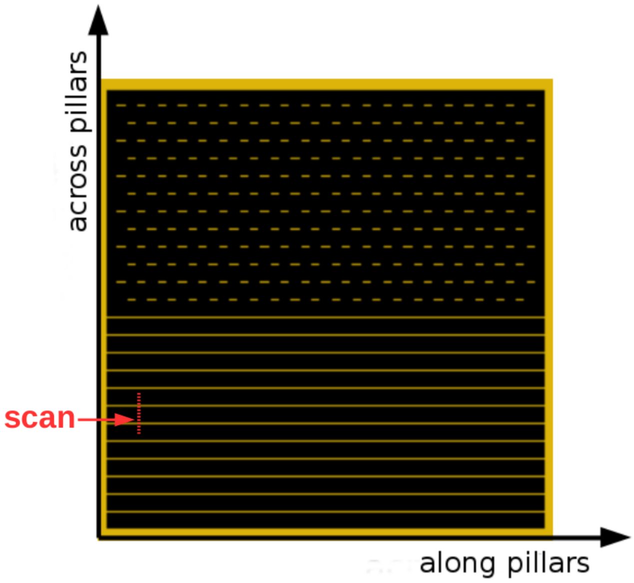

(a)

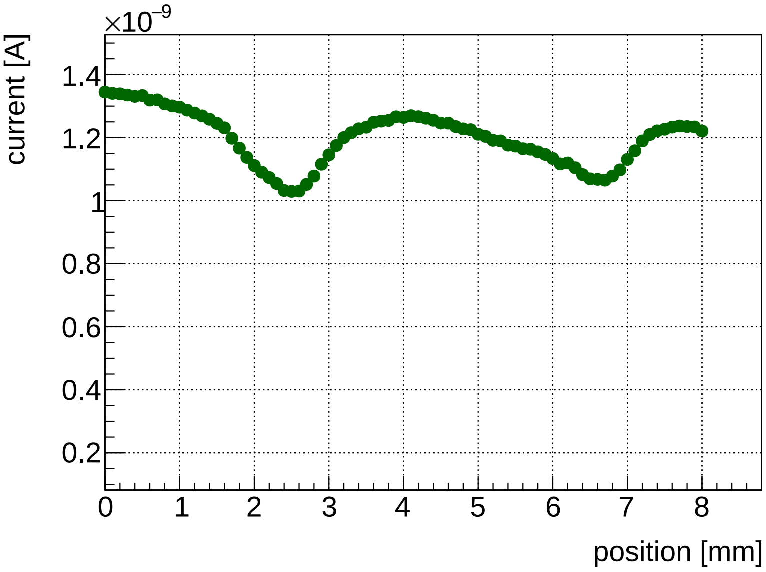

(b)

Figure 6.11: (a) Pillar layout. The red dashed line indicates where the scan was performed; (b) Mesh current as a function of the position.

Figure 6.12 shows the MCA spectra at different positions. Far away from the pillar we observe the expected spectrum with the main and the escape peak well separated (Fig. 6.12(a)). Close to the pillar the shape of the spectrum changes and on top of a pillar the Ar escape peak is no longer distinguishable (Fig. 6.12(b)-6.12(d)). The fact that the spectrum gets worse close to the pillar is due to electrons that are lost and not amplified.

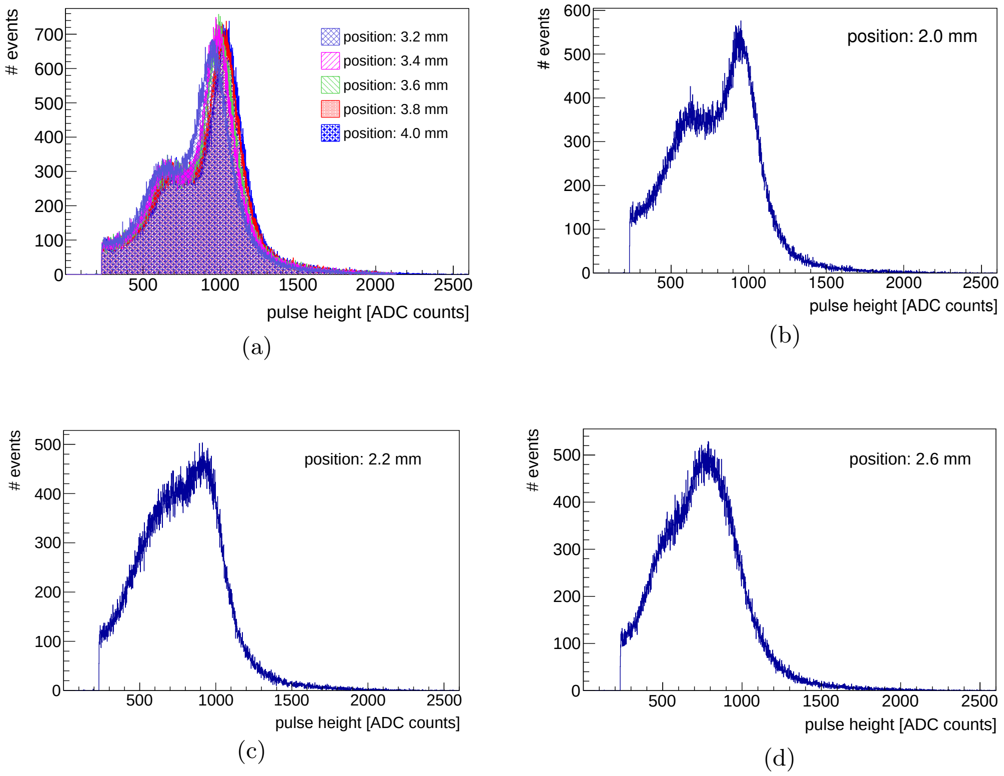

(a)

(b)

(c)

(d)

Figure 6.12: Cu X-ray photon energy spectra (a) far away from the pillar at the positions 3.2 mm, 3.4 mm, 3.6 mm, 3.8 mm, and 4.0 mm; close to a pillar in positions (b) 2.0 mm, (c) 2.2 mm and (d) 2.6 mm.

Another effect that we see when the X-ray gun approaches a pillar, is a slow increase of the current with time within each single measurement as shown in Fig. 6.13(a). Here the current is shown as a function of position and time. The increase is marked with red lines in a few measurements. Figure 6.13(b) shows the development of the current as a function of time for a single position close to a pillar. One observes a fast drop of the signal (charge-up effect, see below) but then a slow increase of the current which stabilizes after a few minutes. The increase of the current in this case from t=7835 s until it reaches a stable value is 4.5 %.

The drop of the current if the X-ray beam hits close to or on the pillars and the slow increase of the current when it approaches the pillars is not yet fully understood.

It is most likely related to the charging up of the pillar surface above the mesh[14]. This in turn leads to a distortion of the electrical field lines and an increase of the electric field close to the pillars (see Fig. 6.15(a)–6.15(c)). The latter leads to a reduction of the mesh transparency and could explain the lower currents close to the pillars.

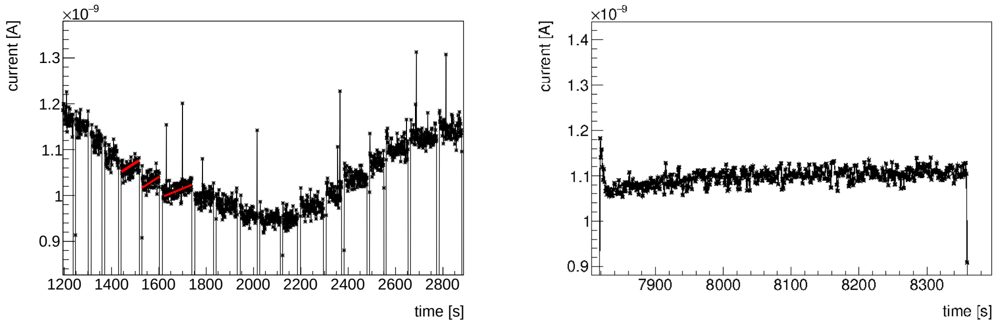

(a) (b)

Figure 6.13: (a) Mesh current as a function of time close to the first pillar; (b) Increase of the current on top of a pillar.

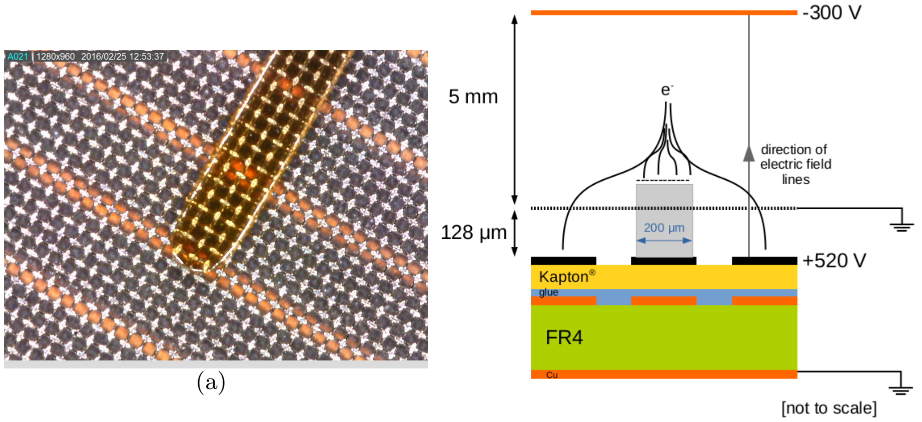

(a) (b)

Figure 6.14: (a) Photo from a microcamera of the TLP detector showing the mesh, a pillar, the resistive strips which are black colored and the readout strips which are orange coloured. The mesh is embedded in the pillars; (b) Sketch of the electron path (black curly lines) on top of a pillar.

---

[14] In the bulk-Micromegas detectors the mesh is embedded in the pillars (Fig. 6.14(a)). An extra 64 µm layer of the dielectric pillar material sits on top of the mesh as shown in Fig. 6.14(b).

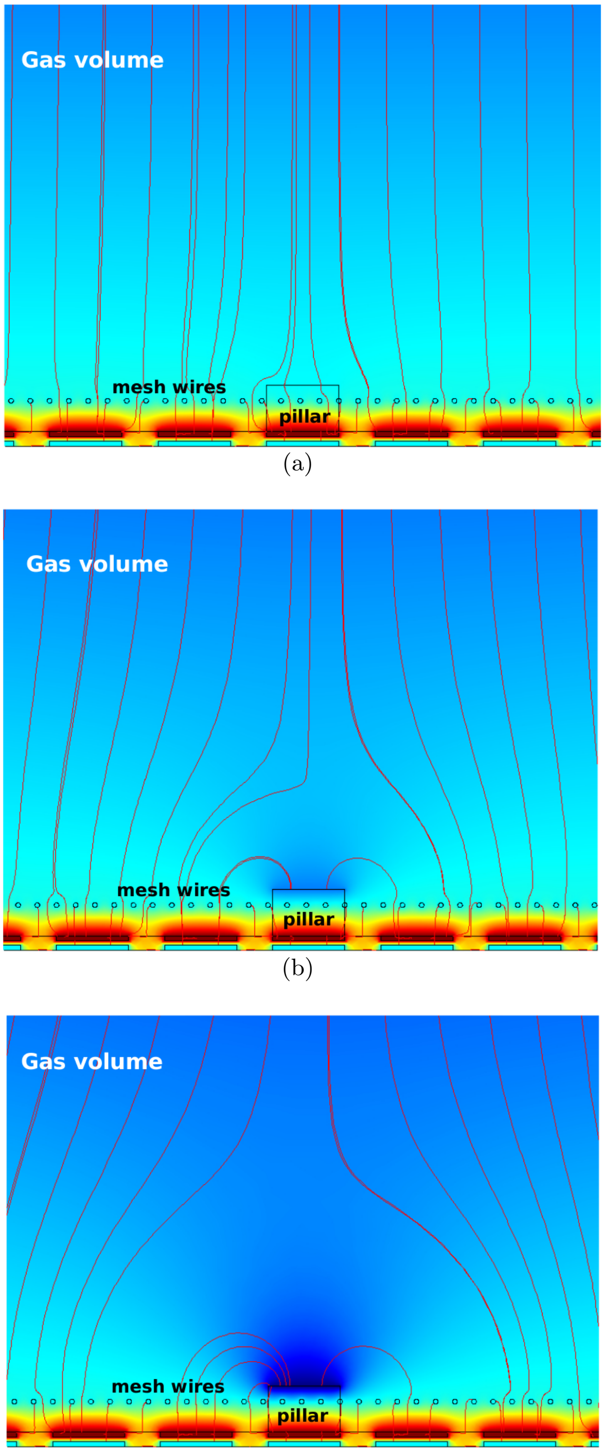

(a)

(b)

(c)

Figure 6.15: Electrical field strength and field lines (not all shown here) in the vicinity of a pillar when (a) 0 V, (b) -100 V and (c) -300 V has been applied to the extra 64 μm layer of the pillar material sitting on top of the mesh (Courtesy of F. Resnati and J. Samarati, simulation with COMSOL Multiphysics®)

To summarize, the pillars affect the detector response. How this affects the detector performance will be discussed in Section 6.3.

6.2.5 Charge-up

The charge accumulation or charge-up is well-known in detectors containing dielectric materials. It is coming from electrons and ions liberated in the amplification process that are then collected on dielectric surfaces. In Micromegas detectors, the electrically insulating material that is used for the pillars, the Kapton ® substrate that is used between the copper and the readout strips, and the PCB (FR4) are examples of dielectric materials.

The charge-up was measured with the Cu X-ray gun with the same collimator and the same set-up as discussed in Section 6.2.4. Figure 6.16 shows an example of the charge-up. When the X-ray shutter is opened there is a maximum value (I_{max}) that the current reaches in the very beginning but it drops relatively fast until it reaches a stable value (I_{mean}). The relative current drop ($\frac{I_{max}-I_{mean}}{I_{max}}$) and the time that has elapsed to reach a stable current depends on the rate of the gamma interactions.

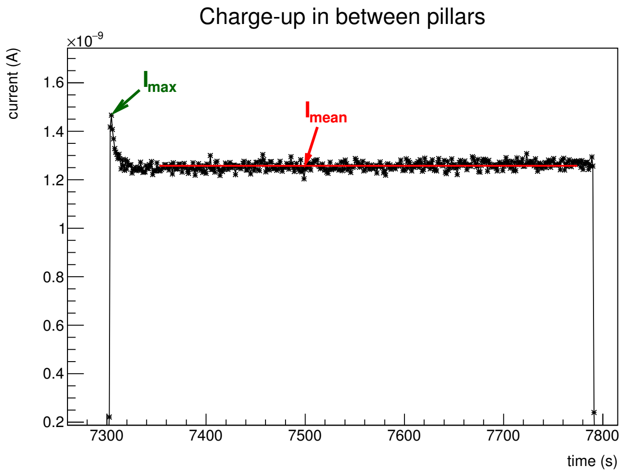

Figure 6.16: Charge-up measured in between pillars.

In the following, two measurements will be discussed. The charge-up as a function of the rate, and the charge-up when scanning along the pillar direction in between two pillars. These measurements were performed in the region of the 10 mm long pillars. The detector was operated at an amplification voltage of 520 V and at a drift voltage of -300 V.

(I) Charge-up as a function of the rate

A scan varying the tube current was performed in the same position on the detector in between two pillars to study the charge-up as a function of different rates. Figure 6.17 shows the currents acquired with the picoammeter. In the first measurement the tube current was set to 26 μA, in the second one to 18 μA and in the third one to 113 μA. Between two consecutive measurements the X-ray shutter was closed for at least 20 min in order to evacuate all charges from the detector.

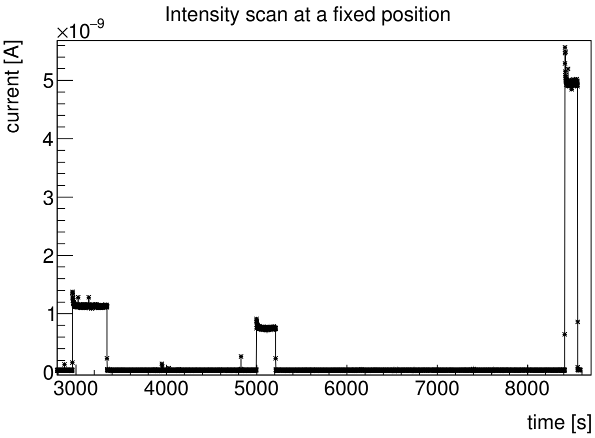

Figure 6.17: Intensity scan in the same position of the detector in between pillars.

The maximum and the mean currents as a function of rate are shown in Fig. 6.18. As expected, the currents increase linearly as a function of the rate. The interaction rates at which the measurements were taken are 3.7, 5.7, and 22.4 kHz over an impact area of ≃0.1 cm^2, much in excess of the maximum rate of 15 kHz/cm^2 expected for the NSW.

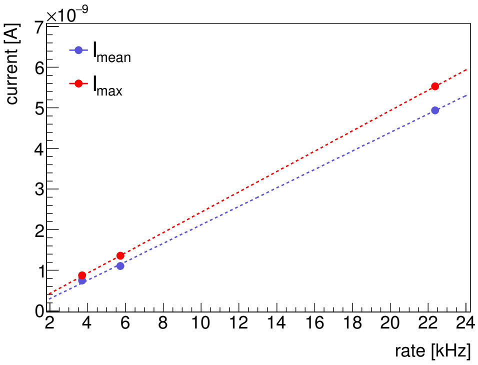

Figure 6.18: Maximum and mean currents as a function of the rate.

The relative current drop is shown in Fig. 6.19(a). It increases from ∼15% to 19% as the rate increases from 3.7 kHz to 5.7 kHz, but then it drops to 11% at ∼22 kHz. The same behaviour was also observed in similar measurements with other resistive and not resistive Micromegas detectors [84]. The time it takes the detector to reach a stable current after charging-up is 26 s at 3.7 kHz and decreases linearly to ∼4.5 s at the maximum rate of ∼22 kHz (Fig. 6.19(b)). The higher the rate the faster the detector reaches a stable current.

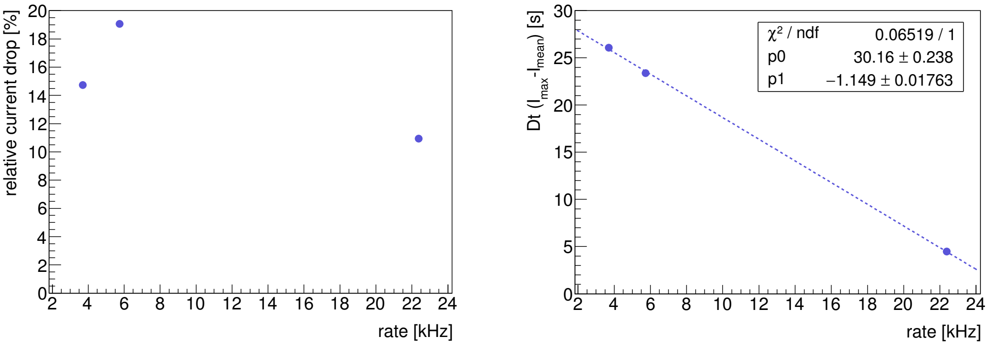

(a) (b)

Figure 6.19: (a) Relative current drop and (b) time elapsed until the current is stable, as function of the rate.

Figure 6.20 shows the MCA spectra for these measurements and the 8 keV peak position as function of the rate. The main peak moves to lower ADC counts as the rate increases. This behaviour is not caused by an ohmic voltage drop in the resistive strips as shown in Fig. 6.18. A plausible explanation is a bandwidth limitation in the charge removal from the resistive strips. A 5 MΩ strip resistance and a capacitance of 5 pF give an RC constant of 25 µs and a cut-off frequency of ≃6.4 kHz. This would result in a lower effective voltage and thus a lower gain.

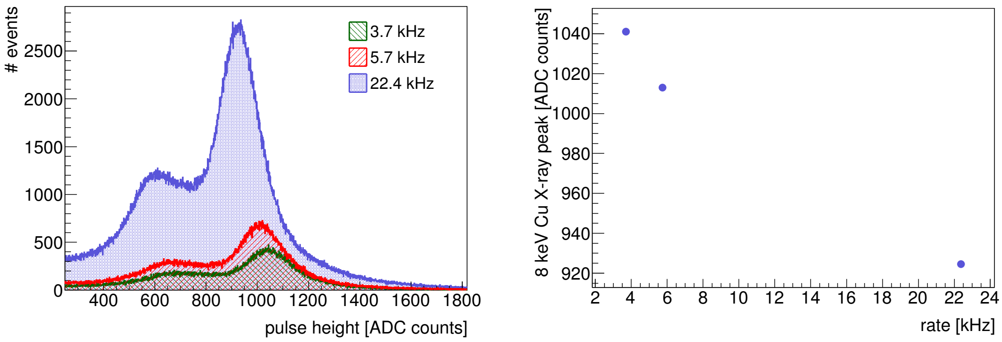

(a) (b)

Figure 6.20: (a) MCA spectra acquired for different rates; (b) 8 keV Cu X-Ray peak position as a function of the rate.

(II) Scan along pillar direction in between two pillars

The charge-up was also measured between two pillars as shown in Fig. 6.21(a). Seven measurements were taken at the same y-coordinate with a step of 4 mm in x. By this measurement we wanted to check if the charge-up is a local effect or it influences the detector few mm away. Figure 6.21(b) shows the currents acquired for each measurement as a function of time. Figure 6.22(a) shows the charge spectra for the seven measurements. The fact that the mean current is not the same for all position measurements is most likely the result of small gain variations and not important for these measurements. Figure 6.22(b) shows the mesh current divided by the rate, which is proportional to the gain, as a function of the position measurement. It is clearly seen that there are fluctuations around the mean value of 1.9×10^{-13}.

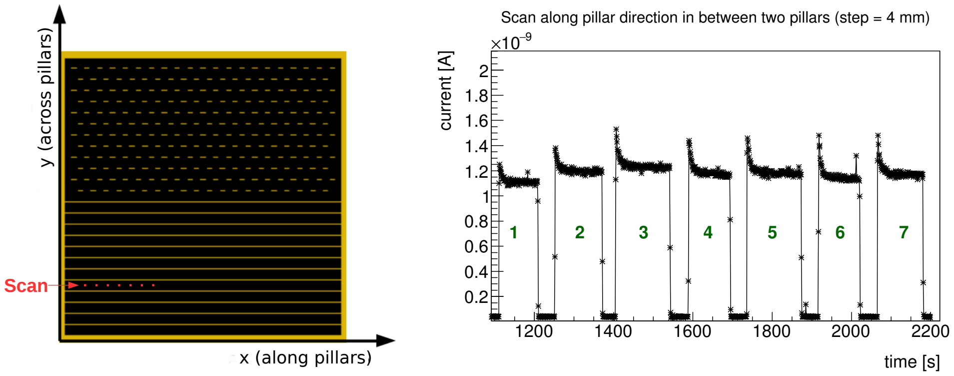

(b)

(a)

Figure 6.21: (a) View of the detector; the red dashed line indicates the position of the scan;(b) Mesh currents acquired in between two pillars as a function of time for seven different measurement positions; The distance between each measurement position is 4 mm.

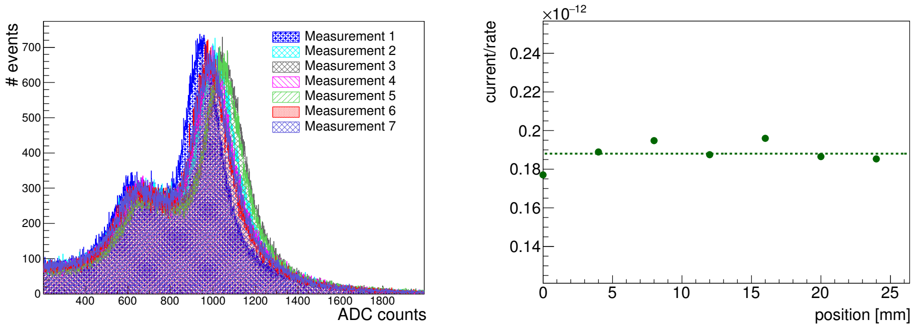

(a)

(b)

Figure 6.22: (a) MCA spectra acquired in between two pillars; (b) Current divided by the rate as a function of the position measurement.

The relative current drop for the measured rate (6 kHz) between I_{max} and I_{mean} is shown in Fig. 6.23(a) as a function of the measurement position, assuming that the first measurement starts at zero. It is on average 20%. The time it takes the detector to reach a stable current (mean current) after it is charged-up is 20±2 s.

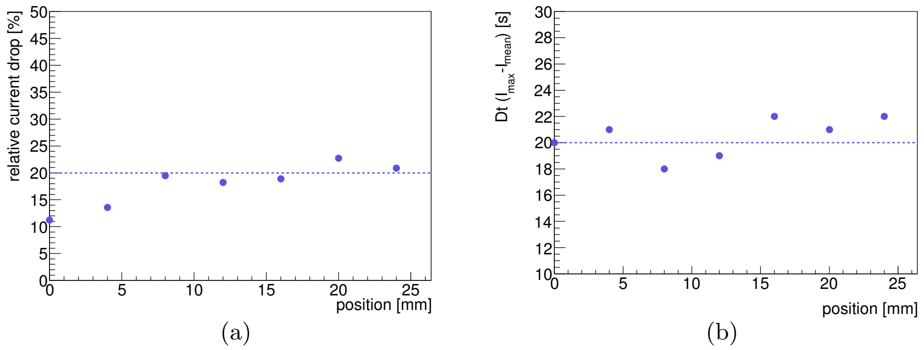

(a) (b)

Figure 6.23: (a) Relative current drop and (b) time elapsed until the current is stable, as a function of the distance.

The results of these measurements show that the charge-up is a local effect and does not affect the detector in the regions were it is not irradiated. Fig. 6.24 shows a series of measurements where the detector was each time moved by the indicated distance. The time between two measurements is 30–50 s. As long as we move away ∼2 mm from an area that was previously irradiated charge-up is observed. If instead we move in small steps very little or no charge-up is seen. This shows that the detector has some memory of the irradiation that is not present some mm away.

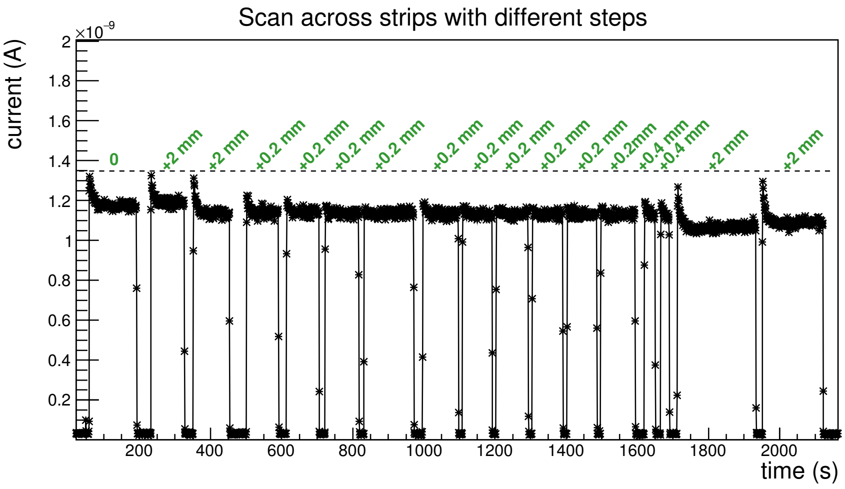

Figure 6.24: Currents acquired from a scan in between pillars with different steps. The distance of each step with respect to the previous measurement is indicated.

In summary, the charge-up depends on the particle rate. The higher the rate the faster the detector reaches a stable current. We have measured that the relative current drop increases from ~14.5% to ~19% as the rate increases from 3.7 kHz to 5.7 kHz, but then it drops to ~11% at ~22 kHz. The recovery time measured with several resistive and non-resistive Micromegas detectors is ~ 15 min [84]. The latter suggests that the charge-up is caused by dielectric materials. It is a local effect and does not affect regions that are not irradiated.

6.3 The effect of the pillars on the detector performance

The effect of the pillars on the performance of a resistive-strip Micromegas detector, i.e. efficiency and resolution, was studied in a 150 GeV/c muon beam at the Super Proton Synchrotron (SPS) at CERN. For these studies three different types of resistive-bulk Micromegas with dimensions 10×10 cm^2 were used. Figure 6.25 shows the experimental set-up. The so-called MM detectors are two-dimensional (X-Y). The X readout strips are perpendicular to the Y readout strips. The resistive strips are parallel to the X readout strips and perpendicular to the Y readout strips. These detectors are used as reference to reconstruct the position of the muons in the X-Y plane. The detectors called T4 and TLP4 are one-dimensional. The latter is as described in Section 6.1 with the two different regions of elongated pillars. The MM and T4 detectors have circular pillars. The characteristics of all detectors are listed in Table 6.1.

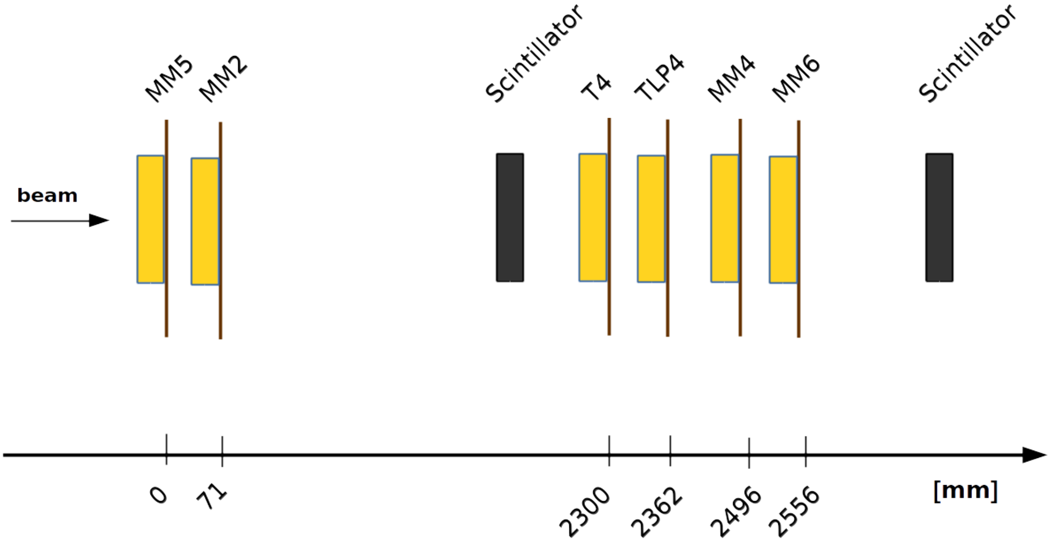

Figure 6.25: Experimental set-up at SPS, not to scale.

Table 6.1: Characteristics of detectors

Chamber name	**# of strips**	**Strip pitch [mm]**	**Strip width [mm]**	**Pillar type**	**Pillar area [mm^2]**	**Pillar pitch across strips [mm]**	**Pillar pitch along strips [mm]**
MM	368	0.25	0.15	circular	0.07 - 0.13	2.5	2.5
T4	256	0.4	0.3		0.07 - 0.13	2.5	2.5
TLP4	256	0.4	0.3	elongated	2 x 0.2	4.8	4.2
					100 x 0.2	-	4.2

In all detectors the height of the pillars below the mesh is ∼128 µm and the drift gap height is 5 mm. All detectors were operated with an Ar:CO$_2$ 93:7 gas mixture at NTP. The amplification voltage of the reference detectors was set to V_A = 550 V and the drift voltage to V_D = -300 V while for the T4 and TLP4 the amplification voltages range from $V_A = 480\,\text{V}$ to $V_A = 520\,\text{V}$, at a fixed drift voltage of $V_D = -300\,\text{V}$. The charge and time information were recorded with the APV-25 Front End ASICs and the RD51 Scalable Readout System (see Appendix E). The trigger was generated by the coincidence of the signals of the two 10×10 cm^2 scintillators (see Fig. 6.25).

Figure 6.26 shows a muon event where the charge and time for a single particle passing through all detectors is displayed. Clean hits are observed in each layer, characterized by a cluster of neighbouring strips[15]. A cluster of strips is defined by the following criteria:

- the strips are contiguous and not separated by more than one missing strip; this requirement is important to allow for faulty readout strips or problems in the readout electronics

- the sum of all strip charges (cluster charge) must be above a minimal threshold

The cluster position is defined as the charge-weighted average position of all strips of the cluster which is valid for perpendicular incoming particles.

---

[15] In the Y-coordinate of the MM detectors the signal is spread over many more strips than in the X-coordinate and the signal arrival time has typically a v-shape. This is because the Y-readout strips are perpendicular to the resistive strips and sample the charge ”decaying” along the resistive strips.

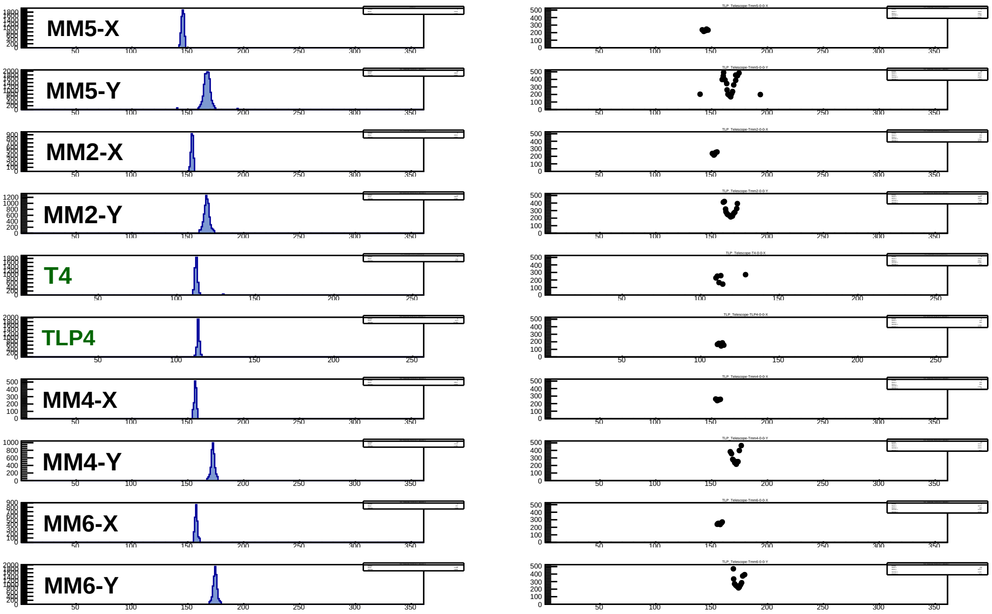

Figure 6.26: (left) Charge per strip and (right) signal arrival time, as a function of the strip position.

6.3.1 Detector alignment and rotation corrections

Prior to the track reconstruction, the detectors are aligned and corrected for relative rotations between them using single clusters per chamber as following. Starting with the first MM detector closest to the beam pipe (MM5), the difference between the cluster position of the MM5 detector and the cluster position of any other detector, called residual, is calculated. Figure 6.27 shows an example of the residual distribution between the clusters recorded in the MM5-X plane and the TLP4 detector, before and after the alignment correction. The distribution before the alignment correction is fitted with a Gaussian function. The mean value of the fit reveals the misalignment between the two chambers. Afterwards, when re-processing the data event by event this mean value is added to the cluster position in order to correct for the misalignment. After the alignment correction the distribution is well centred around zero. The cluster position of the three other MM detectors is corrected in the same way for both x and y coordinates.

To correct the relative rotations of the chambers around the z axis, the residual between the x coordinates of the cluster in the chamber to be corrected and in the reference chamber is plotted in a two-dimensional histogram as a function of the cluster position in y. Figure 6.28(a) shows, as an example, the residuals between the cluster positions in the MM5-X plane and in the TLP4 detector as a function of the cluster positions measured in the MM5-Y readout plane. The two-dimensional histogram is fitted with a linear function. If the two detectors were perfectly aligned the mean values of the residuals would be independent of y and the slope would be zero. Any non-zero slope indicates a rotation between the two chambers. Afterwards, when re-processing the data the cluster positions measured with the TLP4 detector are corrected, event by event, using the slope of the fitted line and the y position as measured in the MM5-Y plane (Fig. 6.28(b)).

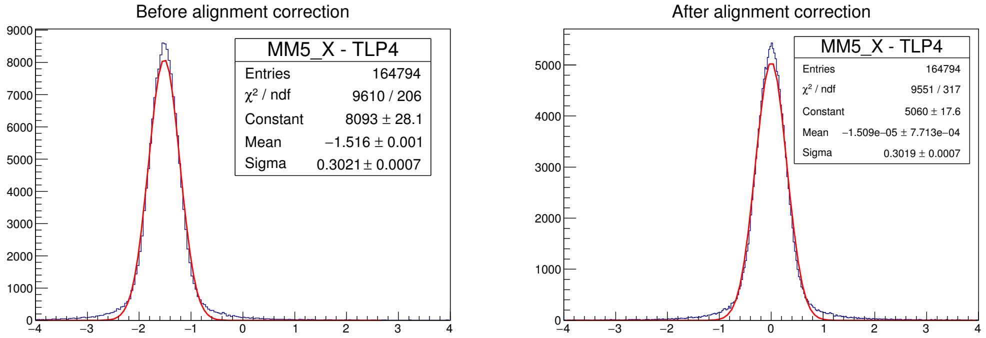

(a)

(b)

Figure 6.27: Residual distribution between the MM5-X plane and the TLP4 detector (a) before and (b) after the alignment correction.

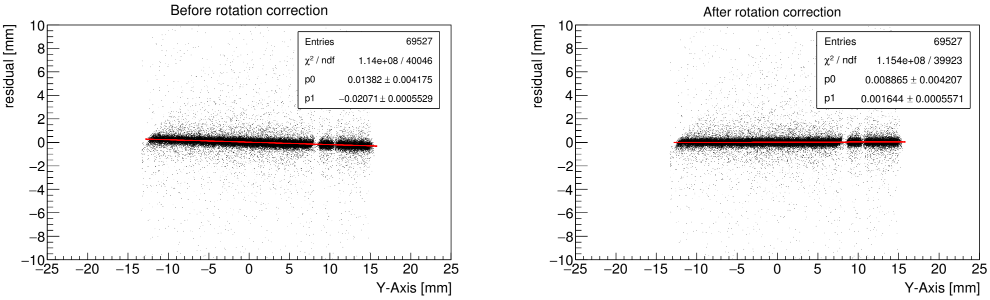

(a)

(b)

Figure 6.28: Residuals between the positions measured in the MM5-X plane and the TLP4 detector as a function of the y position in the MM5 detector (a) before and (b) after the rotation correction around the z-axis.

6.3.2 Track reconstruction

After the alignment and rotation corrections, the track of a muon is reconstructed using the four MM detectors. The z-axis is considered along the beam direction as shown in Fig. 6.25. The most upstream detector is considered to be in the position z=0. The distance between all chambers was measured during the installation of the set-up.

The selection of the reference tracks is as following. It is required that one and only one cluster is present in either of the two readout planes (x and y). For these events, tracks are then fitted separately in the x-z and y-z planes using the least-square method. Figure 6.29 shows an example of the particle position reconstruction in the x-z plane for a single event. Perpendicular tracks are afterwards selected by applying a cut in the reconstructed angle on both x-z and y-z planes of 0.02° (Fig. 6.30).

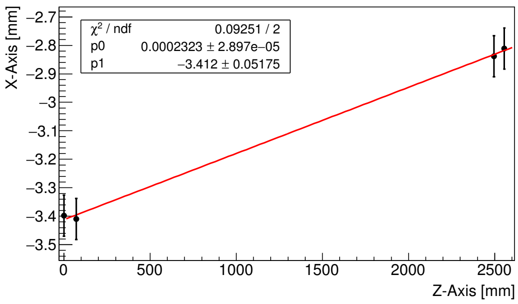

Figure 6.29: Track reconstruction in the x-z plane with the four MM detectors for a single track.

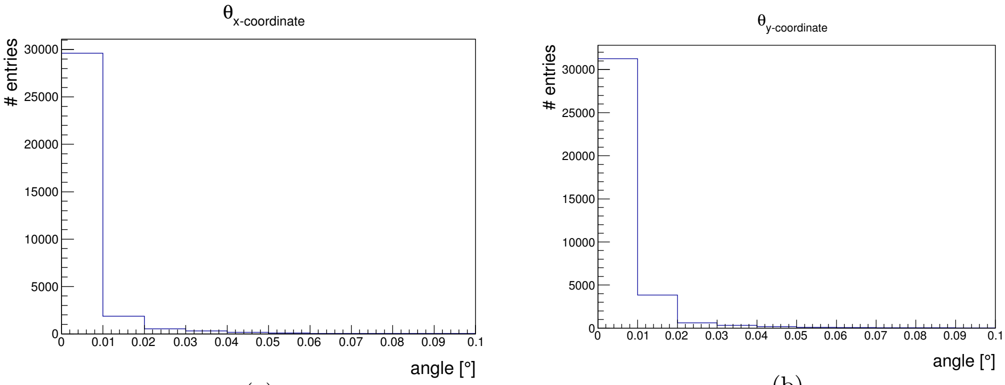

(a)

(b)

Figure 6.30: Reconstructed angle in the (a) x-z plane and in the (b) y-z plane.

The T4 and TLP4 detectors are considered as detectors under test. For these detectors the efficiency and spatial resolution was measured as a function of the amplification voltage and will be discussed in the following.

6.3.3 Efficiency measurements

To study the efficiency of the detectors under test, the tracking algorithm is applied for the prediction of the cluster position in these detectors. A cluster is defined as correctly reconstructed if its position is within 1.5 mm from the predicted position.

Figure 6.31 shows the track efficiency of the two detectors. The TLP4 detector shows a clear turn-on curve reaching 98% in the plateau region for $V_{\mathrm{A}} \geq 500\,\mathrm{V}$. For the T4 detector it seems that at an amplification voltage for $V_{\mathrm{A}} \geq 490\,\mathrm{V}$ the detector has already reached a plateau with an efficiency of ~97%.

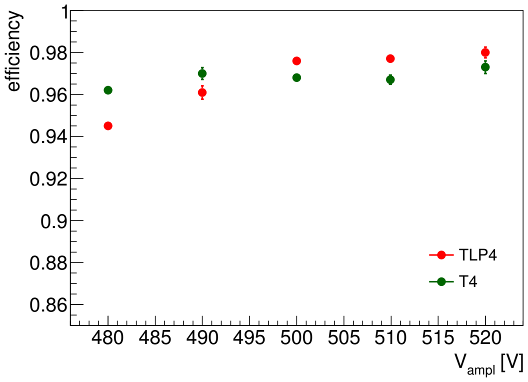

Figure 6.31: Track efficiency of T4 and TLP4 as a function of the amplification voltage.

The inefficiencies created by the pillars can be seen in Fig. 6.32 for the amplification voltage of $V_\mathrm{A} = 480\,\mathrm{V}$. Figures 6.32(a) and 6.32(b) show the efficiency as a function of the y position of the extrapolated reference tracks in the y-z plane for the TLP4 and the T4 respectively. Figures 6.32(c) and 6.32(d) show the inefficient areas in a two-dimensional representation where the extrapolated reference track positions in the x-z and the y-z plane for the TLP4 and the T4 detectors are shown. The TLP4 detector at $V_\mathrm{A} = 480\,\mathrm{V}$ reaches an efficiency of ∼95% in the positions located in between the pillars. In the region with the long pillars (100 mm × 0.2 mm), the efficiency in the position of the pillars is ∼50%, while in the region with the 2 mm × 0.2 mm pillars the efficiency is ∼80%. At the same amplification voltage, the T4 detector has reached an efficiency of ∼96% in between the pillars and ∼92% where the small circular pillars with 0.3–0.4 mm diameter are located.

However, as the amplification voltage increases and the detectors reach a higher efficiency the effect of the pillars becomes smaller. Figure 6.33 shows the same plots at $V_\mathrm{A} = 515\,\mathrm{V}$[16]. The TLP4 detector in between the pillars reaches an efficiency of ∼97%. The longest pillars with dimensions 100 mm × 0.2 mm create a lower efficiency of ∼80% while the shortest pillars of 2 mm × 0.2 mm create a lower efficiency of ∼90%. For the T4 detector at $V_\mathrm{A} = 515\,\mathrm{V}$ the effect of the pillars is no more visible.

In conclusion, when the detectors are operated at low HV (gain) the signals are too small. An example is shown in Fig. 6.34 where the cluster charge distribution for the TLP4 detector is plotted for hits in between the pillars and close to the pillars at $V_\mathrm{A} = 480\,\mathrm{V}$. In between the pillars the MPV is around ∼350 ADC counts while close to the pillars it is even lower with ∼250 ADC counts. In both regions, clusters with very low pulse height have been lost owing to the pedestal subtraction. This is the reason why the pillar pattern is more evident at low gain.

---

[16] The sample at $V_\mathrm{A} = 520\,\mathrm{V}$ is dominated by low statistics and for this reason it is not shown here.

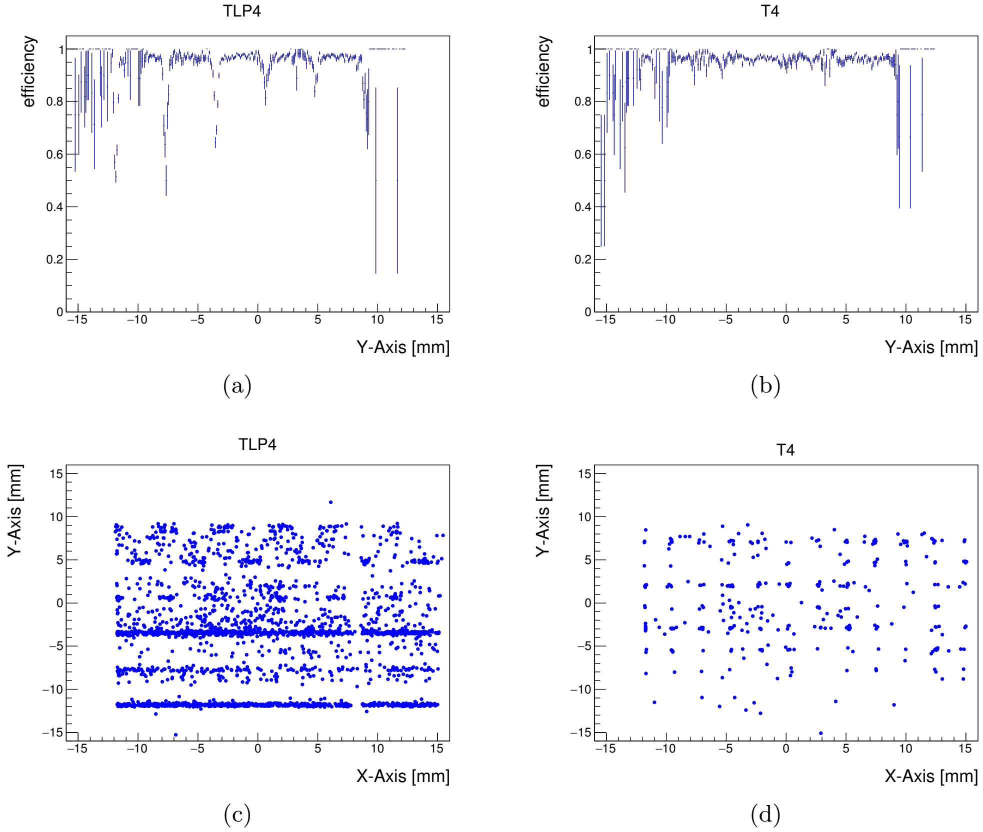

(a) (b) (c) (d)

Figure 6.32: Efficiency as a function of the reconstructed track position in the y-plane for the TLP4 detector (a) and the T4 detector (b) at an amplification voltage of $V_\mathrm{A} = 480\,\mathrm{V}$. Two-dimensional inefficiency map for the TLP4 detector (c) and the T4 detector (d) at an amplification voltage of $V_\mathrm{A} = 480\,\mathrm{V}$.

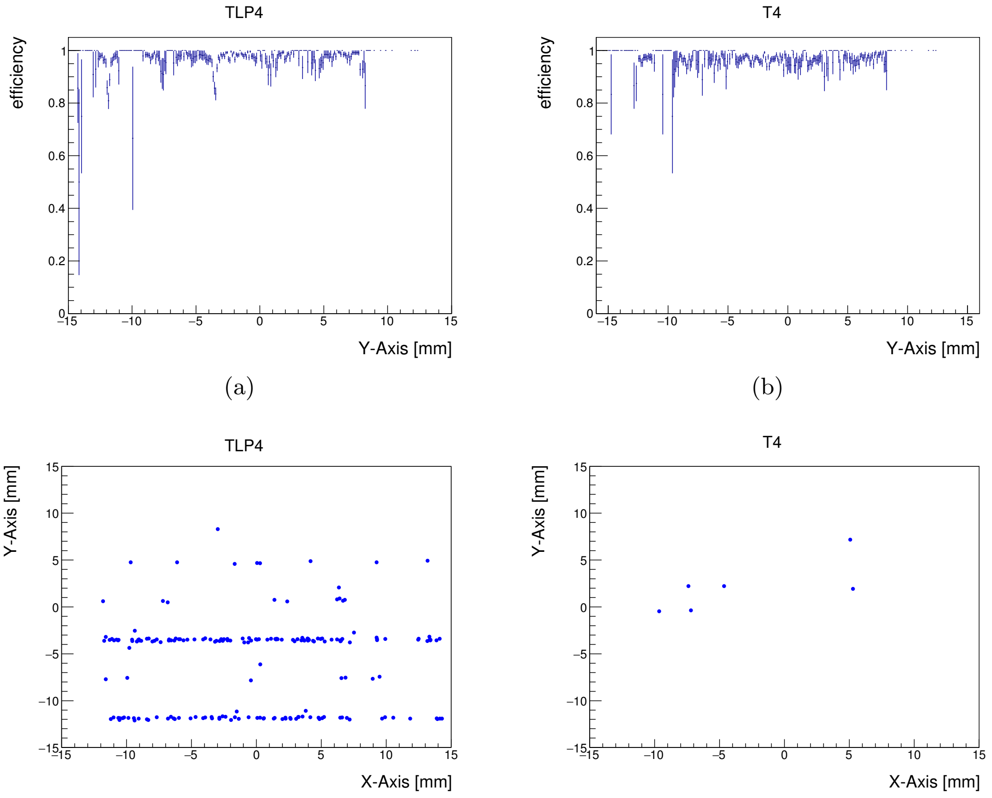

(a) (b)

(c) (d)

Figure 6.33: Efficiency as a function of the reconstructed track position in the y-plane for the TLP4 detector (a) and the T4 detector (b) at an amplification voltage of $V_\mathrm{A} = 515\,\mathrm{V}$. Two-dimensional inefficiency map for the TLP4 detector (c) and the T4 detector (d) at an amplification voltage of $V_\mathrm{A} = 515\mathrm{V}$.

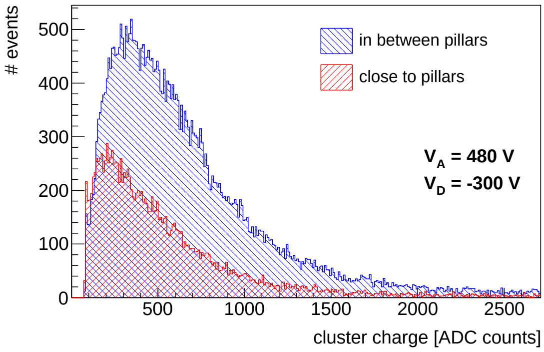

Figure 6.34: Cluster charge distribution from the TLP4 detector in between the pillars and ±1 mm from the center of the pillars in the region with the 100 mm × 0.2 mm pillars for $V_\mathrm{A} = 480\,\mathrm{V}$ and $V_\mathrm{D} = -300\,\mathrm{V}$.

6.3.4 Spatial resolution

To compare the spatial resolution of different detectors they should be operated at the same gain. Figure 6.35(a) shows an example of the cluster charge distribution of the muons as measured with the T4 detector at $V_A = 480\,\mathrm{V}$. This distribution is fitted with a Landau function in order to extract the MPV. The MPVs of the two detectors under test as a function of the amplification voltage are shown in Fig. 6.35(b)[17]. The two detectors have the same gain when they are operated at an amplification voltage difference of 20 V which corresponds to an amplification gap difference of 5 μm. Even if the two bulk detectors have been constructed in the same way, it seems that the embedded mesh on the T4 detector is at a lower distance from the anode than the TLP4. A plausible explanation for this observation could be related to the T4 pillar surface that is smaller than the TLP4 pillar surface; in the production process, during the stabilisation at high temperature, the mesh is sinking more into the coverlay material for the T4 detector than for the TLP4 detector. Another explanation could be small variations in the thickness of the coverlay foils that were used to produce the pillars.

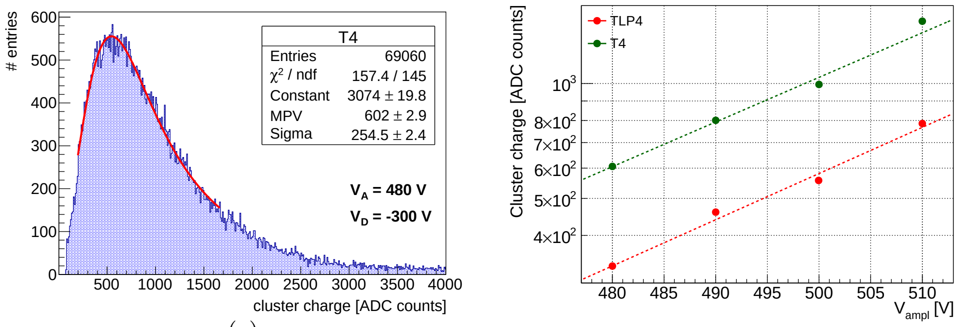

(a)

(b)

Figure 6.35: (a) Cluster charge distribution as measured with T4 at $V_A = 480\,\mathrm{V}$ and $V_D = -300\,\mathrm{V}$; (b) MPV of cluster charge distribution as a function of the amplification voltage for the T4 and the TLP4 detectors.

To determine the spatial resolution of the two detectors, the reference track is extrapolated to the respective detector positions in z. The predicted particle positions are compared with the measured positions. The difference of the two positions yields a distribution of residuals of width σ_{ex}; an example is shown in Fig. 6.36 for both detectors. The spatial resolution (σ_{SR}) of the detectors under test is calculated from this width and the track accuracy (σ_{track}) using the following equation:

$$\sigma_{\mathrm{SR}} \approx \sqrt{\sigma_{\mathrm{ex}}^2 - \sigma_{\mathrm{track}}^2} \tag{6.5}$$

---

[17] For higher amplification voltages the APV25 reaches a saturation (see Appendix E) and the cluster charge distribution cannot be fitted with a Landau distribution. For this reason larger HV points are not shown here.

The track accuracy is calculated from the spatial resolution of the reference detectors ($\sigma_{\mathrm{ref_i}}$). The latter has been determined by the geometric mean method [85]. More details concerning the determination of the spatial resolution can be found in Appendix F.

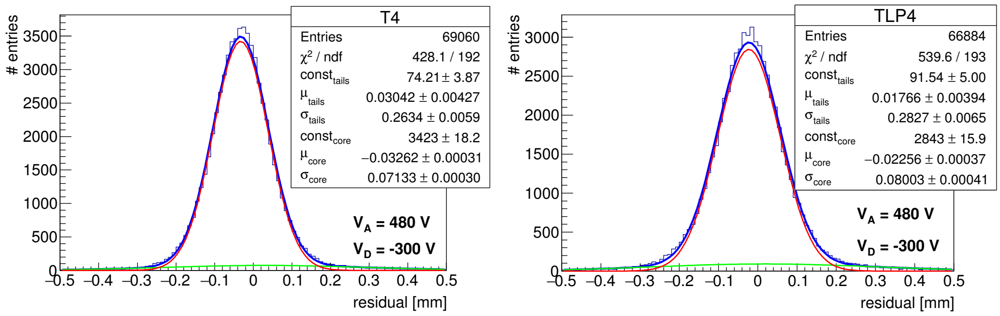

(a) (b)

Figure 6.36: Residual distribution of the predicted particle position and the measured position (σ_{ex}) for the T4 detector (a) and the TLP4 detector (b), at $V_{\mathrm{A}} = 480\,\mathrm{V}$ and $V_{\mathrm{D}} = -300\,\mathrm{V}$.

Figure 6.37(a) shows the spatial resolution calculated from Eq. 6.5 of the T4 and the TLP4 detectors, as well as the resolution of the TLP4 detector in the region with the 100 mm × 0.2 mm pillars and in the region with the 2 mm × 0.2 mm pillars as a function of the amplification voltage. For the TLP4 detector there is no essential difference between the two different pillar regions. Operated at the same gain the T4 has a better resolution than the TLP4 but the difference accounts only for $\leq$7 µm. Both detectors show a slightly improved resolution with increasing amplification voltage as expected. The track accuracy in the position of these detectors is shown in Fig. 6.37(b), it is ∼40 µm.

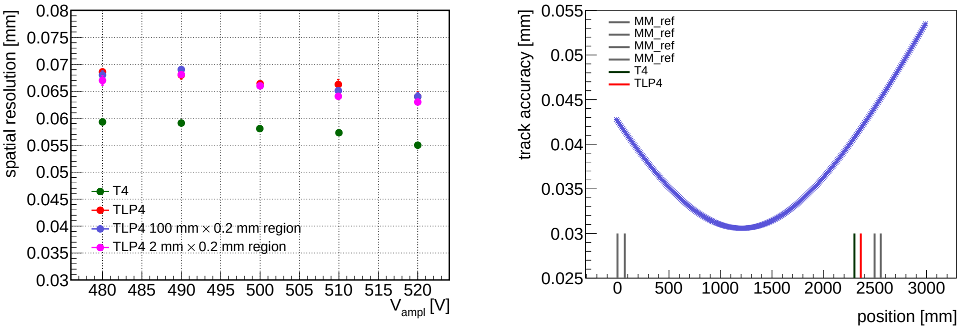

(a) (b)

Figure 6.37: (a) Spatial resolution of the T4 and the TLP4 detector as calculated with Eq. 6.5; (b) Track accuracy as a function of the position along the beam direction.

The effect of the pillars on the spatial resolution of the TLP4 detector has been measured as follows. According to Fig. 6.32(c) where the position of the pillars is more evident, the spatial resolution has been calculated in the regions lying in between the pillars and from the position of the pillars ±1 mm across the strips in the region with the 100 mm × 0.2 mm pillars and in the region with the 2 mm × 0.2 mm pillars. Figure 6.38 shows these distributions before the track accuracy has been subtracted in quadrature. The difference between the residuals close to the pillars and in between the pillars is $\leq$10 μm. 10 μm difference corresponds to an additional error of 40 μm in quadrature. This difference corresponds to tracks that have been reconstructed close to the circumference of the pillars that in reality should have been reconstructed in the pillar area.

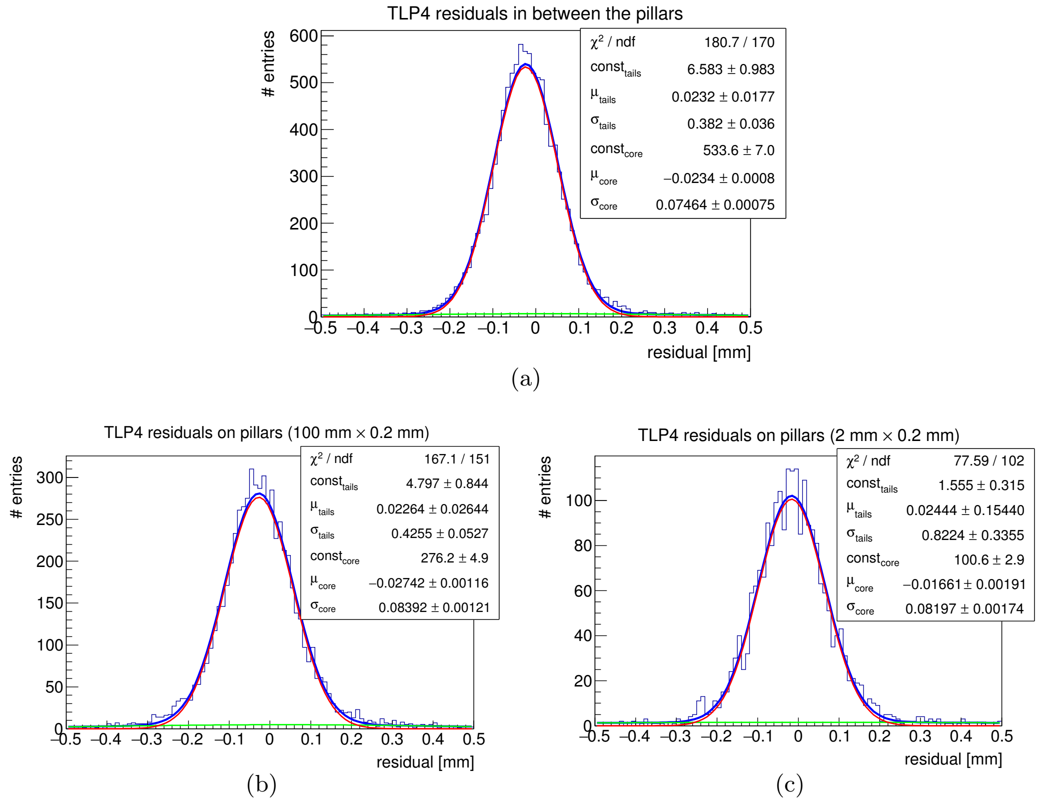

Figure 6.38: Residuals of the TLP4 detector (a) in between the pillars, (b) close to the pillars in the region with the 100 mm × 0.2 mm pillars and (c) close to the pillars in the region with the 2 mm × 0.2 mm pillars.

The same distributions have been calculated for the T4 detector using the pillar positions from Fig. 6.32(d). Figure 6.39 shows the residuals from the predicted and the measured position of the T4 detector in between the pillars and in a radial distance of 1 mm from the center of a pillar. Here the difference accounts only for 5 μm which corresponds to an additional error of 26 μm in quadrature.

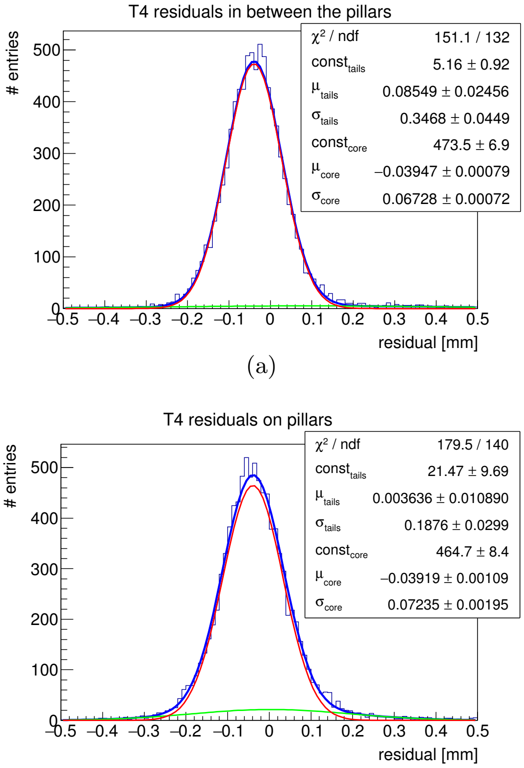

(a)

(b)

Figure 6.39: Residuals of the T4 detector (a) in between the pillars and (b) in a radial distance of 1 mm from the center of the pillars.

6.4 Conclusions

The insulating material of the pillars is charged up negatively deforming the electric field close to them. This leads to a systematic position mismeasurement of tracks in the vicinity of a pillar and a small degradation of the spatial resolution.

For the NSW Micromegas detectors, the initial shape of the pillars was circular with a diameter of 220 µm at a distance of 7 mm to reduce as much as possible these effects. However, during the quality control of the first readout boards produced in industry missing or weakly attached pillars have been observed. To overcome this issue a new elongated pillar shape with dimensions 1 mm × 0.2 mm with 7 mm pitch was proposed. These pillars are placed perpendicular to the strips to minimise as much as possible the impact on the detector performance.

The TLP detector was constructed to study the effect of the larger area of the elongated pillars on the detector performance. The active area of the detector was split in two sections with two different pillar shapes. The results of these studies show that the effect of the pillars on the detector efficiency is negligible when the Micromegas detectors are operated at high gain. The degradation of the spatial resolution introduced by the elongated pillar shape was measured to be $\leq$10 µm which corresponds to an additional error of 40 μm in quadrature.

X-Ray measurements performed with the Cu X-Ray gun have shown a reduction of the current on top of the elongated pillars of 15–20% with respect to the current measured in between the pillars. This suggests that electrons generated close to the pillars are lost. On the other hand, we saw that just on top of a pillar there is a slow increase of the current of $\simeq$ 5% until it reaches a stable value. The pillar in the beginning seems to charge-up negatively due to the first electrons that arrive creating a negative potential in the extra pillar material that sits on top of the mesh in the bulk-Micromegas detectors. This deforms the electric field in the vicinity of the pillars pushing away the electrons from the pillar. For the non-bulk Micromegas where the mesh touches the pillars when electric field is applied this phenomenon is not expected to be present.

In addition we studied the charge-up behaviour of the TLP detector. We saw that the charge-up depends on the particle rate. The higher the rate the faster the detector reaches a stable current. We measured that the relative current drop increases from $\sim$15% to 19% as the rate increases from 3.7 kHz to 5.7 kHz, but then it drops to 11% at $\sim$22 kHz. We demonstrated that it is a local effect and does not affect regions that are not irradiated. The exact working mechanism of the charge-up effect has not yet been fully understood. However, the effect is present in both resistive and non-resistive Micromegas [84]. The relatively long recovery time of $\sim$15 min [84] suggests that the phenomenon is caused by dielectric materials which charge up.

Summary and Conclusions

In this thesis, the characterization of the first resistive-strip Micromegas quadruplet prototypes, the characterization of the resistive protection scheme used in the ATLAS NSW Micromegas detectors, and the influence of the pillars on the detector response and performance were presented. The summary and conclusions of each study are given in the following.

The first medium-size resistive-strip Micromegas quadruplet prototypes: In 2014, two resistive-strip Micromegas quadruplet prototypes have been built at CERN to evaluate detector design, construction and performance issues relevant for the construction of the NSW Micromegas detectors. The two quadruplets follow as much as possible the layout of the NSW Micromegas detectors, however, not full size. The dimensions of the quadruplets were chosen such that one of these detectors could be installed on the existing Small Wheel behind the currently installed Cathode Strip Chambers in the ATLAS cavern thus their name MicroMegas Small Wheel (MMSW). For this reason there was the need to develop a data acquisition system and integrate it into the ATLAS Trigger and DAQ infrastructure. The project was cancelled one year later. By this time a DAQ system based on the official ATLAS TDAQ software had been successfully tested within the ATLAS partition during cosmic runs before the start of Run 2.

Each quadruplet consists of three drift panels, two readout panels and four gas gaps. The readout panels carry identical Micromegas structures on both sides mounted back-to-back. On one of the readout panels the strips on both sides are parallel to the long side of the trapezoid (η-panel) for measuring the precision coordinate. On the second panel the strips are inclined by ±1.5° with respect to the η-coordinate (stereo-panel) to measure both the precision and the second coordinate. The mesh of these detectors is integrated on the drift panels.

The alignment between the strips on the two faces of the η-panel has been measured with a laser tracker and with an Ag X-ray gun. The two measurements gave comparable results with an average alignment better than 20 µm and a rotation of less than 25 µm over the length of the strips. The relative alignment between the η-panel and the stereo-panel was measured only with the X-ray gun. Without the use of special precision pins to align the two panels, an alignment of better than 25 µm was found.

The gain uniformity of all MMSW layers was measured with X-rays and cosmics. Both measurements show the same relative behaviour. With the cosmics a maximum gain non-uniformity of ±24% was measured, corresponding to a <2 μm variation of the amplification gap thickness.

An average signal reconstruction efficiency of ≥95% per layer was found for an amplification voltage $V_A \geq 580$ V, homogeneous across the full detector.

The intrinsic spatial resolution was determined in an electron beam of 855 MeV to be better than 90 μm in the precision coordinate and 2.3 mm in the second coordinate. Comparable results were also found in a 10 GeV/c proton beam for MMSW-1 and in a 150 GeV/c pion beam for MMSW-2.

All the results obtained from these measurements are well within the specifications of the NSW Micromegas detectors.

Characterization of the resistive protection scheme:

For the ATLAS type Micromegas detectors a resistive protection layer is used on top of the readout electrode to protect the detector from electrical discharges and/or voltage breakdown. The protection layer consists of a 50 μm thick Kapton® substrate on top of which resistive paste is deposited to form the resistive strips with the same pattern as the one of the copper readout strips.

Two types of Kapton® substrates with different thermal and hygroscopic expansion coefficients were studied; the HN-type produced in Europe and the EN-type produced in Japan. The studies aim to understand the changes of the strip resistance as a function of humidity and temperature. The results are compared with tests performed with the same resistive paste deposited on a ceramic (Al_2O_3) substrate. The ceramic is insensitive to humidity and has a two to three times lower thermal expansion coefficient than the Kapton® substrates; for these reasons the ceramic is used as a reference.

The studies have shown that the resistive paste itself follows the changes of the humidity and temperature almost immediately and that this dependence is linear. As the humidity increases the strip resistance also increases and vice versa. On the contrary, as the temperature increases the strip resistance decreases and vice versa. The observed changes of the resistance are $\Delta R/R < 8\times10^{-4}/°C$ and $\Delta R/R < 5\times10^{-4}/\%R.H.$ and thus negligible for all practical considerations in the NSW. The measurement also showed that the (thermal and hygroscopic) expansion of the Kapton® substrate contributes to the change of the resistance with $\simeq 8\times10^{-5}/\mu m$. The thermal and hygroscopic expansion and retraction of the Kapton® happens on a much longer and different time scale. The thermal expansion time of the HN-type Kapton® is about 10 minutes while the retraction takes about 2 hours. The hygroscopic expansion of the HN-type takes about 30 hours while the shrinkage takes more than 3 weeks. Since the thermal and hygroscopic expansion coefficients of the EN-type are about two times lower than those of the HN-type we expect that only half of the time is needed for the EN-type for these processes.

For the NSW Micromegas detectors the EN-type Kapton® was chosen for its lower thermal and hygroscopic expansion coefficients. The detectors will be operated in the ATLAS cavern at very low humidity (in theory 0% owing to the gas circulation). At the QA/QC laboratories the humidity can change by ∼50% within a day and the temperature not more than 20°C. In these conditions, a 10% change in R.H. corresponds to ~1% change in the strip resistance. For a 10°C temperature change the strip resistance changes by <1%. These changes are negligible for our application. Thus we conclude that the resistive protection scheme is insensitive to environmental changes and measurements performed with the NSW Micromegas protection layers in non-controlled environments are not affected by changes of the strip resistance.

Ageing effects were studied without irradiation by accumulating a total amount of current equivalent to 100 years of operation at the HL-LHC. In addition, ageing tests have been performed with gamma irradiation in the Gamma Irradiation Facility at CERN. These studies have shown that the resistive paste does not show any charge depletion behaviour and does not suffer from ageing effects.

Influence of the pillars on the detector response and performance:

The pillars in a Micromegas chamber define the distance between the mesh and the anode. They are produced by photo-lithography from thin layers of insulating material laminated to the anode and can take any shape.

Electrons that are generated above a pillar charge up the pillar surface. This result in a deformation of the electric field and a displacement of the electrons from their original position. It was shown that this effect leads to a small systematic position mismeasurement for tracks in the vicinity of a pillar and a degradation of the spatial resolution.

For the NSW Micromegas detectors, the initial shape of the pillars was circular with a diameter of 220 μm at a distance of 7 mm to reduce as much as possible these effects. However, during the quality control of the first readout boards produced in industry missing or weakly attached pillars have been observed. To overcome this issue a new elongated pillar shape with dimensions 1 mm × 0.2 mm with 7 mm pitch was proposed. A 10×10 cm^2 resistive-strip bulk Micromegas detector with elongated pillars was built to study the effect of the larger area of the elongated pillars on the detector performance.

It was shown that when the detector is operated at high gain the effect of the pillars on the detector efficiency is negligible. The degradation of the spatial resolution introduced by the elongated pillar shape was measured to be $\leq$10 μm.

In addition the charge-up behaviour of the detector was studied. It was shown that the charge-up is a local effect and does not affect regions that are not irradiated, and that it depends on the particle rate. The higher the rate the faster the detector reaches a stable current.

Appendices

Appendix A

The physics of gaseous detectors

In this chapter, the main physics processes that govern the operation of gaseous detectors, and thus the Micromegas detectors, are discussed. Sections A.1 and A.2 describe the interaction of charged particles and highly energetic photons passing through matter. In Sections A.3–A.5 the ionization phenomena that occur in a gas volume after the passage of charged particles, the transport of the primary ionization charge and the charge amplification are discussed. The relevant theory is mostly taken from Ref. [86–89].

A.1 Interaction of charged particles with matter

When a charged particle traverses a gaseous detector the main interactions that occur with the gas molecules are electromagnetic interactions. These are the ionization and excitation processes, the production of Čerenkov radiation, bremsstrahlung and the production of transition radiation.

The Micromegas detectors exploit the electrons created by ionization radiation. The presence of residual excited states, ions or photons is relevant when they induce secondary phenomena such as recombination, charge transfers and photoelectric effects that will be discussed in the following. The other electromagnetic interactions will not be discussed here.

A.1.1 Stopping power at intermediate energies

The mean rate of energy loss per unit length is described by the Bethe equation with an accuracy of a few % for charged particles with $0.1 \lesssim \beta\gamma \lesssim 1000$[1] and for intermediate Z materials :

$$\left\langle -\frac{dE}{dx} \right\rangle = K z^2 \frac{Z}{A} \frac{1}{\beta^2} \left[\frac{1}{2} \ln \frac{2 m_e c^2 \beta^2 \gamma^2 W_{max}}{I^2} - \beta^2 - \frac{\delta(\beta\gamma)}{2} \right] {}^{2} \tag{A.1}$$

---

[1] For lower and higher particle velocities corrections to Eq. A.1 need to be taken into account.

[2] $K = 4\pi N_A r_e^2 m_e c^2 = 0.307$ MeV mol^{-1} cm^2 with $N_A = 6.022 \times 10^{23}$ mol^{-1} (Avogadro's number), $r_e = 2.818$ fm is the classical electron radius, and $m_e c^2 = 0.5111$ MeV; z is the charge number of indicent particle; Z, A are the atomic number and mass of the absorber; $\beta = v/c$ is

The important features that can be extracted from Eq. A.1 are the following:

- It is independent of the mass of the incoming particle so it is an universal curve;
- It depends quadratically on the charge and velocity of the particle $\sim z^2/\beta^2$;
- It is relatively independent of the absorber. It enters only via the term Z/A which is constant over a large range of materials;
- There is a minimum in the energy loss for $2 \lesssim \beta\gamma \lesssim 8$ with dE/dx $\approx$ 1–2 MeV cm^2 g^{-1} (see Fig. A.1). Particles in this energy range are called minimum ionizing (MIPs).

For mixtures and compounds the mean energy loss can be calculated by the weighted mean energy loss of the j_{th} element and is given by the formula:

$$\left\langle \frac{dE}{dx} \right\rangle = \sum w_j \left\langle \frac{dE}{dx} \right\rangle_j \tag{A.2}$$

Figure A.1 shows the mean energy loss in several materials. Particles at a fixed $\beta\gamma$ have similar rates of energy loss in different materials, except in liquid hydrogen. At high energies the difference between the gaseous helium and the other materials is the result of the density-effect correction $\delta(\beta\gamma)$.

---

the velocity of the incident particle; $\gamma = 1/\sqrt{1-\beta^2}$ is the Lorentz factor; W_{max} is the maximum energy transferred to an electron in a single collision which is $W_{max} = 2m_e c^2\beta^2\gamma^2$ for $2\gamma m_e \ll M$ or $W_{max} = Mc^2\beta^2\gamma^2$ for $2\gamma m_e \gg M$ with M the particle mass; I is the mean excitation energy; $\delta(\beta\gamma)$ is the density effect correction to ionization energy loss

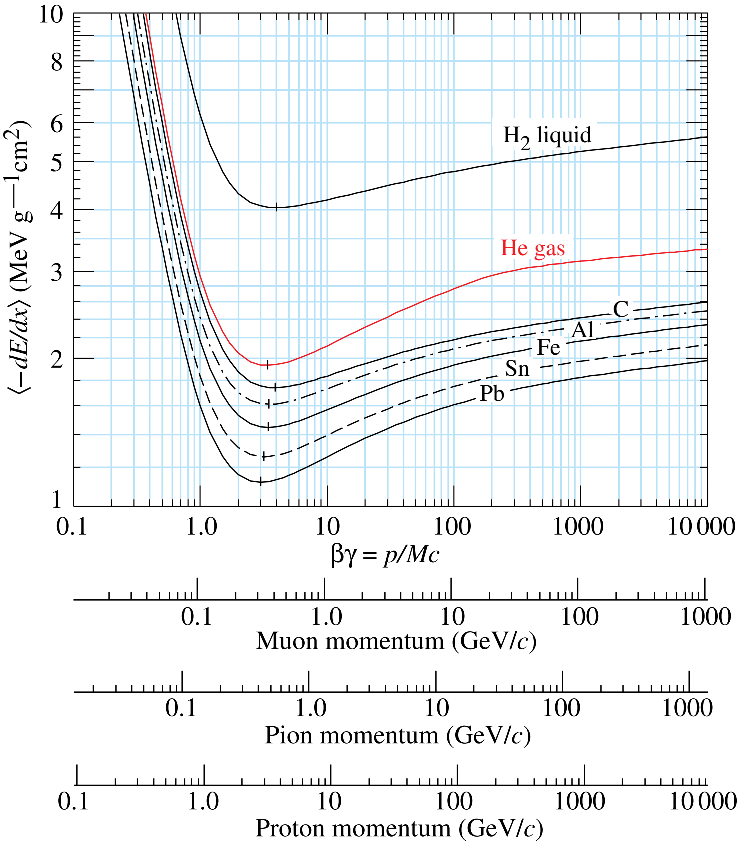

Figure A.1: Mean energy loss rate in liquid (bubble chamber) hydrogen, gaseous helium, carbon, aluminum, iron, tin, and lead [88].

The mean energy loss as it is described in Eq. A.1 is difficult to be measured precisely by detectors as the mean is affected by rare events[3] with high-energy-transfer collisions. The mean of an experimental distribution has large fluctuations and it is sensitive to cuts. Instead usually the most probable energy loss is used as described by the Landau (or Landau-Vavilov) distribution for moderate thickness detectors like gaseous detectors. The most probable energy loss is given by:

$$\Delta_p = \xi \Big[ln \frac{2mc^2\beta^2\gamma^2}{I} + ln\frac{\xi}{I} + j - \beta^2 - \delta(\beta\gamma) \Big] \tag{A.3}$$

where $\xi = (K/A)\langle Z/A\rangle(x/\beta^2)$ MeV for a detector with thickness x in g cm^{-2}, and j=0.200. The other parameters are as described in Eq. A.1. The most probable energy loss, unlike the mean energy loss, depends on the thickness.

Fig. A.2 shows a typical distribution of the energy loss in a thin layer of absorber or a low density material. The most probable energy loss is considerably lower than

---

[3] Mainly δ-electrons which can generate hundred or thousand secondary electrons.

the mean energy loss as given by the Bethe equation. The mean falls into the tail of the distribution.

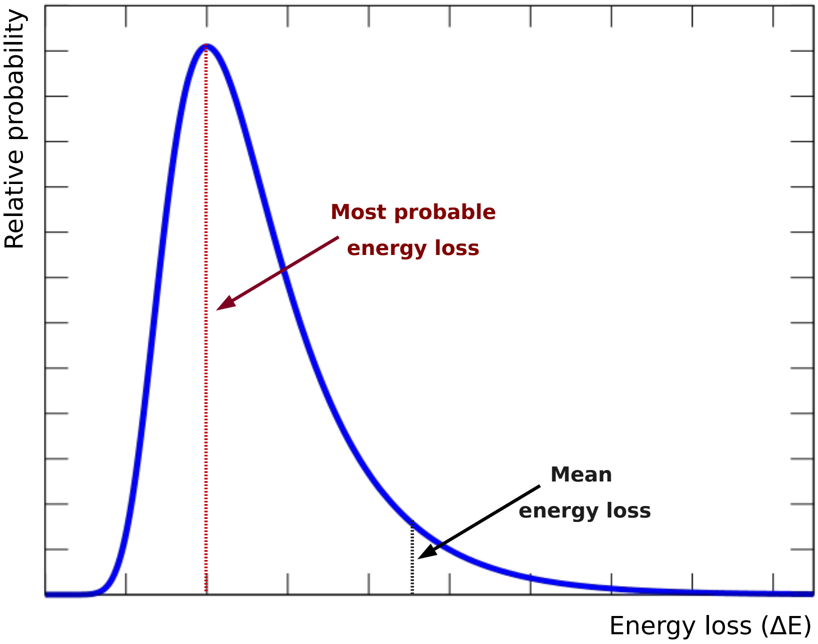

Figure A.2: Typical distribution for energy loss in a thin layer of absorber or a low density material.

A.2 Interaction of photons with matter

The interaction of photons with matter is different from that of charged particles. The main interactions that take place between photons and matter are the photoelectric effect, the Compton scattering and the pair production.

Fig. A.3 shows the energy dependent cross sections for Ar:CO_2 93:7[4]. For energies smaller than 100 keV the photoelectric effect dominates although Compton and Rayleigh[5] scattering also add small contributions. For energies greater than 10 MeV nuclear pair production[6] has the highest influence although electron pair production also has a small contribution. In the intermediate range Compton scattering is the dominant effect. The photoelectric cross section is steeply falling and is characterized by a sharp rise at 3.2 keV corresponding to the X-ray absorption edge of the argon K-shell.

---

[4] This is the gas mixture used in the ATLAS Micromegas detectors.

[5] Coherent scattering without excitation or ionization of the material.

[6] Pair production in the proximity of a nucleus is called nuclear pair production while in the proximity of an electron is called electron pair production.

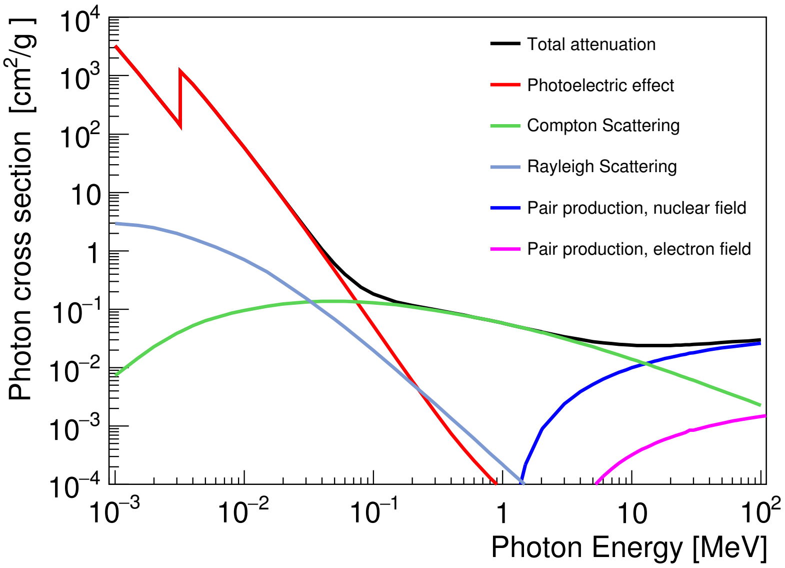

Figure A.3: Photon cross section in Ar:CO_2 93:7 [90].

The relevant processes that take place either absorb the photon or scatter them out. Mono-energetic photons traversing material of thickness x will be attenuated as:

$$I(x) = I_0 e^{-\frac{\mu}{\rho}x} \tag{A.4}$$

where I_0 is the incident beam intensity, μ/ρ is the mass attenuation coefficient and ρ is the density of the material.

For a chemical compound or a mixture, the mass attenuation coefficient can be approximately evaluated from the coefficients μ_i/ρ_i of the constituent elements according to the weighted average:

$$\frac{\mu}{\rho} = \sum_i w_i \cdot \frac{\mu_i}{\rho_i} \tag{A.5}$$

The mass attenuation coefficient is proportional to the total photon interaction cross section per atom and is given by the relation:

$$\frac{\mu}{\rho} = \sigma_{tot} \cdot \frac{N_A}{M} \tag{A.6}$$

where σ_{tot} is the sum of the cross sections for all the elementary scattering and absorption process, N_A is the Avogadro number and M is the atomic weight of the absorber material.

The inverse of the mass attenuation coefficient is called mean free path which represents the average distance travelled by a photon between successive interactions.

A.2.1 Photoelectric Effect

If a photon has an energy higher than the binding energy of an electron in a shell then the photon is absorbed by that electron. Subsequently the electron overcomes its binding energy and is liberated from the atom (ejected photoelectron) as shown in Fig. A.4. The energy of the outgoing electron is:

$$E = h\nu - B.E. \tag{A.7}$$

where $B.E.$ is the binding energy of the electron.

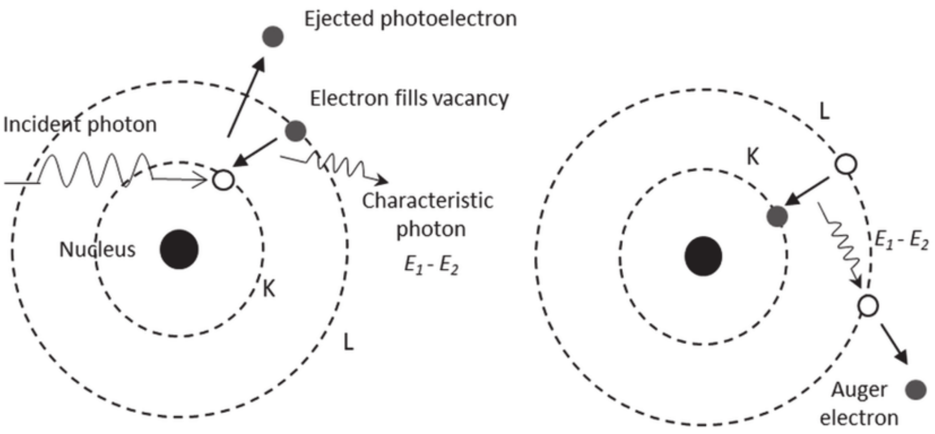

Figure A.4: (left) Absorption of an X-ray by an electron in the K shell followed by the emission of a fluorescence X-ray after the photoelectron is ejected; (right) An Auger electron is emitted with a kinetic energy equal to the difference of the shell energy levels.

The vacancy left by the ejected photoelectron is quickly filled by an electron from a higher shell. This electron re-arrangement emits a fluorescence photon. A competitive effect to that is the Auger effect where the transition energy of the electron filling the vacancy is transferred to a weakly bound electron of the same shell. The photoelectric effect always occurs on bound and not on free electrons with the nucleus absorbing the recoil momentum.

A.2.2 Compton Scattering

Compton scattering is the interaction of a photon with free electrons or loosely bound valence shell (outer shell) electrons (Fig. A.5). The incident photon gets scattered (changes direction) transferring part of its energy to the electron (recoil electron). The scattered photon will have a different wavelength and thus a different energy. Energy and momentum are conserved in this process.

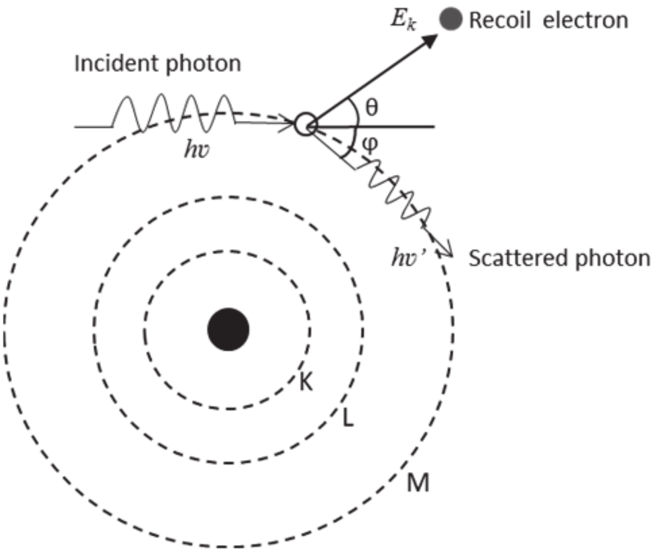

Figure A.5: Compton scattering in loosely bound valence shell.

Compton derived the mathematical relationship between the shift in wavelength and the scattering angle of the X-rays by assuming that each scattered X-ray photon interacts with only one electron:

$$\lambda^{'} - \lambda = \frac{h}{m_e c}(1 - cos\theta) \tag{A.8}$$

where λ is the initial wavelength, $\lambda^{'}$ is the wavelength after scattering, h is the Planck constant, m_e is the electron rest mass, c is the speed of light and θ is the scattering angle.

A.2.3 Pair production

Pair production involves the transformation of a photon into an electron-positron pair. This can occur only if the photon energy exceeds twice the rest mass of an electron ($m_e c^2 = 0.511$ MeV) (Fig. A.6). In this process the energy of the photon is converted into the kinetic energy and mass of the electron and positron. After the pair production, two photons are usually emitted owing to the positron being annihilated within the medium.

X-ray and γ-ray sources used in the context of this thesis are in the range of keV thus this process is impossible to occur.

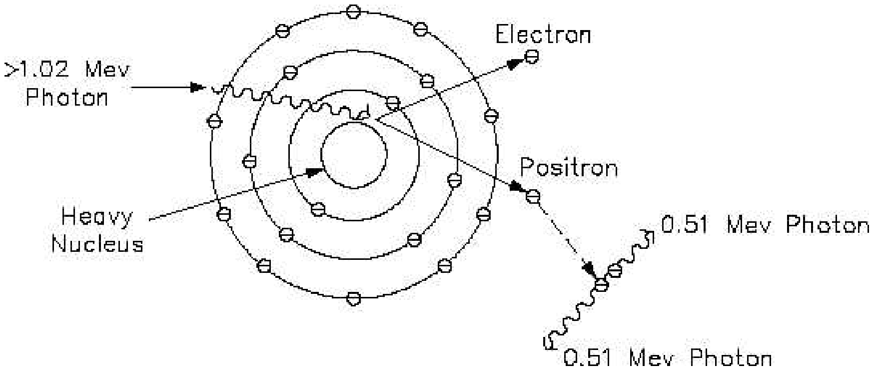

Figure A.6: Pair production

A.3 Ionization phenomena in gases

In a gaseous detector charged particles lose energy which is transferred to the bound electrons[7] of the atoms causing atomic excitation or ionization. If p is a charged particle, the excitation of an atom X is expressed as:

$$X + p \rightarrow X^* + p \tag{A.9}$$

The minimum energy that is required for this process depends on the excitation potential of the atoms or molecules in the gas. Typical cross sections in noble gases for this process are of the order of 10^{-17} cm^2. The excited molecule or atom may participate in ionization processes.

The ionization process is expressed as:

$$X + p \rightarrow X^+ + p + e^- \tag{A.10}$$

and typical cross sections in noble gases for this process are as high as 10^{-16} cm^2. However, since the ionization energy threshold is higher than the excitation potential, the excitation reactions dominate.

The ionization process in a gas leads to electron-ion pairs depending on the nature and energy of the particle and it is known as primary ionization. It follows Poisson statistics:

$$P_k^n = \frac{n^k}{k!} e^{-n} \tag{A.11}$$

where n and k are the average and actual numbers of pairs.

The minimum energy that is required for this process depends on the ionization potential of the atoms or molecules in the gas. Figure A.7 shows the first ionization potential versus the atomic number. In the noble gases, the higher the atomic

---

[7] If the bound electrons acquire very high energy secondary ionization takes place producing δ-rays.

number the smaller is the ionization potential required to release an electron from the outer shell.

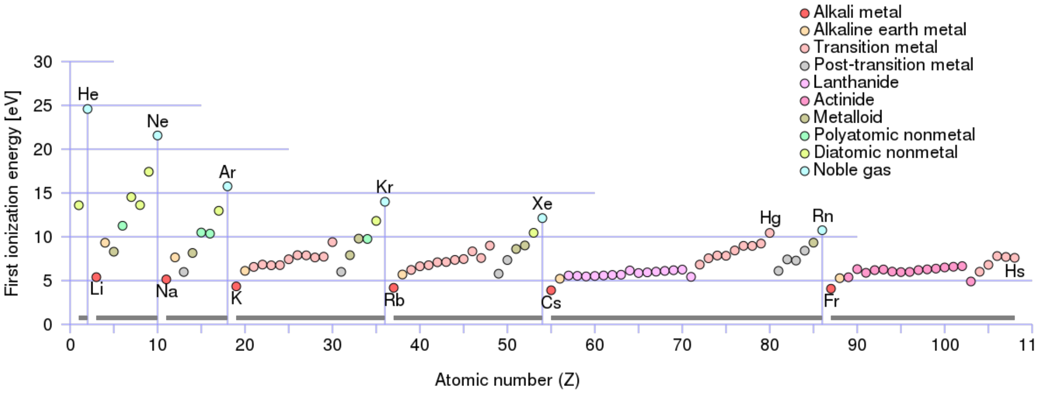

Figure A.7: First ionization potential as a function of the atomic number.

If the energy of the primary electrons is large enough to further ionize the gas molecules then more electron-ion pairs will be created until the energy threshold of ionization is reached. This process is called secondary ionization.

Other mechanisms that take place in ionization processes are the Penning Effect and the formation of molecular ions. The Penning Effect refers to the interaction between an excited atom X^* and a target molecule M. The collision results in:

$$X^* + M \rightarrow X + M^+ + e^- \tag{A.12}$$

This effect occurs when the target molecule has an ionization potential lower than the energy of the excited-state atom or molecule.

The formation of molecular ions happens when a positive gas ion interacts with a neutral atom of the same type, as for example:

$$Ar^+ + Ar \rightarrow Ar_2^+ \tag{A.13}$$

A.3.1 Mean number of electron-ion pairs created

The occurrence of the ionization reactions is statistical and therefore two identical atoms will not produce the same number of electron-ion pairs. The average energy (W_i) needed to produce an electron-ion pair in a gas mixture is experimentally measured. The total number of electron-ion pairs (n_t) can be estimated from:

$$n_t = \frac{\Delta E}{W_i} \tag{A.14}$$

where ΔE can be extracted from the mean energy loss for minimum ionizing particles. Table A.1 summarizes some properties of the most common gases. The quantities W_i, dE/dx, n_p and n_t refer to charged particles at the ionization minimum and should be considered approximate. Note, that W_i is higher than the ionisation energy (I_0) due to excitation collisions.

Table A.1: Properties of the most common gases at NTP. E_0, I_0: first excitation, ionization energy; W_i: average energy per ion pair; $dE/dx|\min$, n_p, n_t: differential energy loss, primary and total number of electron-ion pairs per cm, for minimum ionizing particles [88].

Gas	Z	A	d (mg/cm^3)	E_0 (eV)	I_0 (eV)	W_i (eV)	dE/dx|min (keV cm^{-1})	n_p (cm^{-1})	n_t (cm^{-1})
He	2	4	0.179	19.8	24.6	41.3	0.32	3.5	8
Ne	10	20.2	0.839	16.7	21.6	37	1.45	13	39
Ar	18	39.9	1.66	11.6	15.7	26	2.53	25	97
Xe	54	131.3	5.495	8.4	12.1	22	6.87	41	312
CO_2	22	24	1.84	7.0	13.8	34	3.35	35	100
CH_4	10	16	0.667	8.8	12.6	30	1.61	28	54

Examples of ionization yields in argon from various kinds of radiation are shown in Table A.2.

Table A.2: Ionization yields in argon at NTP from various kinds of radiation [86].

Particle	**Primary electron-ion pairs**	**Total electron-ion pairs**
UV photon	1	1
1 keV X-Ray	1	50
100 keV electron	1000 cm^{-1}	3000 cm^{-1}
1 GeV proton	25 cm^{-1}	100 cm^{-1}
5 MeV α particle	$\sim 10^4$	$\sim 3 \times 10^4$

A.3.2 Recombination and electron attachment

In the absence of an electric field recombination effects take place under the force of their electric attraction by emitting a photon:

$$X^+ + e^- \rightarrow X + h\nu \tag{A.15}$$

Electron attachment involves the capture of free electrons by electronegative atoms or molecules to form negative ions by emitting a photon:

$$e^- + X \rightarrow X^- + h\nu \tag{A.16}$$

Examples of electronegative molecules are SF_6, O_2, H_2O, CCl_4 etc. The presence of electronegative gases in gaseous devices diminishes the efficiency of electron collection because they trap the electrons before reaching the electrode. On the other hand, they are necessary for reasons that will be explained in the following.

A.4 Charge transport

In the absence of an electric field, the electron and ions diffuse from their point of creation. They suffer multiple collisions with the gas molecules and lose their energy. If we consider N molecules in a gas of volume V being like spheres and by ignoring all interactions among them then the probability that a gas molecule has a velocity (u) within a small volume is given by the Maxwell-Boltzmann distribution:

$$F(u) = 4\pi u^2 \sqrt{\left(\frac{m}{2\pi k_B T}\right)^3}\, e^{-\frac{mu^2}{2k_B T}} \tag{A.17}$$

with k_B the Boltzmann constant and T the temperature. The characteristic velocities that can be extracted from this distribution are the most probable speed $\hat{u} = \sqrt{\frac{2k_BT}{m}}$, the average speed $\langle u \rangle = \sqrt{\frac{8k_BT}{\pi m}}$ and the root mean square speed $\sqrt{\langle u^2 \rangle} = \sqrt{\frac{3k_BT}{m}}$ as shown in Fig. A.8.

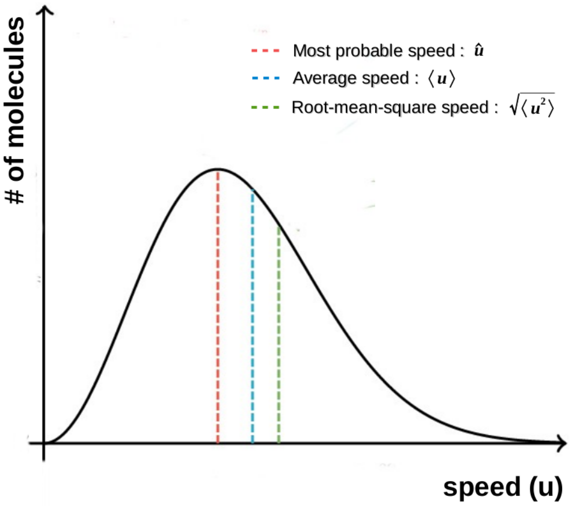

Figure A.8: Maxwell-Boltzmann distribution indicating the position of the characteristic velocities.

The mean free path (λ) of a gas molecule with an effective cross-sectional area πd^2 is defined as the average distance travelled between collisions and is given by:

$$\lambda = \frac{V}{N}\frac{1}{\pi d^2} = \frac{1}{n\pi d^2} \tag{A.18}$$

where $n = N/V$ is the density of the gas. Fig. A.9 shows the velocity distribution of some noble gas molecules and of an electron at NTP calculated from Eq. A.17. The average speed of electrons is much higher than the speed of atoms owing to their smaller mass. At NTP, the electrons have a speed of 10^7 cm/s while the speed of the atoms and consequently the ions is of the order of 10^4–10^5 cm/s.

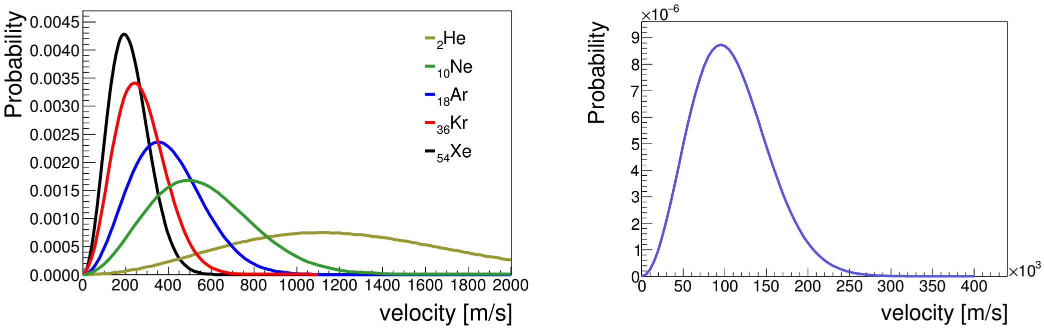

(a)

(b)

Figure A.9: Velocity distribution of (a) some noble gas molecules and (b) of an electron, at NTP.

The corresponding probability of finding an atom or molecule having an energy E is given by:

$$F(E) = 2\sqrt{\frac{E}{\pi(kT)^3}}e^{-\frac{E}{kT}} \tag{A.19}$$

and it is independent of the mass of the atom or molecule. Fig. A.10 shows the energy distribution of atoms or molecules at NTP calculated from Eq. A.19 with the most probable thermal energy at E=0.016 eV.

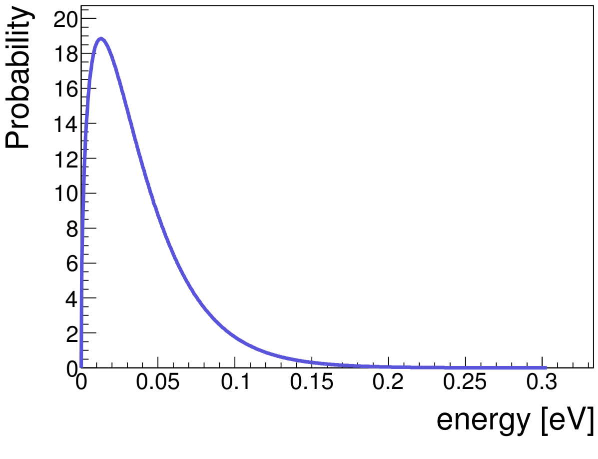

Figure A.10: Energy distribution of atoms or molecules at NTP.

A.4.1 Drift and mobility

In the presence of an electric field, electrons and ions follow the electric field lines and move towards the anode and the cathode respectively. Their acceleration is hindered by collisions with the gas molecules which limits the average velocity that could be obtained. The motion of a nonrelativistic electron or a gas molecule under the influence of the electric ($\vec{E}$) and magnetic ($\vec{B}$) fields is given by:

$$m\frac{d\vec{u}}{dt} = e\vec{E} + e[\vec{u} \times \vec{B}] - K\vec{u} \tag{A.20}$$

where m and e are the mass and electric charge of the particle or gas molecule, $\vec{u}$ the velocity vector, and K describes a frictional force proportional to $\vec{u}$ that is caused by the interaction of the particle with the gas. The ratio $\tau = m/K$ expresses the mean time between collisions. Neglecting the magnetic field component, the solution to Eq. A.20[8] gives the drift velocity along the electric field:

$$\vec{u} = \frac{e}{m}\tau\vec{E} = \mu\vec{E} \quad \text{with} \quad \mu = \frac{\mathrm{e}}{\mathrm{m}}\tau \tag{A.21}$$

The mobility (μ) of a charge is defined as the ratio of the drift velocity and the electric field in the absence of a magnetic field. It is proportional to the mean time between collisions (τ) and carries the charge sign (e).

The mobility of ions and electrons varies significantly owing to the fact that ions are much heavier than electrons. Under the influence of the electric field, electrons are accelerated more rapidly than ions and lose very little energy when colliding elastically. The electrons can reach energies far in excess of the energy of the thermal motion, and quite often they surpass the threshold of inelastic excitation of molecules in the gas. In this case the electron mobility becomes a function of the energy loss that is associated with such excitation. On the other hand, ions in similar fields acquire the same amount of energy on one mean free path as the electrons but a good fraction of this energy is lost in the collisions. Therefore the random[9] energy of ions is mostly thermal, and only a small fraction is due to the electric field. For low electric fields the ion drift velocity is:

$$u = \sqrt{\left(\frac{1}{m} + \frac{1}{M}\right)}\sqrt{\frac{1}{3kT}}\frac{eE}{N\sigma} \tag{A.22}$$

while for high electric fields it is:

$$u = \sqrt{\frac{m}{M}\left(1 + \frac{m}{M}\right)}\sqrt{\frac{eE}{mN\sigma}} \tag{A.23}$$

where N is the gas density, σ is the cross section, m is the mass of the drifting ion and M is the mass of a gas molecule. From Eq. A.22 and A.23 we see that for low electric fields the ion drift velocity is proportional to E while for high electric fields it is proportional to $\sqrt{E}$.

Fig. A.11 shows the electron and ion drift velocities in several Ar:CO$_2$ mixtures. The ion drift velocity increases as $\sqrt{E}$ in high electric fields. The electron drift velocity shows a strong dependence on the gas mixture. In pure argon, the electron drift velocity has the same behaviour as the ion drift velocity but is much smaller

---

[8] Analytic calculations can be found in Ref. [89].

[9] Here, the random energy refers to the random motion after a collision.

than the drift velocities that can be acquired in gas mixtures. Adding small amounts of CO_2 leads to a dramatic increase of the electron drift velocity.

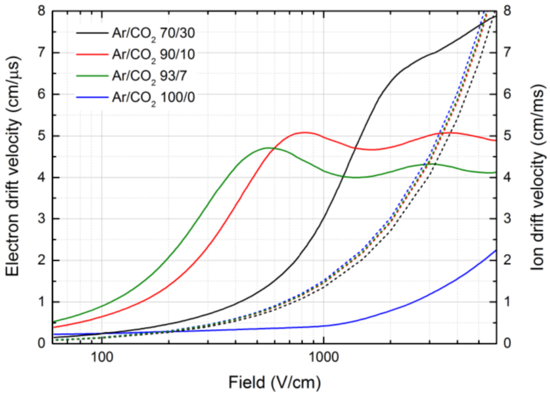

Figure A.11: Electron and ion drift velocities in Ar:CO_2 mixtures with different CO_2 concentrations. The solid lines represent the electron drift velocities while the dashed lines the ion drift velocities. Courtesy of P. Thuiner [91].

The explanation for the strong dependence of the electron drift velocity on the gas mixture can be found in Fig. A.12 and Fig. A.13 where the electron cross sections are shown for argon, CO_2 and Ar:CO_2 mixtures. In pure argon (Fig.A.12(a)) the minimum of the elastic collisions at 0.23 eV is the characteristic Ramsauer–Townsend minimum[10]. At electron energies up to 1 eV, the cross section of CO_2 is an order of magnitude larger than the cross section of argon. When adding a small amount of CO_2, the cross section increases substantially while the Ramsauer–Townsend minimum shifts to higher energies.

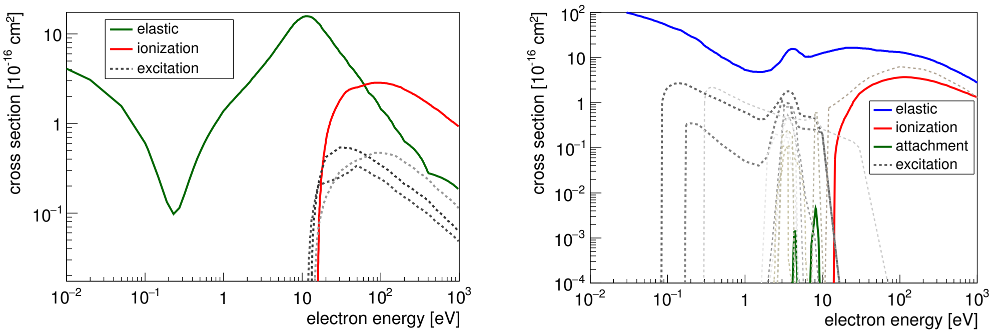

(a) (b)

Figure A.12: Electron cross sections for (a) argon and (b) CO_2 [92], [93].

---

[10] The Ramsauer–Townsend minimum is due to quantum mechanical processes in the scattering of the electron with the argon atom.

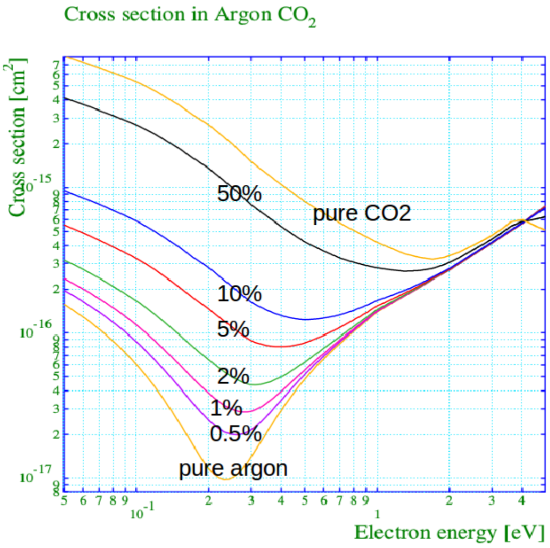

Figure A.13: Electron cross sections for Ar:CO$_2$ mixtures with different CO$_2$ concentrations. Courtesy of R. Veenhof [94].

A.4.2 Diffusion

Considering that the density of gas molecules is not a constant but a function of time and space the diffusion equation in one dimension is:

$$\frac{\partial n}{\partial t} = D\frac{\partial^2 n}{\partial x^2} \tag{A.24}$$

where the diffusion constant is $D = \langle \Delta x^2 \rangle / 2\Delta t$. The solution to Eq. A.24, considering that all N gas molecules starting at the origin at $t = 0$, is a Gaussian distribution:

$$\frac{dN}{N} = \frac{1}{\sqrt{4\pi Dt}} e^{-\frac{x^2}{4Dt}} dx \tag{A.25}$$

where dN/N is the fraction of particles found in a distance x from their origin after a time t. The average distance travelled by a gas molecule is the width of the distribution:

$$\langle x^2 \rangle = \sqrt{2Dt} \tag{A.26}$$

and in three dimensions it is:

$$\langle \vec{x}^2 \rangle = \sqrt{6Dt} \tag{A.27}$$

Table A.3 shows values for the mean free path, velocity and diffusion coefficient for some selected atoms and molecules at NTP.

Table A.3: Mean free path (λ), velocity (u) and diffusion coefficient(D) for some selected atoms and molecules at NTP [86].

Gas	λ (cm)	u (cm/s)	D (cm^2/s)
H_2	1.8×10^{-5}	2×10^5	0.34
He	2.8×10^{-5}	1.4×10^5	0.26
Ar	1×10^{-5}	4.4×10^4	0.04
O_2	1×10^{-5}	5.0×10^4	0.06

The diffusion coefficient (D) is related to the mobility by the Einstein equation:

$$\frac{D}{\mu} = k_B T \tag{A.28}$$

where $k_B T$ is the average thermal energy equal to 0.026 eV.

Under the influence of an electric field, the diffusion of the electron along the drift lines (longitudinal diffusion) and perpendicular to the drift lines (transverse diffusion) differs. Fig. A.14 shows the electron and ion diffusions as a function of the electric field for different Ar:CO_2 mixtures. Adding CO_2 reduces the transverse diffusion and thereby increases the drift velocity. For the ATLAS Micromegas detector at 600 V/cm which is the usual operating drift field and Ar:CO_2 93:7 the transverse diffusion is ~ 380 µm/cm and the longitudinal diffusion is 200 µm/cm.

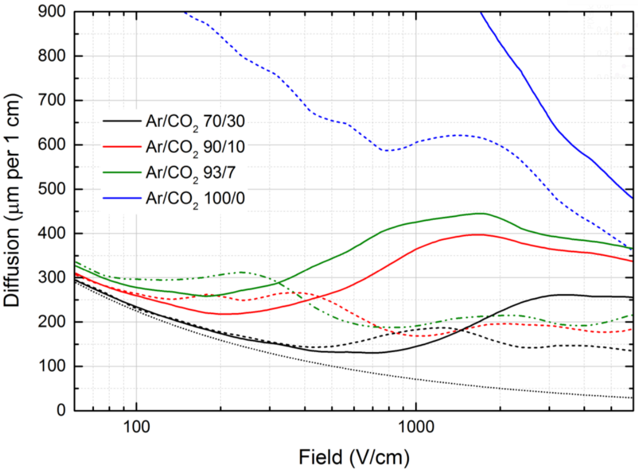

Figure A.14: Electron transverse (solid) and longitudinal diffusion (dashed) as a function of the electric field in several Ar:CO_2 mixtures, compared to ion diffusion (dotted). The ion diffusion is the same for all Ar:CO_2 mixtures. For clarity only the ion diffusion for Ar:CO_2 70:30 is plotted. Courtesy of P. Thuiner [91].

A.5 Charge amplification

When the primary ionization electrons gain sufficient energy from the accelerating electric field to further ionise gas molecules, the formation of an avalanche takes place. The probability of an ionization per unit length, is known as the first Townsend coefficient and expressed as the inverse of the mean free path (λ) of the electron for a secondary ionizing collision:

$$\alpha = \frac{1}{\lambda} \tag{A.29}$$

If there are n electrons, then over a distance dx, dn new electrons will be created:

$$dn = n\alpha dx \tag{A.30}$$

The integration of equation A.30, yields the total number of electrons created in a path x:

$$n = n_0 e^{\alpha x} \tag{A.31}$$

where n_0 is the primary number of electrons. The multiplication factor $e^{\alpha x}$ is also known as gas gain.

A.5.1 Charge amplification modes

When an electric field is applied there are different amplification modes that a gaseous device can reach. Figure A.15 shows an example of the number of ions (and electrons) collected as a function of the applied voltage in a single wire gas chamber.

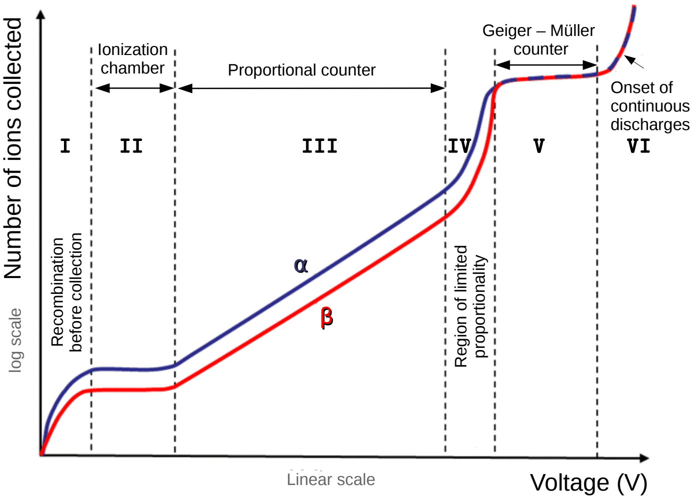

Figure A.15: Number of ions collected versus applied voltage in a single wire gas chamber [95]

At zero voltage or very low electric field (region I), no charge is collected as the ion-electron pairs recombine under their own electrical attraction. As the current is increasing more and more ion-electron pairs are collected before recombination. When all created ion-electron pairs are collected (region II) a further increase of the voltage does not show any effect. If the voltage is increased beyond region II then the electric field is strong enough to accelerate free electrons so that they will have enough energy to further ionize the gas molecules and multiply. This will result in an ionization avalanche or cascade. The detected charge is proportional to the originally deposited charge through the exponential ($e^{\alpha x}$) multiplication factor, thus the name proportional counter. Beyond region III, a further increase in voltage will result in a large amount of ionization which creates space charges that distort the electric field close to the anode. This region is known as region of limited proportionality (region IV). Increasing the voltage above this region a chain reaction of avalanches (discharges) start to occur. These avalanches are created by photons emitted by de-excitation. To stop discharges the addition of a polyatomic gas (for example methane or alcohol) or inorganic gases (for example CO_2, BF_3) can act as quenchers by absorbing the photons and dissipating this energy through elastic collisions or dissociation. Detectors working in this region are called Geiger-Müller. Finally, if the voltage is further increased (region VI) a continuous breakdown occurs with or without irradiation. The discharges in this case can damage the detector, thus this operation mode should be avoided.

The Micromegas detectors are operated in the proportional mode.

Appendix B

Additional material for Chapter 4

Table B.1: Reduction of the photon flux in the materials used in an external drift panel of the MMSW detector

Object	**z**	**Material**	**Thickness**		**Filling**	**X0**	**X**	**X/X0**	**Density**	**Abs. length (g/cm2)**						**t**	**Remaining photon flux [1 - $e^{-t/a}$]**					
	(mm)		(mm)	(g/cm2)	factor	(mm)	(mm)		(g/cm3)	10 keV	20 keV	30 keV	50 keV	100 keV	600 keV	(g/cm2)	10 keV	20 keV	30 keV	50 keV	100 keV	600 keV
Cu shield		Cu	0.017	0.0152	1	14.35	0.017	0.00118	8.96	0.007	0.04	0.12	0.5	3	10	0.015232	0.113	0.683	0.881	0.970	0.995	0.998
FR4	0	Glass/epoxy	0.500	0.0900	1	170	0.5	0.00294	1.8	0.03	0.2	0.6	2	5	10	0.09	0.050	0.638	0.861	0.956	0.982	0.991
Glue		Araldite 2011	0.250	0.0238	0.05	335	0.0125	0.00004	0.95	1	2.5	3	4	5	10	0.0011875	0.999	1.000	1.000	1.000	1.000	1.000
Honeycomb		Al	5.000	1.3500	0.02	89	0.1	0.00112	2.7	0.03	0.2	0.6	2	5	10	0.027	0.407	0.874	0.956	0.987	0.995	0.997
Glue		Araldite 2011	0.250	0.0238	0.05	335	0.0125	0.00004	0.95	1	2.5	3	4	5	10	0.0011875	0.999	1.000	1.000	1.000	1.000	1.000
FR4		Glass/epoxy	0.500	0.0900	1	170	0.5	0.00294	1.8	0.03	0.2	0.6	2	5	10	0.09	0.050	0.638	0.861	0.956	0.982	0.991
Cu electrode		Cu	0.017	0.0152	1	14.35	0.017	0.00118	8.96	0.007	0.04	0.12	0.5	3	10	0.015232	0.113	0.683	0.881	0.970	0.995	0.998
Total								0.00945									0.000	0.166	0.549	0.848	0.949	0.976

Table B.2: Reduction of the photon flux in the materials used in the middle drift panel of the MMSW detector

Object	**z**	**Material**	**Thickness**		**Filling**	**X0**	**X**	**X/X0**	**Density**	**Abs. length (g/cm2)**						**t**	**Remaining photon flux [1 - $e^{-t/a}$]**					
	(mm)		(mm)	(g/cm2)	factor	(mm)	(mm)		(g/cm3)	10 keV	20 keV	30 keV	50 keV	100 keV	600 keV	(g/cm2)	10 keV	20 keV	30 keV	50 keV	100 keV	600 keV
Cu electrode		Cu	0.017	0.0152	1	14.35	0.017	0.00118	8.96	0.007	0.04	0.12	0.5	3	10	0.015232	0.113	0.683	0.881	0.970	0.995	0.998
FR4	0	Glass/epoxy	0.500	0.0900	1	170	0.5	0.00294	1.8	0.03	0.2	0.6	2	5	10	0.09	0.050	0.638	0.861	0.956	0.982	0.991
Glue		Araldite 2011	0.250	0.0238	0.05	335	0.0125	0.00004	0.95	1	2.5	3	4	5	10	0.0011875	0.999	1.000	1.000	1.000	1.000	1.000
Honeycomb		Al	5.000	1.3500	0.02	89	0.1	0.00112	2.7	0.03	0.2	0.6	2	5	10	0.027	0.407	0.874	0.956	0.987	0.995	0.997
Glue		Araldite 2011	0.250	0.0238	0.05	335	0.0125	0.00004	0.95	1	2.5	3	4	5	10	0.0011875	0.999	1.000	1.000	1.000	1.000	1.000
FR4		Glass/epoxy	0.500	0.0900	1	170	0.5	0.00294	1.8	0.03	0.2	0.6	2	5	10	0.09	0.050	0.638	0.861	0.956	0.982	0.991
Cu electrode		Cu	0.017	0.0152	1	14.35	0.017	0.00118	8.96	0.007	0.04	0.12	0.5	3	10	0.015232	0.113	0.683	0.881	0.970	0.995	0.998
Total								0.00945									0.000	0.166	0.549	0.848	0.949	0.976

Table B.3: Reduction of the photon flux in the materials used in a readout panel of the MMSW detector

Object	**z**	**Material**	**Thickness**		**Filling**	**X0**	**X**	**X/X0**	**Density**	**Abs. length (g/cm2)**						**t**	**Remaining photon flux [1 - $e^{-t/a}$]**					
	(mm)		(mm)	(g/cm2)	factor	(mm)	(mm)		(g/cm3)	10 keV	20 keV	30 keV	50 keV	100 keV	600 keV	(g/cm2)	10 keV	20 keV	30 keV	50 keV	100 keV	600 keV
Mesh	2.5	Fe	0.027	0.0209	0.75	17.5	0.019875	0.00114	7.87	0.007	0.04	0.12	0.5	3	10	0.015641625	0.107	0.676	0.878	0.969	0.995	0.998
Pillars			0.128	0.0192	0.01	286	0.00128	0.00000	1.5	1	2.5	3	4	5	10	0.000192	1.000	1.000	1.000	1.000	1.000	1.000
R-strips	2.6	C/Epoxy	0.030	0.0054	0.75	200	0.0225	0.00011	1.8	1	2.5	3	4	5	10	0.00405	0.996	0.998	0.999	0.999	0.999	1.000
Kapton		Kapton	0.050	0.0070	1	286	0.05	0.00017	1.4	1	2.5	3	4	5	10	0.007	0.993	0.997	0.998	0.998	0.999	0.999
Glue		Epoxy	0.025	0.0025	1	200	0.025	0.00013	1	1	2.5	3	4	5	10	0.0025	0.998	0.999	0.999	0.999	1.000	1.000
R/o strips		Cu	0.017	0.0152	0.75	14.35	0.01275	0.00089	8.96	0.007	0.04	0.12	0.5	3	10	0.011424	0.196	0.752	0.909	0.977	0.996	0.999
FR4	0	Glass/epoxy	0.500	0.0900	1	170	0.5	0.00294	1.8	0.03	0.2	0.6	2	5	10	0.09	0.050	0.638	0.861	0.956	0.982	0.991
Glue		Araldite 2011	0.250	0.0238	0.05	335	0.0125	0.00004	0.95	1	2.5	3	4	5	10	0.0011875	0.999	1.000	1.000	1.000	1.000	1.000
Honeycomb		Al	5.000	1.3500	0.02	89	0.1	0.00112	2.7	0.03	0.2	0.6	2	5	10	0.027	0.407	0.874	0.956	0.987	0.995	0.997
Glue		Araldite 2011	0.250	0.0238	0.05	335	0.0125	0.00004	0.95	1	2.5	3	4	5	10	0.0011875	0.999	1.000	1.000	1.000	1.000	1.000
FR4		Glass/epoxy	0.500	0.0900	1	170	0.5	0.00294	1.8	0.03	0.2	0.6	2	5	10	0.09	0.050	0.638	0.861	0.956	0.982	0.991
R/o strips		Cu	0.017	0.0152	0.75	14.35	0.01275	0.00089	8.96	0.007	0.04	0.12	0.5	3	10	0.011424	0.196	0.752	0.909	0.977	0.996	0.999
Glue		Epoxy	0.025	0.0025	1	200	0.025	0.00013	1	1	2.5	3	4	5	10	0.0025	0.998	0.999	0.999	0.999	1.000	1.000
Kapton		Kapton	0.050	0.0070	1	286	0.05	0.00017	1.4	1	2.5	3	4	5	10	0.007	0.993	0.997	0.998	0.998	0.999	0.999
R-strips	2.6	C/Epoxy	0.030	0.0054	0.75	200	0.0225	0.00011	1.8	1	2.5	3	4	5	10	0.00405	0.996	0.998	0.999	0.999	0.999	1.000
Pillars			0.128	0.0192	0.01	286	0.00128	0.00000	1.5	1	2.5	3	4	5	10	0.000192	1.000	1.000	1.000	1.000	1.000	1.000
Mesh	2.5	Fe	0.027	0.0209	0.75	17.5	0.019875	0.00114	7.87	0.007	0.04	0.12	0.5	3	10	0.015641625	0.107	0.676	0.878	0.969	0.995	0.998
Total								0.01196									0.000	0.091	0.447	0.803	0.937	0.971

Table B.4: Reduction of the photon flux in all the materials of the MMSW detector (2 external drift panels, 2 readout panels, 1 middle drift panel)

Remaining photon flux [1 - e$^{-t/a}$]					
10 keV	**20 keV**	**30 keV**	**50 keV**	**100 keV**	**600 keV**
0	0	0.0330	0.3932	0.7506	0.8780

Appendix C

Additional material for Chapter 5

C.1 Additional results from humidity scans

The humidity scans performed with the Al_2O_3 and the Kapton® substrates are listed in Table C.1.

Table C.1: Humidity Scans

Measurement	**Stable Condition**	**Scan**	**Step**	**Time of step**
Humidity Scan	20 °C	45 - 80 % R.H.	5% R.H.	10 min.
		80 - 45 % R.H.		
	25 °C	30 - 85 % R.H.		
		85 - 30 % R.H.		
	60 °C	10 - 95 % R.H.		
		95 - 10 % R.H.		

Figure C.1 shows the average of the data points at each step of both cycles for the three humidity scans fitted with a linear function for the Al_2O_3 substrate.

Figure C.2 shows the relative humidity, the strip resistance, and the temperature as a function of time for the three humidity scans performed with the HN-type Kapton® substrate. The strip resistance as a function of the relative humidity when averaging the data points at each step of both cycles for the three humidity scans are shown in Fig. C.3. The corresponding plots for the EN-type Kapton® are shown in Fig. C.4 and C.5 respectively.

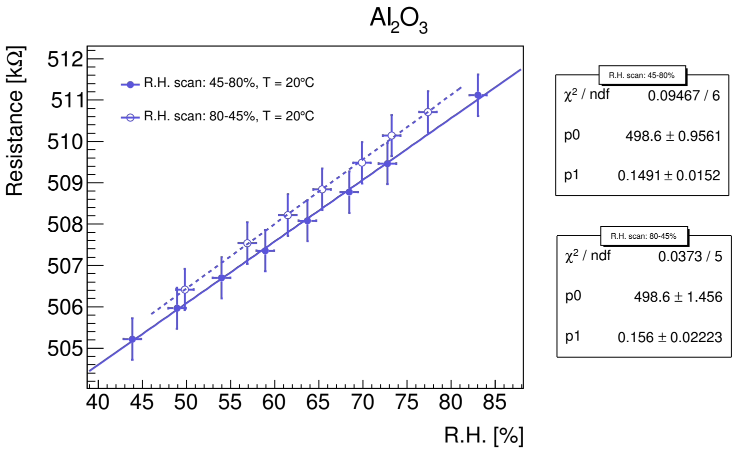

(a)

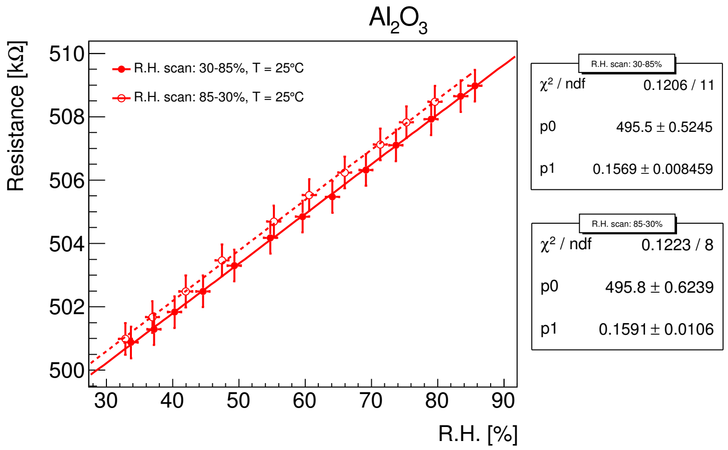

(b)

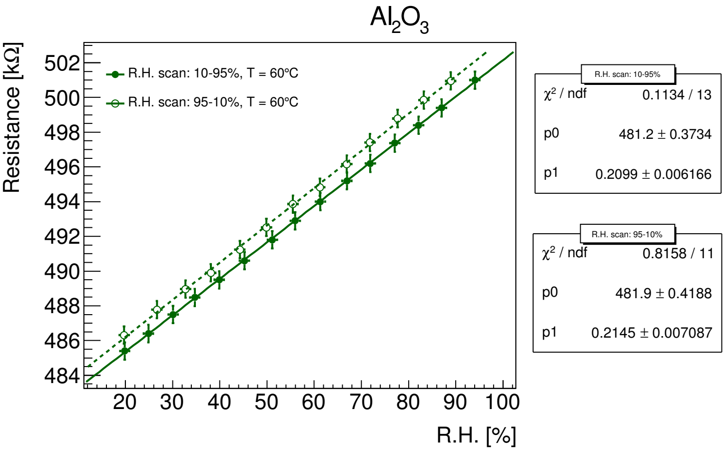

(c)

Figure C.1: Average of the data points at each step of both cycles for the three humidity scans fitted with a linear function for the Al_2O_3 substrate.

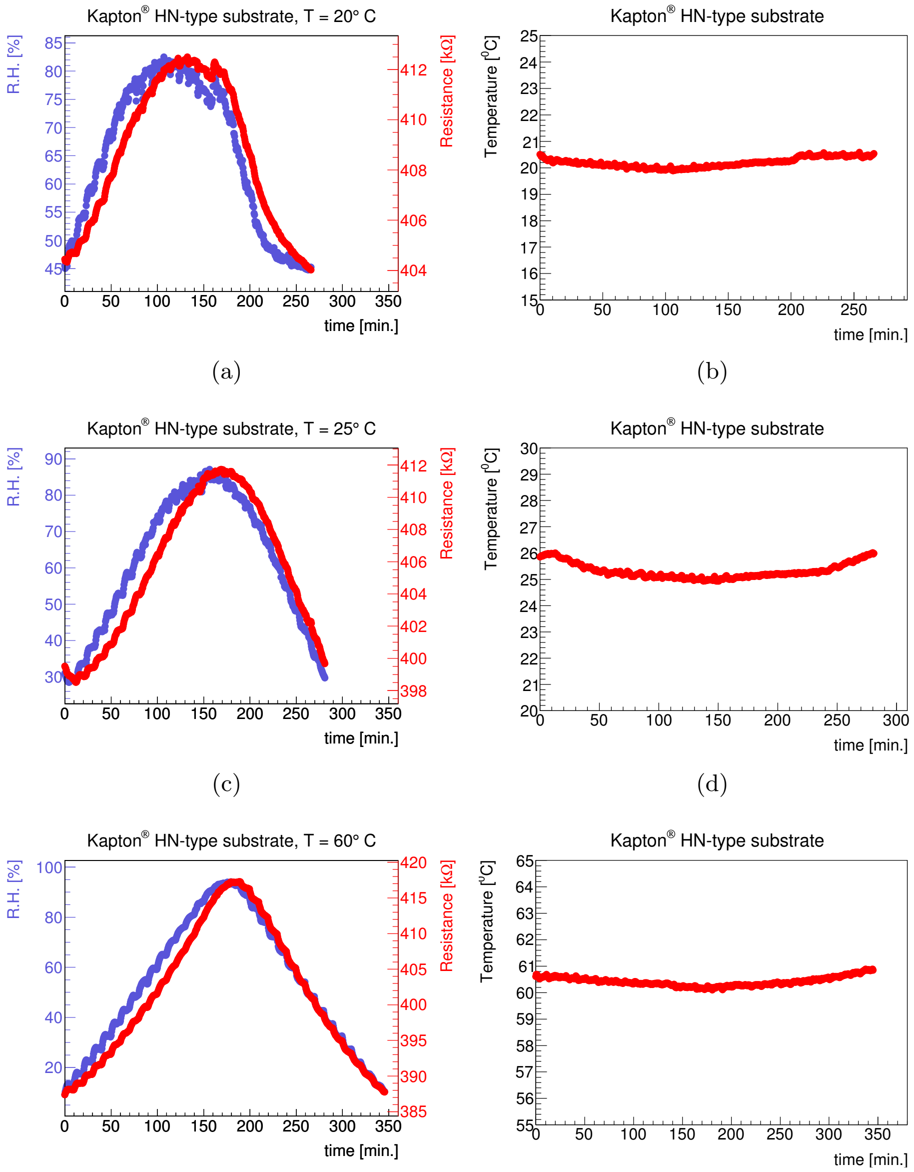

(a) (b)

(c) (d)

(e) (f)

Figure C.2: (left) Relative humidity and strip resistance as a function of time; (right) Temperature as a function of time with the HN-type Kapton® substrate.

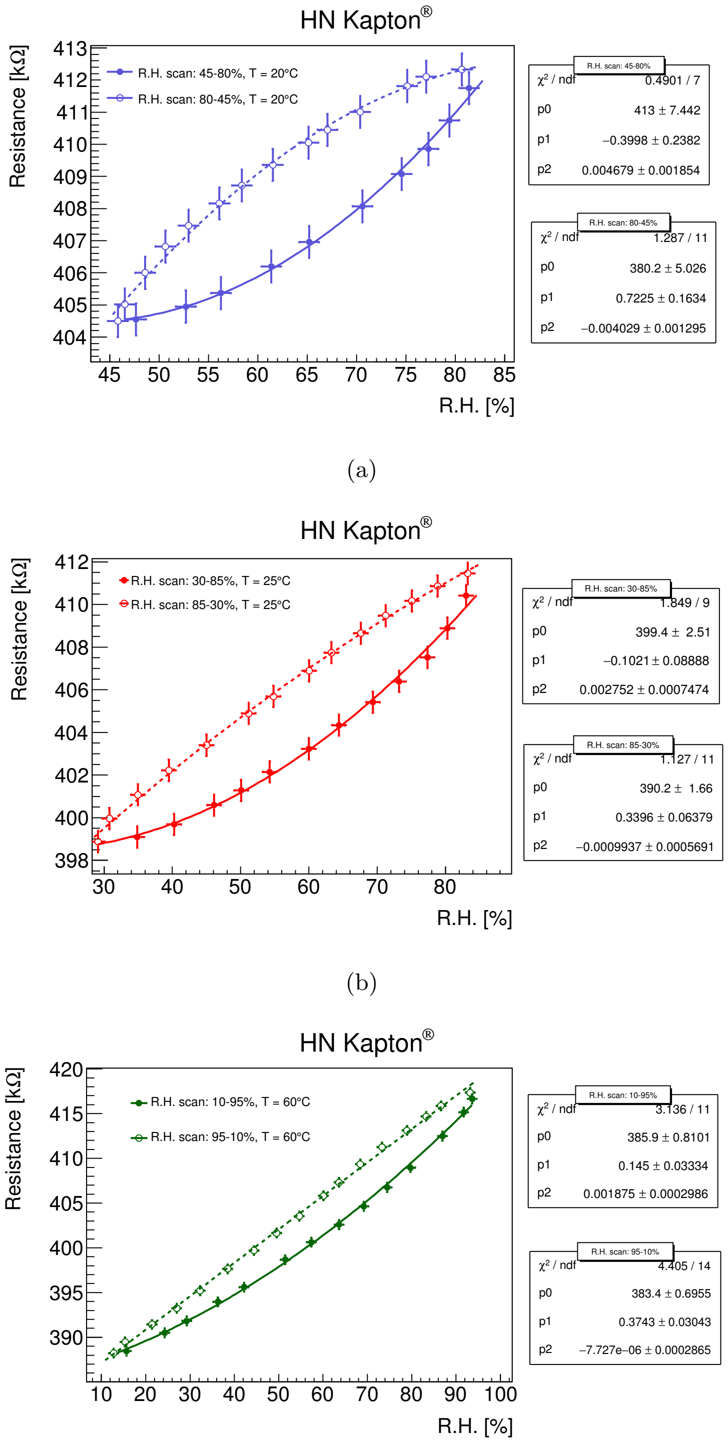

(a)

(b)

(c)

Figure C.3: Strip resistance of the HN-type Kapton® substrate as a function of relative humidity; (a) scan 45–80–45% at 20°C, (b) scan 30–85–30% at 25°C, (c) scan 10–90–10% at 60°C. Average of the data points at each R.H. step.

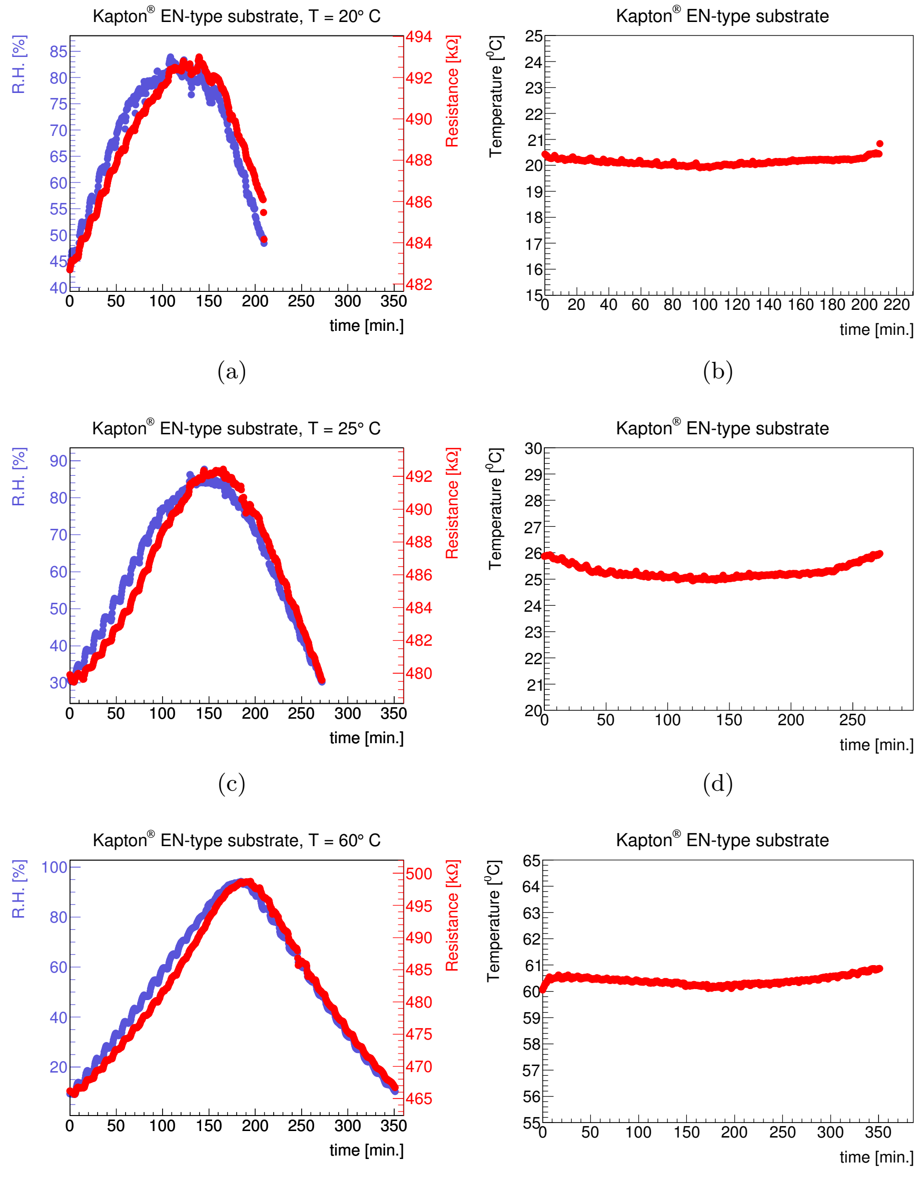

(a) (b)

(c) (d)

(e) (f)

Figure C.4: (left) Relative humidity and strip resistance as a function of time; (right) Temperature as a function of time with the EN-type Kapton® substrate.

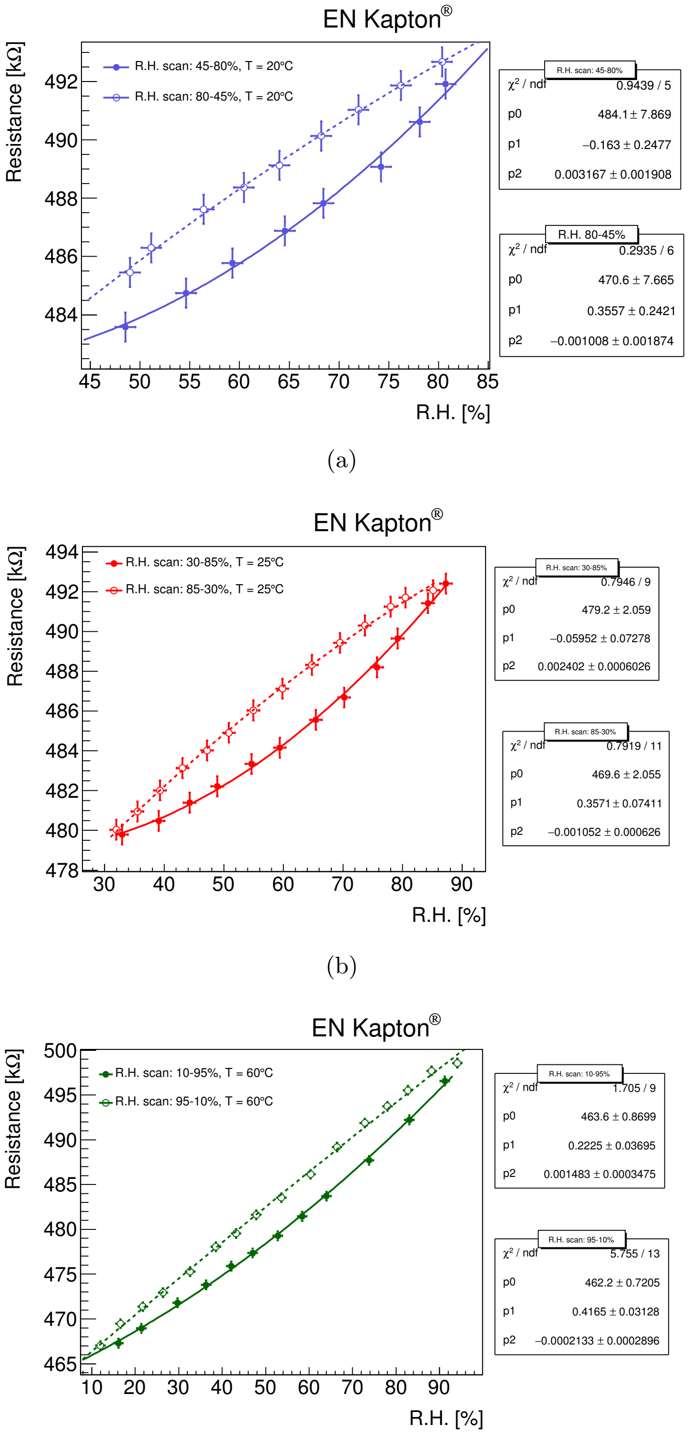

(a)

(b)

(c)

Figure C.5: Strip resistance of the EN-type Kapton® substrate as a function of relative humidity; (a) scan 45–80–45% at 20°C, (b) scan 30–85–30% at 25°C, (c) scan 10–90–10% at 60°C. Average of the data points at each R.H. step.

C.2 Strip resistivity as a function of the transferred charge

C.2.1 Data conversion from Arduino®

The ADC resolution of the Arduino® MEGA 2560 is 10 bits which correspond to 1024 different values. The output of the Arduino® is ADC counts that can be converted to voltage by using the formula:

$$\Delta \mathrm{V_{out}} = \frac{\mathrm{ADC_{count}} \cdot \mathrm{V_{max}}}{\mathrm{ADC_{max}}} \tag{C.1}$$

where:

$$\begin{gathered} \mathrm{ADC_{count}} = \mathrm{AnalogRead(port)}^{1} \\ \mathrm{V_{max}} = 1.1\ \mathrm{V}^{2} \\ \mathrm{ADC_{max}} = 1023 \end{gathered}$$

The accuracy of the resolution is:

$$\tfrac{1.1}{1024} = 1.07\ \mathrm{mV}$$

C.2.2 Calibration of small resistors

To check the stability of the small resistors with respect to the relative humidity and temperature, the resistive strips were replaced by equivalent resistors. Table C.2 shows the resistors values used in both circuits.

Table C.2: The values of the resistors for each circuit.

Circuit	$\mathrm{R_{equiv}}$(kΩ)	$\mathrm{R_{control}}$(kΩ)
A0	544	5.62
A1	547	5.82

To increase the humidity inside the plexi-glass box the gas was switched off. Figure C.6 shows the voltage drop on each small resistor and the relative humidity as a function of time. The current was the same as in the measurement of the foils, ∼70–80μA. During this scan the temperature was stable at 20.5±0.5°C. For a relative humidity in the range 17% to 38% the small resistors are stable. The fluctuations of ±1 mV which correspond to ±0.8kΩ are expected according to the accuracy of the ADC resolution.

---

[1] Built-in function of Arduino®.

[2] The default maximum voltage of the Arduino® MEGA 2560 is 5 V, but one can use the reference pin to change this value. For the specific measurement the 1.1 V reference pin was used.

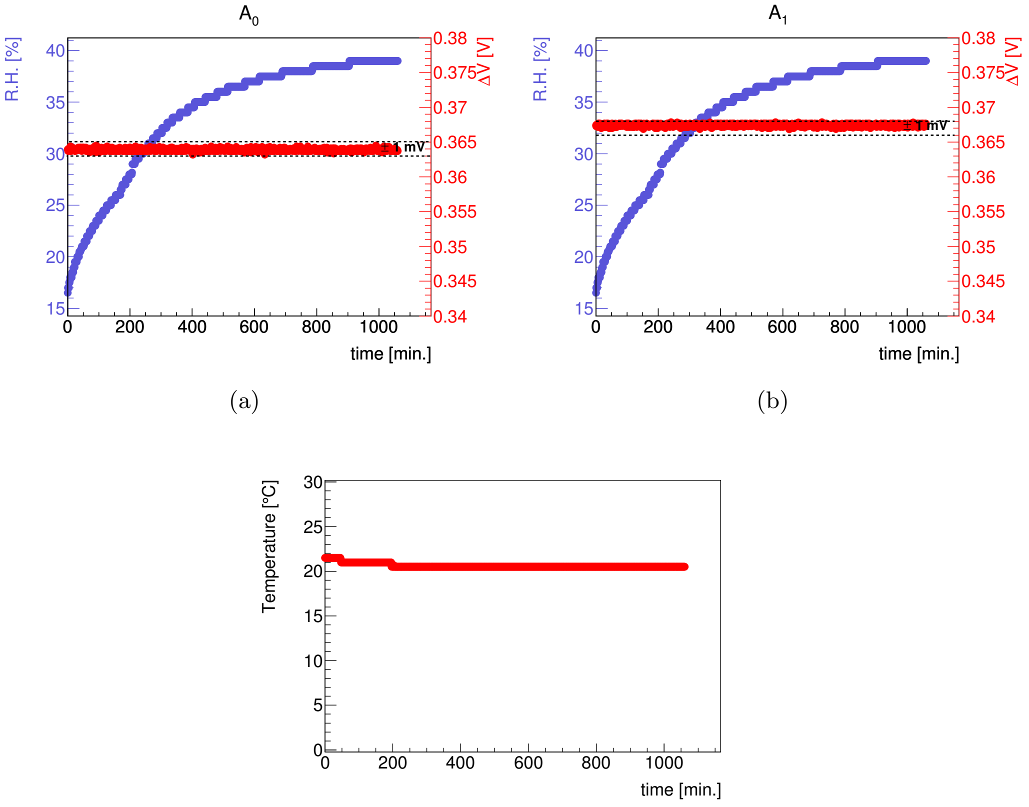

(a)

(b)

(c)

Figure C.6: Voltage drop on the small resistors, (a) A_0 and (b) A_1, and relative humidity as a function of time; (c) temperature as a function of time during the humidity scan.

For the thermal scan an infrared lamp was used to increase the temperature inside the plexi-glass box as shown in Figure C.7. An infrared camera[3] was also used to check the area of irradiation on the surface of the plexi-glass box.

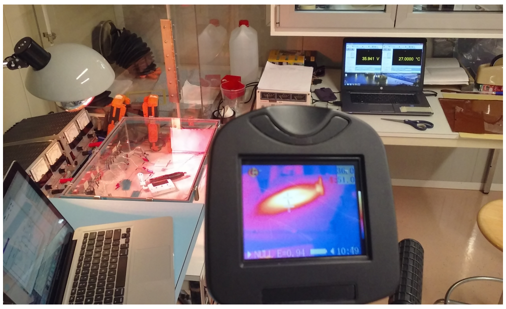

Figure C.7: Temperature scan performed with the use of an infrared lamp.

---

[3] RayCAm C.A 1884 IR CAMERA.

Figure C.8 shows the voltage drop on the small resistorss and the temperature as a function of time. The temperature increased from 22°C to 43°C, while the relative humidity decreased from 40% to 16%. The resistors in this temperature range show a stable behaviour with the expected fluctuations of ±1 mV.

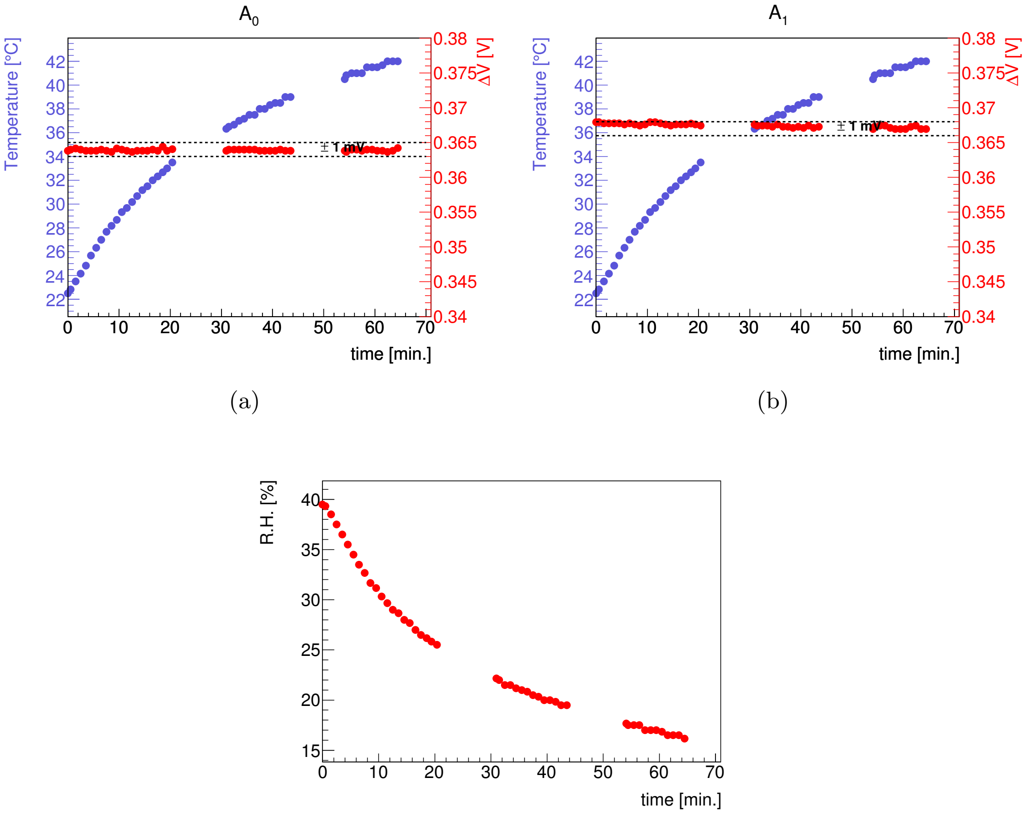

(a)

(b)

(c)

Figure C.8: Small resistors, (a) A_0 and (b) A_1, and temperature as a function of time; (c) relative humidity as a function of time during the temperature scan.

Appendix D

The CERN Gamma Irradiation Facility (GIF++)

The Gamma Irradiation Facility at CERN (GIF++) [78] is located in the North Area of the Super Proton Synchrotron (SPS) in the EHN1 hall. It is in operation since spring 2015. The GIF++ combines a high intensity ^{137}Cs source (16.65 TBq measured in May 2014) with a high-energy particle beam in the SPS H4 beam line.

The half-life of ^{137}Cs is about 30 years. In 95% of the cases it decays by beta emission to a metastable nuclear isomer of barium (^{137m}Ba) while the remainder populates the ground state of stable ^{137}Ba. The metastable ^{137m}Ba having a half-life of about 153 s emits gamma rays with a main photon peak of 662 keV (Fig. D.1).

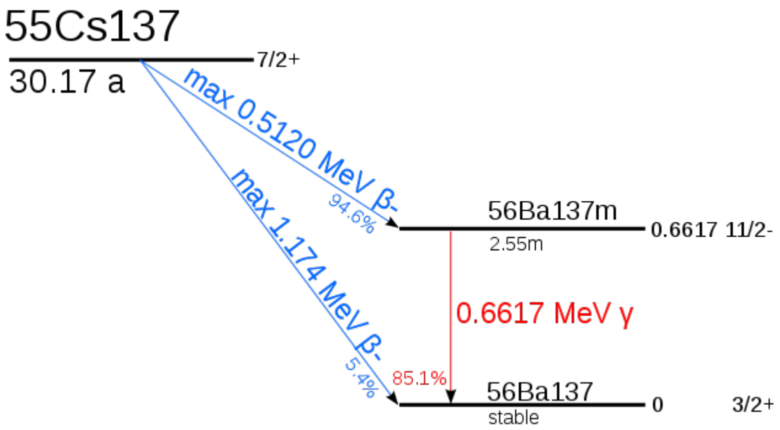

Figure D.1: Simplified decay schema of the ^{137}Cs [96]

Figure D.2 shows the layout of the GIF++. The irradiator emits γ-rays into two different regions as denoted on the same figure. The flux of the gamma rays can be tuned by a system of filters that can be set independently for the two γ-field regions.

Figure D.3 shows the simulated photon current of the gamma particles when the source is fully open [97].

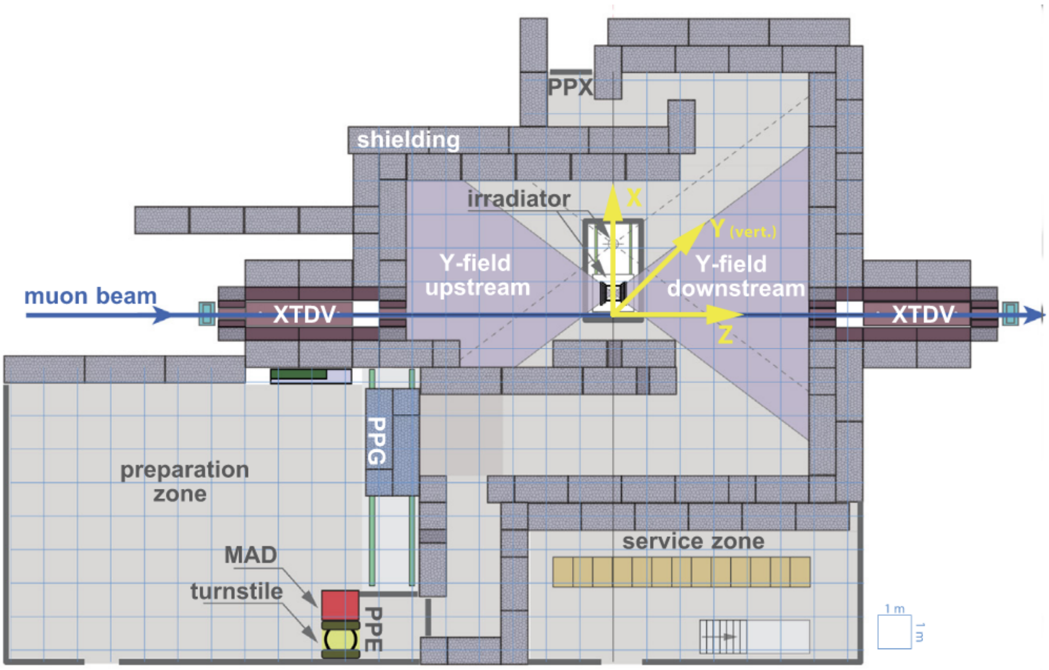

Figure D.2: Layout of the Gamma Irradiation Facility (GIF++) [97].

The high gamma flux (up to 4.4×10^7 Hz/cm^2) permits the users to perform fast studies, e.g., of detector occupancy and rate capability as a function of gamma background but also to study cumulative effects like detector ageing for extended exposure time. Moreover, using the H4 beam, the response of the detectors to pions or muons can be studied as a function of the high intensity gamma background.

Figure D.4 shows the simulated energy spectrum of the photons at three different upstream positions. About half of the integrated flux is constituted by the 662 keV gammas; the other half is about equally distributed between E = 100 keV and 661 keV.

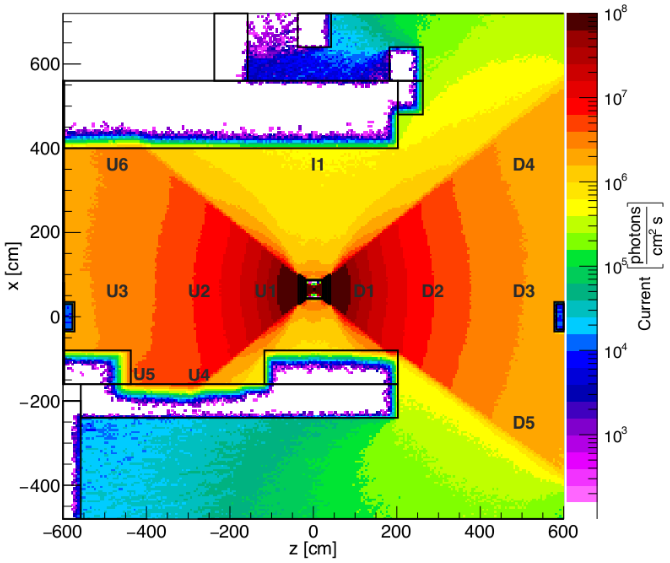

Figure D.3: Simulation of the photon current with the source fully open. Photons are emitted in two cones with an opening angle of ±37 degrees into the upstream (U) and downstream (D) regions [97].

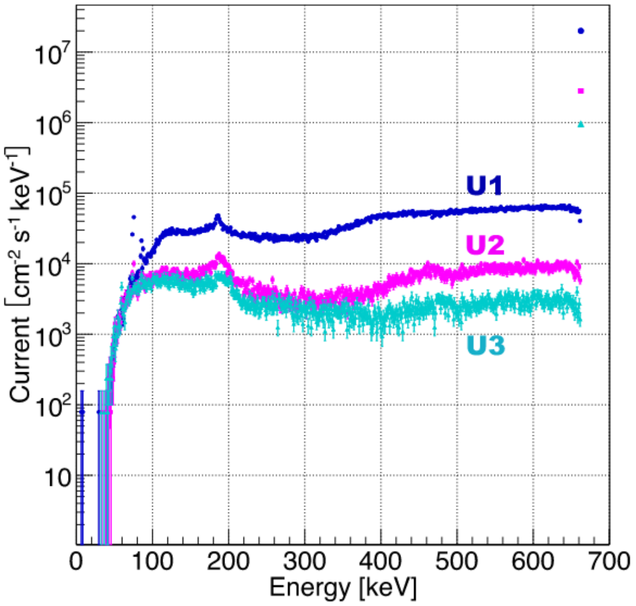

Figure D.4: Energy spectrum of photons as a function of the photon current, at the upstream positions U1, U2 and U3 [97].

Appendix E

RD51 Readout electronics for Micro-Pattern Gaseous Detectors

E.1 The Scalable Readout System (SRS)

The Scalable Readout System (SRS) is a collective effort within the RD51 [39] collaboration started in 2009 initially for the R&D of the MPGD technologies and the associated readout electronics. It is a general purpose multichannel readout solution for a wide range of micro–pattern detector types.

Figure E.1 shows the schematics of the SRS DAQ system. With the SRS system different front-end hybrids, with either analog or digital readout, can be connected over a customizable interface to the DAQ system [101]. This interface is implemented via a generic adapter card which is connected with edge-mounted PCIe connectors to the core component of the SRS DAQ system, the Front End Concentrator (FEC) [100] card. The FEC card is the common interface for all applications. It is based on a Virtex Xilinx FPGA (versions 3–6), integrating a 2 Gbit DDR2 memory chip, one SFP connector for Gigabit Ethernet communication, general purpose NIM and LVDS interfaces and two LVDS DTCC ports. The FEC board also interfaces with various adapter boards not only ADC based.

The adapter card includes all the necessary resources to readout the front-end hybrids on detector, for example ADCs in the case when analog front-end hybrids are connected. Up to 8 FEC cards together with the adapter cards can be hosted in a standard 6U Eurocrate, reaching up to more than 16,000 detector channels.

The scalability of this system relies on the fact that while the FEC remains fixed for all applications the front-end ASICs and the adapter card can be exchanged depending on the application [101]. Upstream from the adapter cards the components are common for all the DAQ systems. For small and medium size system the FEC cards can be connected via Gigabit Ethernet to a pc or a network switch, while for large size system DTCC [102] (Data, Trigger, Clock and Control) links can be connected to a Scalable Readout Unit (see Chapter 4.4).

Overall, the scalable architecture is based on high-speed point-to-point links with no buses thus providing more bandwidth and flexibility for longer distances between all the DAQ components.

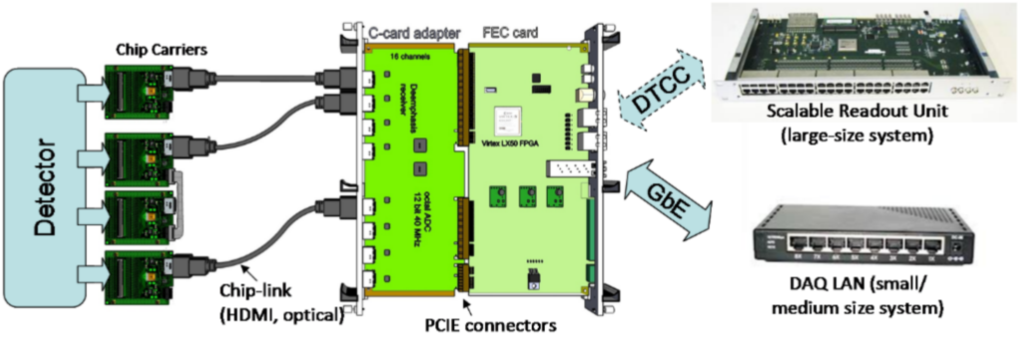

Figure E.1: Schematics of the SRS DAQ system [56].

For the ATLAS Micromegas detectors the SRS system is widely used. The Micromegas detectors are readout with front-end hybrids (APV25 hybrid) which host the APV25 chip.

E.2 The APV25 chip

The APV25 (Analogue Pipeline Voltage chips with 0.25 µm CMOS technology) [98] was initially developed to readout silicon micro-strips in the CMS tracker, but it has also been used by the MPGD community over the past years. Each of the 128 APV25 channels contains a preamplifier and a shaper followed by a 192 time step deep memory. The APV25 chip delivers analog CR-RC shaped signals sampled at 40 MHz. Since it was developed for silicon strip readout, it uses a short integration constant that is not optimized for the Micromegas with a longer charge collection time.

To readout Micromegas detectors, we use the APV25 in the multi-mode trigger mode. For each trigger N times 3 samples are read out with a frequency of 40 MHz[1]. In this mode we can sample the integrated charge over up to 27 time bins of 25 ns.

E.3 The APV25 hybrid

Figure E.2 shows a hybrid [56] based on the APV25 analogue chip. The 128 input channels of the APV25 ASIC[2] are AC coupled to the detector via the RD51 detector connector (Panasonic) and protected against electrostatic discharges by diode arrays. There are two types of hybrids that can be connected together; one master and one slave.

---

[1] The APV25 chip can be also configured to run at a frequency of 20 MHz.

[2] Application-Specific Integrated Circuit

The master hybrid contains the PLL[3]25 [99] chip that provides precise clock timing and clock refreshing, such that two hybrids can be daisy chained in a master-slave configuration via a Samtec FTSH-180 connector and a corresponding FFSD-08 flat cable. The hybrid uses HDMI cables as electrical interface. The HDMI cable carries two serial analogue data streams so that two hybrids (the master and the slave) can be readout simultaneously. The ground connection to the chamber is realized via low-ohmic RF coaxial connectors that can be placed on the sides of the hybrid.

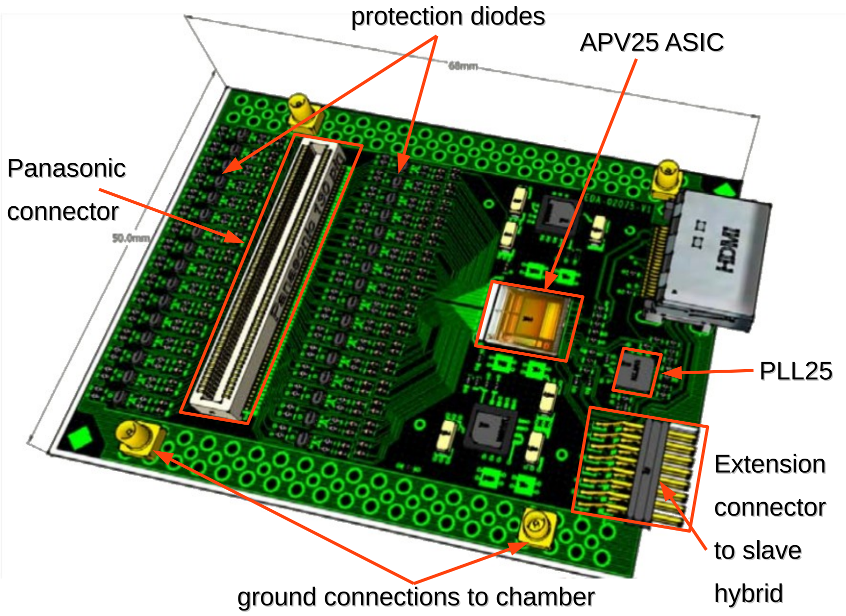

Figure E.2: The master front-end hybrid for the APV25 chip [56]

E.4 Data output

Data transmission is based on UDP[4] packets. Fig. E.3 shows a raw UDP frame from one APV25 hybrid. Each slice, after the APV header, is a time bin frame of 25 ns that contains the output of data from the 128 channels. The amplitude of the signals is shown on the y-axis of this figure.

---

[3] Phase-Locked Loop

[4] User Datagram Protocol

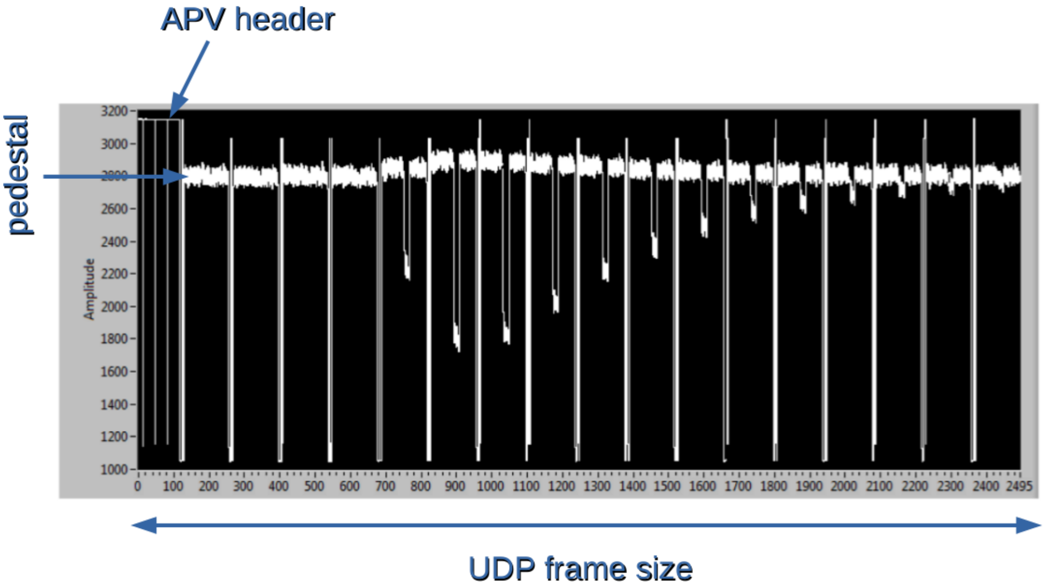

Figure E.3: Raw UDP frame.

Figure E.4 shows the APV25 output signal for one readout channel. Each data point is the integrated charge sampled in a single time bin. In this example the APV25 was configured to output data for 21 time bins per trigger. The charge of a readout strip is defined as the maximum of the integrated charge samples. The time stamp is defined as the maximum of the first derivative of the rising edge of the signal (or the half rising time) when the signal is fitted with a Fermi-Dirac function.

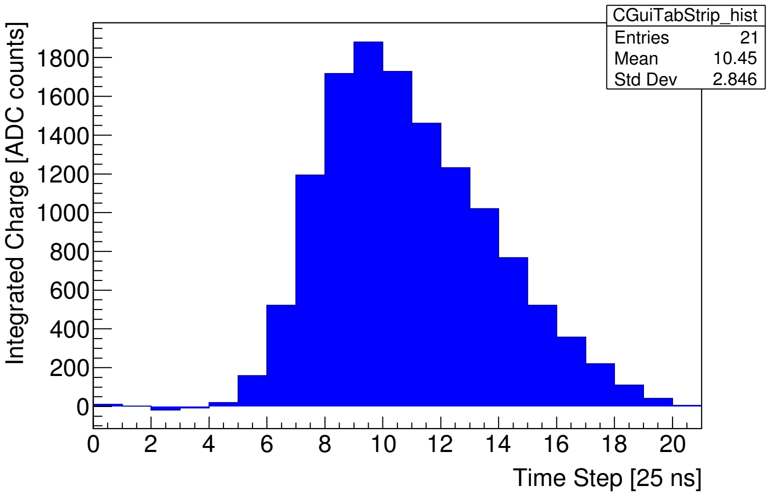

Figure E.4: APV25 output signal on one readout strip with a maximum charge of 1900 ADC counts, showing the development of the integrated charge for 21 time bins of 25 ns.

One of the drawbacks of the APV25 is its limited dynamic range of ∼2000 ADC counts. For larger charges time and charge information are no longer reliable. An example is shown in Fig. E.5(a) where the maximum charge has reached 2000 ADC counts. In this case the rising part of the APV25 output signal is steep and for time bins >16 the integrated charge falls in negative ADC counts. Figure E.5(b) shows the distribution of all charges for this detector. Charges $\geq$ 2000 ADC counts are accumulated in the last bins. In order to avoid this saturation the operating conditions of a detector should be adjusted accordingly.

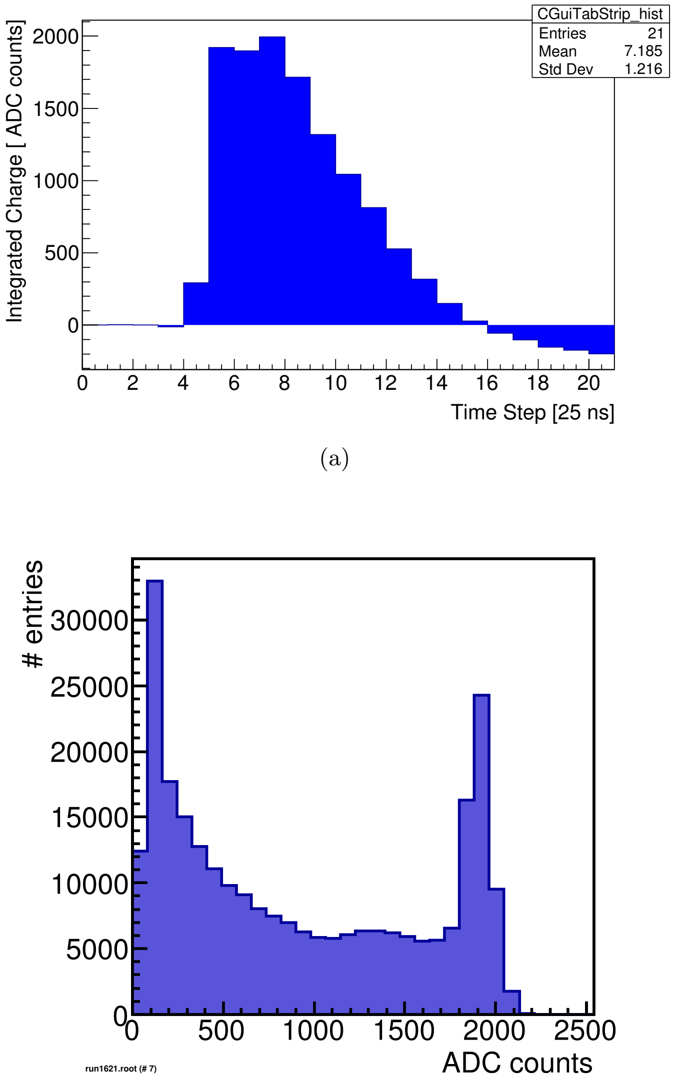

(a)

(b)

Figure E.5: (a) APV25 output signal on one readout strip with a maximum charge of 2000 ADC counts, showing the development of the integrated charge for 21 time bins of 25 ns; (b) Distribution of all charges recorded in a Micromegas detector.

Appendix F

Determination of the spatial resolution

The determination of the spatial resolution of a position-sensitive detector using the geometric-mean method [85] has been used extensively in studies of Micro Pattern Gaseous detectors [103–105]. It has been demonstrated that this method works well when the detectors have the same characteristics and were built in a same way [106, 107]. For this reason, in Section 6.3, the geometric-mean method is used to estimate the resolution of the track position reconstructed with the reference detectors (MM detectors in Fig. F.1).

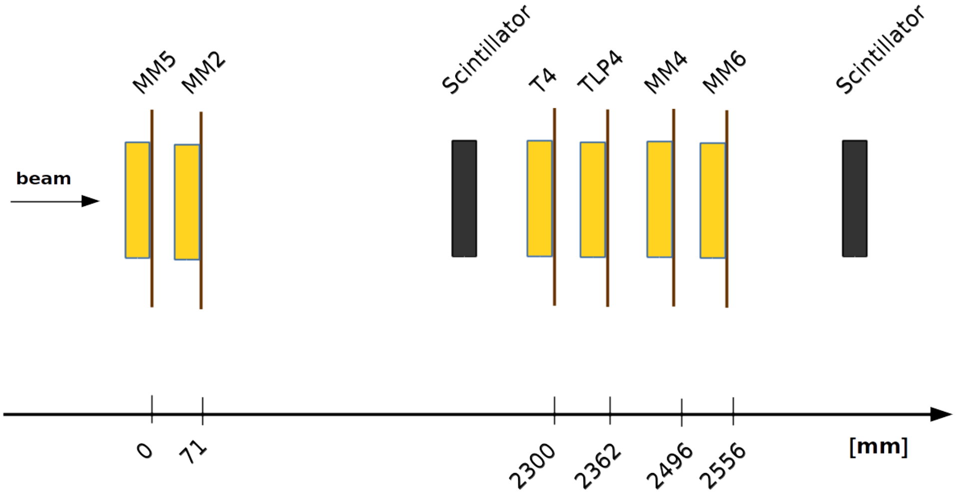

Figure F.1: Experimental set-up at SPS, not to scale.

The geometric-mean method is based on a straight track fit which is performed with the least-square method. The track parameters of the fit are used to estimate the predicted hit position in a detector. The residuals between the measured and the predicted hit position yields a distribution which can be fitted with a Gaussian function. When a reference detector is included in the fit the width of the Gaussian distribution, σ_{in}, is smaller than the intrinsic spatial resolution of the detector (Fig. F.2(a)). If the detector is explicitly excluded from the track fit, the width of the Gaussian distribution, σ_{ex}, is larger than the intrinsic spatial resolution of the detector since the track is less constrained (Fig. F.2(b)).

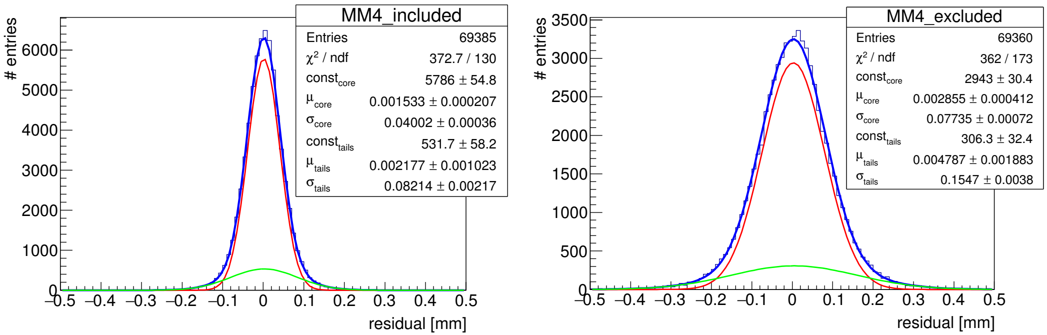

(a) (b)

Figure F.2: Residual distribution between the measured and the predicted hit position of MM4 when the detector is included in the fit (a) and when it is excluded (b).

The geometric-mean method takes into account both included and excluded distributions such that the spatial resolution of a reference detector i can be estimated by the following equation:

$$\sigma_{\text{SR}_{\text{ref,i}}} \approx \sqrt{\sigma_{\text{in,i}} \cdot \sigma_{\text{ex,i}}} \tag{F.1}$$

Knowing the spatial resolution of the reference detectors the track accuracy, σ_{track} [108, 109], can be calculated by:

$$\sigma_{\text{track}} = \sqrt{\frac{\Lambda_{22} - 2z\Lambda_{12} + z^2\Lambda_{11}}{D}} \tag{F.2}$$

where:

- z is defined along the beam direction
- $D = \Lambda_{11} \cdot \Lambda_{22} - \Lambda_{12}^2$
- $\Lambda_{11} = \sum_i \frac{1}{\sigma^2_{\text{SR}_{\text{ref,i}}}}$
- $\Lambda_{22} = \sum_i \frac{z_i^2}{\sigma^2_{\text{SR}_{\text{ref,i}}}}$
- $\Lambda_{12} = \sum_i \frac{z_i}{\sigma^2_{\text{SR}_{\text{ref,i}}}}$

The spatial resolution of a detector under test (T4 or TLP4 in Fig. F.1) which is explicitly excluded from the fit is then given by:

$$\sigma_{\mathrm{SR}} = \sqrt{\sigma_{\mathrm{ex}}^2 - \sigma_{\mathrm{track}}^2} \tag{F.3}$$

Bibliography

[1] ATLAS Collaboration, "Observation of a new particle in the search for the Standard Model Higgs boson with the ATLAS detector at the LHC," *Phys. Lett. B 716 (2012) 1.* [Online]. Available: http://dx.doi.org/10.1016/j.physletb.2012.08.020

[2] CMS Collaboration, "Observation of a new boson at a mass of 125 GeV with the CMS experiment at the LHC," *Phys. Lett. B 716 (2012) 30.* [Online]. Available: http://dx.doi.org/10.1016/j.physletb.2012.08.021

[3] CMS Collaboration, "Observation of a new boson with mass near 125 GeV in pp collisions at $\sqrt{s}$=7 and 8 TeV," *JHEP 06 (2013) 081.* [Online]. Available: http://dx.doi.org/10.1007/JHEP06(2013)081

[4] ATLAS Collaboration, "The ATLAS Experiment at the CERN Large Hadron Collider," *Journal of Instrumentation*, vol. 3, no. 08, p. S08003, 2008. [Online]. Available: http://dx.doi.org/10.1088/1748-0221/3/08/S08003

[5] CMS Collaboration, "The CMS experiment at the CERN LHC," *Journal of Instrumentation*, vol. 3, no. 08, p. S08004, 2008. [Online]. Available: http://dx.doi.org/10.1088/1748-0221/3/08/S08004

[6] P. W. Higgs, "Broken Symmetries and the Masses of Gauge Bosons," *Phys. Rev. Lett. 13, 508 (1964).* [Online]. Available: https://doi.org/10.1103/PhysRevLett.13.508

[7] F. Englert and R. Brout, "Broken Symmetry and the Mass of Gauge Vector Mesons," *Phys. Rev. Lett. 13, 321 (1964).* [Online]. Available: https://doi.org/10.1103/PhysRevLett.13.321

[8] The LHC working group, "Large Hadron Collider in the LEP tunnel," *ECFA-CERN Workshop, on Large Hadron Collider in the LEP tunnel*, 1984. [Online]. Available: http://dx.doi.org/10.1016/0920-5632(90)90637-A

[9] U. Amaldi, "Physics and detectors at the Large Hadron Collider and at the CERN Linear Collider," *Workshop on Physics at Future Accelerators, La Thuile, Italy*, vol. DOI:10.5170/CERN-1987-007-V-1.323, 1987.

[10] J.H. Mulvey, "The feasibility of experiments at high luminosity at the Large Hadron Collider : report of the High-Luminosity Study Group to the CERN

Long-Range Planning Committee," *CERN Yellow Reports: Monographs*, vol. CERN-88-02, 1988.

[11] Y. Baconnier, G. Brianti, Ph. Lebrun, A.G. Mathewson, R. Perin, "LHC: the Large Hadron Collider accelerator project," *ECFA-CERN Workshop, on Large Hadron Collider in the LEP tunnel*, vol. CERN-AC-93-03-LHC, 1993.

[12] M. Benedikt, P. Collier, V. Mertens, J. Poole, K. Schindl, "LHC Design Report," vol. CERN-2004-003, 2004.

[13] CERN. Geneva. LHC Experiments Committee, "ATLAS : technical proposal for a general-purpose pp experiment at the Large Hadron Collider at CERN," vol. CERN-LHCC-94-43 ; LHCC-P-2, 1994.

[14] L. Evans and P. Bryant, "LHC machine," *Journal of Instrumentation*, vol. 3, no. 08, p. S08001, 2008. [Online]. Available: http://dx.doi.org/10.1088/1748-0221/3/08/S08001

[15] ALICE Collaboration, "The ALICE experiment at the CERN LHC," *Journal of Instrumentation*, vol. 3, no. 08, p. S08002, 2008. [Online]. Available: http://dx.doi.org/10.1088/1748-0221/3/08/S08002

[16] LHCb Collaboration, "The LHCb Detector at the LHC," *Journal of Instrumentation*, vol. 3, no. 08, p. S08005, 2008. [Online]. Available: http://dx.doi.org/10.1088/1748-0221/3/08/S08005

[17] G. Apollinari, I. Béjar Alonso, O. Brüning, M. Lamont, L. Rossi, "High-Luminosity Large Hadron Collider (HL-LHC). Preliminary Design Report," *CERN-2015-005, (CERN, Geneva, 2015)*, 2015. [Online]. Available: http://dx.doi.org/10.5170/CERN-2015-005.1

[18] The ATLAS Muon Collaboration, "The ATLAS Muon spectrometer: Technical design report," *CERN-LHCC-97-22*, May 1997.

[19] ATLAS Collaboration, "The ATLAS Inner Detector commissioning and calibration," *European Physical Journal C*, vol. 70, no. 3, pp. 787–821, 2010. [Online]. Available: http://dx.doi.org/10.1140/epjc/s10052-010-1366-7

[20] ATLAS Collaboration, "ATLAS Insertable B-Layer Technical Design Report," *CERN-LHCC-2010-013 , ATLAS-TDR-19*, September 2010.

[21] B. Mindur on behalf of the ATLAS Collaboration, "ATLAS Transition Radiation Tracker (TRT): Straw tubes for tracking and particle identification at the Large Hadron Collider." *Nuclear Inst. and Methods in Physics Research, A, Volume 845, p. 257-261.*, 2017. [Online]. Available: http://dx.doi.org/10.1016/j.nima.2016.04.026

[22] ATLAS Collaboration, "Technical Design Report for the ATLAS Inner Tracker Strip Detector," *CERN-LHCC-2017-005 ; ATLAS-TDR-025*, April 2017.

[23] H. Zhang on behalf of the ATLAS Liquid Argon Calorimeter Group, “The ATLAS Liquid Argon Calorimeter: Overview and Performance,” *Journal of Physics: Conference Series*, vol. 293, no. 1, p. 012044, 2011. [Online]. Available: http://dx.doi.org/10.1088/1742-6596/293/1/012044

[24] P. Francavilla on behalf of the ATLAS Collaboration, “The ATLAS Tile Hadronic Calorimeter performance at the LHC,” *Journal of Physics: Conference Series*, vol. 404, no. 1, p. 012007, 2012. [Online]. Available: http://dx.doi.org/10.1088/1742-6596/404/1/012007

[25] Yu Nakahama on behalf of the ATLAS Collaboration, “The ATLAS Trigger System: Ready for Run-2,” *Journal of Physics: Conference Series 664 (2015) 082037*. [Online]. Available: https://doi.org/10.1088/1742-6596/664/8/082037

[26] M. J. Woudstra, “Precision of the ATLAS muon spectrometer,” *CERN-THESIS-2003-015*. [Online]. Available: http://cds.cern.ch/record/620198?ln=en

[27] A. Schricker, “The Alignment System of the ATLAS Muon End-Cap Spectrometer,” *CERN-THESIS-2002-045*. [Online]. Available: http://cds.cern.ch/record/1316176?ln=en

[28] ATLAS Collaboration, “Technical Design Report for the Phase-I Upgrade of the ATLAS TDAQ System,” *CERN-LHCC-2013-018; ATLAS-TDR-023*, November 2013.

[29] ATLAS Collaboration, “Performance of the ATLAS Trigger System in 2015,” *Submitted to Eur. Phys. J. C*, 2016. [Online]. Available: arXiv:1611.09661

[30] ATLAS Collaboration G. Aad, B. Abbott et al. , “Muon reconstruction performance of the ATLAS detector in proton–proton collision data at $\sqrt{s}$ = 13 TeV,” *Eur. Phys. J. C (2016) 76:29*. [Online]. Available: https://doi.org/10.1140/epjc/s10052-016-4120-y

[31] L. Marchese on behalf of the ATLAS Collaboration, “Muon reconstruction performance of the ATLAS detector in 2016,” *EPJ Web of Conferences in proceedings*. [Online]. Available: https://cds.cern.ch/record/2292925/files/ATL-PHYS-PROC-2017-246.pdf

[32] B. Bittner, J. Dubbert, H. Kroha, R. Richter and P. Schwegler, “Tracking and Level-1 triggering in the forward region of the ATLAS Muon Spectrometer at sLHC,” *Journal of Instrumentation*, vol. 7, no. 01, p. C01048, 2012. [Online]. Available: http://stacks.iop.org/1748-0221/7/i=01/a=C01048

[33] B. Bittner et al., “Performance of drift-tube detectors at high counting rates for high-luminosity LHC upgrades,” *Nuclear Instruments and Methods in Physics Research Section A*, pp. 250–254, December 2013. [Online]. Available: http://dx.doi.org/10.1016/j.nima.2013.07.076

[34] ATLAS Collaboration, “Measurements of the properties of the Higgs-like boson in the four lepton decay channel with the ATLAS detector using 25 fb^1 of proton-proton collision data,” *ATLAS-CONF-2013-013.*

[35] ATLAS Collaboration, “New Small Wheel Technical Design Report,” *CERN-LHCC-2013-006; ATLAS-TDR-020*, July 2013.

[36] “CERN Engineering and Equipment Data Management Service.” [Online]. Available: https://edms.cern.ch

[37] Y. Giomataris et al., “Micromegas: a high-granularity position-sensitive gaseous detector for high particle-flux environments,” *Nuclear Instruments and Methods in Physics Research Section A 376*, pp. 29–35, December 1996. [Online]. Available: http://dx.doi.org/10.1016/0168-9002(96)00175-1

[38] T. Alexopoulos et al., “Development of large size Micromegas detector for the upgrade of the ATLAS muon system,” *Nuclear Instruments and Methods in Physics Research Section A617*, pp. 161–165, 2010. [Online]. Available: http://dx.doi.org/10.1016/j.nima.2009.06.113

[39] “CERN RD51 Collaboration: Development of Micro-Pattern Gas Detectors Technologies.” [Online]. Available: http://rd51-public.web.cern.ch/rd51-public/

[40] F. Kuger, “Signal Formation Processes in Micromegas Detectors and Quality Control for large size Detector Construction for the ATLAS New Small Wheel,” *CERN-THESIS-2017-106*. [Online]. Available: http://cds.cern.ch/record/2277011/files/CERN-THESIS-2017-106.pdf

[41] H. Raether, “Electron Avalanches and Breakdown in Gases.” *London : Butterworths*, 1964.

[42] T. Alexopoulos et al., “A Spark-Resistant Bulk-Micromegas Chamber for High-Rate Applications.” *Nuclear Instruments and Methods in Physics Research Section A640*, pp. 110–118, 2011. [Online]. Available: http://dx.doi.org/10.1016/j.nima.2011.03.025

[43] A. Ochi, “Development of large area resistive electrodes for ATLAS NSW Micromegas,” *EPJ Web of Conferences*, MPGD 2015, accepted for publication.

[44] P. Lösel, “Construction and Quality Assurance of Large Area Resistive Strip Micromegas for the Upgrade of the ATLAS Muon Spectrometer at LHC/CERN,” *JINST, Volume 12, June 2017.* [Online]. Available: http://dx.doi.org/10.1088/1748-0221/12/06/C06005

[45] P. Lösel and R. Müller, “Design and Construction of Large Size Micromegas Chambers for the Upgrade of the ATLAS Muon Spectrometer,” *arXiv:1508.02541 [physics.ins-det]*. [Online]. Available: https://arxiv.org/pdf/1508.02541.pdf

[46] M. Bianco, O. Sidiropoulou et al., "Construction of two large-size four-plane micromegas detectors," *Nucl. Instr. Meth.* **A 814** *(2016) 117-130.* [Online]. Available: http://dx.doi.org/10.1016/j.nima.2016.01.049

[47] A. Ochi et al., "Carbon Sputtering Technology for MPGD detectors," *PoS TIPP2014 (2014) 351.*

[48] " Mini-X X-Ray Tube System for XRF ." [Online]. Available: http://amptek.com/products/mini-x-ray-tube/

[49] T. Alexopoulos et al., "Stereo Information in Micromegas Detectors," *ATL-MUON-PUB-2015-001.* [Online]. Available: http://cds.cern.ch/record/2052206/files/ATL-MUON-PUB-2015-001.pdf

[50] T.H. Lin et al., "Signal Characteristics of a Resistive-Strip Micromegas Detector with an Integrated Two-Dimensional Readout," *arXiv:1406.6871.* [Online]. Available: http://dx.doi.org/10.1016/j.nima.2014.09.002

[51] T.H. Lin., "Measurement of the W boson charge asymmetry in proton-proton collisions at $\sqrt{s} = 8$ TeV and developments towards the upgrade of the ATLAS Muon Spectrometer," *Phd thesis submitted on September 2017.*

[52] K. Ntekas, "Performance characterization of the Micromegas detector for the New Small Wheel upgrade and Development and improvement of the Muon Spectrometer Detector Control System in the ATLAS experiment," *CERN-THESIS-2016-019.* [Online]. Available: http://cds.cern.ch/record/2143887/files/CERN-THESIS-2016-019.pdf

[53] J. Bortfeldt et al. , "Performance Tests of a Resistive Micromegas Detector Quadruplet," *IEEE 2016 Nuclear Science Symposium and Medical Imaging Conference.*

[54] M. Bianco, P.J. Loesel, S. Martoiu, O. Sidiropoulou and A. Zibell, "Development and test of a versatile DAQ system based on the ATCA standard," *PoS TIPP2014 (2014) 202 .*

[55] M. Bianco, S. Martoiu, O. Sidiropoulou and A. Zibell on behalf of the ATLAS Muon Collaboration, "Development and test of the DAQ system for a Micromegas prototype to be installed in the ATLAS experiment," *Journal of Physics: Conference Series 664 (2015) 082056.* [Online]. Available: https://doi.org/10.1088/1742-6596/664/8/082056

[56] S. Martoiu, H. Muller, A. Tarazona and J. Toledo, "Development of the scalable readout system for micro-pattern gas detectors and other applications," *Journal of Physics: Conference Series 8 (2013) C03015.* [Online]. Available: https://doi.org/10.1088/1748-0221/8/03/C03015

[57] AdvancedTCA®. [Online]. Available: https://www.picmg.org/openstandards/advancedtca/

[58] "Preliminary MMFE-8 Specification ver 0.5, February 2015." [Online]. Available: http://atlas.physics.arizona.edu/~kjohns/downloads/0301-MMFE-8/0301-MMFE-8-Specification/MMFE-8-Specification-020515.pdf

[59] G. De Geronimo et al., "VMM1-An ASIC for Micropattern Detectors," *IEEE Trans. On Nuclear Sci, vol. 60, no. 3, pp. 2314-2321, May 2013.*

[60] P. Gkountoumis, "Level-1 Data Driver Card of the ATLAS New Small Wheel upgrade," *Nuclear Science Symposium and Medical Imaging Conference (NSS/MIC), 2015 IEEE.* [Online]. Available: https://doi.org/10.1109/NSSMIC.2015.7581785

[61] A. Zibell and O. Biebel, "High-rate irradiation of 15mm muon drift tubes and development of an ATLAS compatible readout driver for micromegas detectors," *PhD thesis 2014.* [Online]. Available: http://inspirehep.net/record/1429514

[62] P. Gallno, "The ATLAS Local Trigger Processor (LTP)," *ATL-DA-ES-0033, EDMS ID 374560.* [Online]. Available: http://edms.cern.ch/document/374560

[63] S. Baron, "The TTC System." [Online]. Available: http://ttc.web.cern.ch/TTC/intro.html

[64] P. Gallno, "The ATLAS ROD BUSY Module," *EDMS ID 319209.* [Online]. Available: https://edms.cern.ch/document/319209/1

[65] Ph. Farthoua, "LTP INTERFACE." [Online]. Available: https://twiki.cern.ch/twiki/bin/viewfile/Main/MyATLASDocumentation?rev=1.1;filename=Interface_spec-v4.3.pdf

[66] J. Almeida, M. Dobson, A. Kazarov, G. Lehmann Miotto, J.E. Sloper, I. Soloviev and R. Torres , "The ATLAS DAQ System Online Configurations Database Service Challenge ," *Journal of Physics: Conference Series 119 (2008) 022004.* [Online]. Available: https://doi.org/10.1088/1742-6596/119/2/022004

[67] S. Chakraborty, K. Nemoto, K. Hara and P T Lai, "Moisture sensitive field effect transistors using $SiO_2/Si_3N_4/Al_2O_3$ gate structure," *Smart Mater. Struct.* ***8*** *274 (1999)* . [Online]. Available: https://doi.org/10.1088/0964-1726/8/2/014

[68] "Fluke." [Online]. Available: http://en-us.fluke.com/

[69] "ElectroScience." [Online]. Available: http://www.czpartner.com/upfile/15-12613QQ_103250212_57bUqqPDxv33717.pdf

[70] Climats®, "Environmental test chamber." [Online]. Available: http://www.climats.hu/images/PDF/Excal.pdf

[71] "CERN Quality Assurance & Reliability Testing Lab." [Online]. Available: https://bondlab-qa.web.cern.ch/bondlab-qa/Climatic_Chamber.html

[72] DUPONT^{TM} KAPTON® , "Summary of properties." [Online]. Available: http://www.dupont.com/content/dam/dupont/products-and-services/membranes-and-films/polyimde-films/documents/DEC-Kapton-summary-of-properties.pdf

[73] J. Galan et al., "Aging studies of Micromegas prototypes for the HL-LHC," *JINST **7** (2012) C01041* . [Online]. Available: https://doi.org/10.1088/1748-0221/7/01/C01041

[74] F. Jeanneau et al., "Performances and ageing study of resistive-anodes Micromegas detectors for HL-LHC environment," *IEEE Trans. Nucl. Sci. **59** (2012) 1711-1716*. [Online]. Available: https://doi.org/10.1109/TNS.2012.2198492

[75] J. Galan et al., "An ageing study of resistive micromegas for the HL-LHC environment," *JINST **8** (2013) P04028* . [Online]. Available: https://doi.org/10.1088/1748-0221/8/04/P04028

[76] O. Sidiropoulou, B. Alvarez Gonzalez, M. Bianco, E.M. Farina, P. Iengo, L. Longo, D. Pfeiffer, J. Wotschack, "Performance studies under high irradiation and ageing properties of resistive bulk Micromegas chambers at the new CERN Gamma Irradiation Facility," *Nucl. Instrum. Methods Phys. Res. A, 845 (2017), pp. 293-297* . [Online]. Available: https://doi.org/10.1016/j.nima.2016.06.062

[77] B. Alvarez Gonzalez, J. Bortfeldt, M. T. Camerlingo, E.Farina, P. Iengo, L. Longo, J. Samarati, O. Sidiropoulou, J. Wotschack, "Radiation studies on resistive bulk-micromegas chambers at the CERN Gamma Irradiation Facility ," *PoS(EPS-HEP2017)477* .

[78] "CERN Gamma Irradiation Facility ." [Online]. Available: https://espace.cern.ch/sba-workspace/gifpp/SitePages/Home.aspx

[79] J. Va'vra, "Attempt to correlate the ionic model with observations in BaBar RPC chambers and R&D tests," *IEEE T. Nucl. Sci.***51 (2004) 2145** . [Online]. Available: http://dx.doi.org/10.1109/TNS.2004.836063

[80] M. Morales et al., "Conductivity and charge depletion aging of resistive electrodes for high rate RPCs," *JINST* **8 P01022 (2013)**. [Online]. Available: http://dx.doi.org/10.1088/1748-0221/8/01/P01022

[81] M. Morales et al., "Aging and conductivity of electrodes for high rate tRPCs from an ion conductivity approach," *PoS(RPC2012)024*.

[82] F. Kuger and P. Iengo on behalf of the ATLAS Muon Collaboration, "Design, construction and quality control of resistive-Micromegas anode boards for

the ATLAS experiment," *in proceedings of the MPGD 2015 in EPJ Web of Conference*, 2015. [Online]. Available: cds.cern.ch/record/2108985

[83] O. Sidiropoulou et al., "Characterization of Micromegas with elongated pillars," *JINST 12 C02076*, 2017. [Online]. Available: http://dx.doi.org/10.1088/1748-0221/12/02/C02076

[84] J. Samarati et al., "Study of the charge-up effect in Micromegas detectors." *5th International conference on Micro-pattern gas detectors (MPGD 2017). In proceedings.* .

[85] Carnegie et al., "Resolution studies of cosmic-ray tracks in a TPC with GEM readout," *Nucl. Instr. and Meth. A 538 (2005) 372 – 383.*

[86] F. Sauli, "Gaseous Radiation Detectors: Fundamentals and Applications," *Cambridge University Press* , 2014.

[87] W. R. Leo, "Techniques for Nuclear and Particle Physics Experiments," *Springer-Verlag* , 1994.

[88] C. Patrignani et al., "Particle Data Group," *Chin. Phys. C, 40, 100001 (2016) and 2017 update* . [Online]. Available: http://pdg.lbl.gov/

[89] W. Blum, W. Riegler and L. Rolandi, "Particle Detection with Drift Chambers," *2008 Springer-Verlag Berlin Heidelberg.*

[90] M. J. Berger et al., "NIST XCOM: Photon Cross Sections Database." [Online]. Available: https://www.nist.gov/pml/xcom-photon-cross-sections-database

[91] P. Thuiner, "Ion space-charge effects in multi-GEM detectors: challenges and possible solutions for future applications," *CERN-THESIS-2016-199.* [Online]. Available: http://cds.cern.ch/record/2238855/files/CERN-THESIS-2016-199.pdf

[92] "ANU database, retrieved on September 16, 2017." [Online]. Available: http:www.lxcat.net

[93] G.J.M. Hagelaar and L.C. Pitchford, "Solving the Boltzmann equation to obtain electron transport coefficients and rate coefficients for fluid models," *Plasma Sci Sources and Tech 14, 722 (2005).*

[94] R. Veenhof, "Garfield++: a toolkit for the detailed simulation of particle detectors that use gas and semi-conductors as sensitive medium." [Online]. Available: {http://garfieldpp.web.cern.ch/garfieldpp/}

[95] A.C. Melissinos, "Experiments in Modern Physics," *Academic Press*, New York 1966.

[96] "Caesium-137." [Online]. Available: https://en.wikipedia.org/wiki/Caesium-137#/

[97] D. Pfeiffer et al., "The Radiation Field in the New Gamma Irradiation Facility GIF++ at CERN," *Nuclear Inst. and Methods in Physics Research, A 866*, pp. 91–103, 2017. [Online]. Available: https://doi.org/10.1016/j.nima.2017.05.045

[98] M.Raymond et al. , "The APV25 0.25 μm CMOS readout chip for the CMS tracker ," IEEE Nucl. Sci. Symp. Conf. Rec **2** *(2000), 9/113*. [Online]. Available: https://doi.org/10.1109/NSSMIC.2000.949881

[99] P. Placidi, A. Marchioro and P. Moreira , "CMS Tracker PLL Reference Manual ," *CERN - EP/MIC, Geneva Switzerland, July 2000*. [Online]. Available: http://cms-ecal-monitoring.web.cern.ch/cms-ecal-monitoring/datasheets/tpll.pdf

[100] J. Toledo et al. , "The Front-End Concentrator card for the RD51 Scalable Readout System ," JINST **6** *C11028 (2011)*. [Online]. Available: https://doi.org/10.1088/1748-0221/6/11/C11028

[101] S. Martoiu et al. , "Front-end electronics for the Scalable Readout System of RD51 ," *Nuclear Science Symposium and Medical Imaging Conference (NSS/MIC), IEEE (2011)*. [Online]. Available: https://doi.org/10.1109/NSSMIC.2011.6154414

[102] A. Tarazona et al. , " A point-to-point link for data, trigger, clock and control over copper or fibre ," JINST **9** *T06004 (2014)*. [Online]. Available: https://doi.org/10.1088/1748-0221/9/06/T06004

[103] D.C. Arogancia et al., "Study in a beam test of the resolution of a Micromegas TPC with standard readout pads," *Nucl. Instrum. and Meth. A 602 (2009) 403-414*. [Online]. Available: https://doi.org/10.1016/j.nima.2009.01.014

[104] J.E. Ducret et al., "Heavy-ion test of detectors with conventional and resistive Micromegas used in TPC configuration," *Nucl. Instrum. and Meth. A 628 (2011) 166-171*. [Online]. Available: https://doi.org/10.1016/j.nima.2010.06.309

[105] K. Gnanvo et al., "Large size GEM for Super Bigbite Spectrometer (SBS)," *Nucl. Instrum. and Meth. A 782 (2015) 77-86*. [Online]. Available: https://doi.org/10.1016/j.nima.2015.02.017

[106] T. Alexopoulos et al., "Examining the geometric mean method for the extraction of spatial resolution," *JINST 9 P01003 (2014)*. [Online]. Available: https://doi.org/10.1088/1748-0221/9/01/P01003

[107] A. Zhang and M. Hohlmann , "Accuracy of the geometric-mean method for determining spatial resolutions of tracking detectors in the presence of multiple Coulomb scattering," *JINST 11 P06012 (2016)*. [Online]. Available: https://doi.org/10.1088/1748-0221/11/06/P06012

[108] S. Horvat, "Study of the Higgs Discovery Potential in the Process pp $\to$ H $\to$ 4μ," *PhD thesis (CERN-THESIS-2005-036), Zagreb University, 2005.*

[109] J. Bortfeldt, “Development of Floating Strip Micromegas Detectors,” *PhD thesis, Munich, 2014*. [Online]. Available: http://d-nb.info/1052911137

Acknowledgements

Since this part of the thesis is the last one written and the more relaxed I would like to take the opportunity and acknowledge all the people who helped me during my PhD studies and all those with whom we worked together.

First of all, I would like to thank my university supervisor Thomas Trefzger, my supervisor at CERN Christoph Rembser and the responsible of the BMBF Gentner scholarship at CERN Michael Hauschild who accepted me and helped me to do my PhD studies at CERN. I would like also to thank the particle physics group of the University of Würzburg with Raimund Ströhmer and my colleagues, especially Giovanni Siragusa and Verena Herget with whom we had a very nice time during the DPG conferences in different places each time in Germany and during their visits at CERN.

My deep gratitude is with Jörg Wotschack with whom we spend a lot of time doing several nice, interesting measurements and analysis work. I am deeply grateful also for all your help and your time that you have dedicated to go through this write-up many times and provide me with comments and suggestions. It is more than a pleasure to work with you as one can learn a lot and profit from your knowledge! Jörg many thanks for all your help and support during all these years!

From the EP-ADE-MU group, I would like also to thank first of all Paolo Iengo. Paolo thank you very much for all the nice projects that you have assigned to us and your support to send all of us in several conferences. I think we are all grateful for all your effort to keep a balance in the different projects that we had all these years and keep this group united. I think also our former and current colleagues of this group would agree on that namely Michele Bianco, Edoardo Farina, Barbara Alvarez Gonzalez, Jona Bortfeldt, Jerome Samarati, Fabian Kuger. Guys thanks a lot for the nice time that we have and had inside and of course outside CERN. In the same context, I would like also to thank Luigi Longo involved in some measurements and providing us with a nice DCS tool; our summer students Dimitra Andreou and Katie Louise Spencer for their help in the GIF++ activities; Maria Teresa Camerlingo who joined us in several activities for three months and Orestis Karapiperis, a young school student full of enthusiasm that joined us for a month back in 2015. Thank you very much for your help!

More than a pleasure though was spending almost four complete years in the RD51/GDD laboratory at CERN, in blg 154, and have the chance to meet all these wonderful people who work there or even come for a while from times to times. I have no words to express my feelings. To my opinion, this group is something unique at CERN and more than providing help in this laboratory and keep us always up-to-date in the field of micro pattern gaseous detectors, the working environment is more than an enjoyment! I am most thankful to my friends Leszek Ropelewski, Eraldo Oliveri, Filippo Resnati, Dorothea Pfeiffer, Hans Müller, Patrik Thuiner, Florian Brunbauer and Michael Lupberger. I will really miss a lot these years! The same is true for my friend Silvia Franchino working back then in the MPT workshop, Rui de Oliveria and his team for their production and advises to optimize measurements, Diego Gonzalez Diaz and Jeremie Merlin who worked in the RD51/GDD some time ago. Thank you all a lot for the nice time that we have spent and we still spend together!

For several measurements that we did with the MMSW quadruplet I would like also to thank Matthias Schott, Tai Hua Lin and Andreas Düdder from the university of Mainz. We had a really nice time back then together with Jörg Wotschack, Paolo Iengo, Michele Bianco, Givi Sekhniaidze and Edoardo Farina. Edo many thanks for Fig. 5.40 and 5.41 and Tai-Hua for Fig. 5.47 and 5.48.

For the DAQ that was developed for the MMSW I would like to thank Andre Zibell, Sorin Martoiu and Hans Müller. For the integration of this DAQ system in the ATLAS TDAQ software I am more than thankful to Wainer Vandelli, Kostas Kordas, Antonis Leisos, Andrei Kazarov, Giovanna Lehmann Miotto, Serguei Kolos, Thilo Pauly, Kristof Schmieden, Nicoletta Garelli, Philipp Fleischmann, Enrico Pasqualucci, Stephanie Zimmermann, Markus Joos and to the ATLAS TDAQ Sysadmin group for their continuous help till the successful integration.

For the Kapton foils I would like to thank Atsuhiko Ochi, Tatsuya Masubuchi and Masahiro Yamatani. Thank you all very much for the nice and interesting discussions that we have related to this subject.

For the tests performed with the Kapton foils in the environmental chamber in the Quality Assurance & Reliability Testing Lab at CERN, I would like to thank Julien Bonnaud and Florentina Manolescu from the EP-DT-DD department for their valuable and interesting discussions that we had during the periods of these measurements.

Many thanks also to you Kosta Korda, Chara Petridou, Spyridon Tzamaria, Dimo Samsonidi from the Aristotle University of Thessaloniki for all your support during my studies at CERN.

A big thank also to my dearest friends in Greece who every time I go there they are waiting for me and even change their vacations plan to meet altogether!

Last but not least, I am more than grateful to my mother Eleni, my brother George, my sister Zoe, my grandfathers, my uncles, my aunts and my cousins (big greek family :)) who didn't see me very often all these years but they are always next to me! And of course to Kostas for his continues support! Thank you all very much for what you did for me!

This thesis is dedicated to the memory of my father ...